

Pulsar Characteristics Across The Energy Spectrum



Agnieszka Słowikowska
Nicolaus Copernicus Astronomical Center
Department of Astrophysics in Toruń

Ph. D. Thesis written under the supervision of
Dr. Bronisław Rudak

Warsaw 2006

I dedicate this thesis to my husband

Acknowledgements

I am deeply grateful to many people for their help and support during my studies. In particular, I would like to thank Dr. Bronisław Rudak for giving me the opportunity to work as a member of a pulsar group at Copernicus Astronomical Center, and for supervising my PhD thesis. I am grateful to the Director of CAMK for offering me the fellowship, support, and excellent conditions to study and work. I am grateful to both, the European Association for Research in Astronomy Marie Curie Training Site and Deutsche Akademischer Austausch Dienst for the EARASTAR-GAL and DAAD fellowships, respectively. This work was also supported by KBN grant 2P03D.004.24.

I am very grateful to Bronek Rudak for all his help, support and advice during my PhD. I would especially like to thank him for reading the thesis and for giving me comments and advice on how to significantly improve it. I appreciate very much his help in organising the formal preparation of getting the degree. I am thankful for financial support, for sending letters of recommendation, and for allowing me to present my work at various conferences and meetings. Additionally, for encouraging me to apply for different fellowships and for giving me opportunities to work outside Poland. I am most grateful for his friendship.

I would like to thank Gottfried Kanbach, Axel Jessner, Lucien Kuiper, Wim Hermsen, Roberto Mignani and Werner Becker for giving me the possibilities to work with them. Special thanks to Gottfried Kanbach for his support during the application for the EARA and DAAD fellowships. Very deep thanks to Jarek Dyks for always being ready to explain and discuss theoretical pulsar aspects. Special thanks to Gottfried Kanbach, Axel Jessner and Roberto Mignani for writing recommendation letters.

All my work could not have been done without help from Jurek Borkowski and Michał Jaśtak. Thank you very much for being patient and ‘user-friendly’ computer administrators. I am grateful to all people from CAMK

administration department for being very helpful with all administrative procedures.

I am thankful to all my astronomical and non-astronomical friends that I met in Poland, Holland and Germany, not only for astronomical discussions, but also for great time that I spent with them. Special thanks to all my Polish friends for a great time spent far away from the computer.

I would like to thank my family, especially my husband Tomek for being so patient with me, for forgiving all my strange ideas and for his unconditional love. I am grateful to my parents, Marek and Ela, for their love, support and help during my PhD: to my Daddy for pushing me with writing the thesis, and to my Mom for designing and building our great house. Many thanks to my private doctors, my sis Iza and her's husband Adam. To Iza for taking care of my health, and to Adam and Dr. Brycki for the greatest surgic operation ever done. Thank you.

Contents

1	Introduction	1
1.1	Neutron stars and pulsars	1
1.2	Observational characteristics of pulsars	6
1.3	Distribution of pulsars in the Galaxy	12
1.4	Pulsars across the electromagnetic spectrum	12
1.5	The Crab pulsar and its nebula	17
1.6	An outline of the thesis and statement of originality	19
2	Enhanced radio emission from the Crab pulsar	21
2.1	Introduction	21
2.2	Giant radio pulses	26
2.3	Effelsberg observations	26
2.3.1	EPOS - the Effelsberg Pulsar Observation System	27
2.3.2	LeCroy oscilloscope - an ultra-high resolution detection system	28
2.4	EPOS data analysis	28
2.4.1	GRPs statistics	29
2.4.2	Polarisation	32
2.5	High resolution detections	35
2.6	Conclusions	35
3	Optical polarimetry of the Crab pulsar	39
3.1	Introduction	39
3.2	Observations	40
3.2.1	Nordic Optical Telescope	40
3.2.2	OPTIMA instrument	41
3.2.3	Weather and seeing conditions during the observations	47
3.3	Data reduction	51
3.3.1	Flat field correction	51

CONTENTS

3.3.2	Raw data binning	51
3.3.3	Rotating polarisation filter characteristics	53
3.3.4	Polarisation data analysis	62
3.3.5	The HST polarisation standards	73
3.4	Results	78
3.4.1	Nebular contribution	78
3.4.2	Time alignment between optical and radio wavelengths	82
3.4.3	Polarisation characteristics of the Crab pulsar	84
3.4.4	Polarisation characteristics of the Crab pulsar after DC subtraction	89
3.5	Summary and discussion	89
3.6	Conclusions	97
4	PSR B0540-69 - the Crab twin in the Large Magellanic Cloud	98
4.1	Introduction	98
4.2	The <i>INTEGRAL</i> satellite	99
4.3	Observations	100
4.4	IBIS/ISGRI data analysis and results	102
4.5	JEM-X data analysis and results	111
4.6	Summary	115
5	PSR B1929+10 revisited in X-rays	116
5.1	Introduction	116
5.2	Previous results	117
5.3	Observations	118
5.4	Timing analysis	120
5.4.1	ROSAT PSPC-B	120
5.4.2	ROSAT HRI	122
5.4.3	ASCA GIS	123
5.4.4	RXTE PCA	125
5.5	Comparison of the X-ray and radio profile	127
5.6	Spectral analysis	128
5.6.1	High value of the neutral hydrogen column density	131
5.7	The X-ray emitting trail	133
5.8	Summary and conclusions	134
6	Closing remarks	142

A OPTIMA data files	145
B ROSAT timing	147

Chapter 1

Introduction

1.1 Neutron stars and pulsars

The discovery of pulsars

In 1934 Baade and Zwicky suggested that stars might end their lives as neutron stars (Baade & Zwicky 1934a,b). This hypothesis was introduced in an effort to account for liberation of tremendous amount of energy in supernova explosions. They suggested the existence of stars and cores of stars with the average density of nuclear matter. It took more than 30 years to confirm the existence of these objects in the Universe.

The first object (which eventually turned out to be a rapidly rotating highly magnetised neutron star) - CP 1919 - was discovered by Jocelyn Bell and Antony Hewish at Cambridge in 1967 (Hewish et al. 1968). The pulse period of 1.3373 s was much shorter than the time scale on which normal stars can vary, and the recurrence of the pulses was extremely regular. This object is known as PSR B1919+21¹ now.

Radially pulsating white dwarf stars were proposed at first as an explanation and remained popular for some time (Hewish et al. 1968). In contrast to neutron stars, white dwarfs had been observed and relatively well understood for some time. This idea was even more supported when the second periodicity in the original pulsar, having the source in the drifting subpulses, was observed (Drake & Craft 1968). It was considered as higher harmonics of fundamental frequency. By the end of the year 1968 the situation changed dramatically. Two new pulsars were discovered: in the Vela supernova remnant a 0.089 s pulsar was found (Large et al. 1968), and the Crab Nebula turned out to host a 0.033 s pulsar (Staelin & Reifenstein 1968). These new

¹PSR stands for Pulsating Source of Radio, while the numbers refer to its position at the sky, and the letter B refers to the coordinate system 1950. The modern convention is for all pulsars to have a J designation (2000 coordinates) and to retain the B designation only for those published prior to about 1993.

1. INTRODUCTION

observations were not speaking in favour of the oscillating white dwarf hypothesis. The rapidity of the pulsation ruled out this hypothesis. Moreover, pulsars were linked clearly to supernovae now.

Various phenomenological models of possible sources of these ‘pulsing’ signals were proposed. One of them was a ‘neutron star lighthouse’ model proposed by Gold (1968) and by Pacini (1967). Franco Pacini and Tommy Gold interpreted the repeating signals as the ‘lighthouse’ effect. They concluded independently that the radio beams were being emitted by a rotating, highly magnetised neutron star. Strong magnetic fields and subluminal rotation speeds would lead to relativistic velocities in any plasma in the surrounding magnetosphere, leading to anisotropic radiation in the form of a rotating beacon. This explanation - in which the radio waves are produced by synchrotron radiation from relativistic particles that are accelerated by the star’s magnetic field - was then positively verified.

The discovery by Richards & Comella (1969) that the Crab pulsar is slowing down its rotation was a firm confirmation of a rotating neutron-star model. The measured slow-down rate could be well explained by a dipolar magnetic field, which had to be strong to power the Crab Nebula (Pacini 1967). The observed value of the slow-down and the moment of inertia of a neutron star implied an energy loss rate that closely matched the observed luminosity of the nebula. Evidently, energetic particles, fed by the rotational energy, were responsible for it (Gold 1969).

The idea of neutron stars

Neutron stars (NS) are compact objects with masses comparable to that of the Sun but compressed into a volume with radius of about 10 to 15 km. They are formed in supernova explosions as the result of gravitational core-collapse of a massive (with initial mass between $\sim 8M_{\odot}$ and $\sim 30M_{\odot}$) star. Such collapse of the iron core occurs at the end of a massive ($M \gtrsim 8M_{\odot}$) star’s lifetime when its nuclear fuel is exhausted and it is no longer supported by the release of nuclear energy.

The question of internal structure of NSs was addressed by Oppenheimer and Volkoff long before the pulsar discovery (Oppenheimer & Volkoff 1939). The structure is determined by an equation of state (EOS) that relates its pressure to its density. One of the major goals in neutron-star astronomy is to constrain the EOS. Major global parameters of NS (like mass and radius) are obtained from the exact EOS; see for example Fig. 1.1 for mass and radius relation.

The density of a neutron star is close to that of a nucleus, but depends on its precise EOS. The NS’s composition can vary from neutrons with some addition of electrons

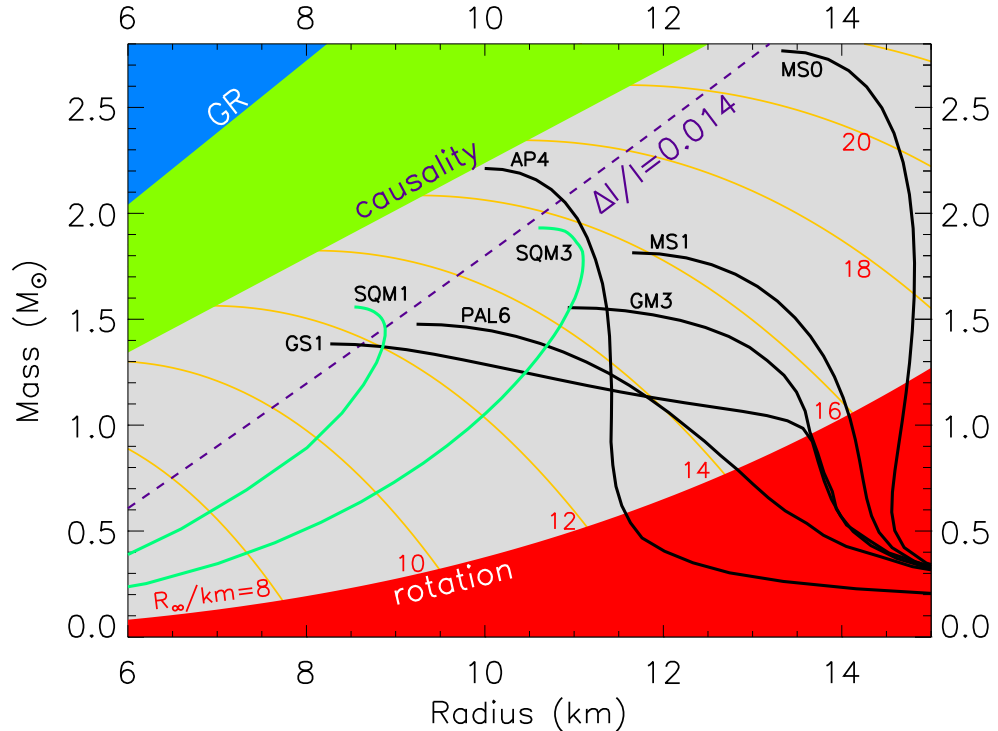


Figure 1.1: Mass-radius diagram for neutron stars. Black and green curves are for normal matter and for ‘strange quark matter’ (SQM) equation of state [for definition of the labels, see [Lattimer & Prakash \(2001\)](#)]. Regions excluded by general relativity (GR, the Schwarzschild condition $R \leq 2GM/c^2$), causality ($R \lesssim 3GM/c^2$) and rotation ($R = (\frac{G}{\Omega^2} M)^{1/3}$) constraints are indicated. For small masses, SQM stars are nearly incompressible ($R \propto M^{1/3}$). Contours of radiation radii $R_{\infty} = R(1+z)$, where R_{∞} is a value derived from the spectral fit, and z is the gravitational redshift, are given by the orange curves. The dashed line labeled $\Delta I/I = 0.014$ is a radius limit estimated from Vela pulsar glitches. [Figure after [Lattimer & Prakash \(2004\)](#)].

and protons to hyperons - particles that contain strange quarks - and possibly even free quarks. A $1.6 M_{\odot}$ NS, for example, would require an EOS that incorporated ‘exotic’ matter. However, most measured NS’s masses are close to $1.35 M_{\odot}$, albeit with interesting exceptions. Currently, the masses of more than 20 pulsars in binary systems are determined via precise timing ([Stairs 2004](#)). Better statistics expected from future very sensitive instruments (e.g. Square Kilometre Array) will allow deeper studies of the range of the NS masses.

On the other hand, available methods to determine the radii of NS are far less precise for the time being. They rely on spectral modelling of surface X-ray radiation due to initial cooling and require accurate distance estimates to the NS. The method

1. INTRODUCTION

is biased by influence of strong gravity, as well as magnetised atmospheres of unknown composition. Reliable measurements of NS radii are therefore, difficult to obtain and to use them to constrain the models.

Milestones

Pulsar observations have given us by far the most accurate confirmation of general relativity, and the first observations of the process of emission of gravitational waves, as well as many other new astronomical data.

Pulsar research has been driven by numerous surveys with many different radio telescopes over the years. These searches have discovered exciting new objects. At the moment there are 1627 pulsars known. The most important discoveries of pulsar radio astronomy are presented in Tab. 1.1.

Table 1.1: Milestones of pulsar radio astronomy (ordered chronologically)

Object	Description
PSR B1919+21	Cambridge discovery of pulsars, Hewish et al. (1968)
PSR B0531+21	Discovery of the Crab pulsar, Staelin & Reifenstein (1968)
PSR B1913+16	The first binary pulsar; experimental demonstration of the existence of gravitational waves, Hulse & Taylor (1974)
PSR B1937+21	The first millisecond pulsar, $\nu = 642$ Hz; for long time remains the most rapidly spinning NS known, Backer et al. (1982)
PSR B0540-69	The first extra-galactic pulsar, Seward et al. (1984)
PSR B1821-24	The first pulsar in globular cluster, M21, Lyne et al. (1987)
PSR B1257+12	The first pulsar planetary system; at the same time the first extra-solar planetary system discovered, Wolszczan & Frail (1992)
PSR B1620-26	The first triple system: a pulsar, a white dwarf, and a Jupiter-mass planet, Backer et al. (1993) , Thorsett et al. (1993)
PSR J0737-3039	The first ‘double pulsar’ system consisting of a 22.7 ms and 2.77 s pulsars; gives even more stringent constraints on gravitational theories than PSR B1913+16 Burgay et al. (2003) , Lyne et al. (2004) , Kramer et al. (2006)
PSR J1748-2446ad	The fastest spinning pulsar, $\nu = 716$ Hz, this pulsar located in Terzan 5 globular cluster beat the previous record of 642 Hz from PSR B1937+21, Hessels et al. (2006)

Present surveys

Many of the discoveries in the past six years, including the discovery of the first double pulsar J0737-3039 (see Tab. 1.1), were made using the 64-m Parkes telescope. The Parkes multi-beam pulsar survey¹ (PMBPS) is a sensitive survey of a strip along the Galactic plane with $|b| < 5^\circ$ and $l = 260^\circ$ to $l = 50^\circ$. It uses the multi-beam receiver system to collect data at 1.4 GHz from thirteen independent points in the sky (Manchester et al. 2001). The 1.4 GHz operating frequency of the PMBPS is particularly well suited for pulsar searches in the Galactic plane. Lower frequencies suffer from deleterious effects of pulse broadening due to interstellar scattering and dispersion, while pulsar flux densities typically are much reduced at higher frequencies. Therefore, the strong inverse frequency dependence of scattering clearly favours searches carried out at higher frequencies. More than one half of all known pulsars, including the slowest radio pulsar (Young et al. 1999), have been discovered with this system. Moreover, several pulsars with inferred magnetic field exceeding the critical field of $\sim 4.3 \times 10^{13}$ G were discovered. By this survey the large increase in the number of nulling pulsars - where radio emission appears to abruptly ‘switch off’ for many pulse period - is observed. The large number of radio pulsars discovered in this survey resulted also in a number of candidate associations between young pulsars and the unidentified EGRET sources. However, the EGRET sources have large positional error, thus such associations naturally are uncertain. To confirm these matches we need to wait for new γ -ray satellite missions like for example *AGILE* and *GLAST* that will greatly reduce positional uncertainties.

On the other hand, the recently started Arecibo L-band Feed Array (ALFA) pulsar survey aims to find ~ 1000 new pulsars (Cordes et al. 2006). The new survey is enabled by several innovations. ALFA is a seven-beam feed and receiver system designed for large-scale surveys in the 1.2–1.5 GHz band. The ALFA frontend is similar to the 13-beam system used for the extremely prolific PMBPS and will complement it in its sky coverage. Moreover, their initial and next-generation spectrometer systems have much finer resolution in both time and frequency than the spectrometer used with the PMBPS. This will allow to increase the detection volume of millisecond pulsars by an order of magnitude. Additionally, the sensitivity of the Arecibo telescope allows for short pointings that simplify the detection of binary pulsars undergoing strong acceleration. J. van Leeuwen et al. report already the results of their preliminary analysis: in the first months they have already discovered 21 new pulsars (van

¹<http://www.atnf.csiro.au/research/pulsar/pmsurv/>

1. INTRODUCTION

[Leeuwen et al. 2006](#)).

Radio pulsars catalogues can be found in the archive maintained at the Parkes Observatory operated by the Australia Telescope National Facility¹ (ATNF) and at the European Pulsar Network² (EPN). Although, the EPN data base contains smaller number of pulsars than the ATNF data base, it has a great advantage over the Australian catalogue. It provides not only the basic pulsar parameters, but also pulsar profiles at different frequencies, and in some cases the polarisation information, i.e. intensity profiles for all Stokes parameters.

Current population studies of pulsars suggest that our Galaxy contains $\sim 10^5 - 10^6$ active radio pulsars. Looking further ahead, the next-generation radio telescope - the Square Kilometre Array³ (SKA) - is expected to detect essentially $\sim 20,000$ (for some estimates even $\sim 30,000$) active radio pulsars. This telescope will have the sensitivity of more than 100 times that of the Parks telescope and should be ready to operate in 2015.

1.2 Observational characteristics of pulsars

Basic pulsar observables

Rotation-powered pulsars (RPPs) are generally referred to as ‘radio pulsars’, because in the vast majority of cases, they are observed only just at radio wavelengths. Rotational frequency ν (or corresponding period of rotation, $P = 1/\nu$) is the basic observational parameter of each pulsar. If possible its spin-down rate - first time derivative of ν - is measured also. Additionally, for some pulsars the second frequency derivative can be derived if only the regular, long term timing observations are performed.

A neutron star spinning with angular velocity $\Omega = 2\pi/P$, that decreases with time at the rate of $\dot{\Omega} = -2\pi P^{-2}\dot{P} < 0$, loses its rotational energy $E_{rot} = \frac{1}{2}I\Omega^2$. Thus the rate of the rotational kinetic energy loss is given by $\dot{E}_{rot} = I\Omega\dot{\Omega} = -4\pi^2 I\dot{P}/P^3$ with the assumption that stellar moment of inertia $I = kM_{NS}R_{NS}^2$ is constant, i.e. does not change with time. Coefficient k amounts to 0.4 for a sphere of uniform density distribution. For a NS, the exact value of k depends on the density profile, hence, on the equation of state. For most practical calculations $I \simeq 10^{45}$ g cm² is derived from the canonical NS parameters, $M_{NS} = 1.4 M_{\odot}$, $R_{NS} = 10$ km and $k = 0.4$.

¹<http://www.atnf.csiro.au/research/pulsar/psrcat/>

²<http://www.mpifr-bonn.mpg.de/div/pulsar/data/>

³<http://www.skatelescope.org/>

1.2 Observational characteristics of pulsars

The so called spin-down luminosity L_{sd} is directly related to the rotational kinetic energy loss rate by

$$L_{sd} = |\dot{E}_{rot}| \simeq 3.95 \times 10^{31} I_{45} \dot{P}_{-15} P^{-3} \text{ erg s}^{-1} \quad (1.1)$$

where P is in seconds, $\dot{P}_{-15} \equiv \dot{P}/10^{-15}$ and $I_{45} \equiv I/10^{45} \text{ g cm}^2$. One way of estimating pulsar magnetic field is to equate the rotational energy loss rate (Eq. 1.1) with that from a classical magnetic dipole radiation of a rotating magnetic dipole (Eq. 1.2). This estimate was first given by Ostriker and Gunn (Ostriker & Gunn 1969). The dipole (which represents the star) with its magnetic moment set by $B_s R_{NS}^3$, rotating in vacuum will lose energy at the rate

$$L_{magn} = \frac{2}{3c^3} B_s^2 \sin^2 \alpha R_{NS}^6 \Omega^4, \quad (1.2)$$

where α is an inclination angle between the dipole magnetic axis and the spin axis, and B_s is the strength of the magnetic field at the equator of the neutron star. Consequently, the inferred surface dipolar magnetic field B_s for an orthogonal rotator case, i.e. $\alpha = 90^\circ$, is

$$B_s \simeq 10^{12} \sqrt{P \dot{P}_{-15}} \text{ G} \quad (1.3)$$

for $I_{45} = 1$ and $R_{NS} = 10 \text{ km}$. Another model for estimating the pulsar magnetic field, where the dipolar radiation is replaced with a magnetospheric wind of particles, leads to a similar result, but it is independent of the inclination angle α .

Those two simple models give a differential equation for period P :

$$\dot{P} = KP^{-1}, \quad (1.4)$$

where B_s is now hidden in the parameter K .

This is a special case within the more general model for magnetic braking, which reads

$$\dot{P} = KP^{2-n}. \quad (1.5)$$

The parameter n is the braking index that reflects the true spin-down behaviour and K is usually assumed to be constant. For the simple model discussed above $n = 3$. In terms of ν the equation 1.5 corresponds to

$$\dot{\nu} = -K\nu^n. \quad (1.6)$$

The braking index can be determined, if in addition to $\dot{\nu}$, the second derivative of the spin frequency $\ddot{\nu}$ can be obtained from radio timing observations. By differentiating

1. INTRODUCTION

Eq. 1.6 and eliminating constant K , the braking index is related with the pulsar rotational parameters via

$$n = \frac{\nu\ddot{\nu}}{\dot{\nu}^2}. \quad (1.7)$$

Usually, the observed $\ddot{\nu}$ is contaminated by timing noise, therefore to get reliable value a long observational time span is needed. Thus, only for a few pulsars a determination of n has been possible. The values range from $n = 1.4$ to $n = 2.9$ (e.g. [Kaspi & Helfand 2002](#)).

By integrating Eq. 1.5 with the assumption of a constant K and $n \neq 1$ we obtain the age of the pulsar

$$T = \frac{P}{(n-1)\dot{P}} \left[1 - \left(\frac{P_0}{P} \right)^{n-1} \right]. \quad (1.8)$$

However, the spin period at birth P_0 is unknown. Assuming that the initial period is negligibly short ($P_0 \ll P$) and taking the braking index $n = 3$ the above equation leads to the so-called characteristic age

$$\tau_c \simeq \frac{P}{2\dot{P}} \simeq 15.8 \frac{P}{\dot{P}_{-15}} \text{ Myr}, \quad (1.9)$$

also known as the spin-down age. This quantity does not necessarily provide a reliable age estimate. For the Crab pulsar $\tau_c \simeq 1240$ yr, which is comparable to the age of about 950 years known from the Chinese observation of the supernova explosion. However, for some other objects larger discrepancies are known.

The pulsar magnetosphere is bounded by the ‘light cylinder’ of radius

$$R_{LC} = \frac{cP}{2\pi} \simeq 4.77 \times 10^4 P \text{ km}, \quad (1.10)$$

which is the distance from the spin axis at which the co-rotational speed equals the speed of light and it sets a natural limit on the size of the neutron star magnetosphere. The magnetic field strength at the light cylinder is given by

$$B_{LC} = B_s \left(\frac{\Omega R_{NS}}{c} \right)^3 \equiv B_s \left(\frac{2\pi R_{NS}}{cP} \right)^3 \simeq 9.2 P^{-5/2} \dot{P}_{-15} \text{ G}. \quad (1.11)$$

All field lines which cross the light cylinder are then considered as open lines, and their footpoints on the stellar surface define two polar caps of radius

$$R_{PC} = \sqrt{\frac{2\pi R_{NS}^3}{cP}} \equiv R_{NS} \sqrt{\frac{R_{NS}}{R_{LC}}} \simeq 150 P^{-1/2} \text{ m}. \quad (1.12)$$

The $P-\dot{P}$ diagram

The observed pulsar spin period P as well as the corresponding rate of spin-down \dot{P} can be obtained with very high accuracy through regular radio timing measurements. These values give us insights into the pulsar spin evolution. The best way to present it is to use the ‘ $P-\dot{P}$ diagram’ shown in Fig. 1.2. Two main groups of pulsars are clearly visible. The most numerous group is the group of ~ 1500 ‘normal pulsars’ ($P \sim 0.5$ s and $\dot{P} \sim 10^{-15}$ s s $^{-1}$) out of 1627¹ already known. Within this class of pulsars we can distinguish three subclasses. RPPs are called either young, or middle-age, or old if their spin-down age (Eq. 1.9) is of order a few times $10^3 - 10^4$, $10^5 - 10^6$, and $\geq 10^6$ years, respectively. Their inferred magnetic fields (Eq. 1.3) span the range from $\sim 10^{11}$ G to $\sim 10^{13}$ G. The second group, occupying the lower left part of the diagram, contains a hundred of ‘millisecond pulsars’ ($P \sim 5$ ms and $\dot{P} \sim 10^{-20}$ s s $^{-1}$). Their inferred magnetic fields span the range from $\sim 10^8$ G to $\sim 10^{10}$ G. In addition to rotational characteristics, a very important difference between normal and millisecond pulsars (MSPs) is binarity of most of the MSPs. The orbiting companions are either white dwarfs, main sequence stars or other NSs (i.e. double neutron stars binaries - DNS). Evolutionary, it is possible that some binaries include a black-hole companion. However, this kind of systems still remains the Holy Grail in pulsar astronomy.

The range of spin-down luminosity values L_{sd} covered by known pulsars is impressively wide. The largest value, $L_{sd} \simeq 4 \times 10^{38}$ erg s $^{-1}$, is reached by the Crab pulsar and PSR J0537-6910. The minimal value, $L_{sd} \simeq 4 \times 10^{28}$ erg s $^{-1}$, is ten orders of magnitude smaller and it is reached by the slowest radio pulsar detected so far (PSR J2144-3933, $P \sim 8.5$ s, Young et al. (1999)).

The DNS group, placed on the $P - \dot{P}$ diagram between normal and MSPs, is a rather small group (eight members), but certainly not negligible. On the $P - \dot{P}$ diagram the DNS pulsars are located near the line of a constant magnetic field of 10^{10} G. An excellent example of DNS is the original binary pulsar B1913+16 (Tab. 1.1) in which the orbital period is observed to decrease at the rate predicted by general relativity due to emission of gravitational waves (Taylor & Weisberg 1989). So far only in one system, PSR J0737-3039, two pulsars (named A and B) are observed. This system turned out to be the best testbed for the theory of General Relativity. In particular, the Shapiro delay measured for this system remains in agreement with the delay predicted by GR with an uncertainty of $\sim 0.05\%$ (Kramer et al. 2006).

¹According to The Australia Telescope National Facility Pulsar Catalogue, <http://www.atnf.csiro.au/research/pulsar/psrcat/>, Manchester et al. (2005).

1. INTRODUCTION

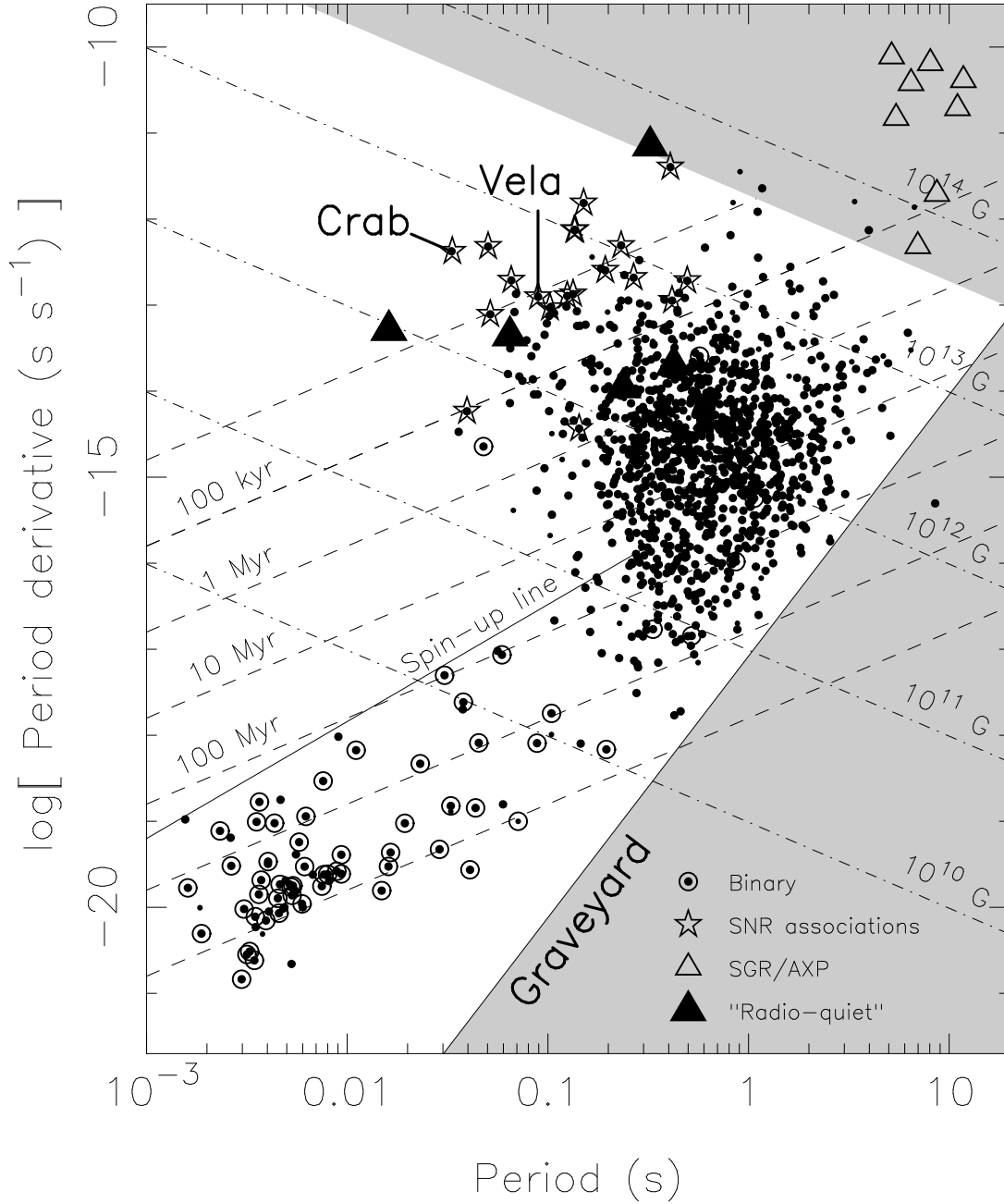


Figure 1.2: The $P - \dot{P}$ diagram showing the current sample of radio pulsars. Binary pulsars are marked as an open circle. Pulsars associated with supernova remnant are marked with stars. For soft gamma repeaters (SGRs) and anomalous X-ray pulsars (AXPs) open triangles are used, whereas 'radio-quiet' pulsars are highlighted with filled triangles. Lines of constant magnetic field B_s (Eq. 1.3) and characteristic age τ_c (Eq. 1.9) are indicated. Regions indicated with grey are areas where radio pulsars are not predicted to exist by theoretical models. The 'spin-up' line denotes the terminal period for objects moving to the left in the diagram due to accretion and become 'recycled' millisecond pulsars once it ceases. The 'graveyard' marks the region where radio pulsars emit less radiation or turn off entirely. [Courtesy M. Kramer].

1.2 Observational characteristics of pulsars

Moreover, observations of relativistic effects in binary pulsars like J0737-3039 allow precise determination of their masses.

Pulsars are ‘born’ with very short rotation periods P_0 , of the order of 1 to 10 milliseconds, and large slow down rates \dot{P}_0 of the order of $\sim 10^{-9} \text{ s s}^{-1}$ to $\sim 10^{-12} \text{ s s}^{-1}$. Then, they slow down along the lines of constant magnetic field values (Eq. 1.3). Their magnetic fields may decay on time scales longer than 1 Myr. When they cross the pulsar ‘death line’, the conditions for the pair creation are not fulfilled any more, therefore no radio emission is produced and the pulsars become invisible. The lower right region on the $P - \dot{P}$ diagram defined by the ‘death line’ is commonly called a ‘graveyard’. In the standard picture all pulsars start as normal pulsars. Millisecond pulsars are also called ‘recycled pulsars’ due to their evolutionary path. It is believed that future MSPs enter the ‘graveyard’ as members of binary systems. As the companion evolves, mass and angular momentum are transferred from the companion to the pulsar, spinning it up. Once ‘spun-up’, the pulsar is ‘recycled’ as a millisecond pulsar. This model predicts that all millisecond pulsars are members of binary systems.

Additionally, in the upper right part of the diagram a group extraordinary of objects is located: the Soft Gamma Repeaters (SGRs) and Anomalous X-ray Pulsars (AXPs). SGRs emit bright, repeating flashes of low-energy (soft) gamma rays. The physical nature of these stars was a mystery for many years. Late in 1992, it was proposed that SGRs are magnetically-powered neutron stars, or magnetars. Subsequent observational studies support this hypothesis. AXPs are also magnetars – young, isolated, highly magnetised neutron stars. These energetic X-ray pulsars are characterised by slow rotation periods of $\sim 5 - 12 \text{ s}$ and large magnetic fields of $\sim 10^{13} - 10^{15} \text{ G}$, some have also been found to emit SGR-like bursts. Very likely, SGRs and AXPs are essentially connected to each other. Their behaviour is now best described by the magnetar model, in which the decay of an ultra-strong magnetic field ($B \gtrsim 10^{14} \text{ G}$) powers the high-luminosity bursts and also a substantial fraction of their X-ray emission. For the recent review about these sources see [Woods & Thompson \(2004\)](#).

There are also pulsars, for which the pulsations have been detected at high energies but not at radio frequencies. In most cases such pulsation are seen in the X-ray regime. This may be due to a misaligned radio beam or due to very low radio luminosity. Pulsars characterise by this behaviour are called ‘radio quiet’ pulsars. A prototype of this group is a well known Geminga pulsar.

1.3 Distribution of pulsars in the Galaxy

Most of known pulsars are Galactic, residing in or near the disc of the Galaxy. Some of them (millisecond pulsars) are located in globular clusters. Twenty pulsars have been found to date in the Magellanic Clouds (Manchester et al. 2006). No pulsars have been detected in other galaxies. The reason is a limited sensitivity of radio telescopes in confrontation with pulsars as actually very weak radio sources. Moreover, propagation effects make the task of finding pulsed emission from distant sources more difficult. For these reasons we observe only a tiny fraction of a much larger pulsar population. The observed pulsar sample is biased towards the brighter and nearby objects that are easiest to detect. The extent to which the sample is incomplete is well demonstrated by the projection of all pulsars known to date onto the Galactic plane in Fig. 1.3 *left panel*. The gathering of pulsars around the Sun clearly differs from the distribution of other stellar populations that show a radial distribution about the Galactic centre. Their cumulative number distribution as a function of distance from the Galactic centre is shown in Fig. 1.3, *middle panel, solid red line*. This may be compared with the simulated distribution of pulsars with no selection effects (Fig. 1.3, *middle panel, dotted black line*). A strong deficit in the observed number distribution becomes visible beyond a few kpc. Very sensitive SKA pulsar survey will allow to discover $\sim 20,000$ pulsars including $\sim 1,000$ millisecond pulsars (Fig. 1.3, *right panel*). The SKA will provide a complete sampling of pulsars in both the Galaxy and in Galactic globular clusters. Information collected by the SKA will provide a detailed map of electron density and magnetic fields in the Galaxy, the dynamics of the pulsar systems, and their evolutionary history. A huge sample of detected pulsars will allow statistical studies of pulsars.

1.4 Pulsars across the electromagnetic spectrum

Pulsars are known emitters across the whole electromagnetic spectrum. They are observed not only in the radio band, but also in optical, X-rays and γ -rays. In contrast to more than 1600 pulsars already detected in radio, we know just six optical pulsars, around eighty X-ray pulsars, and seven (high-confidence) gamma-ray pulsars. The pulsars seen in optical are: Crab, Vela, Geminga, PSR B0540-69, PSR B0656+14 and PSR B1929+10 (e.g. Mignani et al. 2004; Shearer & Golden 2002). The first four objects show clear pulsed emission. PSR B0656+14 and PSR B1929+10 are less

1.4 Pulsars across the electromagnetic spectrum

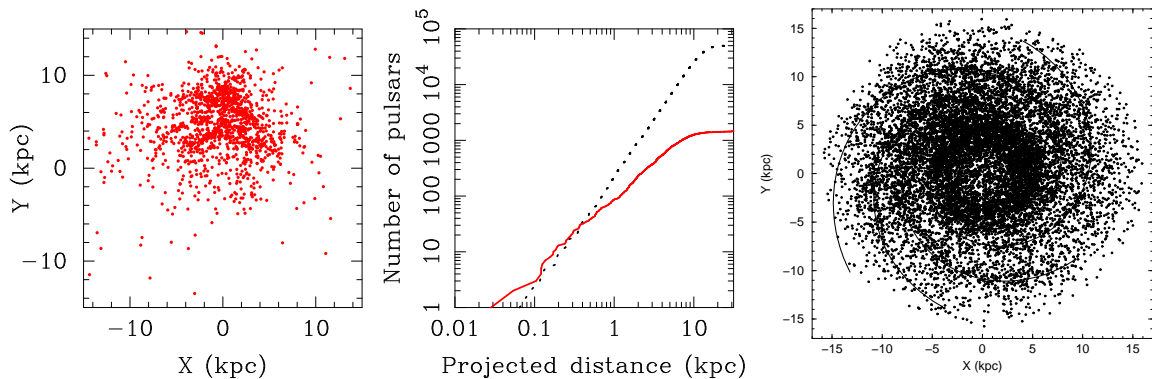


Figure 1.3: *Left*: The current sample of all known radio pulsars projected onto the Galactic plane. The Galactic centre is at (0, 0) and the Sun is at (0, 8.5) kpc. *Middle*: Cumulative number of pulsars as a function of projected distance from the Sun. The solid red line shows the observed sample while the dotted black line shows a model population free from selection effects. [Reproduced from Lorimer (2005)]. *Right*: Simulated pulsar population projected onto Galactic plane. The $\sim 20,000$ pulsars estimated to be discovered by SKA survey are shown together with the spiral arms structures. Coordinates are the same as on the left panel. [Credit Cordes et al. (2004)].

clear cases in terms of pulsed versus unpulsed character of their emission. In particular, PSR B1929+10 proper motion yielded the confirmation of its optical counterpart (Mignani et al. 2002), but only a marginal detection of optical pulsations exists (Mignani, private communication). The brightest pulsed source is the Crab pulsar. It is strong enough to allow extensive studies of its single pulses. Moreover, it is the only pulsar for which phase-resolved polarisation characteristics could have been obtained (Jones et al. (1981), Smith et al. (1988), and very recent results by A. Słowikowska, see Chap. 3).

In the past decade we observed the growing number of RPPs detected in X-rays. It is mostly due to recent observations performed by sensitive instruments on board the *XMM-Newton* and *Chandra* satellites (~ 80 pulsars). *ROSAT* and *ASCA* yielded ‘only’ 33 detections, including 7 X-ray pulsars that were already known from earlier missions - the *Einstein* X-Ray Observatory and *EXOSAT*. X-ray observations of pulsars offer more direct insight into the magnetospheric plasma densities and processes in comparison to not fully understood coherent radio emission. However, in many pulsars the observed X-ray emission is a mixture of thermal and non-thermal emission that can not always be discriminated by the available data. Thermal emission may originate from the stellar surface as a consequence of stellar interior cooling. Additionally, it may be caused by heated polar caps due to backflowing particles.

1. INTRODUCTION

In the latter case X-ray flux modulation are expected due to rotation. In any case, the thermal emission from pulsars is expected to deviate from a simple blackbody radiation; significant modifications are due to presence of a magnetised atmosphere on the NS surface. In contrast to thermal X-rays, non-thermal X-ray emission, as well as gamma-ray emission, is exclusively a direct consequence of magnetospheric activity of the pulsar. For different models different regions in pulsars magnetospheres are considered as a particle accelerators. Particles are accelerated to ultrarelativistic energies, and in turn they induce electromagnetic cascades with curvature radiation, synchrotron radiation, and radiation due to inverse Compton scattering. The non-thermal emission spreads then from optical, through X-rays, to γ -rays frequencies. For seven pulsars - Crab, B1509-58, Vela, B1706-44, B1951+32, Geminga and B1055-52 - strongly pulsed gamma-ray emission was detected (e.g. [Kanbach 2002](#)). Their light curves and phase-averaged spectral energy distributions from radio to gamma-rays are presented in Figs. [1.4](#) and [1.5](#), respectively. Important features of these light curves are: (a) for each pulsar the pulse shape changes with energy, sometimes very dramatically; (b) not all seven objects are seen at hard γ -ray energies - the case of PSR B1509-58, (c) three pulsars (Crab, Vela and Geminga) show a common feature above 100 MeV: a double peak structure.

The energy spectra in Fig. [1.5](#) show the distinction between the radio emission (that originate from a coherent emission) and the high-energy emission (originating in incoherent processes). It is particularly visible for the Crab and Vela pulsar. These spectra clearly emphasise that the emission in X-rays and γ -rays dominates the radiation budget of these pulsars. The spectra of the pulsed emission are generally harder than a power law spectrum with a photon index of -2 (which would give a horizontal line in the spectral plot). The spectra have a cut-off or a turnover at a few GeV (with the exception of PSR B1509-58 mentioned before). Their interpretation is model dependent.

The emission processes in the magnetospheres of RPP have been studied in great details from many years. Yet, they are still not well understood. The radio emission must be a coherent process requiring significant particle densities and probably electron-positron pairs, and the emission at higher energies requires acceleration of particles to energies of at least ~ 10 TeV.

Several mechanisms of the radio emission have been proposed. These are: maser curvature emission, linear acceleration emission, anomalous Doppler instability, curvature-drift instability and relativistic plasma emission (review [Melrose 2004](#)).

1.4 Pulsars across the electromagnetic spectrum

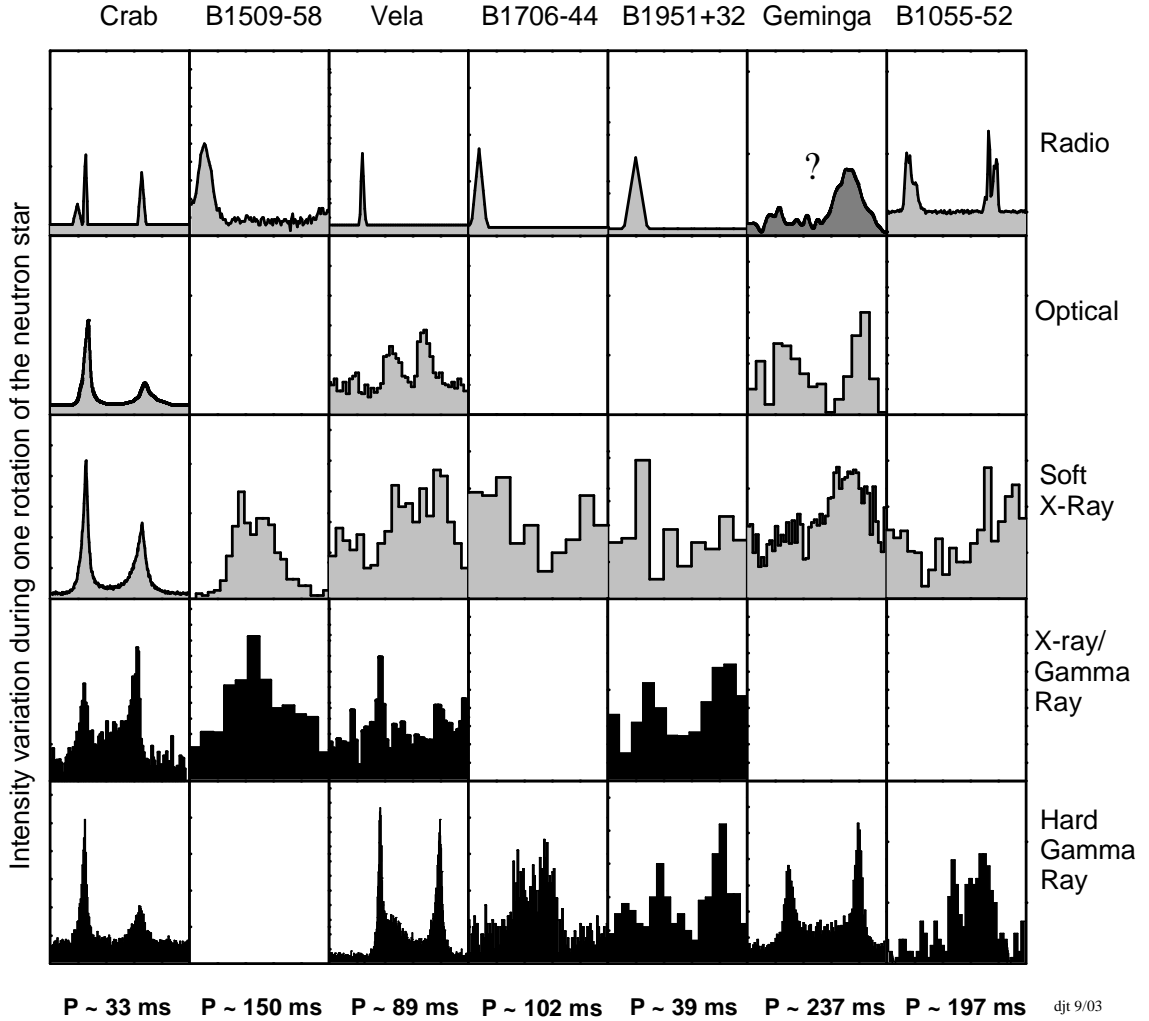


Figure 1.4: Light curves of seven γ -ray pulsars in five energy bands (given on the right side of the plot), from left to right in order of characteristic age τ_c (Eq. 1.9). Each panel show one full rotation of the neutron stars. [Figure from Thompson (2004a), references of data source in Thompson (2004b)].

The models of pulsed high-energy emission are based on physics of particle acceleration, which results from the strong electric fields that are induced along open magnetic field lines. Two accelerator sites have been studied in details and two main types of models have been developed: polar cap models and outer gap models. Polar cap models are based on particle acceleration near the magnetic poles (Ruderman & Sutherland 1975) and outer gap models are based on acceleration in vacuum gaps in the outer magnetosphere (Cheng et al. 1986; Romani 1996). Additionally, pulsed emission from the wind zone, the striped wind model, has also been proposed (Pétri & Kirk 2005). Both types of models significantly evolved in recent years. More recent

1. INTRODUCTION

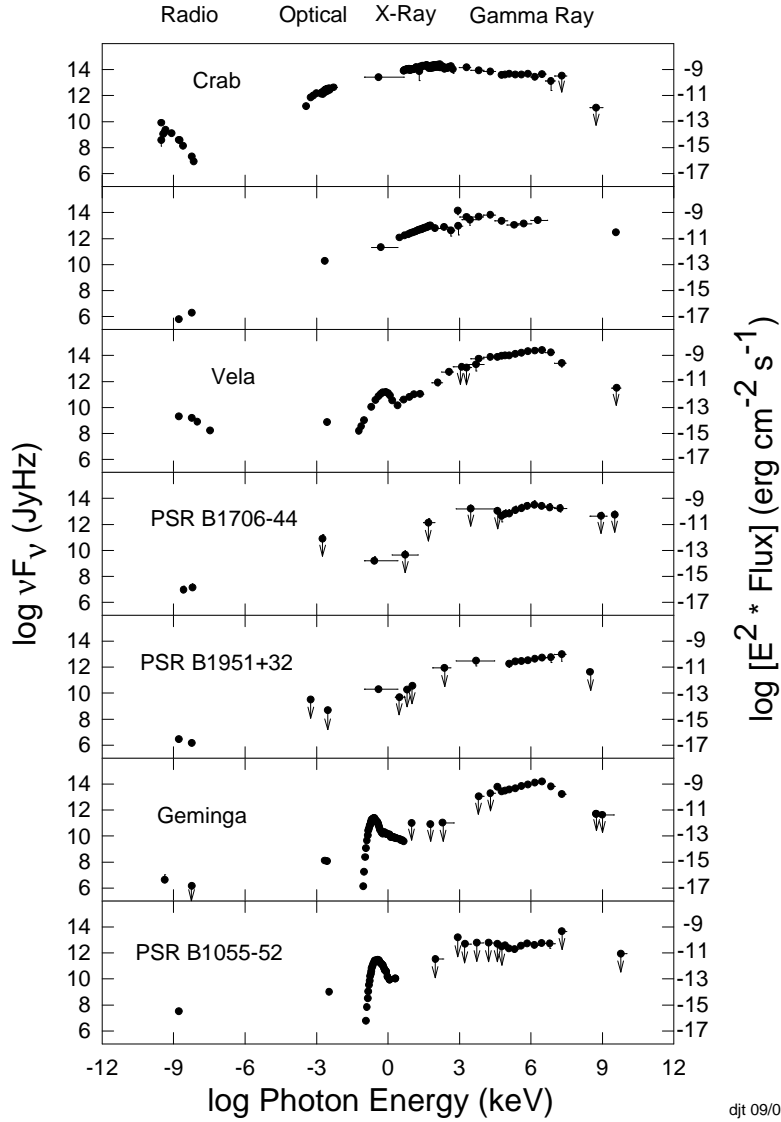


Figure 1.5: Multiwavelength spectra of seven γ -ray pulsars. The second panel from the top is for PSR B1509-58. [Figure from [Thompson \(2004a\)](#), references of data source in [Thompson \(2004b\)](#)].

version of the polar cap model ([Muslimov & Harding 2003, 2004](#)) explores acceleration in a ‘modified slot gap’ - a narrow region bordering the last open field line in which the electric field is unscreened. On the other side, the so called two-pole caustic (TPC) model was developed ([Dyks et al. 2004a; Dyks & Rudak 2003](#)). The TPC model was successful in reproducing the double-peak light curves of Crab and Vela as well as in reproducing optical polarisation characteristics of Crab. The model

stimulated a significant revision of outer gap models very recently.

So far none of the proposed models is able to reproduce all observational pulsar features, i.e. their light curves, spectra (also phase resolved) and polarisation properties.

1.5 The Crab pulsar and its nebula

The Crab pulsar is surrounded by bright diffuse nebula, that is about six light years across, and expands outward at 4.8 million km per hour. The filamentary system visible in optical is near the outer boundary of this expansion. Both, the Crab Nebula and the pulsar are bright sources of non-thermal radiation extending from radio to gamma-rays (the nebula was the first TeV source detected in the sky).

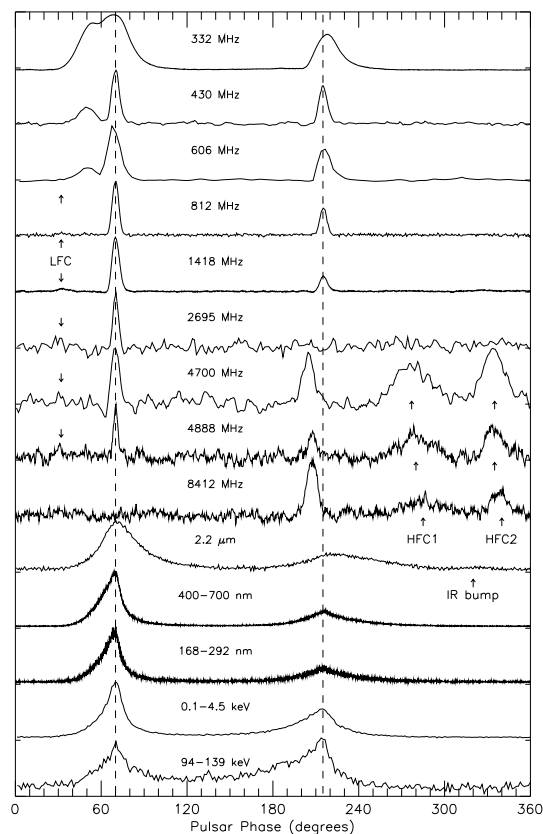


Figure 1.6: Multiwavelength light curves of the Crab pulsar. [Moffett & Hankins (1996)].

The Crab pulsar is very characteristic for its light curve in different wavelengths. It is the only pulsar for which the main features in the light curve persist over all

1. INTRODUCTION

wavelengths, from radio to gamma-rays. The light curve shows two basic components - the main pulse (MP) and the inter pulse (IP). This double-peak structure remains phase-aligned over all available wavelengths (Figs. 1.4 and 1.6). However, there are some extra features present: at low radio frequencies a precursor to the first peak is visible. Moreover, an additional low frequency component (LFC) is present between 1 and 5 GHz. Above 4.7 GHz two additional components trailing the IP show up. They are known as high frequency components: HFC1 and HFC2. In the optical domain the light curve is much less structured than in radio. Both, the MP and the IP are slightly asymmetrical: in the MP the signal falls off more sharply than it rises, whereas the opposite situation prevails for the IP. The peak of the MP is surprisingly sharp, and it plummets down in only 40 μ s. The X-ray shape is interesting because both the MP and the IP are of about the same intensity. There is a ‘bridge’ component between the MP and the IP at high energies. At optical and X-rays the flux level before the MP never reaches the zero level (Golden et al. 2000a; Tennant et al. 2001). Presently there is no theoretical concept that would explain all these extra features in the Crab light curve.

The Crab pulsar emits maximum power at about 100 keV (Fig. 1.5). Its spectrum can be well described by a broken power law extending from the optical (~ 1 eV) to about 10 GeV. In addition to the pulsed emission the Crab pulsar shows a strong unpulsed component at high energies. This component has been interpreted as coming from the inner part of the Crab Nebula: as synchrotron radiation below a few GeV and as inverse Compton radiation, upscattered from optical photons, up to TeV energies.

Comparison of the X-ray, optical, infrared, and radio images of the Crab Nebula shows that it is most compact in X-rays and largest in the radio (Fig. 1.7). The X-ray nebula shown in the Chandra image is about 40% as large as the optical nebula, which is in turn about 80% as large as the radio image. Chandra’s X-ray image of the Crab Nebula directly traces the most energetic particles being produced by the pulsar. This image reveals an unprecedented level of details about how the energetic wind of particles (mostly electrons) interacts with the nebular matter and its magnetic field. While the electrons move outward, they lose energy to radiation. The diffuse optical light comes from intermediate energy particles produced by the pulsar. The optical filaments are identified as expanding gases, consisted of the matter that was once ejected by the supernova explosion. The gas temperature is of the order of tens of thousand degrees Kelvin. The infrared radiation comes from dust grains mixed in with the hot gas in the filaments. Radio waves can travel the largest distance and define the full extent of the nebula.

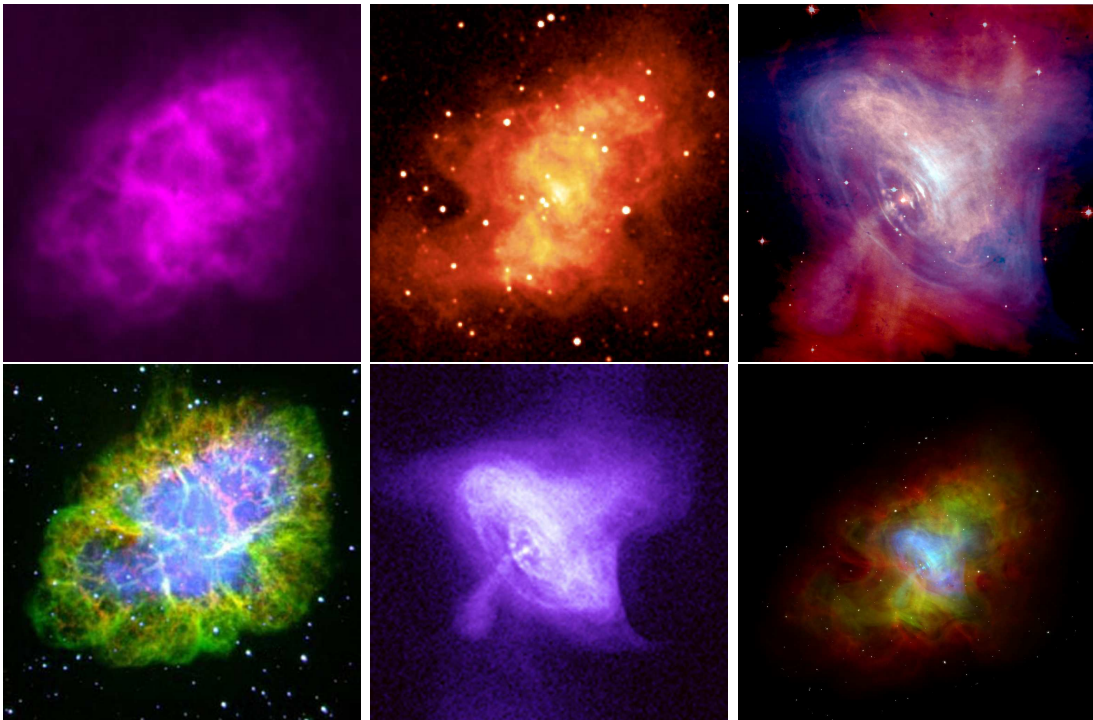


Figure 1.7: Multiwavelength Crab Nebula images. From upper left to bottom right: radio, infrared, optical-X-ray superposition, optical, X-ray, and radio-optical-X-ray superposition, respectively. Radio credit: VLA/NRAO, 5 GHz, FoV $7' \times 7'$; infrared credit: 2MASS/UMass/IPAC-Caltech/NASA/NSF, optical credit: Palomar Obs. This image is a colour composite of pictures, The colours are green [OIII] emission, red $H\alpha$ emission, and blue line - free continuum at 547 nm - i.e. the synchrotron emission nebula. X-ray credit: NASA/CXC/SAO - image is $2.5'$ on a side, Chandra ACIS/HETG 0.3-3 keV. Images are not scaled.

1.6 An outline of the thesis and statement of originality

This thesis presents the results of my involvement in four projects in pulsar astronomy. Their objective was to derive radiation characteristics at a wide range of energy domains for three particular pulsars: PSR B0531+21 (Crab), PSR B0540-69, and PSR B1929+10.

Chapters 1 and 2 refer to the radio and optical observation of the Crab pulsar, respectively. The radio observations performed at the 100-m Effelsberg telescope at 8.35 GHz frequency allowed for the first time to detect the Crab ‘giant radio pulses’ at the rotational phases, where they have never been observed before. Among the three brightest optical pulsars (Crab, Vela, PSR B0540-69) only the Crab is sufficiently

1. INTRODUCTION

bright for individual pulse work to be performed. Furthermore, it is the only pulsar for which the Stokes parameters can be accurately measured throughout the pulsar's rotation period. Optical polarisation of the Crab pulsar, obtained with $30 \mu\text{s}$ time resolution is presented and discussed in Chapter 2. The next two chapters refer to the X-ray observations. Chapter 3 is dedicated to the PSR B0540-69 results obtained from the *INTEGRAL* satellite, whereas Chapter 4 presents the results of the reanalysis of the available X-ray archive data of PSR B1929+10.

Three projects (Chapters 1 to 3) started with observational campaigns and were followed by data reduction and data analysis. In all these cases I have been assisted by other members of observational proposals submitted in order to obtain telescope time. The remaining project (Chapter 4) consisted of data reduction and analysis. My analysis was carried out mostly at the Department of Astrophysics, Nicolaus Copernicus Astronomical Center Toruń, and at MPE-MPG Garching between 2001 and 2006.

Except where otherwise acknowledged, the work presented in this thesis is my own. Significant contributions from other people are as follows:

Chapter 1: Effelsberg proposal to detect giant radio pulses from the Crab pulsar; PI of the proposal: A. Słowikowska. Other members of the team: Dr. Axel Jessner (MPIfR) performed the observations; together with Dr. Bernd Klein (MPIfR) he installed and run, for the first time, the Le Croy oscilloscope at the 100-m Effelsberg radio telescope; during the data analysis I have used some scripts written by Axel Jessner.

Chapter 2: Optical polarimetric observations with Nordic Optical Telescope; PI of the proposal: Dr. G. Kanbach (MPE). The observations were performed jointly by all members of the team: G. Kanbach, A. Słowikowska, A. Stefanescu (MPE) and Fritsch Schrey (MPE).

Chapter 3: INTEGRAL observations of PSR B0540-69; PI of the proposal: Dr. G. Kanbach. The RXTE ephemeris of PSR B0540-69 used in my analysis were derived by Dr. Lucien Kuiper (SRON).

Chapter 4: Lucien Kupier performed the analysis described in the Appendix B. For some parts of data analysis I used his scripts.

Chapter 2

Enhanced radio emission from the Crab pulsar

2.1 Introduction

The occurrence of sporadic radio emission of very strong pulses by NP 0532, the very first name of the Crab pulsar, has been known since its discovery by Staelin and Reifenstein ([Staelin & Reifenstein 1968](#)). They discovered the dispersed pulse signals from the Crab Nebula. These strong pulses were not periodic (see [Fig. 2.1](#)), therefore the rotational period of the Crab was not established. However, considering the source as a periodic one, Staelin and Reifenstein were able to give the upper limit of 0.13 s for its period. Noteworthy is that the pulsar would not have been discovered if it had not shown the strong radio pulses, that were later called the giant radio pulses (GRPs). A single pulse of average flux density can not be detected because of the high radio emission from the plerionic nebula. The strongest pulses exceed the total radio emission from the nebula itself by an order of magnitude. For a long time it was the only known pulsar showing the GRP phenomenon. The rotational period of the pulsar was measured by Comella, who used the 305 m reflector at the Arecibo Observatory ([Comella et al. 1969](#)), whereas its slowdown rate was given by Richards and Comella a few months later ([Richards & Comella 1969](#)). The optical emission was for the first time reported by Cocke, Disney and Taylor ([Cocke et al. 1969](#)), and later confirmed by other groups (e.g. [Nather et al. 1969](#)). Fishman, Harnden and Haymes reported the detection of the pulsar at hard X-rays ([Fishman et al. 1969](#)), Bold, Desai and Holt, as well as Fritz et al. in soft X-rays ([Boldt et al. 1969](#); [Fritz et al. 1969](#)), and Neugebauer et al. in the infrared wavelengths ([Neugebauer et al. 1969](#)).

2. ENHANCED RADIO EMISSION FROM THE CRAB PULSAR

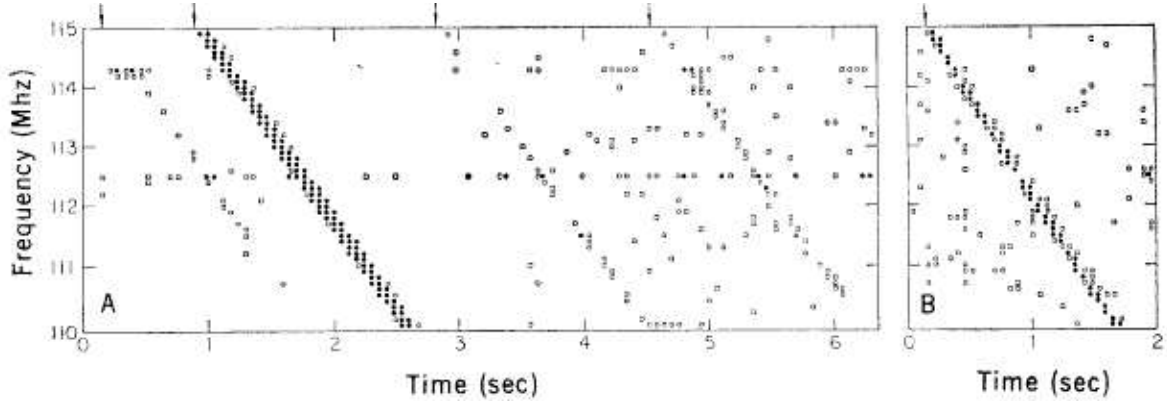


Figure 2.1: Time-frequency diagram of radio pulses observed with circular polarisation. *Left*: One strong and three weak pulses (marked with arrows) received from PSR B0531+21 on 21 October 1968. *Right*: One typical pulse received from PSR B0531+21 on 19 October 1968. Open squares and closed circles represent deviations from the mean of 4.2σ and 8.3σ , respectively. Horizontal axis is a time scale in seconds. Within one second the Crab pulsar rotates around 30 times. [Staelin & Reifenstein (1968)].

Following studies of its pulse shape as a function of radio frequency have shown that Crab is very unique (Figs. 2.2, 2.3). The average pulse profile is determined by averaging the data from thousands of sequentially recorded single pulses. The results show that the averaged radio pulse profile consists of two main components: an intense but narrow ‘main pulse’ (MP), lasting about $250\ \mu\text{s}$ with respect to the 33 ms pulsar period, and a broader and weaker ‘inter pulse’ (IP) following the MP by 13.37 milliseconds. IP does not occur exactly between successive main pulses; the phase separation between the MP and the IP is ~ 0.4 . At lower frequencies $\sim 300 - 600\ \text{MHz}$ another broad and weak component is visible. It precedes the MP by 1.6 milliseconds. It is called ‘precursor’ (P). New and unseen before 1996 profile components were discovered by Moffett and Hankins, Fig. 2.3 (Moffett & Hankins 1996). In the average pulse shape at 1.4 GHz the precursor vanishes, due to its steep spectral index, leaving only the MP, IP, and a weak but distinct low frequency component (LFC). It is $\sim 36^\circ$ ahead of the MP, therefore it is not coincident with the position of the precursor apparent at lower frequency (Fig. 2.3, second panel from the top). Two additional components appear in the profiles obtained for frequencies between 5 and 8 GHz. These two broad components with nearly flat spectrum are referred to as high frequency component 1 and 2, i.e. HFC1 and HFC2, respectively. The existence of the extra components at high frequency and their strange, frequency-dependent behaviour is unlike anything seen in other pulsars. It can not easily be

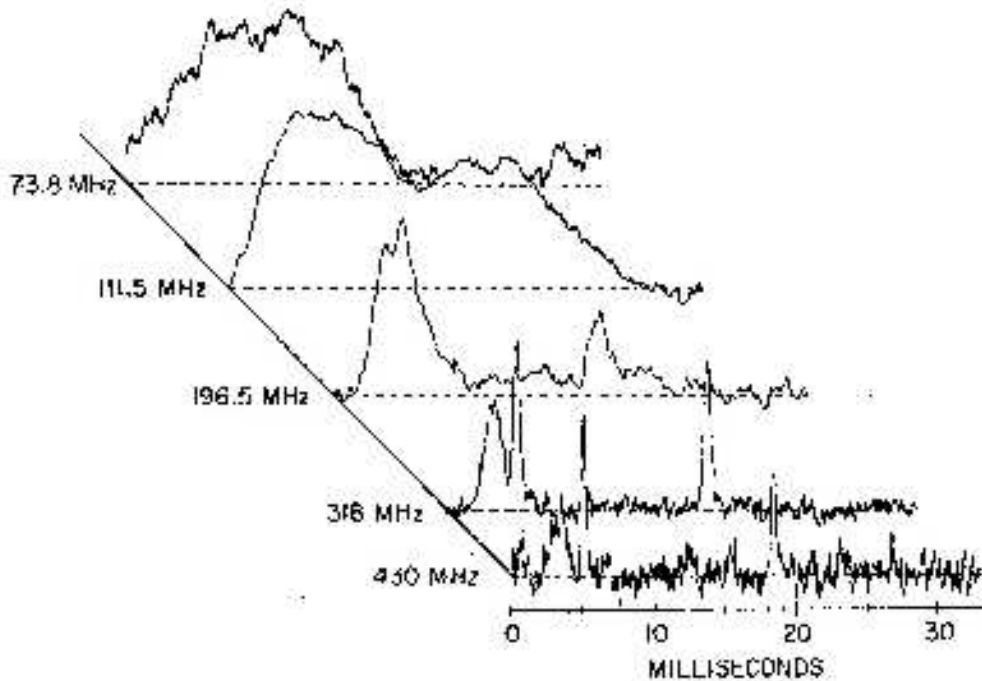


Figure 2.2: Average Crab pulsar pulse shape at 73.8, 111.5, 196.5, 318, and 430 MHz, respectively from the top to the bottom. Phases of pulses are arbitrary. [Rankin et al. (1970)].

explained by emission from a simple dipole field geometry. Two main components, i.e. the MP and the IP, have counterpart non-thermal emission from the infrared to the gamma-ray energies (Fig. 1.6).

The pulse shape changes markedly across all radio frequencies (Fig. 2.3). The changes are caused by intrinsic as well as propagation effects. At lower frequencies the pulse shape becomes more washed out as the well-defined features seen at 430 MHz broaden (Fig. 2.4). These changes are due to the effects of radio wave propagation in the interstellar medium between the Earth and the pulsar (e.g. Lorimer & Kramer 2005). Individual waves from the pulsar get scattered by the electrons in the interstellar medium, and thus the signal that actually reaches the radio telescope is the superposition of signals from very many slightly different paths through the medium. At a sufficiently low frequency the waveform will be smeared out so much as to be indistinguishable from continuous steady emission. This effect is illustrated in Fig. 2.4. The strong inverse frequency dependence of scattering clearly favours pulsar searches carried out at high frequencies. Besides scattering, two other distinct propagation effects occur: dispersion and scintillation. The dispersion effect is a frequency dependence of the radio waves group velocity as they propagate through

2. ENHANCED RADIO EMISSION FROM THE CRAB PULSAR

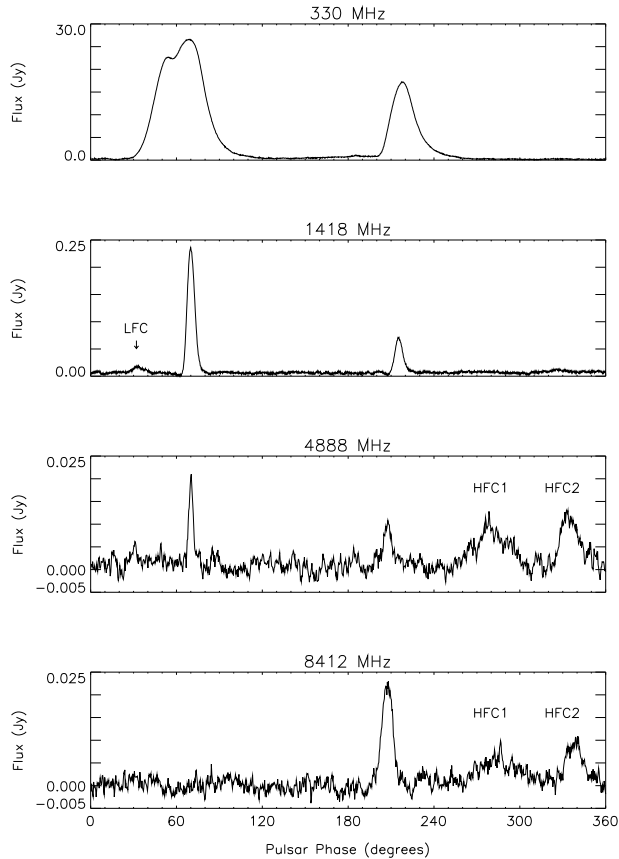


Figure 2.3: The aligned, average radio intensity profiles of the Crab pulsar obtained at 0.33, 1.4, 4.9 and 8.4 GHz with Very Large Array (VLA) showing several components: the main pulse (MP), interpulse (IP), precursor (visible at 330 MHz, just before MP), low frequency component (LFC), and two broad high frequency components (HFC1, HFC2), waxing and waning with radio frequency. [Moffett & Hankins (1996)].

the ionised component of the interstellar medium (ISM). The delay in pulse arrival time is inversely proportional to observing frequency, thus pulses observed at higher frequencies arrive earlier at the telescope than their lower frequency counterparts. During the observations the de-dispersion procedure is used to correct for this effect. Because the ISM is highly turbulent and inhomogeneous, its irregularities produce phase modulation on the propagating pulsar signal. This scintillation effect causes the observed intensity to fluctuate on a variety of timescales and bandwidths.

(Comment: Figs. 2.1, 2.2, 2.4 and 2.5 are reproduced from papers published in late 60's and early 70's. Because the only available source of these figures are scanned images, therefore they are of poor quality.)

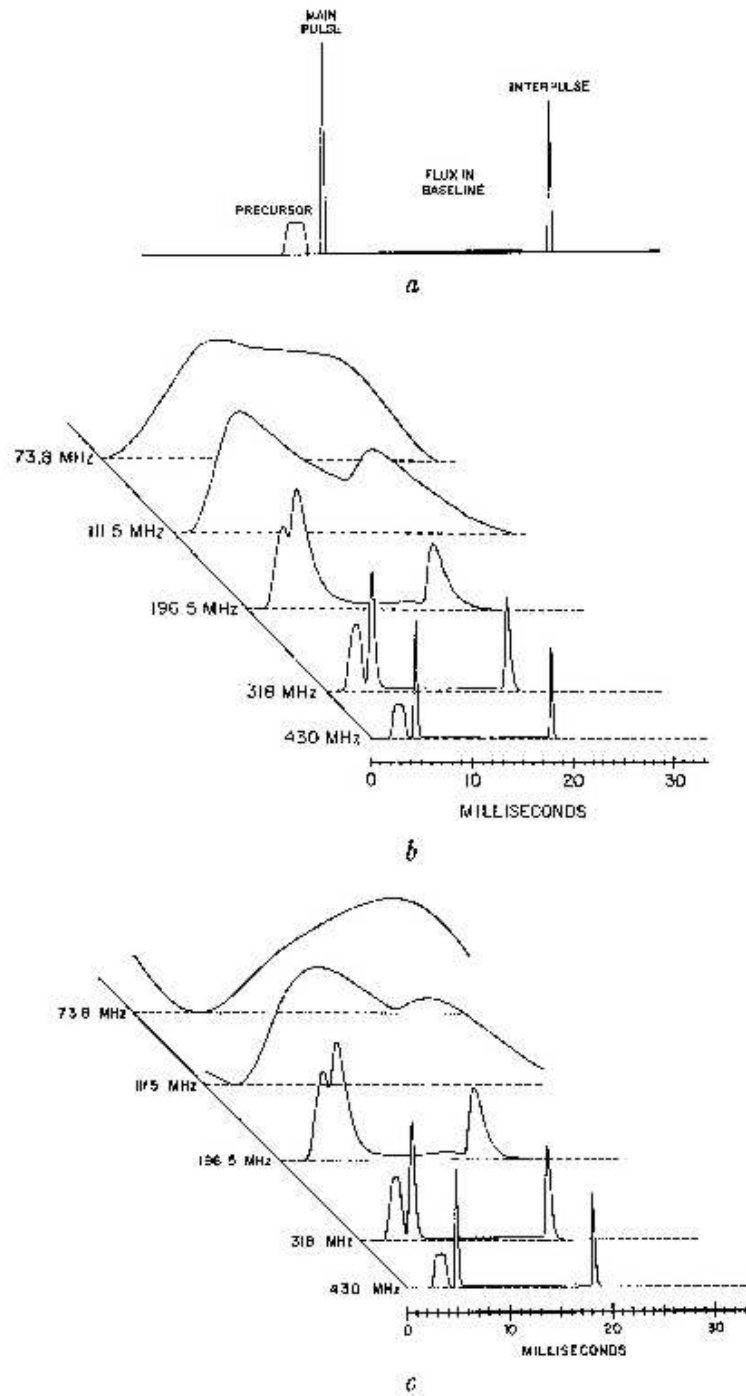


Figure 2.4: (a) Intrinsic pulse shape assumed in the broadening model. In (b) and (c) the intrinsic pulse is convolved with an exponential and an xe^{-x} probability-density function, respectively, representing multi-path propagation effects in the interstellar medium. (b) and (c) are also convolved with functions representing the pulse-broadening effects of the radiometer, and are thus directly comparable with the observed pulses in Fig. 2.2. [Rankin et al. (1970)].

2.2 Giant radio pulses

For over 25 years, only the Crab pulsar was known to emit GRPs. Actually, it was discovered because of its giant radio pulses at the phases of MP. Its individual GRPs might last just a few microseconds (Hankins et al. 2003). However, they rank among the brightest flashes in the radio sky reaching peak flux densities of up to 1500 Jy even at high radio frequencies. Already four years after its discovery it has been reported that GRPs occur not only at the MP, but also at the IP phases (Gower & Argyle 1972). This discovery is illustrated in Fig. 2.5. Until 2005 the GRP phenomenon in the Crab pulsar had been known to occur exclusively at the phases of the MP and the IP (Cordes et al. 2004; Lundgren et al. 1995; Sallmen et al. 1999). In particular, no GRPs had been detected either in the LFC or at the phases of the high radio frequency components: HFC1 and HFC2. This situation has changed due to the results published by Jessner, Słowikowska et al. (2005). In our observations at 8.35 GHz the IP and both HFCs are clearly visible, whereas the LFC can be seen as a slight rise above the noise level separated by about 0.1 in phase from the MP that is not very intense at this frequency as well (Fig. 2.11, *top panel*). Our observations show that GRPs can be found in all phases of ordinary radio emission including HFC1 and HFC2. This result has potentially important consequences for pulsar emission theory. In particular, it seems that there is no difference in the emission mechanism of the MP, IP and HFCs. High resolution dynamic spectra from our recent observations of giant pulses with the Effelsberg telescope at a centre frequency of 8.35 GHz show distinct spectral maxima within our observational bandwidth of 500 MHz for individual pulses. Their narrow band components appear to be brighter at higher frequencies (8.6 GHz) than at lower ones (8.1 GHz). Moreover, there is an evidence for spectral evolution within and between those structures. High frequency features occur earlier than low frequency ones. Strong plasma turbulence might be a feasible mechanism for the creation of the high energy densities and high brightness temperatures.

2.3 Effelsberg observations

Observations with the Effelsberg 100-m radio telescope began on 25 November 2003 and ended on 28 November 2003. We used a secondary focus cooled HEMT¹ receiver with a centre frequency of 8.35 GHz, providing two circularly polarised IF signals²

¹High Electron Mobility Transistor

²Intermediate frequency signal

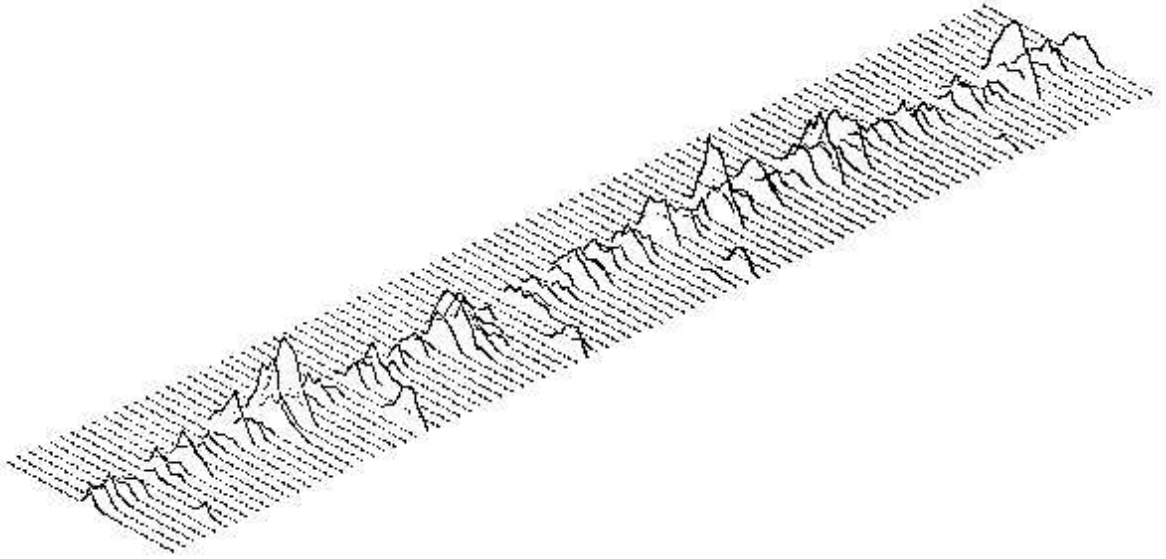


Figure 2.5: Seven giant pulses occurring at the phase of the inter pulse. This 3D plot represents 4 hours' observation of PSR B0531+21 at 146 MHz. [Gower & Argyle (1972)].

with a system temperature of 25 K on both channels. With a sky temperature of 8 K, and a contribution of 33 K from the Crab Nebula, the effective system temperature was 70 K. Two detection systems were used.

2.3.1 EPOS - the Effelsberg Pulsar Observation System

First, a polarimeter with 1.1 GHz bandwidth measured total power of the left-hand and right-hand circularly polarised signals (LHC and RHC respectively), as well as $\cos \angle(\text{LHC}, \text{RHC})$ and $\sin \angle(\text{LHC}, \text{RHC})$. These four signals were then recorded by the standard Effelsberg Pulsar Observation System (EPOS). With the Crab pulsar's dispersion measure of 56.8 pc cm^{-3} , we had an time resolution of $t_{\text{sample}} = 890 \text{ } \mu\text{s}$, while our sampling resolution was fixed at $\sim 640 \text{ } \mu\text{s}$. EPOS was therefore set to continuously record data blocks containing 20 periods divided into 1020 phase bins for all four signals. The minimum detectable flux per bin was $\Delta S_{\text{min}} = 0.117 \text{ Jy}$. Considering the dispersion pulse broadening, the detection limit for a single GRP of duration $\tau_{\text{grp}} = 3 \text{ } \mu\text{s}$ would be $\Delta S_{\text{min}} t_{\text{sample}} / \tau_{\text{grp}} = 25 \text{ Jy}$.

2. ENHANCED RADIO EMISSION FROM THE CRAB PULSAR

2.3.2 LeCroy oscilloscope - an ultra-high resolution detection system

A wide band ultra-high resolution detection system similar to the one of [Hankins et al. \(2003\)](#) was used as well. The two IF signals (100–600 MHz) carrying the LHC and RHC information were sampled and recorded with a fast digital storage oscilloscope (LeCroy LC584AL). A total of 4×10^6 samples per channel were recorded at the rate of 2×10^9 samples per second. The storage scope was used in a single shot mode. We used giant radio pulses to trigger data acquisition by the digital storage scope. The RHC signal was detected, amplified and low-pass filtered (3 kHz), then passed to a second scope (Tektronics 744). The second scope triggered the digital scope whenever pulses stronger than 3–4 times rms (75–100 Jy) were detected. The recorded waveforms were then transferred to disk. This required manual intervention and led to a dead time of about 100 seconds after each pulse.

2.4 EPOS data analysis

About 2.4×10^6 periods were observed with EPOS. Presented results are only based on a third of all observed rotations. This selection was mostly caused by insufficient quality of the data. Because of the Crab pulsar’s weak signal at 8.35 GHz and the strong nebula background, ordinary single pulses were not observable with Effelsberg at that frequency. It takes about 20 min integration to assemble a mean profile at that frequency. The giant pulses come in short outbursts, about 5 to 20 minutes in duration, and appear extremely prominent during such burst phases.

In our subsequent analysis, we set a threshold level of 5 rms = 125 Jy on the sum of RHC and LHC for the same phase bin to count as a detection of a giant pulse. More than 1300 giant pulses were detected that way (Fig. 2.6) and their arrival phases were computed by using the TEMPO¹ pulsar timing package. The data were aligned using the current Jodrell Bank timing model. They were found to be a perfect match to the time of arrivals (TOAs) obtained at Jodrell Bank before and after the Effelsberg observing session (Fig. 2.7). We found that the GRPs occur at all those phases where the radio components of the Crab pulsar emission are observed. Recorded strength (S/N ratio) of 1318 GRPs as a function of rotational pulsar phase are presented in Fig. 2.8.

¹<http://pulsar.princeton.edu/tempo>

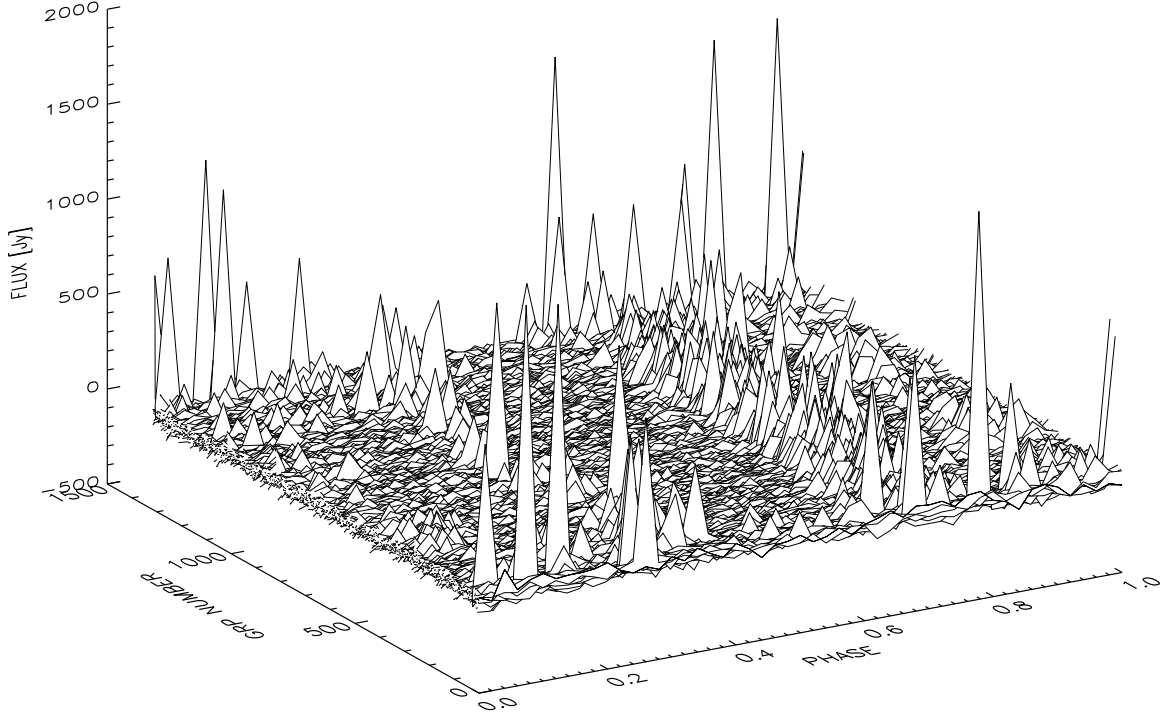


Figure 2.6: A train of strong giant pulses at 8.35 GHz, sum of the right and left handed circular polarisation signals (EPOS, bandwidth $\Delta\nu = 1.1$ GHz). Results obtained during 6.7 hr of observation with the 100 m Effelsberg telescope. Location of the Crab’s pulsar radio components: HFC2: 0.05, LFC: 0.2, MP: 0.3, IP: 0.68, HFC1: 0.9.

2.4.1 GRPs statistics

For all giant pulses, i.e. regardless their phases, the histogram of their peak strengths at 8.35 GHz can be described by a power-law with a slope $\sim -3.34 \pm 0.19$ (Fig. 2.9). This result is consistent with the results obtained by others (e.g. Lundgren et al. 1995). Proportional contribution of a number of GRPs to four different phase components is as follow: IP: 80%, MP: 9%, HFC1: 7%, and HFC2: 4%. In Fig. 2.10, we show the phase resolved distributions of four components: two high frequency components (HFC1 and HFC2), and the main and inter pulse components (IP and MP). Because of the limited statistics we could make a model $(S/N)^\alpha$ fit only for the IP component, where a power-law index $\sim -3.13 \pm 0.22$ was found, and it is consistent with the value of ~ -2.9 presented by Cordes et al. (2004). The MPs from the Crab pulsar at 146 MHz are distributed according to a power-law with the exponent of -2.5, whereas

2. ENHANCED RADIO EMISSION FROM THE CRAB PULSAR

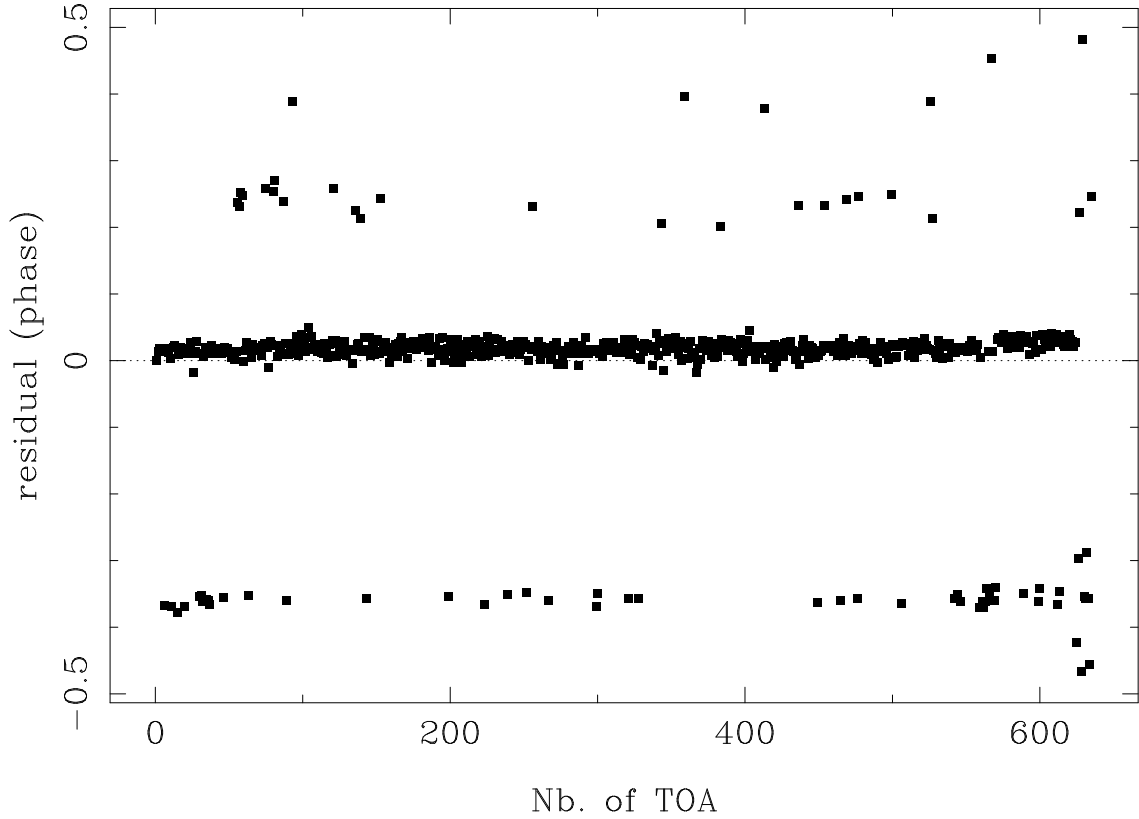


Figure 2.7: Pre-fit phases of pulse time of arrivals (TOAs) in the night of November 27-28, 2003. Data from a single scan were taken. Phases 0 and -0.38 correspond to the location of the IP and MP, respectively. HFCs are located at phases 0.22 and 0.4.

the IPs with -2.8 [Argyle & Gower \(1972\)](#). For comparison at 800 MHz the distribution (regardless the phases of GRPs) has a slope of -3.46 ([Lundgren et al. 1995](#)). It should be noticed that at low radio frequency the main contribution to the number of GRPs comes from main pulses. So far, there is no evidence that the distributions of numbers of GRPs for the HFC1 and HFC2 differ from each other. However, their slopes seem to be steeper than the slope of the same distribution for the IP component.

The results obtained by us suggest that the physical conditions in the regions responsible for HFC emission might be similar to those in the main pulse (MP) and inter pulse (IP) emission regions. We plan to pursue this question further in 2006, when a new observation campaign at two frequencies, 4.85 GHz and 8.35 GHz, of the GRPs of the Crab pulsar is scheduled.

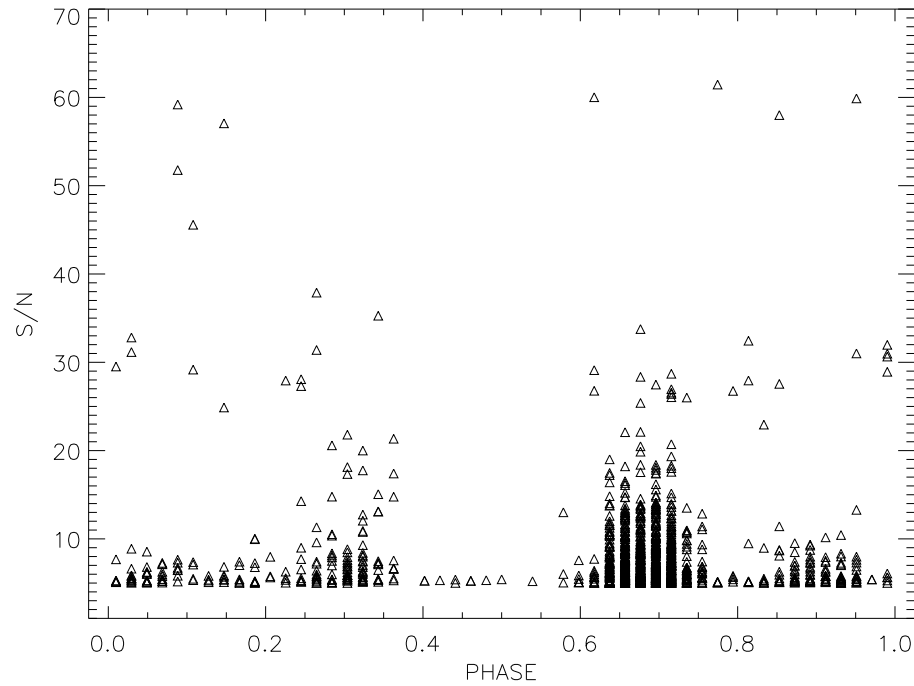


Figure 2.8: Recorded strength and phases of 1318 GRPs. Location of the radio components: HFC2: 0.05, LFC: 0.2, MP: 0.3, IP: 0.68, HFC1: 0.9.

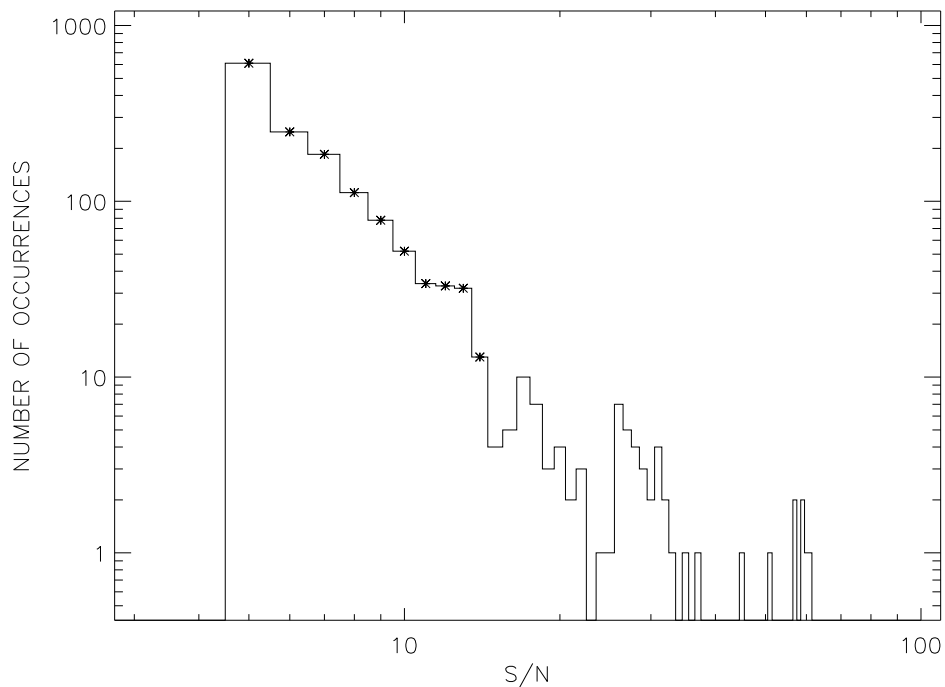


Figure 2.9: Peak strength distribution of giant radio pulses from the Crab pulsar regardless their phases. For the number of occurrences larger or equal to 10 (marked with *) the distribution can be roughly described by a power-law $(S/N)^\alpha$ with index $\alpha \sim -3.34 \pm 0.19$.

2. ENHANCED RADIO EMISSION FROM THE CRAB PULSAR

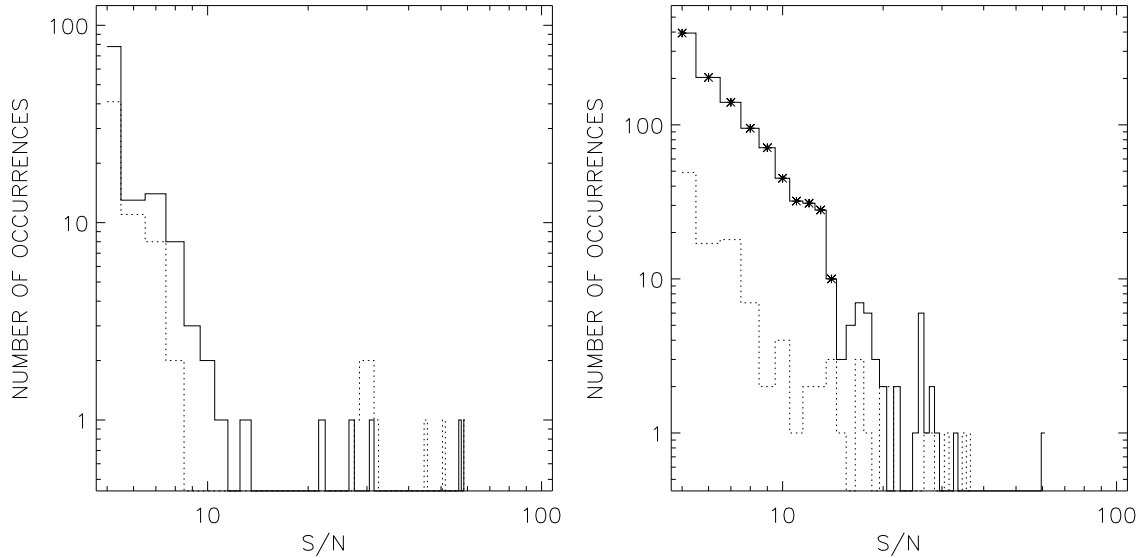


Figure 2.10: Some as in Fig. 4, but for four phase slices. Left panel is for the HFC1 and the HFC2, dotted and solid line, respectively. Right panel is for the MP and the IP, dotted and solid line, respectively. The giant radio pulses for the IP can be described by a power-law $(S/N)^\alpha$ with index $\alpha \sim -3.13 \pm 0.22$ (for the number of occurrences larger or equal 10; marked with *).

2.4.2 Polarisation

In order to obtain the polarisation characteristics of the Crab pulsar GRPs we decided to our best single data set (scan 9525) with the highest ratio of observed GRPs among all observed within the single scan duration pulses. The average polarisation characteristics of these 900 GRPs in some aspects are similar to already published high radio frequencies observations, but in some aspects we do observe significant differences (Słowikowska et al. 2005a). All authors (this work, Moffett & Hankins (1999) and Karastergiou et al. (2004)) find that the relative offset of the position angle (P.A.) between IP and HFCs is on the level of $35 - 45^\circ$. However, the P.A. for the IP, and at the same time for the HFCs differ for all authors. They are as follow, for the IP: 30° , 0° , -30° , and for the HFCs: 60° to 70° , 45° , $5-10^\circ$ according to Moffett & Hankins (1999), Karastergiou et al. (2004) and this work, respectively. Moreover, there is some discrepancy in the degree of polarisation. Almost 100% linear polarisation of all three components has been derived by Karastergiou et al. (2004), whereas in Moffett & Hankins (1999) the IP is polarised in only 50% and HFCs in 80-90%. In our work all components are polarised at the same level of 70-80%. This may be due to the time varying contribution of the nebula to the rotation measure of the pulsar (Rankin et al. (1988): $RM=-43 \text{ rad m}^{-2}$, Moffett & Hankins (1999):

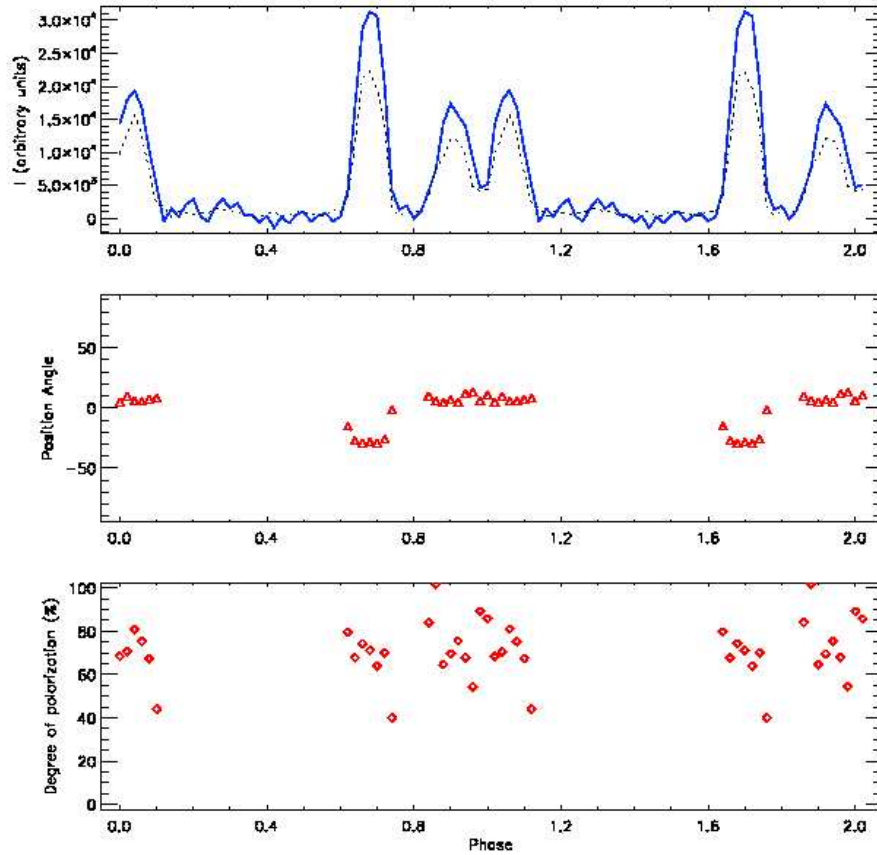


Figure 2.11: The average intensity profile (*top*), the position angle (after Faraday correction, *middle*), and the polarisation degree (*bottom*) obtained from 874 Crab's GRPs recorded at 8.35 GHz. Location of the Crab's pulsar radio components: HFC2: 0.05, LFC: 0.2, MP: 0.3, IP: 0.68, HFC1: 0.9.

$RM = -46.9 \text{ rad m}^{-2}$, [Weisberg et al. \(2004\)](#): $RM = -58 \text{ rad m}^{-2}$). No abrupt sweeps in P.A. are found within pulse components. The S/N ratio was too low to derive reliable values of polarisation degree and angle for the LFC and MP components.

The study of radio polarisation has not essentially improved our knowledge of the emission and magnetic field geometry: e.g., by fitting the rotation vector model to the radio polarisation data utterly opposite conclusions have been reached ([Moffett & Hankins \(1999\)](#), [Karastergiou et al. \(2004\)](#)). [Moffett & Hankins \(1999\)](#) found that the angle between the rotation and magnetic axes is $\alpha = 56^\circ$, while [Karastergiou et al. \(2004\)](#) got nearly aligned rotator with $\alpha = 4^\circ \pm 1^\circ$. They obtained different results for the impact angle as well.

In the Fig. 2.12 the position angle of selected 874 GRPs as a function of rotational phase of the Crab pulsar is shown. In these polarisation characteristics of single pulses we do not observe any sudden changes of the P.A. within the separated components,

2. ENHANCED RADIO EMISSION FROM THE CRAB PULSAR

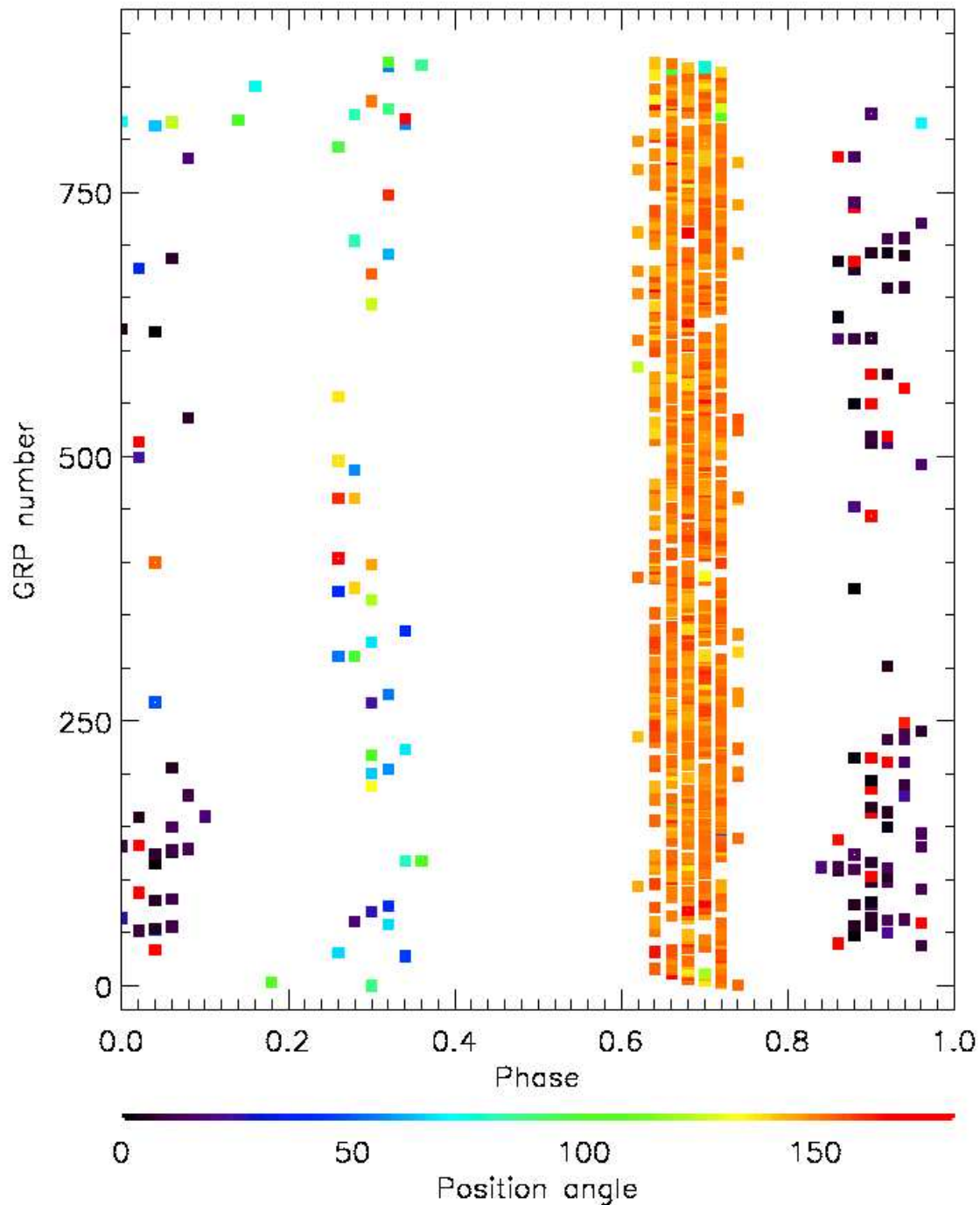


Figure 2.12: The position angle (PA) of selected 874 GRPs as a function of rotational phase of the Crab pulsar. PA is plotted only for points above 4.5σ of the off-pulse noise. Location of the Crab's pulsar radio components: HFC2: 0.05, LFC: 0.2, MP: 0.3, IP: 0.68, HFC1: 0.9.

as it has been noticed for PSR B0329+54 by [Edwards & Stappers \(2004\)](#).

2.5 High resolution detections

Because of the burst-like character of the giant pulse emission and the long dead-times in our data acquisition system, only 150 pulses were observed with the high resolution equipment. One out of the 150 recorded GRPs is shown in [Fig. 2.13](#). The peak strength varied from our threshold of ~ 75 Jy to a few rare events which even exceeded 1500 Jy. We computed dynamic spectra for the LHC and RHC signals by successive Fourier transforms and squaring of the data. Baseline and sensitivity corrections were also applied through the use of bandpass averages. The pulses were typically 2–5 μ s wide and certainly wider than the resolution of our incoherent software de-dispersion, 0.7 μ s. [Hankins et al. \(2003\)](#) showed the strong *temporal* variability within the giant pulses, which are possibly unresolved because of the limited bandwidth of the observations. Although giant pulses can be received over a wide bandwidth, the individual pulses do not have a uniform spectrum, as seen in [Fig. 2.14](#). The strongest emission was predominantly detected in the upper quarter of the accessible bandwidth. The individual pulses consist of ~ 100 MHz-wide clusters of narrow $\delta\nu \sim 2$ MHz spectral lines waxing and waning with time ([Fig. 2.14, left](#)). High frequency features appear earlier than low frequency features. Furthermore, if two giant pulses occur in rapid succession ([Fig. 2.13, 2.14](#)) separated by only 100 μ s, their spectra are similar though not identical. The maximum emission of the leading pulse occurs at higher frequencies than that of the trailing pulse ([Fig. 2.13, right](#)). The separation of spectral maxima also decreases in the trailing pulse. Intrinsic fluctuations of the emission process or - alternatively - scintillation could be the cause.

2.6 Conclusions

The results obtained so far by us suggest that physical conditions in the regions responsible for HFCs emission might be similar to those in the main pulse and inter pulse emission regions. This idea is supported not only by our detection of GRPs phenomenon at LFC and HFCs phases, but also by their polarisation characteristics. Still, the origin of HFCs remains an open question. One of the propositions is inward emission from outer gaps which may produce two additional peaks at requested phases in the light curve of the Crab pulsar ([Cheng et al. 2000](#)).

2. ENHANCED RADIO EMISSION FROM THE CRAB PULSAR

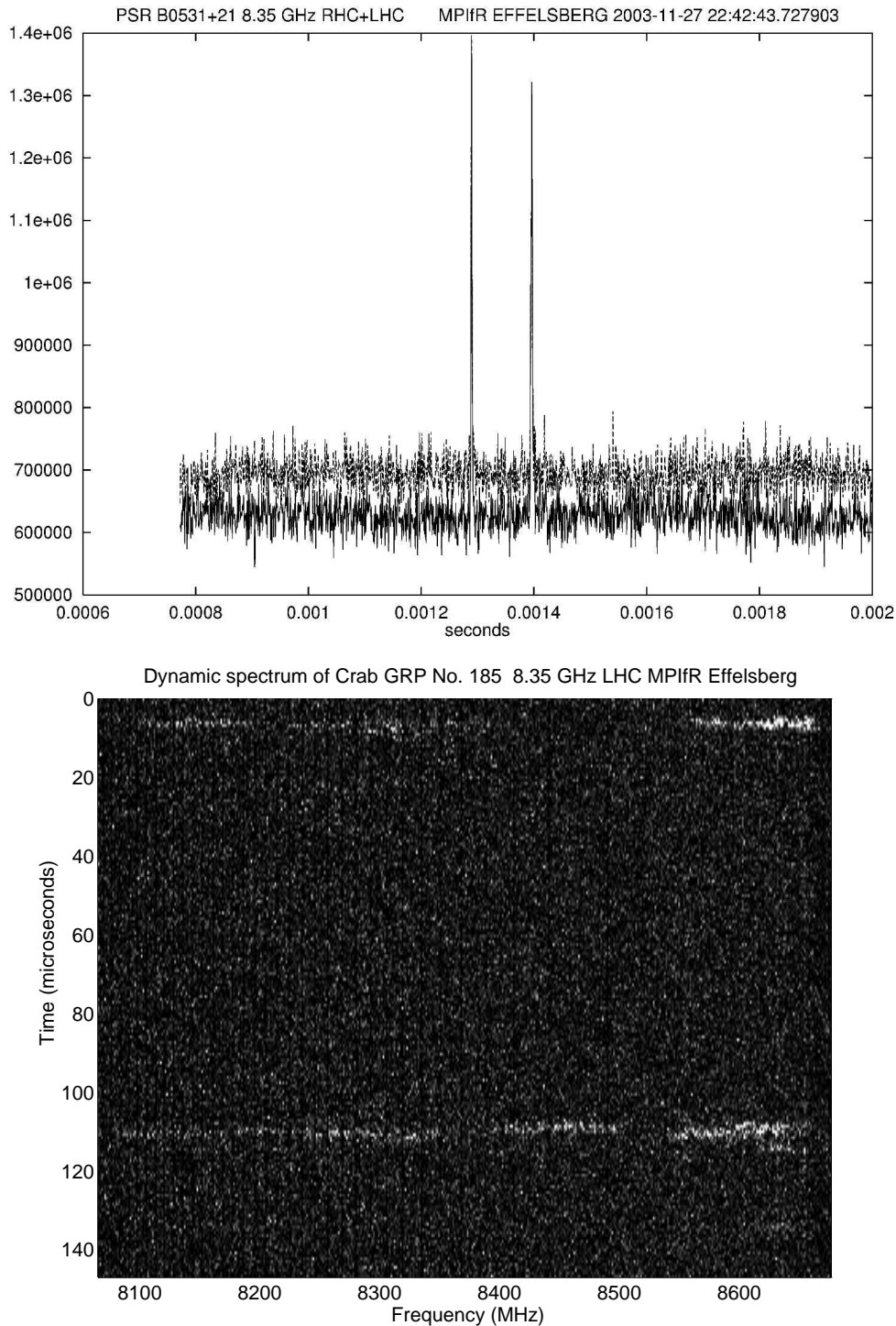


Figure 2.13: Giant pulse with double structure at 8.35 GHz (LHC, RHC), peak strength ~ 116 Jy. *Left*: De-dispersed profiles: LHC solid line, RHC dotted line. *Right*: De-dispersed dynamic spectrum; centre frequency 8.35 GHz, bandwidth 500 MHz, thus the low frequency is 8.1 GHz, and high frequency is 8.6 GHz. The scale is such that 1 pixel corresponds to 1 MHz and 1 μ s at the horizontal and vertical axis, respectively. The GRP is composed of two very sharp and narrow peaks, that are separated from each other by about 100 μ s.

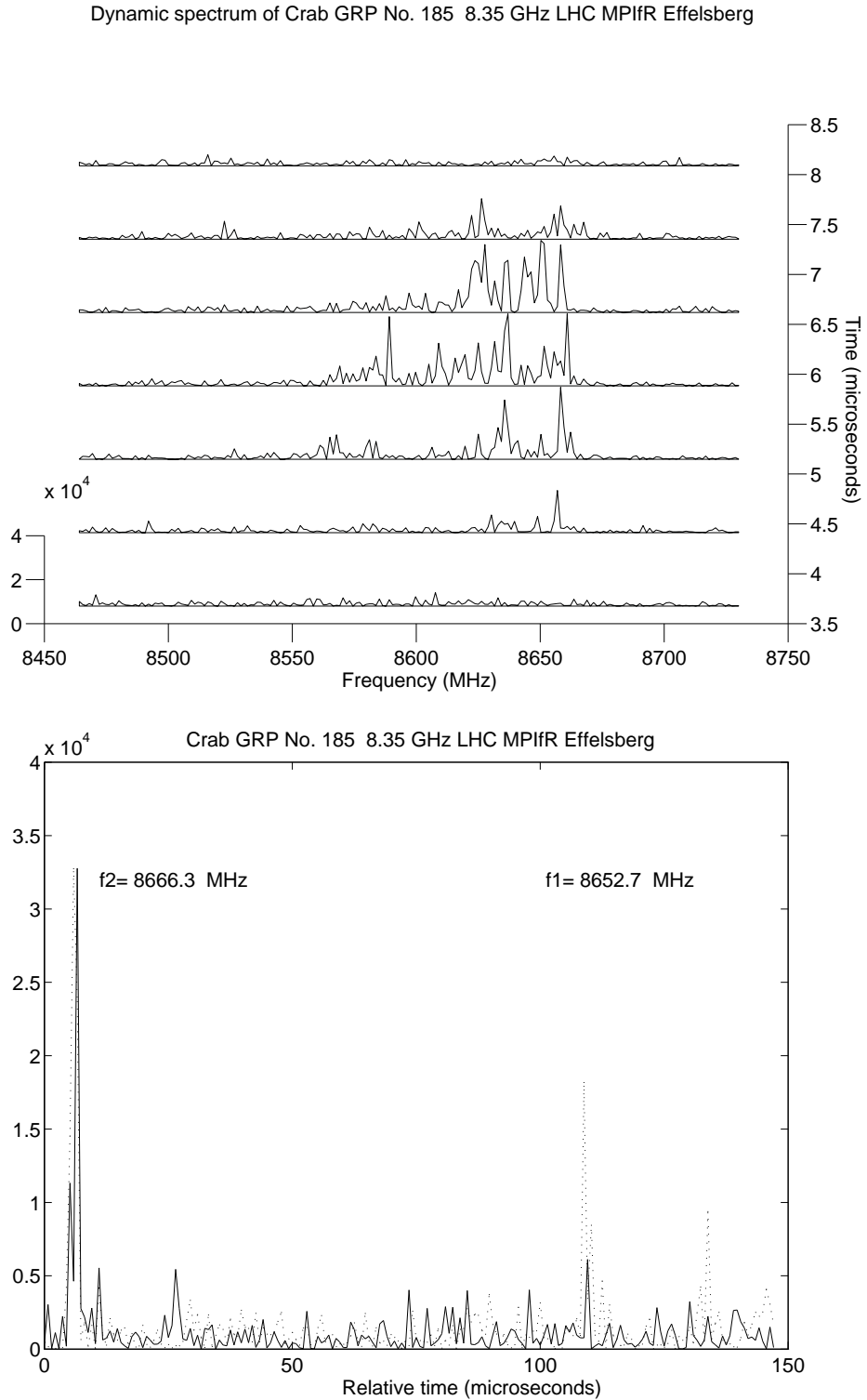


Figure 2.14: Spectral structure of giant pulse components. *Left*: Sequence of spectra of one GRP component. *Right*: Intensity in two spectral channels separated by 13.6 MHz, i.e. at lower frequency 8652.7 MHz (dotted line) and at higher frequency 8666.3 MHz (solid line).

2. ENHANCED RADIO EMISSION FROM THE CRAB PULSAR

Flux density distribution of GRPs that have been detected from different pulsars generally follows power law statistics. GRPs are believed (to some extent) to be associated with non-thermal high energy emission (e.g. in PSR B0531+21, PSR B1937+21, PSR B1821-24, and PSR B0540-69). The Crab pulsar was the best example of this association for a long time. From the group of millisecond pulsars a strong confirmation of this idea comes from the observations of PSR B1821-24 ($P=3.054$ ms). [Romani et al. \(2001\)](#) and more recently [Knight et al. \(2006\)](#) found that GRPs of this pulsar are concentrated in a narrow phase window coincident with the non-thermal pulses seen in hard X-rays, but occur on the trailing edges of the radio components. Recently, more and more features of pulsar radiation showing correlations between radio and high energy emission are observed. For example phase alignment between some optical polarisation features and radio intensity profile (see [Chap. 3](#)). Furthermore, it was found that there is a correlation between X-ray and radio pulses for Vela ([Donovan et al. 2004](#)), whereas [Shearer et al. \(2003\)](#) have detected a correlation between optical emission and GRPs emission in the Crab pulsar. They found that optical pulses coincident with GRPs were of about 3% brighter on average. On the other hand, the characteristics of some pulsars (PSR B1133+16; [Kramer et al. \(2003\)](#)) and the discovery of the Crab's giant radio pulses at phases where no high energy emission is known, do not match to this picture.

Chapter 3

Optical polarimetry of the Crab pulsar

3.1 Introduction

Pulsars are generally very faint objects in the optical energy band. Hence, there are only six known and confirmed optical pulsars, i.e. Crab, Vela, Geminga, PSR B0540-69, PSR B0656+14 and PSR B1929+10 (e.g. [Mignani et al. 2004](#)). Among them for three objects an attempt to measure their polarisation features has been made. However, only for the brightest, i.e. the Crab pulsar ($m_V = 16.6$), fully phase resolved polarisation measurements have been possible so far. The other two objects investigated into optical polarisation characteristics are the LMC pulsar B0540-69 and PSR B0656+14. Observations performed by [Middleditch et al. \(1987\)](#) and [Kern et al. \(2003\)](#) allowed to obtain: upper limits for the polarisation degree in the case of the LMC pulsar and values of the position angles of PSR B0656+14 covering only 30% of its rotational phase.

The first good observation of phase-resolved optical linear polarisation of the Crab pulsar ([Cocke et al. 1970](#); [Kristian et al. 1970](#); [Wampler et al. 1969](#)) showed that the polarisation angle sweeps through each peak and the degree of linear polarisation decreases and then increases with each pulse, reaching the minimum shortly after the pulse peak. These early observations were limited to the main pulse (MP) and inter pulse (IP) phase ranges only. Interpretation of the behaviour of the polarisation pattern has been made in terms of geometrical models ([Cocke et al. 1973](#); [Ferguson 1973](#); [Ferguson et al. 1974](#); [Radhakrishnan & Cooke 1969](#); [Wampler et al. 1969](#)). Some of them offer the possibility of determining the magnetospheric location of the source radiation (e.g. [Cocke et al. 1973](#); [Ferguson et al. 1974](#)).

3. OPTICAL POLARIMETRY OF THE CRAB PULSAR

For a long time it was thought that optical radiation of the Crab pulsar persisted only through both peaks and between them, i.e between MP and IP and not between IP and MP. Peterson et al. (1978) were the first to show that radiation persists throughout the whole pulsar cycle. They found that immediately before the start of MP the radiation is at a level of 3.6% of its maximum intensity. After this discovery, the linear polarisation of optical radiation from the Crab pulsar was measured by Jones et al. (1981) and Smith et al. (1988). Both results confirmed the previous observations and additionally showed the polarisation characteristics during both phase ranges between peaks. However, for the phase range of the minimum intensity the results were not conclusive: the polarisation degree was on the level of 70% and $47 \pm 10\%$ and the position angle was $\sim 118^\circ$ and $\sim 130^\circ$ for Jones et al. (1981) and Smith et al. (1988), respectively.

3.2 Observations

The goal of the project was to obtain polarisation characteristics of the Crab pulsar with very high time resolution as a function of the pulsar rotational phase. We used the 2.56-m Nordic Optical Telescope (NOT) for these measurements. This facility not only provides a mirror with reasonably large collecting area but also has an excellent performance in offset guidance and telescope control, which is important for instruments with very small entrance apertures. Moreover, contrary to many larger optical telescopes, guest instruments can be used at NOT. For the Crab pulsar observations carried out during November, 23–27 2003, we brought the high-speed photo-polarimeter OPTIMA¹ (Optical Pulsar TIMing Analyser, Sec. 3.2.2) to NOT. OPTIMA has been designed, built, and is still being reconfigured and developed at the Max Planck Institute for Extraterrestrial Physics under the supervision of Dr. Gottfried Kanbach.

3.2.1 Nordic Optical Telescope

The Nordic Optical Telescope Scientific Association (NOTSA) was founded in 1984 to construct and operate a Nordic telescope for observations at optical and infrared wavelengths. The associated member countries are: Denmark, Finland, Iceland, Norway and Sweden. NOT, a 2.56 m telescope, is located at the Roque de Los Muchachos Observatory on the Canarian Island of La Palma, Spain. First light at the NOT came

¹<http://www.mpe.mpg.de/gamma/instruments/optima/www/optima.html>

late 1988, and regular observations started during 1989. Technical information about the telescope is presented in Tab. 3.1.

Table 3.1: Technical Details of the Nordic Optical Telescope

Position	Longitude	17° 52' 59".7 W = 1 ^h 11 ^m 32 ^s .0 W
	Latitude	+28° 45' 20".5
	Altitude	2382 m
Telescope	Mounting of telescope	altitude-azimuth
	Total moving weight of telescope	43 tons
	Weight of telescope tube	6800 kg
	Type of optical system	Ritchey-Chretien
	Effective focal length	28160 mm
	Effective focal ratio	f/11
Primary mirror	Diameter	2560 mm
Secondary mirror	Diameter	510 mm
Other	Total field of view	30' (25' unvignetted)
	Focal plane scale	7.325 "/mm, 0.13652 mm/"

3.2.2 OPTIMA instrument

The primary science goal for OPTIMA is to detect and measure the optical light curves of young high-energy pulsars known to emit X- and γ -ray photons. A second, but no less important, class of targets for a fast photometer are compact objects in binary systems (white dwarfs, neutron stars, black hole candidates) and their environment. In these sources quasi-periodic as well as irregular and random intensity fluctuations are expected. This calls for the detection and timing of single photons in order to be able to derive light curves with any suitable binning after the observations. The absolute arrival time of individual photons is also needed for the correlation of OPTIMA data with measurements from other ground or space observatories.

The OPTIMA photometer development started in 1996 (Straubmeier 2001) and used progressively more complete systems on the 1.3-m telescope (Mt. Skinakas, Crete), on the 3.5-m telescope (Calar Alto, Spain), on the 2.1-m Guillermo Haro telescope (Cananea, Mexico), and in the southern hemisphere (74-in. Mt. Stromlo, 2.2-m ESO/La Silla, 1.9-m SAAO/Sutherland).

The following description of the OPTIMA instrument is based on the description presented by Kanbach et al. (2003) with some modifications.

3. OPTICAL POLARIMETRY OF THE CRAB PULSAR

General layout of the instrument

The basic function of a high-speed photometer is to select, record, and time photons from a celestial source with high efficiency and precision. In the case of OPTIMA, which was primarily designed for studying the optical light curves of extremely faint pulsars ($V \approx 25^m$), the observed flux of the astronomical target lies considerably below the brightness of the night sky ($\approx 22^m \text{ arcsec}^{-2}$), even at the best astronomical sites. The pulsar signal can nevertheless be recovered by phase-coherent folding of sufficiently long observations at the pulsar's rotational frequency. To minimise the dilution of the source's signal by the underlying atmospheric background, the flux of the target is isolated in the focal plane of the telescope by the use of an optical fibre pick-up which acts as a diaphragm. Target and sky background photons are then transferred through the fibres to photon detectors.

Fig. 3.1 displays a schematic layout of OPTIMA attached to the Cassegrain focus of a large telescope. The light from the telescope is incident on a slant mirror with an embedded bundle of optical fibres. Optionally one can insert filters or a rotating linear polariser into the incoming beam. The field around the fibres, visible in the mirror (typical size $2' \times 3'$), is imaged with a target acquisition camera (early an ST-7 produced by Santa Barbara Instrument Group, later an AP6, from Apogee Instruments). The optical fibres are arranged in a centre-filled hexagonal array for the target (central fibre) and its close environment (six ring fibres), and a single fibre about $1'$ distant from the target for sky background monitoring. The fibre bundle is shown in the Fig 3.2, *left* in a photograph taken through a microscope. The outer diameter of the metal tube holding the fibres is about 0.7 mm. The fibres are illuminated from the other end, i.e. the side with the connectors to the APDs. The light is red because there were red protective plastic covers on the connectors. The designations of the fibres are indicated on the photograph. We use the designations alternatively, i.e. channel 0 for the central fibre, and channels 1 to 6 for the ring fibres. Although the pure silica core fibres transmit light from 400 nm to ~ 950 nm with better than 99%, the net transmission of the tapered fibres is lower and appears to range between 60% and 90%. Since the fibres are easily exchanged, different sizes can be installed to adapt to the focal scale or the seeing conditions. If broad-band spectro-photometry is desired the target fibre is attached to a prism spectrograph. The four output colour bands of the spectrograph are also picked up with fibres, and go into separate counters. During our November 2003 observations we used "tapered" fibres with $320 \mu\text{m}$ diameter at the pickup and an exit diameter at the detector of $100 \mu\text{m}$. The single fibre size in the focal plane is equivalent to a $\sim 2''.3$ resolution at

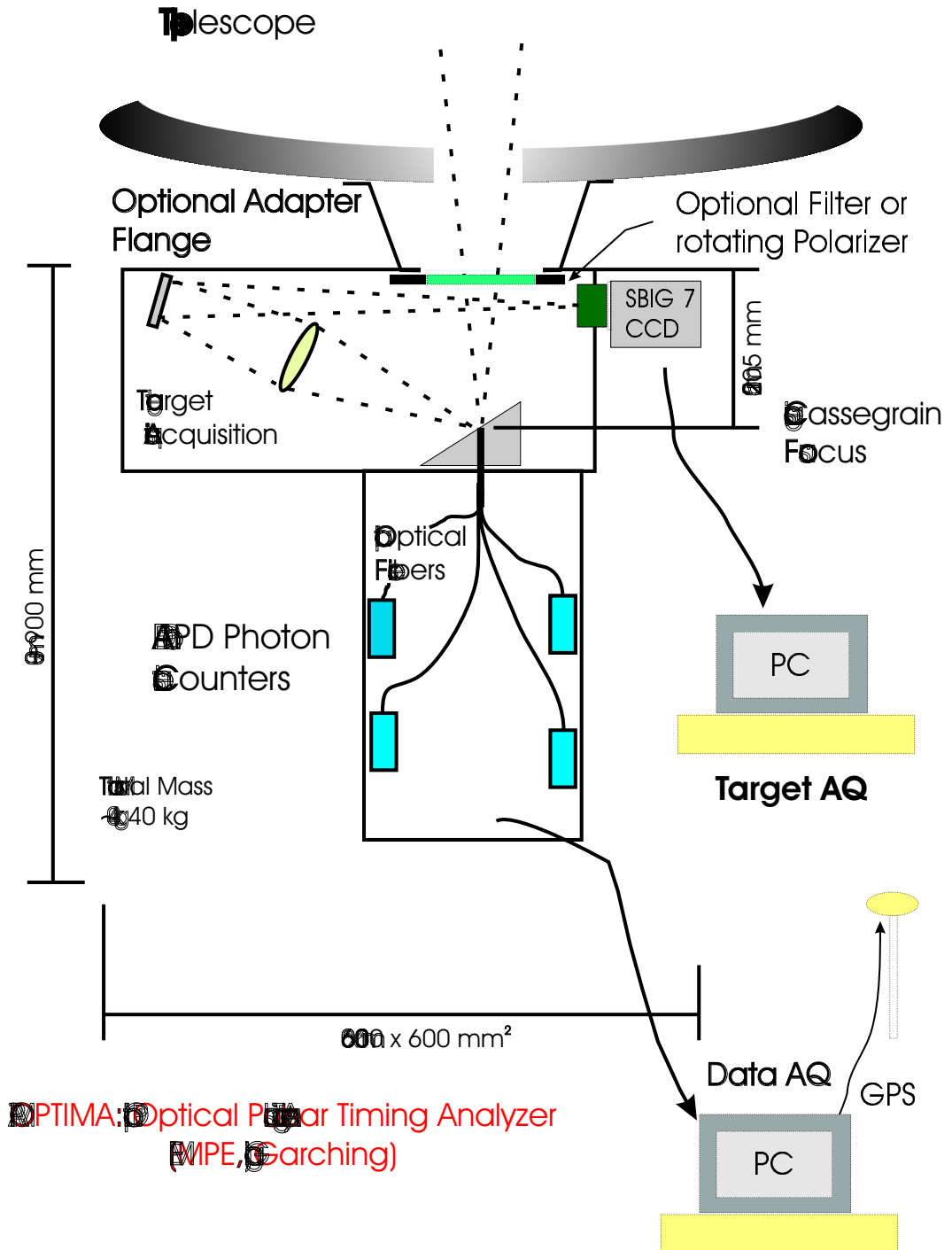


Figure 3.1: A schematic layout of OPTIMA attached to the Cassegrain focus of a large telescope. [Taken from Kanbach et al. (2003)].

3. OPTICAL POLARIMETRY OF THE CRAB PULSAR

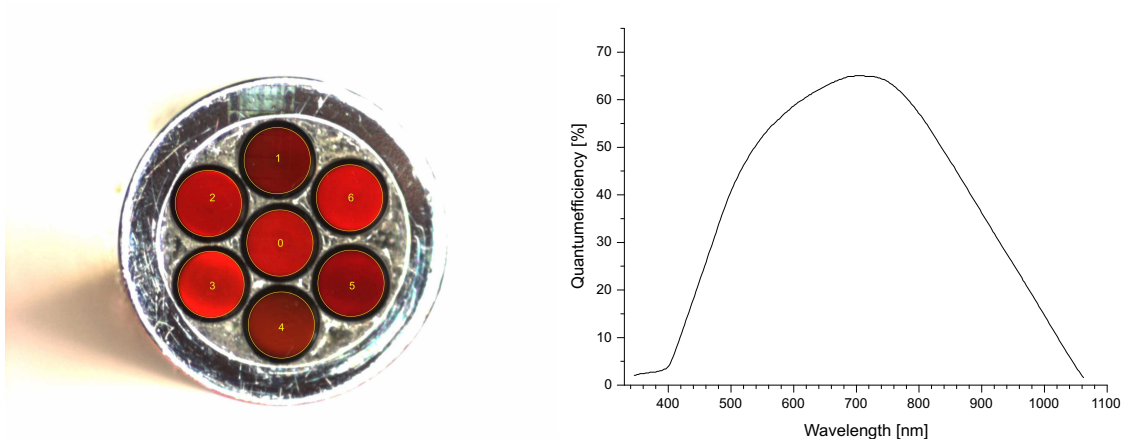


Figure 3.2: *Left:* An OPTIMA centre-filled hexagonal fibre-array, central fibre is for the target (channel 0), and six ring fibres are for its close environment (channels from 1 to 6). *Right:* Quantum Efficiency of the APD Single Photon Counting Modules (type SPCM-AQR-15-FC) produced by EG&G, Laser Components. [Adopted from Kanbach et al. (2003)].

the 2.56-m NOT telescope ($\tan \alpha = \frac{d}{f}$, for $d = 0.32$ mm and $f = 28160$ mm we get $\alpha = 2''.344$).

The timing of individual photons is controlled by signals from the Global Positioning System (GPS) to an absolute accuracy of $\sim 2 \mu\text{s}$, although the readout system limits the resolution to $\sim 4 \mu\text{s}$. The OPTIMA detector is operated with two PCs and is autonomous except for the need to have a good telescope guiding system.

The photometer

For the observation of faint sources it is very important to convert the highest possible fraction of incoming photons into countable signals, i.e. to have detectors with high quantum efficiency over a wide spectral band. Most previous systems for recording single optical photons with time resolutions of a few microseconds used photomultiplier tubes (PMT) or detectors based on a similar technology. Their photo cathodes have a peak quantum efficiency of typically 20% and a narrow wavelength range of sensitivity. Much better quantum efficiencies can be reached with solid state detectors. OPTIMA uses Avalanche Photodiodes (APDs). These new silicon devices have been produced with peak quantum efficiencies of up to 80% and a wide band of sensitivity ranging from 250 to 1100 nm. We use commercially available APD based single photon counting modules of type SPCM-AQR-15-FC produced by EG&G, Laser Components. These highly integrated devices operate in a Geiger counter mode where

a photon initiated avalanche pulse is quenched by the instantaneous reduction of the bias voltage. The diodes have a diameter of 200 μm and are electrically cooled with Peletier elements. The selected units offer low dark count rates of typically less than 50 Hz, are insensitive to electromagnetic interference and are very reliable. They could record photons up to rates of several MHz before noticeable dead-time losses occur. The present data acquisition however can not keep up with such rates. The achieved quantum efficiency of the APD detectors is shown in Fig. 3.2, *right*. Although it falls short of the values mentioned above, it is still above 20% for a spectral range from 450 to 950 nm. Bandwidth and quantum efficiency of APDs result in about a factor of 6 improvement in sensitivity compared to PMT based systems.

Timing and data acquisition

An absolute time base available anywhere is provided by the Global Positioning Satellite system GPS. We use a special receiver (from Datum Inc.) which can process the clock pulses of up to six satellites simultaneously and reaches an absolute time accuracy of better than 2 μs on the “pulse per second (PPS)” GPS signal. This signal disciplines a local high frequency oscillator with the same precision which provides a continuous UTC time signal to the system bus of the PC used for data acquisition (DAQ). The task of the DAQ unit is thus to correlate the electronic signals of the APD detector modules with the high resolution time base and assign UTC arrival times to each detected photon. This association is done on hardware level to ensure a reliable operation even on a non real-time operating system and under high system load. The timing of the conversion cycles of the DAQ card is controlled by the GPS based oscillator, so that the transfer of the APD detector signals is running at a fixed rate. The absolute starting time of each software triggered acquisition sequence is precisely known. The controlling software counts the number of conversion cycles since the start of the sequence and stores this sequential number together with an identifier of the respective detector channel for each detected photon. Conversion cycles without detected photons are skipped. Based on the cycle number, the acquisition frequency and the absolute time of the start of the sequence the UTC arrival time of every recorded photon can be restored during data analysis. The present DAQ system is effectively limited to photon count rates below about 100 kHz because of the speed of the PC bus. Future versions of the DAQ should be able to control higher rates, which are achievable with the photon counters (up to 2 MHz).

Typical count rates from the unfiltered night sky in dark conditions are $\sim 1\text{--}2$ kHz per fibre resulting in several GBytes of data for a night of observing. Data are first

3. OPTICAL POLARIMETRY OF THE CRAB PULSAR

staged to RAM and periodically (\sim every 10 minutes) stored on HDD. Off-line data analysis includes the options to transfer the topocentric photon arrival times to the solar system barycentre. Pulsar phases and light curves can be calculated if the pulsar ephemeris is known. If unknown periodicities or irregular variations are investigated, FFT analysis and rate plots are available.

Rotating polarisation filter

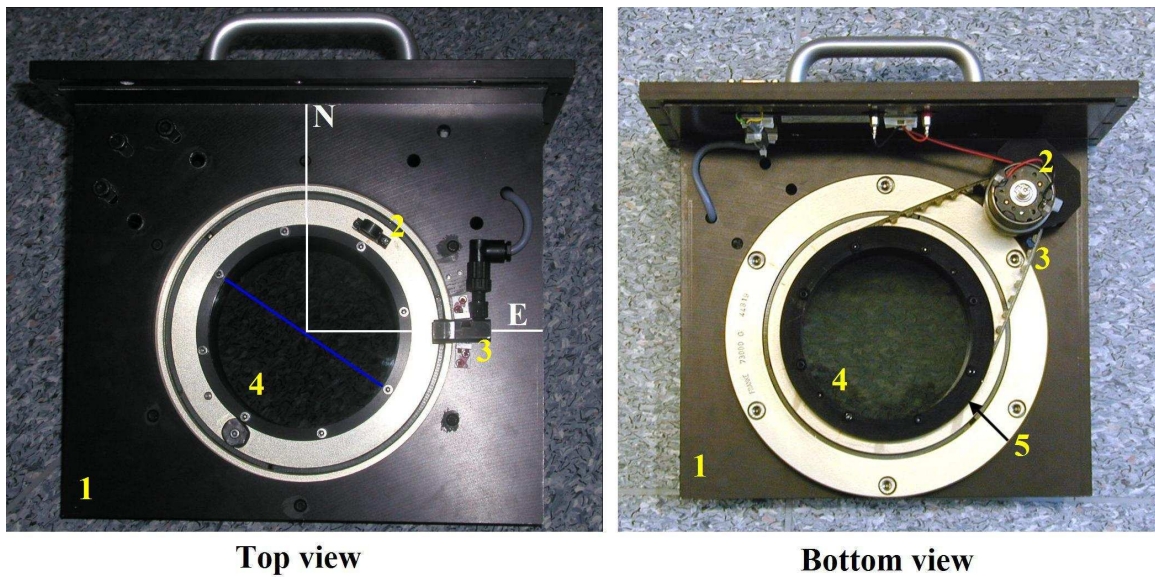


Figure 3.3: Photograph of the OPTIMA rotating polarisation filter. Top view (telescope side): 1 - base plate; 2 - permanent magnet on rotating filter; 3 - Hall sensor switch on base plate mounted at ~ 90 degrees from north to east; 4 - glass covered Polaroid filter; the polarisation direction of the filter is approximately perpendicular to the radius vector to the magnet. The filter rotates from north to east. Bottom view: 2 and 3 assign motor and belt, respectively. The small gear on the motor has 12 sprockets. 5 is the large gear with 40 sprockets.

OPTIMA can be optionally equipped with a rotating polarisation filter (RPF). Fig. 3.3 shows photographs of the polariser seen from top (telescope side) and bottom. The device can be introduced into the incoming beam above the fibre pick-up so that all fibre channels and the CCD image are fully covered. The polarising filter (Type 10K by Spindler & Hoyer) is mounted on a precision roller bearing and is rotated with the motor visible on the bottom view. Typical filter rotation frequencies of up to 10 Hz can be adjusted through the supply voltage of the motor. The small gear on the motor axis has 12 sprockets, and the big gear has 40 sprockets, i.e. the small gear rotates 3

and $1/3$ turns for one full turn of the polarisation filter. Incoming linearly polarised light is modulated at twice the rotation frequency. In the top view a magnetic switch (magnet on the rotating filter, Hall sensor on the base plate) can be seen. The reference position of the filter is given by a signal from the switch. It is registered and timed in the same way as a photon event and stored in a separate channel (i.e. *channel 16* in the DAQ system). This allows us to interpolate the position of the polarising filter for any event using the time difference from the preceding and to the following Hall sensor signal. Slight irregularities in the rotation frequency of the RPF that occur on time-scales longer than fractions of a second, e.g. due to supply voltage drifts or mechanical resistance changes in the bearing and motor, can be corrected with sufficient accuracy. The RPF was tested in the lab with unpolarised and linearly polarised light to ensure and prove that the OPTIMA fibres and detectors have no intrinsic systematic response to polarised light (Kellner 2002). If the incoming light is polarised the filter produces a sinusoidal modulation as it rotates (e.g. see Fig. 3.6 and 3.17, *bottom panels*). Unfortunately, some parts of the rotating polarisation filter module (especially the fast running small motor gear) are not black and reflect any scattered light which might be present in the OPTIMA enclosure. This can cause a low level of synchronised higher frequency intensity variations in the count rates on top of any polarisation modulations. We sometimes observed such quasi-periodical, and not completely understood effects in the sinusoidally modulated RPF light curve of the incoming light. For the analysis of pulsar data that are generally not 'in phase' with the polariser this effect is completely washed out. The polarising filter modulates the incoming light effectively only over a wavelength range of about 470-750 nm. Since the APD response ($QE > 20\%$) extends from about 450 nm to 970 nm and no wavelength information of the individual recorded events is available, it is necessary to block radiation outside the filter modulation range. Such photons, especially towards the near IR, are not modulated and would decrease the estimate for the degree of polarisation. We therefore inserted an IR blocking filter that cuts the wavelength range at about 750 nm.

3.2.3 Weather and seeing conditions during the observations

For our proposal we got five observing nights from 23 to 27 November 2003. With respect to the weather and seeing condition we were half lucky. The weather conditions, i.e. the temperature, humidity, pressure, and wind speed during all observing times are presented in the Fig 3.4. Every vertical line at midnight means a change of date. For good observing conditions during the nights 25/26, 26/27 and 27/28

3. OPTICAL POLARIMETRY OF THE CRAB PULSAR

the seeing values are shown in the Fig. 3.5, respectively. Seeing data were taken from RoboDIMM¹ Isaac Newton Group of Telescopes (ING). The RoboDIMM is a very reliable robotised seeing monitor which can operate completely autonomously. It takes measurements (seeing, extinction, scintillation), analyses the data and stores the results in a database.

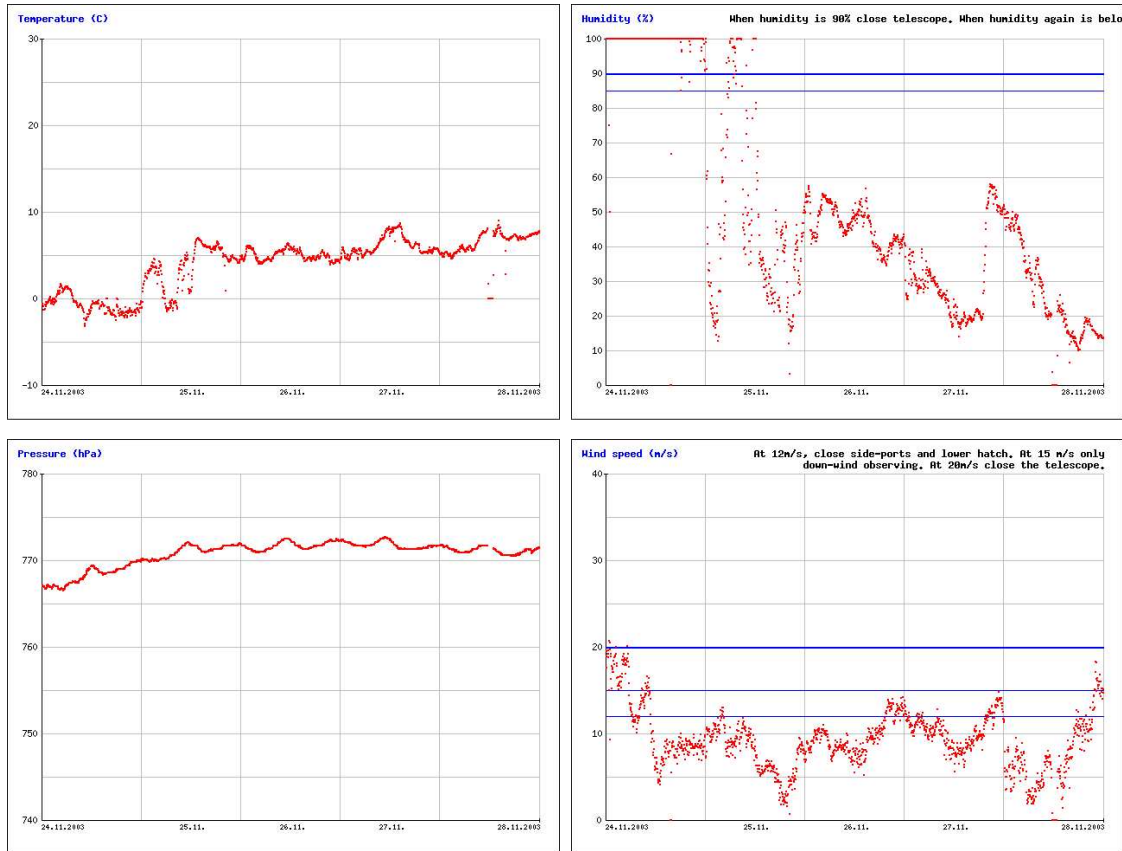


Figure 3.4: Weather conditions during the observations, from *top left* to *bottom right*: temperature, humidity, pressure and wind speed, respectively. Every vertical line at midnight means a change of date. Blue horizontal lines indicate the weather conditions under which the telescope must be protected from possible damage. These include wind speed and humidity for closing the side ports, observing downwind, and closing up the telescope. For details see comments over these figures.

Detailed description of the weather condition and observation actions taken during the following five observing nights are presented below:

23/24 Nov: fog, rain, strong wind, temperature $\sim 0^\circ$, no observations taken, APD counter of channel 3 failed (later replaced by another counter);

¹<http://www.ing.iac.es/ds/robodimm/>

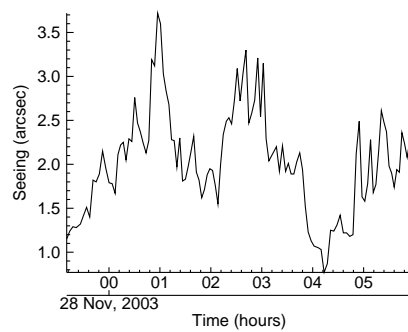
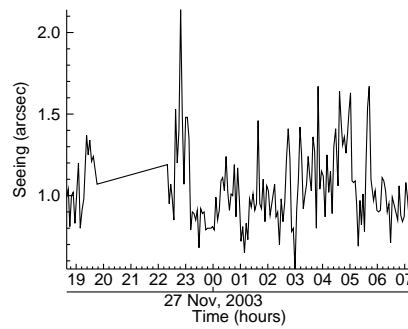
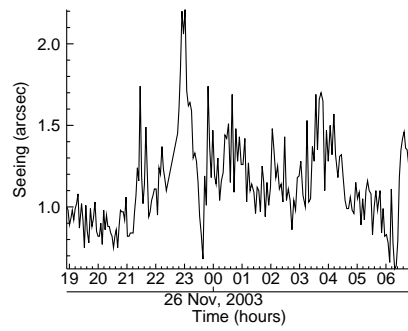


Figure 3.5: All possible seeing data taken by RoboDIMM during three good nights of our observations. *Upper, middle, bottom* panels are for the nights 25/26, 26/27, and 27/28 of November 2003, respectively.

3. OPTICAL POLARIMETRY OF THE CRAB PULSAR

- 24/25 Nov: humidity fluctuates from 100% to 20%, in the morning fog and rain, temperature changes from $\sim -2^\circ$ to $\sim 5^\circ$, some calibration data taken, 27 minutes of unfiltered Crab observations;
- 25/26 Nov: clear sky, humidity on the level of 45%, temperature $\sim 6^\circ$, seeing and transparency changing occasionally (from $2''.2$ to below $1''.0$), RPF and IR filter introduced, channel 3 APD replaced by sky background APD, 8 hours and 15 minutes of Crab pulsar observations;
- 26/27 Nov: sky partly clouded, high Cirrus clouds, humidity fluctuates from $\sim 45\%$ to 25% , temperature on the level of 5° , around midnight wind speed increased to 14 m/s, after midnight seeing below $\sim 1''.5$, 8 hours and 44 minutes of Crab pulsar observations;
- 27/28 Nov: very good weather, clear sky, at the beginning of observations humidity on the level of 20%, around midnight jumps to more than 50%, also the wind speed increases to 15 m/s, temperature $\sim 5^\circ$, seeing and transparency changing from $1''.1$ to even more than $3''.0$, 7 hours and 53 minutes of Crab pulsar observations.

Usually one observation set of the Crab pulsar lasted 10 minutes. For brighter sources it might be shorter because of reaching the data buffer capacity level very quickly. All together, we had 165 files containing the Crab pulsar observations. However, three of them, coming from the morning of November 25, were taken without the RPF and IR filter. Additionally, two of them had very short exposure time, on the level of tenths of seconds. These five files were not taken for further analysis. For the remaining 160 files, and all 7 channels of each file, the count rates in 10 seconds bins were obtained. For good seeing and weather condition, as well as for proper pointing, we had around 30 – 35% of the total counts in the central fibre, and between 5 and 10% in the background (ring) fibres. When the seeing was high (=bad) then it can be observed that the count rate for channel 0 goes down, and consequently goes up for channels 1 ÷ 6. We put a threshold on the level of 30% of total counts in channel 0 for the good data selection. By doing so, our end result was 83 files, being equivalent to 13 hours and 43 minutes of total exposure. 83 selected file names are presented in Tab. A.1 where, additionally to the file name, the starting data acquisition date and the UTC time are given.

3.3 Data reduction

3.3.1 Flat field correction

For flat field correction factors of all channels we used two sets of dark sky observations of the SNR 119.5+10.2 field (CTA-1, $\alpha_{2000} = 00^h06^m6$, $\delta_{2000} = +72^\circ47'$), i.e. pointing at $\alpha = 00^h07^m02^s00$, $\delta = +73^\circ03'28''00$. Both observations were taken on November 25. The data acquisition start time of the first file was 21:39:10 and of the second 21:49:13. The exposure time amounted to 600 and 300 seconds for the first and second observation, respectively. The detected count rates behind the filters fluctuated from 180 Hz for channel 4 up to 240 Hz for channel 6. To obtain the flat field correction factors we assumed that this value was 1.0 for the central fibre, and we scaled the count rates of the rest of the fibres to the central one. We binned the data in 10-seconds intervals, and then calculated the average and uncertainty for each single channel of the ring fibres. The resulting numbers are shown in Tab. 3.2.

Table 3.2: Fibres flat field correction factors

Channel	0	1	2	3	4	5	6
Factor	1.000	1.009	1.074	0.899	0.850	0.956	1.140
Uncertainty	0.012	0.013	0.013	0.012	0.011	0.012	0.014

3.3.2 Raw data binning

For each incoming and detected photon the OPTIMA data acquisition system stores its Time Of Arrival (*TOA*). A more detailed description of the following steps can be found in Sec. 3.2.2. By using the OPTIMA system software (Straubmeier 2001) one can obtain *TOAs* in units of Julian Date (JD). To assure high time accuracy two parts of JD are given, the integer and fractional part referring to the day of observations and to the fractional part of the day, respectively. In order to apply the rotational model of the pulsar derived from radio observations to our optical photons, it is required to measure the *TOAs* in an “inertial observer frame”. Using the NOT position coordinates (Tab. 3.1), the Crab pulsar coordinates (3.3) and as planetary ephemeris the JPL DE200 tabulations (Standish 1982) we transformed the recorded *TOAs* to the commonly used inertial frame, i.e. to *TOAs* at the solar system barycentre.

Parameters of the rotational model of the Crab pulsar (Tab. 3.3) obtained from the radio observations are regularly, once per month, published by the Jodrell Bank

3. OPTICAL POLARIMETRY OF THE CRAB PULSAR

Table 3.3: The Crab pulsar radio ephemeris

Parameter	Value
α_{2000}	$05^h34^m31^s.972$
δ_{2000}	$+22^\circ00'52''.07$
Val. range (MJD)	52944–52975
t_0 (TDB MJD)	52960.000000296
ν_0 (Hz)	29.8003951530036
$\dot{\nu}_0$ (10^{-10} Hz s $^{-1}$)	-3.73414
$\ddot{\nu}_0$ (10^{-20} Hz s $^{-2}$)	1.18

Observatory pulsar group as a Jodrell Bank Crab Pulsar Monthly Ephemeris¹. The derived radio model is optimised (i.e. it includes the rotational frequency and its changes, its first and second derivative, as well as, dispersion measure changes, timing noise effects, glitches and pulsar proper motion) so that it is sufficient to account for the arrival time of any pulse emitted during the time span of the observations and predict the arrival times of subsequent photons belonging to these pulses. The model is based on a Taylor expansion of the angular rotational frequency, $\nu = 2\pi/P$ about a model value ν_0 at some reference epoch t_0 . The model pulsar phase ϕ as a function of barycentric time is thus given by:

$$\phi(t) = \phi_0 + (t - t_0)\nu_0 + \frac{1}{2}(t - t_0)^2\dot{\nu}_0 + \frac{1}{6}(t - t_0)^3\ddot{\nu}_0 + \dots$$

where ϕ_0 is the pulse phase at t_0 . For each recorded *TOA* the corresponding pulse phase was calculated. To obtain a light curve all events are folded according to their phases with time resolution on the level of $33 \mu\text{s}$, that is an equivalent of 1000 bins per rotational period of the Crab pulsar. The chosen resolution assures a good S/N ratio even for the phase ranges where the intensity is very low.

We sort the individual events into a 3D data array. The first dimension of this array is given by the rotational phase of the pulsar. The second dimension is defined by the polarisation filter phase at the photon's *TOA*. This reference position of the filter is derived from the sequence of Hall sensor signals, which are registered and timed in the same way as the photon events and stored in a separate channel. Therefore we can interpolate the position of the polarising filter for any photon event using the time difference from the preceding and the following Hall sensor signal, i.e.

$$\alpha_{RPF}(TOA) = \frac{t_{TOA} - t_b}{t_a - t_b} \cdot 360^\circ,$$

¹see <http://www.jb.man.ac.uk/pulsar/crab.html>

where $\alpha_{RPF}(TOA)$ is the RPF angle at which the event was observed, t_{TOA} is the event time of arrival, whereas t_b and t_a are the recorded times of the Hall signal sensor before and after t_{TOA} , respectively. Thus $(t_a - t_b)$ is nothing else than the period of rotation of RPF, and then consequently the RPF frequency is $\nu_{RPF} = 1/(t_a - t_b)$. Since during one turn of the RPF all possible polarisation angles are measured two times, for all values bigger than 180° exactly 180° was subtracted. Thus we have the second dimension of our 3D array, it spans from 0 to 180 degrees, with 1° intervals. The third dimension of the data array is assigned to the data channels. We repeated the pulsar phase and polarisation filter phase calculation for all the events from all possible channels. The number of channels (seven) defines the length of the 3rd dimension of the data array. The end result is an array of $1000 \times 180 \times 7$ containing the recorded events, with 1000 and 180 bins for the pulsar and polarisation filter phases respectively, and 7 channels of measurement. Here we showed a general description of the first step of the data analysis. However, some irregularities in the rotation frequency of the RPF have been detected. The RPF state of the art is described in detail in Sec. 3.3.3.

The obtained light curve of the Crab pulsar and the sinusoidal modulation of the incoming light due to the RPF are shown in the *upper* and *bottom* panels of Fig. 3.6, respectively. These are the raw data, i.e. without subtracting any nebular or background light recorded in the central fibre. In both cases two periods are shown for clarity. For the pulsar light curve (Fig. 3.6, *upper*) we also indicated its components: main pulse (MP), inter pulse (IP), non-zero intensity level between two peaks - bridge, and DC¹ region, previously known as the so called ‘off-pulse’ component. For our further analysis we define the DC component as the counts between phases 0.78–0.84. The Crab pulsar period during the observations ($P = 1/\nu$, see Tab. 3.3), number of bins used for folding, and the corresponding time resolution are also given. The amplitude of the modulated polarised light, summed over the pulsar phase, is at the level of 8%, whereas the maximum is reached at around 119° (Fig. 3.6, *bottom*).

3.3.3 Rotating polarisation filter characteristics

OPTIMA is configured in such a way that colour filters and/or a rotating linear polariser (Sec. 3.2.2) can optionally be inserted in front of the incoming beam. In Sec. 3.3.2 we described the general algorithm for getting the raw data array. Single

¹ Direct Current or continuous current, in this case refers to continuous emission component that is present along whole rotational phase.

3. OPTICAL POLARIMETRY OF THE CRAB PULSAR

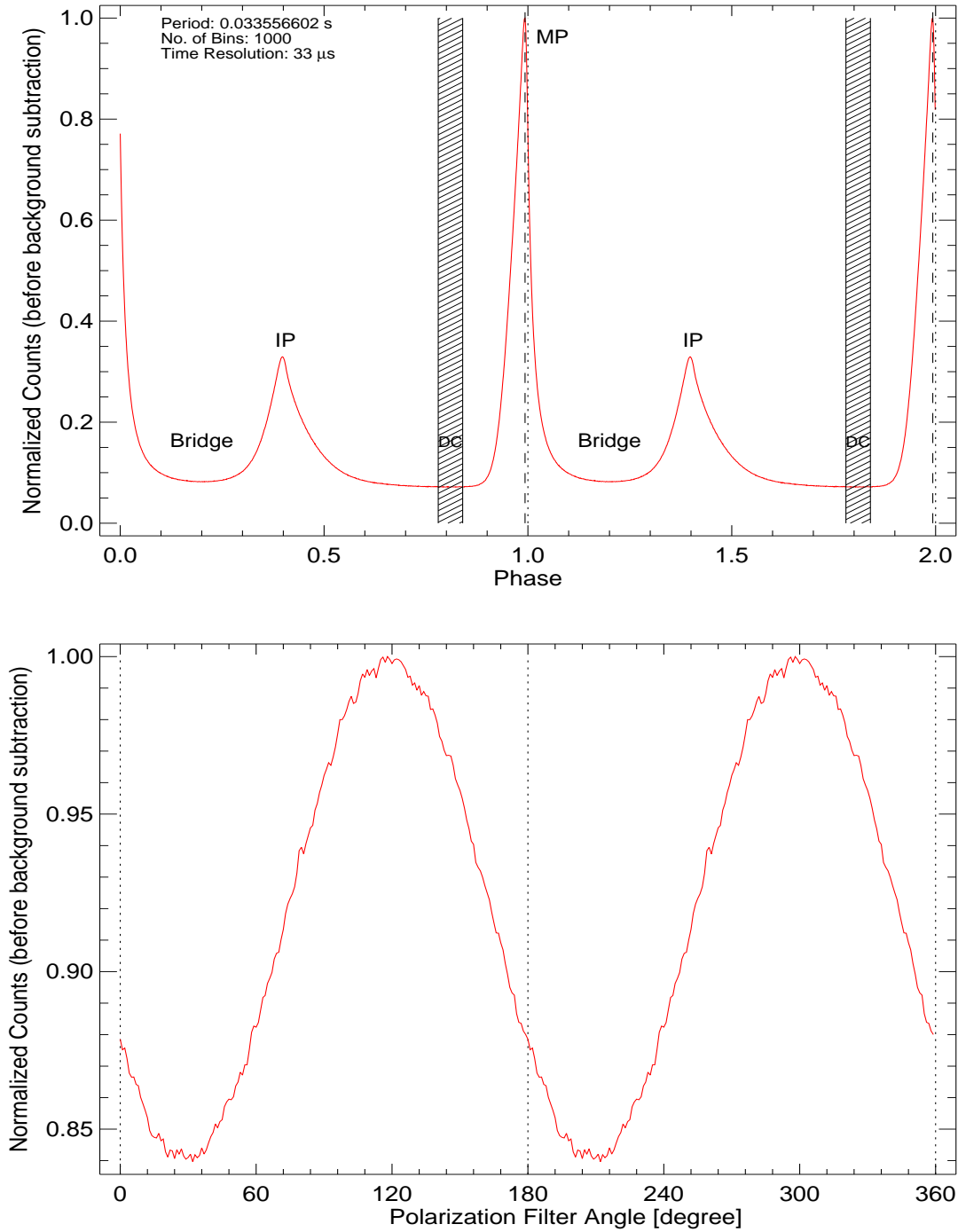


Figure 3.6: *Upper*: The Crab pulsar light curve obtained from photons recorded by the central fibre APD. The components of the light curve are indicated as follows: main pulse MP, inter pulse IP, non-zero intensity level between two peaks - bridge, and DC region, previously known as the so called ‘off-pulse’ component in between the 0.78 – 0.84 phase range. *Bottom*: The sinusoidal modulation of the incoming polarised light, summed over the pulsar phase. Its amplitude is on the level of 8%, and the maximum is reached at around 119°. No background or nebula subtraction has been applied. In both cases two periods are shown for clarity.

photons are recorded with an accuracy of $4 \mu\text{s}$, but to assure the high S/N ratio even for the low intensity parts of the Crab pulsar light curve we bin the data with $33 \mu\text{s}$ resolution. Events are also folded as a function of the RPF phase. To do so we need the information of the RPF frequency as a function of time. Each single signal coming from the Hall sensor is recorded in the same way as a regular photon reaching the fibre bundle and it is stored as a channel 16 event (Sec. 3.2.2). Before calculating $\alpha_{RPF}(TOA)$ for each event we investigated the polarisation filter behaviour over the whole observation run. For single observations (corresponding arbitrary file numbers and the file names containing the observation date can be found in Tab. A.1) we run a short script that does the following:

1. Checks if there is an inversion in time for succeeding $TOAs$ of the Hall sensor signal.
2. Calculates the averaged frequency of the filter rotation by using raw and uncorrected data (e.g. *upper left* panels of Fig. 3.7, 3.8). Further used as a threshold parameter during search for *gaps* and *echos* (described in the next algorithm step).
3. Searches for *gaps* and *echos*. During laboratory test runs of the RPF we found that the tick from a Hall sensor passage is sometimes missing, i.e. the time between two succeeding ticks is twice as long as average; sometimes we observe two ticks with a very short time interval, usually below $10 \mu\text{s}$. The first case we call a *gap*, the second case an *echo*. Number of occurrences of *echos* and *gaps* as a function of the succeeding good files (files names with corresponding arbitrary file numbers are given in Tab. A.1) is presented in the *upper* panel of the Fig. 3.9. The rate of *echos* and *gaps* over the total number of the Hall sensor signals in each file is shown in the Fig. 3.9, *bottom* panel.
4. If any *gap* or *echo* is found the program corrects for this effects. It interpolates the missing event or removes the doubled tick. It is instructive to compare in the *left upper* and *bottom* panels of Fig. 3.7 and 3.8 the raw data with the data corrected by this procedure.
5. Both, short and long time scale variation of the RPF frequency exist (Fig. 3.7, 3.8). For the short one a simple finite impulse response filter procedure as the boxcar filter is applied. The smoothing function returns a copy of events $TOAs$

3. OPTICAL POLARIMETRY OF THE CRAB PULSAR

smoothed with a boxcar average of the specified width. The algorithm is:

$$SMOOTHED TOA_{RPF,i} = \begin{cases} \frac{1}{w} \sum_{j=0}^{w-1} TOA_{RPF,i+j-w/2}, & i = \frac{(w-1)}{2}, \dots, N - \frac{(w+1)}{2} \\ TOA_{RPF,i}, & \text{otherwise,} \end{cases}$$

where N is the recorded number of RPF $TOAs$, and w is the width of the smoothing window. Usually w was on the level of 10 bins, thus taking the averaged RPF frequency gives us the smoothing window on the time scale of 3 seconds. The long time scale variations of the RPF frequency have to be kept as they were.

6. The average RPF frequency during single observations, with its standard deviation σ , over the whole observation is calculated (Fig. 3.10). The RPF frequency averaged over the whole observational time span amounts to 3.4 Hz, whereas the averaged RPF frequency of a single 10 minutes observational set varies from 2.85 Hz up to 3.75 Hz. Moreover, it might be seen that the deviations σ also differ. They strongly depend on the long time scales variation of the RPF, see e.g. *bottom left* panels of the Fig. 3.7 and 3.8.
7. Smoothed $TOAs$ of the RPF events are stored in the file and later are used to calculate for each single event the $\alpha_{RPF}(TOA)$ introduce in Sec. 3.3.2 .

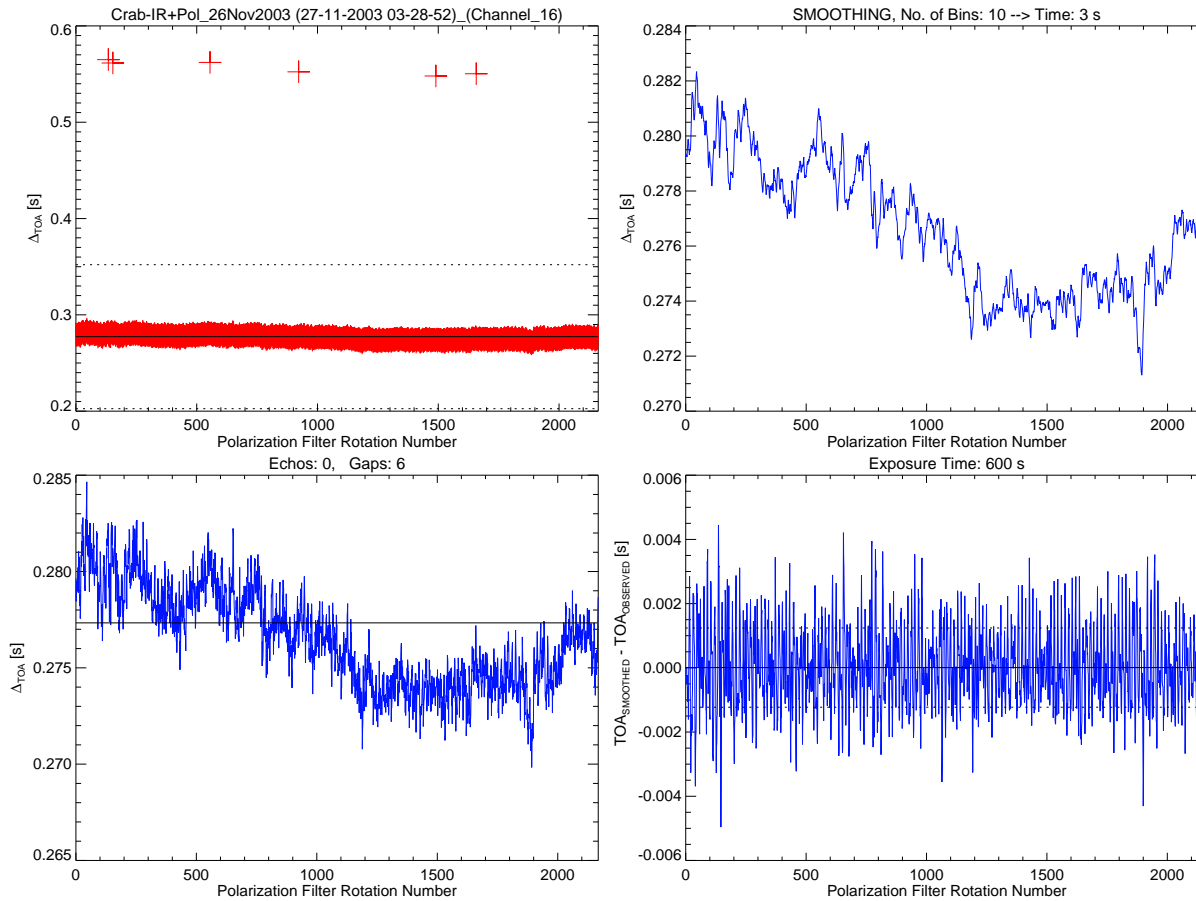


Figure 3.7: Example of the RPF behaviour during one 10 minutes observation. *Upper left:* raw data time intervals between two succeeding RPF *TOAs*. File name is given in the title. Solid line represents the average value, whereas the dashed lines show 5σ of the average value. *Bottom left:* the same as above, but after correcting for the bad events occurrence, i.e. *gaps* and *echos*, for the detailed description see Sec. 3.3.3. Numbers of bad events are given in the title. *Upper right:* time interval between two succeeding RPF *TOAs* after applying the smoothing procedure. The width of the smoothing window is given in the title. *Bottom right:* residuals between the smoothed and observed RPF *TOAs*. Dashed lines show 1σ standard deviation of the expected normal distribution. Additionally exposure time is given in the title.

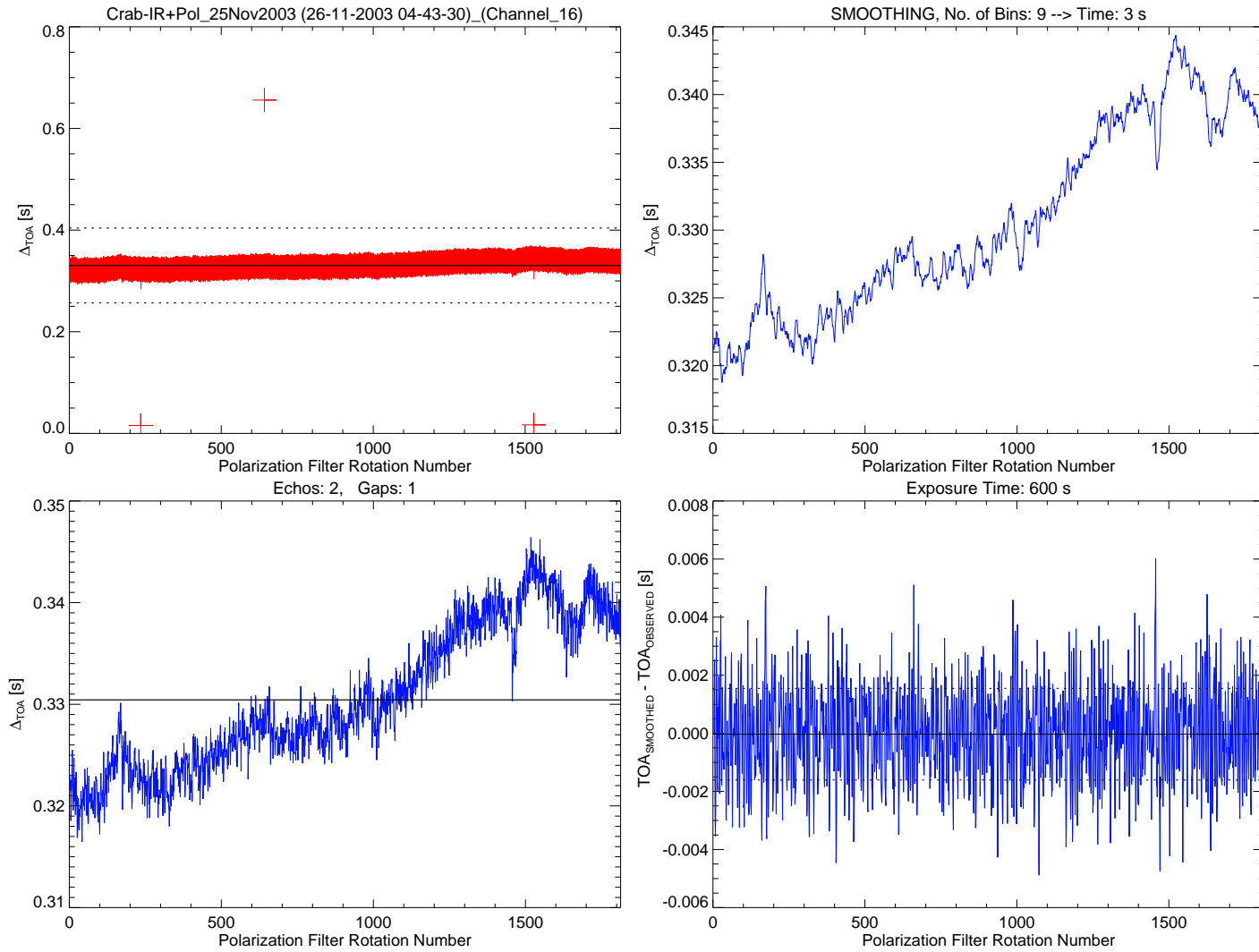


Figure 3.8: The same as for the Fig. 3.8. Some other 10 minutes observation data are shown as an example of the RPF behaviour, suffering from both of the bad timing events, i.e. *gaps* and *echos*.

It is not clear what gives rise to the long time scale variation of the RPF frequency. It might be caused e.g. by a rather unstable voltage supply of the motor, or by different position of the OPTIMA instrument with respect to the ground during the observing night, as well as by changes of the belt resistance with the outdoor temperature. We corrected incoming RPF *TOAs* for the short time scale variation, but still there is an evidence that we have some problems with the angular speed over single rotation of the filter. Quite likely, the speed of the RPF during one rotation was not perfectly constant: let's recall that the small wheel getting the momentum from the motor needs three and 1/3 rotations for one turn of the polarisation filter wheel. If there are any changes in the voltage given to the motor, then they will cause changes in the angular speed of the small wheel, and in consequence also in the rotational speed of the main wheel. Additionally, we might be observing some reflection of starlight from the non-dark parts of the RPF (see Fig. 3.3). This light comes from the stars seen by the CCD mirror. So far these effects have not been corrected. However none of these small systematic effects are synchronous to the Crab pulsar rotation. Their effect on the astronomical result is therefore limited to a possible smearing of any details. The sharpness of resolution of the Crab polarisation confirms, however, that the systematics of the RPF are of minor importance.

3. OPTICAL POLARIMETRY OF THE CRAB PULSAR

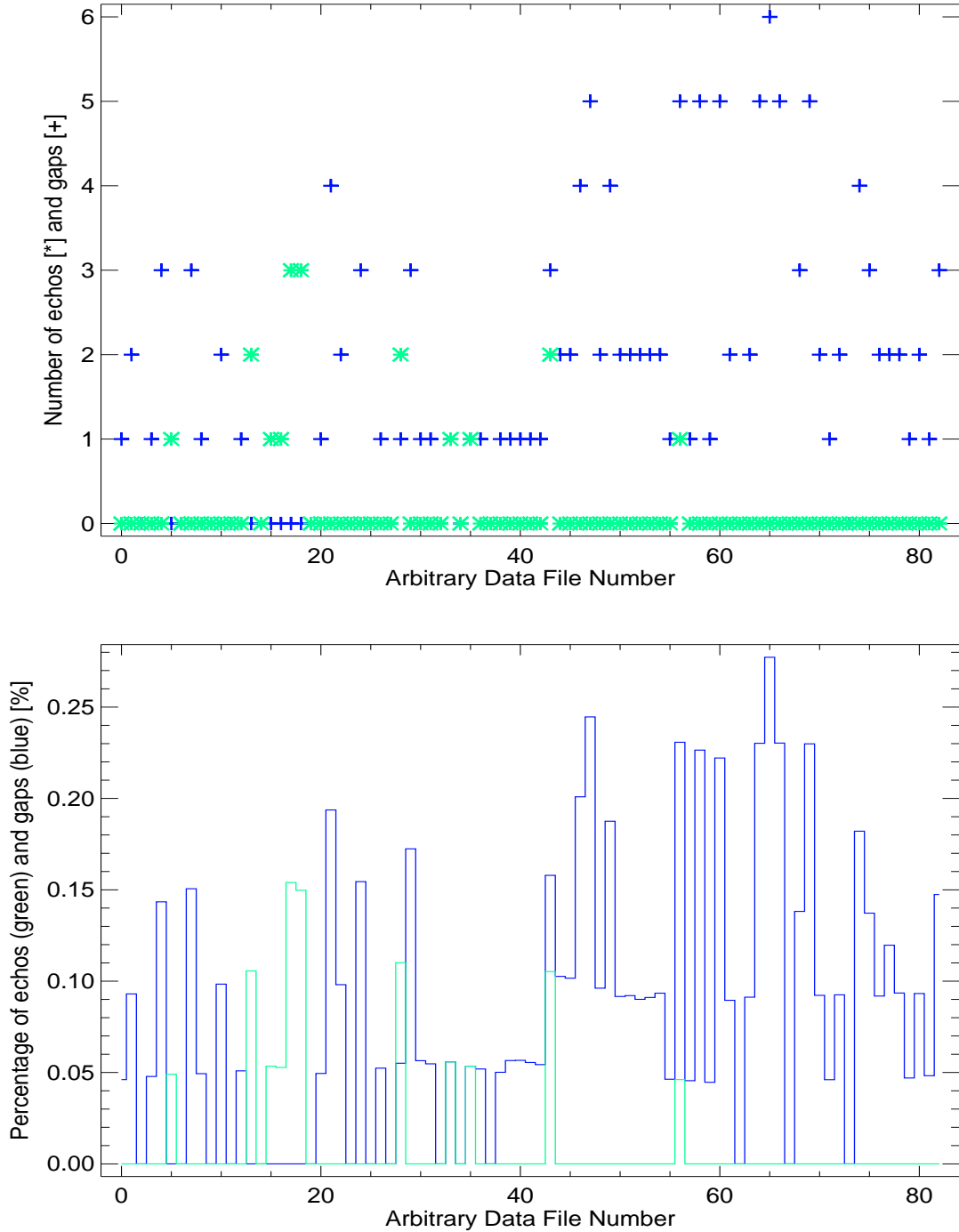


Figure 3.9: *Upper:* Number of occurrences of the *echos* and *gaps* as a function of the succeeding good files (selected file names with corresponding arbitrary file numbers are given in Tab. A.1). *Bottom:* Rate of the *echos* and *gaps* over the total number of Hall sensor signals in each file is shown. For our data set we have never had in a single file more than 0.28% of bad events over the total number of RPF *TOAs* in that file.

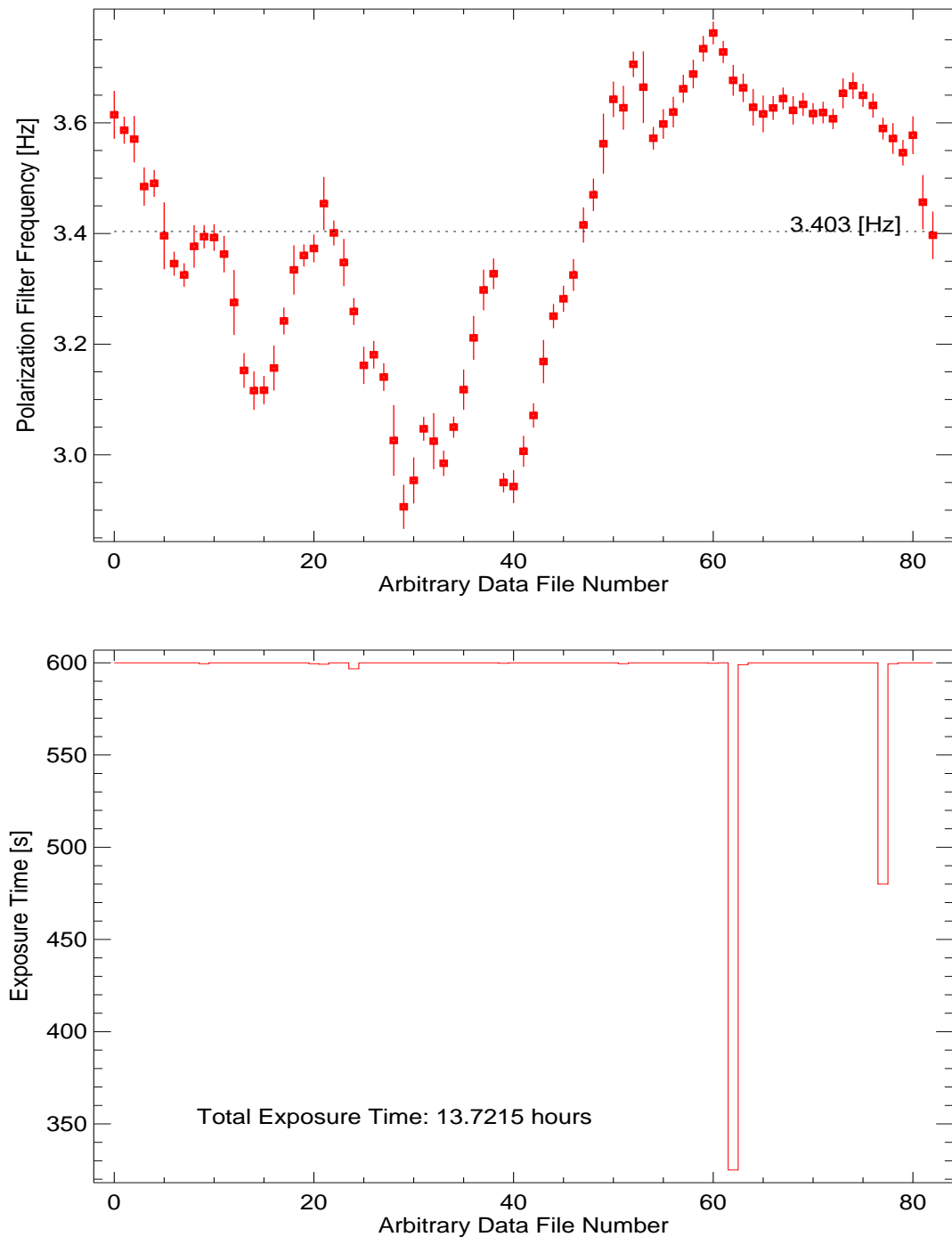


Figure 3.10: *Upper:* The average RPF frequency with its standard deviation as a function of the succeeding good files (selected files names with corresponding arbitrary file numbers are given in Tab. A.1). Averaged over the whole observational time span the RPF frequency is 3.4 Hz, whereas for single files the RPF frequency varies from 2.85 Hz up to 3.75 Hz. The standard deviations differ very much as well. They strongly depend on the long time scales variation of the RPF frequency. *Bottom:* Exposure time of the selected data files. For 81 files the exposure is about 600 seconds; only two files have exposure time shorter than 500 seconds. Total exposure time amounts to ~ 14 hours.

3. OPTICAL POLARIMETRY OF THE CRAB PULSAR

3.3.4 Polarisation data analysis

Accurate derivation of polarisation information about any highly non-thermal astronomical object (pulsars in particular) is an essential step in the investigation of its underlying physical processes. Considering astronomical objects in general, the degree of polarisation is often low, a few percent is a typical value, though both much higher and lower values do occur. A polarimetric measurement is basically that of the ratio of the small difference between two signals to their sum. Different methods have been devised to measure this small difference without systematic bias or drift errors; but detector noise or photon noise of the signal itself is always present. To minimise the contribution of the photometric noise considerable observing time on a large telescope is generally required. Use of large area detectors for imaging and spectroscopy has become commonplace, and frequently such instruments offer a polarisation capability. Processing of polarimetric data, however, is nontrivial, especially when the polarimeter is far from ideal. On the other hand we have to remember that sufficiently accurate polarimetry provides an insight that other methods can not give. Therefore, it is worth to put an effort in performing polarisation observations, analysing polarimetric data, but also in developing polarimetric instrumentation.

Hereafter, we present step-by-step polarisation data analysis by using the methodology described by [Sparks & Axon \(1999\)](#). The rotating polarisation filter inside the OPTIMA instrument provides us with polarimetric data that comprise a series of “images” of an object taken through 180 sets of linear polarisers. Let us remind that we chose one degree resolution of the RPF data, therefore we had 180 polarisers. A single polariser is not a 100% perfect polariser, but its characteristics are well established, and this is essential for the chosen data analysis method. From an input data set of 180 intensities I (measured in counts) and their errors ($\sigma_I = \sqrt{I}$), assumed independent between observations, corresponding to a set of observations through these 180 polarisers (identical but not perfect) we derive the Stokes parameters, following the case of n polarisers after [Sparks & Axon \(1999\)](#), .

Linearly polarised light

A monochromatic linearly polarised electromagnetic wave in vacuum is the simplest concept of polarised light. It has a transverse electric field vector with constant orientation, its strength at any point in space varying strictly sinusoidally with time. The duration of this wave is infinite; it has constant amplitude and frequency at all times. The wave that is 100% polarised, but its amplitude and phase is allowed to

vary slowly and often randomly, is a quasi-monochromatic wave. The faster these variations are, the broader the range of frequencies contained within the wave will be. Fully or 100% linearly polarised polychromatic radiation is a superposition of quasi-monochromatic waves of many different frequencies; there is usually no stable phase relation between the electromagnetic field at different frequencies. There is now no single dominant frequency, amplitude or phase, just a unique orientation of the otherwise often randomly oscillating electric field vector. Random in this case means random within the constraints of the mean flow of radiant energy and of the spectral bandwidth.

It is a matter of convenience to clearly define the dividing line between quasi-monochromatic and polychromatic radiation. The wider the bandwidth (the faster the modulation) the less useful is to regard the polychromatic radiation as a sine wave modulated in phase and amplitude. In this case the polychromatic description is more appropriate. When fractional bandwidth is small enough that one can neglect any frequency dependence of wave amplitude, phase, receiver gain, refractive index etc., one uses a quasi-monochromatic description, whereas when functional dependence on frequency is important, a polychromatic description is needed.

For our purpose we assume that we observe a quasi-monochromatic radiation, i.e. we do not take into account the possibility that within our bandwidth there is any frequency dependence of a sine wave modulation. Most probably it is not true, but so far we were not able to correct for this effect. It could have been done by using not only the polarisation filter, but also one out of three colour filters at that time. However, this combination would give us much lower S/N ratio. Moreover, spectral characteristics of the pulsar radiation change with its rotational phase (see e.g. integrated and phase resolved spectral power laws from photometric analysis performed by [Golden et al. \(2000a\)](#)).

Linearly polarised light requires measurement of three quantities to fully characterise it. There are various ways of expressing it. The most common one involves the total intensity of the light I , the degree of polarisation p , and the position angle θ . An “intermediate” stage between the input data and the solution of polarisation quantities are the Stokes parameters (I , Q , U) that are related through:

$$Q = Ip \cos 2\theta, \quad U = Ip \sin 2\theta, \quad (3.1)$$

or the other way around,

$$p = \frac{(Q^2 + U^2)^{1/2}}{I}, \quad \theta = \frac{1}{2} \arctan \left(\frac{U}{Q} \right). \quad (3.2)$$

3. OPTICAL POLARIMETRY OF THE CRAB PULSAR

These quantities describe all intrinsic properties of the linearly polarised radiation of the source. Here we would like to underline that they should not be confused with the properties of the polarising elements of the polarimeter, which in our case are the properties of the measured intensities in each one of the degree intervals of the RPF, i.e. in each of 180 polarisers.

Polarising element characteristics

A linearly polarising element requires three quantities to characterise its behaviour or response fully. These are:

- its efficiency as a polariser (hereafter ϵ), i.e. the ability to reject and accept polarised light of perpendicular and parallel orientations,
- its overall throughput (hereafter t), in particular to unpolarised light,
- the position angle of the polariser (hereafter ϕ).

There are a variety of conventions commonly used to present these quantities ([Mazzuca et al. 1998](#)). Here, we adopt the convention that the output intensity of a beam with input Stokes parameters (I, Q, U) passing through a polarising element is given by

$$I_k = \frac{1}{2}t_k[I + \epsilon_k(\cos 2\phi_k Q + \sin 2\phi_k U)] \quad (3.3)$$

where the subscript k anticipates that the polarising element is the k -th of a series, t is related to the throughput to unpolarised light, ϵ is the efficiency of the polariser, and ϕ is the position angle of the polariser. In this formalism three perfect polarisers at optimal orientation would have $t_k = 1$, $\epsilon_k = 1$, $(\phi_1, \phi_2, \phi_3) = (0^\circ, 60^\circ, 120^\circ)$, in the contrary to a perfectly bad polariser that would have $t_k = 0$, $\epsilon_k = 0$, and the ϕ_k values can be anything (since ϵ is zero). In the case of n polarisers of arbitrary characteristics a direct observation of the target without any polarising element in the beam may be used as part of the observing sequence. Then the formula above will allow this additional observation to form part of the derivation of polarisation quantities to maximise the obtainable S/N.

We assume that we have made a set of $n = 180$ observations of our target, each using a polarising element of well known, truly exactly the same, characteristics. Our case is the case of repeating observations with the same polariser, OPTIMA RPF. One needs at least three observations to get the solution for the three unknowns in the description of the polarisation of the incoming light. The measured intensity I_k

through the k th polariser is related to the Stokes parameters and polariser characteristics by Eq. (3.3). An uncertainty associated with the I_k measurement is assumed to follow Poisson distribution and it is denoted as σ_k , thus $\sigma_k = \sqrt{I_k}$. We adopted the Sparks & Axon approach to the n polarisers case, but firstly the solution for the case of the required minimum number of polarisers, i.e. three, is presented.

The case of three polarisers

The minimum number of polarisation observations required to determine the three unknowns represented by the Stokes parameters is obviously three. Equation (3.3) above with k in the range 1–3 gives three equations for the three unknowns, (I , Q , U)

$$\begin{aligned} I_1 &= \frac{1}{2}t_1[I + \epsilon_1(\cos 2\phi_1 Q + \sin 2\phi_1 U)], \\ I_2 &= \frac{1}{2}t_2[I + \epsilon_2(\cos 2\phi_2 Q + \sin 2\phi_2 U)], \\ I_3 &= \frac{1}{2}t_3[I + \epsilon_3(\cos 2\phi_3 Q + \sin 2\phi_3 U)]. \end{aligned}$$

This straightforward linear system may be explicitly solved to yield

$$(I, Q, U) = A \begin{pmatrix} I_1 \\ I_2 \\ I_3 \end{pmatrix} \quad (3.4)$$

or to introduce a minor simplification

$$(I, Q, U) = B \begin{pmatrix} I_1^* \\ I_2^* \\ I_3^* \end{pmatrix} \quad (3.5)$$

where $I_k^* = I_k/(0.5t_k)$ (i.e., the matrix A is the matrix B with rows divided by $0.5t_k$) and the matrix B is given by

$$B = \begin{pmatrix} \epsilon_2\epsilon_3 \sin(2\phi_3 - 2\phi_2) & \epsilon_1\epsilon_3 \sin(2\phi_1 - 2\phi_3) & \epsilon_1\epsilon_2 \sin(2\phi_2 - 2\phi_1) \\ \epsilon_2 \sin 2\phi_2 - \epsilon_3 \sin 2\phi_3 & \epsilon_3 \sin 2\phi_3 - \epsilon_1 \sin 2\phi_1 & \epsilon_1 \sin 2\phi_1 - \epsilon_2 \sin 2\phi_2 \\ \epsilon_3 \cos 2\phi_3 - \epsilon_2 \cos 2\phi_2 & \epsilon_1 \cos 2\phi_1 - \epsilon_3 \cos 2\phi_3 & \epsilon_2 \cos 2\phi_2 - \epsilon_1 \cos 2\phi_1 \end{pmatrix} / \Omega \quad (3.6)$$

where

$$\Omega = \epsilon_1\epsilon_2 \sin(2\phi_2 - 2\phi_1) + \epsilon_2\epsilon_3 \sin(2\phi_3 - 2\phi_2) + \epsilon_1\epsilon_3 \sin(2\phi_1 - 2\phi_3). \quad (3.7)$$

For our data analysis we used a similar method, but adapted for n polarisers. It is described below. Having high efficiency, $\epsilon = 0.998$, but low transmittance, $t = 0.32$,

3. OPTICAL POLARIMETRY OF THE CRAB PULSAR

our rotating polarisation filter does not have the characteristics of a perfect polariser. However, with appropriate characterisation it may still be used with excellent effect. For these purpose we use all available data, i.e. 180 polarisers; we then obtain optimal orientation.

The case of n polarisers

An analogous solution can be derived for the case of n ($n > 3$) polarisers, keeping in mind that we still have only three unknowns. This means that the equations are over determined. Sparks & Axon (1999) adopted a maximum likelihood approach, which is equivalent to a least-squares minimisation.

Let us assume that the true underlying values of the Stokes parameters of the target are (I, Q, U) . Then we would expect to observe a mean intensity through the k th polariser of I'_k as in Eq. (3.3):

$$I'_k = \frac{1}{2}t_k[I + \epsilon_k(\cos 2\phi_k Q + \sin 2\phi_k U)]. \quad (3.8)$$

Hence the likelihood of observing a particular value I_k , given an underlying mean of I'_k , is

$$\rho_k = \frac{1}{\sqrt{2\pi}\sigma_k} e^{-(I_k - I'_k)^2 / 2\sigma_k^2},$$

and hence the likelihood of observing a set of n values $\{I_k\}$ is

$$\rho = \rho_1 \rho_2 \dots \rho_n, \quad \rho = \rho_0 \exp \left[-\frac{(I_1 - I'_1)^2}{2\sigma_1^2} - \frac{(I_2 - I'_2)^2}{2\sigma_2^2} - \frac{(I_3 - I'_3)^2}{2\sigma_3^2} - \dots \right],$$

where ρ_0 is a constant.

Maximising the likelihood function ρ is equivalent to minimising the absolute value of the exponent, which is a sum of normalised deviations from the mean value. With this “least-squares” estimate, the problem reduces to minimise

$$\chi^2 = \frac{1}{2} \sum_k \frac{(I_k - I'_k)^2}{\sigma_k^2}. \quad (3.9)$$

The values of I'_k can be substituted into Eq. (3.9) from Eq. (3.8), and minimisation of χ^2 is obtained by taking partial derivatives with respect to each of I, Q, U in turn

and equating to zero. Algebraic manipulation leads to a set of three equations

$$\begin{aligned}
 \sum \frac{I_k t_k}{\sigma_k^2} &= \frac{1}{2} \sum \frac{t_k^2}{\sigma_k^2} I + \frac{1}{2} \sum \frac{t_k^2 \epsilon_k \cos 2\phi_k}{\sigma_k^2} Q + \frac{1}{2} \sum \frac{t_k^2 \epsilon_k \sin 2\phi_k}{\sigma_k^2} U, \\
 \sum \frac{I_k t_k \epsilon_k \cos 2\phi_k}{\sigma_k^2} &= \frac{1}{2} \sum \frac{t_k^2 \epsilon_k \cos 2\phi_k}{\sigma_k^2} I + \frac{1}{2} \sum \frac{t_k^2 \epsilon_k^2 \cos^2 2\phi_k}{\sigma_k^2} Q + \\
 &\quad + \frac{1}{2} \sum \frac{t_k^2 \epsilon_k^2 \sin 2\phi_k \cos 2\phi_k}{\sigma_k^2} U, \\
 \sum \frac{I_k t_k \epsilon_k \sin 2\phi_k}{\sigma_k^2} &= \frac{1}{2} \sum \frac{t_k^2 \epsilon_k \sin 2\phi_k}{\sigma_k^2} I + \frac{1}{2} \sum \frac{t_k^2 \epsilon_k^2 \sin 2\phi_k \cos 2\phi_k}{\sigma_k^2} Q + \\
 &\quad + \frac{1}{2} \sum \frac{t_k^2 \epsilon_k^2 \sin^2 2\phi_k}{\sigma_k^2} U,
 \end{aligned} \tag{3.10}$$

where \sum denotes a sum over index k of the n polariser observations. This means that again we have a set of three equations and three unknowns. It is very similar in form to the set of three equations for the three-polariser case solved above and, in fact, is identical if we define a set of ‘‘effective three-polariser characteristics’’ using these weighted sums.

That is, the three terms on the left hand side of Eqs. (3.10) can be used as (I_1, I_2, I_3) in Eq. (3.3). We label these new parameters as I''_k , to get the new three-component vector of effective measurements:

$$I''_1 = \sum \frac{I_k t_k}{\sigma_k^2}, \quad I''_2 = \sum \frac{I_k t_k \epsilon_k \cos 2\phi_k}{\sigma_k^2}, \quad I''_3 = \sum \frac{I_k t_k \epsilon_k \sin 2\phi_k}{\sigma_k^2}. \tag{3.11}$$

The error estimate for each measured intensity (=counts) is based on Gaussian statistics; therefore $I_k = \sigma_k^2$ and the corresponding factors reduce to unity. The results of calculating the effective intensity components I''_1, I''_2 and I''_3 are shown in Fig. 3.11. In our case these values are constant. I''_1 is just a sum over the same 180 polarisers with the same throughput to unpolarised light, i.e. $t = 0.32$. Therefore we get: $I''_1 = 180 \times 0.32 = 57.6$. Whereas, $I''_2 = 180t\epsilon \sum \cos 2\phi_k$ and $I''_3 = 180t\epsilon \sum \sin 2\phi_k$, where \sum denotes a sum over index k of the 180 polarisers. Knowing that $\epsilon = 0.998$ and the integrals of $\cos 2\phi_k$ and $\sin 2\phi_k$ over the range from 0 to 180 we expect $I''_2 \sim I''_1 \sum \cos 2\phi_k$ and $I''_3 \sim I''_1 \sum \sin 2\phi_k$, within available numerical precision, to be very close to zero.

Similarly, we can define a three-component vector of effective transmittances:

$$t''_1 = \sum \frac{t_k^2}{\sigma_k^2}, \quad t''_2 = \sum \frac{t_k^2 \epsilon_k \cos 2\phi_k}{\sigma_k^2}, \quad t''_3 = \sum \frac{t_k^2 \epsilon_k \sin 2\phi_k}{\sigma_k^2}. \tag{3.12}$$

In Fig. 3.12 three components of the vector of effective transmittance, t''_1, t''_2 and t''_3 (Eqs. (3.12)), as a function of the pulsar rotation are presented.

3. OPTICAL POLARIMETRY OF THE CRAB PULSAR

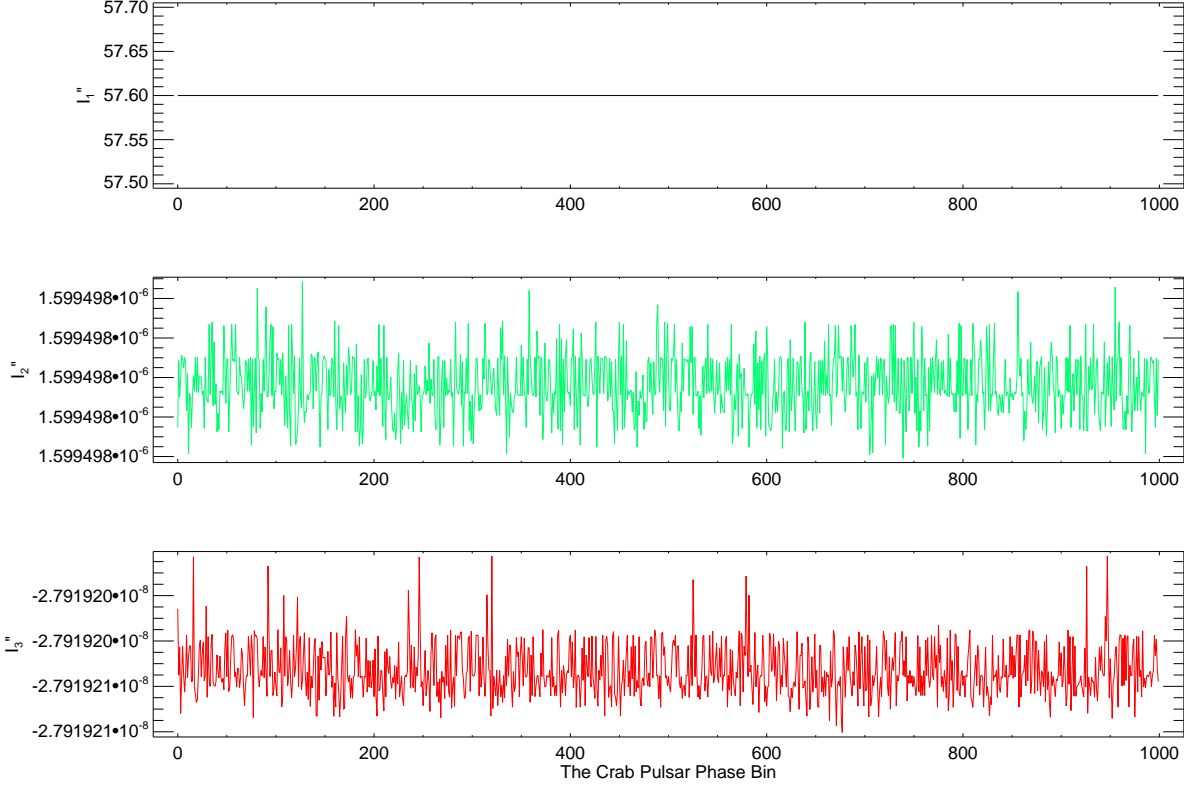


Figure 3.11: Effective intensity I''_1 , I''_2 and I''_3 derived from 180 polarisers as a function of the Crab pulsar rotation phase (1 cycle = 1000 bins).

The vector of effective efficiencies is as follows:

$$\begin{aligned}
 \epsilon''_1 &= \frac{1}{\sum t_k^2 / \sigma_k^2} \sqrt{\left(\sum \frac{t_k^2}{\sigma_k^2} \epsilon_k \cos 2\phi_k \right)^2 + \left(\sum \frac{t_k^2}{\sigma_k^2} \epsilon_k \sin 2\phi_k \right)^2}, \\
 \epsilon''_2 &= \frac{1}{\sum t_k^2 \epsilon_k \cos 2\phi_k / \sigma_k^2} \sqrt{\left(\sum \frac{t_k^2}{\sigma_k^2} \epsilon_k^2 \cos^2 2\phi_k \right)^2 + \left(\sum \frac{t_k^2}{\sigma_k^2} \epsilon_k^2 \sin 2\phi_k \cos 2\phi_k \right)^2}, \\
 \epsilon''_3 &= \frac{1}{\sum t_k^2 \epsilon_k \sin 2\phi_k / \sigma_k^2} \sqrt{\left(\sum \frac{t_k^2}{\sigma_k^2} \epsilon_k^2 \sin 2\phi_k \cos 2\phi_k \right)^2 + \left(\sum \frac{t_k^2}{\sigma_k^2} \epsilon_k^2 \sin^2 2\phi_k \right)^2}.
 \end{aligned} \tag{3.13}$$

In Fig. 3.13 the components of the effective efficiency vector, i.e. ϵ''_1 , ϵ''_2 and ϵ''_3 (Eqs. (3.13)), as a function of the pulsar rotation are shown.

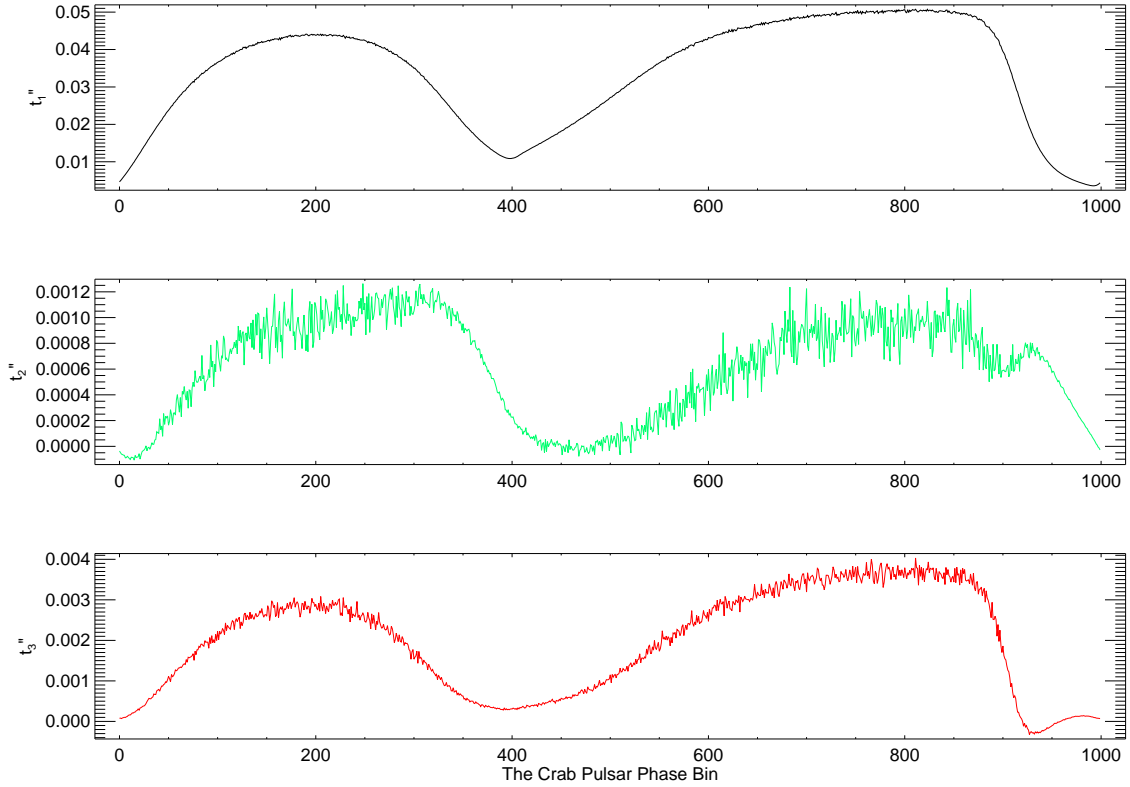


Figure 3.12: Effective transmittance t''_1 , t''_2 and t''_3 derived from 180 polarisers as a function of the Crab pulsar rotation phase (1 cycle = 1000 bins).

Finally a vector of effective “position angles” is defined as:

$$\begin{aligned}
 \phi''_1 &= \frac{1}{2} \arctan \left(\frac{\sum \frac{t_k^2}{\sigma_k^2} \epsilon_k \sin 2\phi_k}{\sum \frac{t_k^2}{\sigma_k^2} \epsilon_k \cos 2\phi_k} \right), \\
 \phi''_2 &= \frac{1}{2} \arctan \left(\frac{\sum \frac{t_k^2}{\sigma_k^2} \epsilon_k^2 \sin 2\phi_k \cos 2\phi_k}{\sum \frac{t_k^2}{\sigma_k^2} \epsilon_k^2 \cos^2 2\phi_k} \right), \\
 \phi''_3 &= \frac{1}{2} \arctan \left(\frac{\sum \frac{t_k^2}{\sigma_k^2} \epsilon_k^2 \sin^2 2\phi_k}{\sum \frac{t_k^2}{\sigma_k^2} \epsilon_k^2 \sin 2\phi_k \cos 2\phi_k} \right).
 \end{aligned} \tag{3.14}$$

The results of calculating the effective position angle components ϕ''_1 , ϕ''_2 and ϕ''_3 (Eqs. (3.14)) are shown in the Fig. 3.14.

By making these substitutions, the solution given by Eq. (3.5) and Eq. (3.6) can be used immediately. In this way we obtained the Stokes parameters (Fig. 3.15).

That is, a set of observations with n polarisers *can be made equivalent to a set of observations through three polarisers.*

In the actual case of $n = 3$, it can also be shown that the maximum likelihood

3. OPTICAL POLARIMETRY OF THE CRAB PULSAR

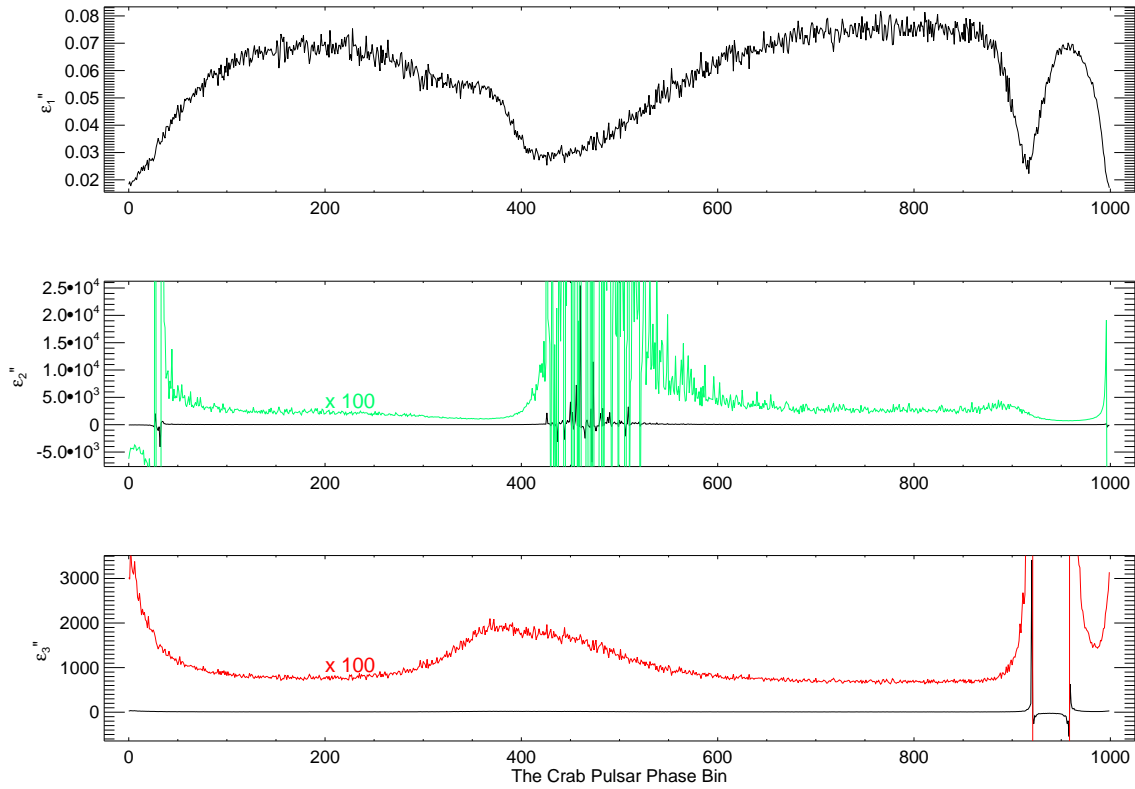


Figure 3.13: Effective efficiency ϵ_1'' , ϵ_2'' and ϵ_3'' derived from 180 polarisers as a function of the Crab pulsar rotation phase (1 cycle = 1000 bins).

or least-squares solution is identical to the direct matrix inversion used for the three-polariser case.

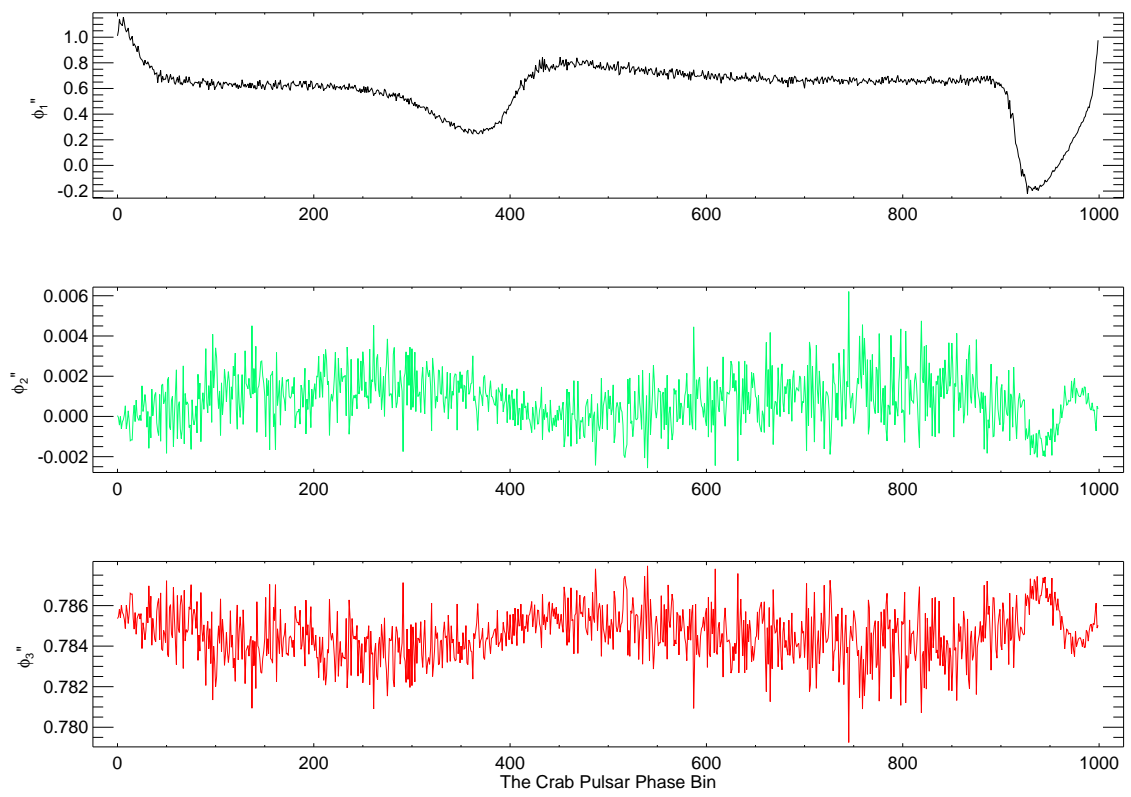


Figure 3.14: Effective position angle ϕ_1'' , ϕ_2'' and ϕ_3'' derived from 180 polarisers as a function of the Crab pulsar rotation phase (1 cycle = 1000 bins).

3. OPTICAL POLARIMETRY OF THE CRAB PULSAR

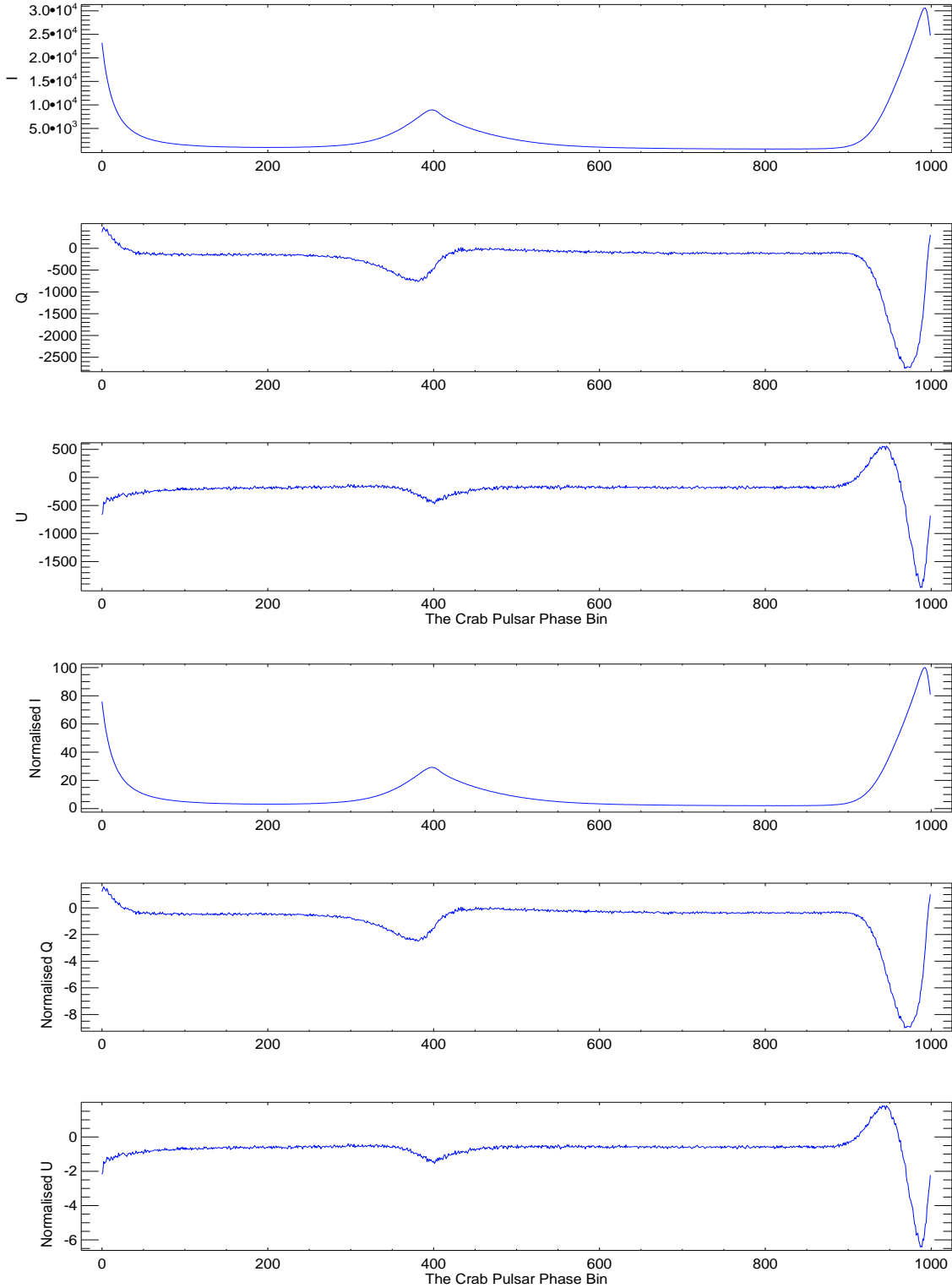


Figure 3.15: Raw (*upper three panels*) and normalised (*bottom three panels*) Stokes parameters I , Q , U derived from 180 polarisers as a function of the Crab pulsar rotation phase (1 cycle = 1000 bins). Normalisation was such that $I = 100$ at the maximum, and Q and U are normalised to I . These values corresponds to the values shown on the QU plane in the Fig. 3.19.

3.3.5 The HST polarisation standards

In order to understand the intrinsic polarisation and the response of the instrument to known polarised stars we have performed observations of such reference stars (Tab. 3.4). Since OPTIMA is very sensitive and limited in its capacity for data acquisition at a high rate (count rate above 37 kHz, Mühlegger (2006)) we selected three of the weakest stars from the list of Turnshek et al. (1990): two polarisation standards, and one photometric standard (see Tab. 3.4). The first one of two polarisation standard stars is highly polarised, on the level of 6%, whereas the second star has a very low polarisation degree of $\sim 1\%$. Unfortunately for our measurements both stars are quite bright for the OPTIMA instrument. Therefore, we also performed optical polarisation measurements of a dimmer star, i.e. a photometric standard from Turnshek et al. (1990) list, expecting its light not to be polarised.

Table 3.4: HST polarisation and photometric standards (Turnshek et al. 1990)

Name	FK5 2000.0 Coordinates	Spectral Type	Comments
HST Polarisation Standards			
BD+64 106	00 ^h 57 ^m 36 ^s .70 +64° 51' 34".9	B1V	V = 10.34 P: 5.65 ± 0.053% θ : 96.8°
G191B2B	05 ^h 05 ^m 30 ^s .61 +52° 49' 51".9	WD	V = 11.79 P: 0.09 ± 0.048%
HST Photometric Standards			
GD50	03 ^h 48 ^m 50 ^s .20 −00° 58' 31".2	WD	V = 14.06

We have performed observations of the HST polarisation standard BD+64 106 two times during our observational campaign for 4.5 and 6.17 minutes on November 25th and 27th, respectively (see Tab. 3.5, *left* side). In both cases the observing conditions were very different, thus the results differ as well. Hereafter, we would like to discuss them in details. In between 22:06:45 and 22:12:56 of Nov 25th the average seeing was on the level of 1".27 (RoboDIMM measurements, see Fig. 3.5, *upper* panel), whereas for the time span between 21:33 and 21:40 of Nov 27th no information about the seeing conditions were provided by the RoboDIMM telescope. At the beginning of the night the weather was very good. But later, during less than two hours, between 20:00 and 22:00, the humidity changed from 20 to almost 60%, and the wind speed increased up to 15 m/s. Therefore the seeing was probably larger than during the first observations, likely more than 2".0. This dissimilarity in the seeing values causes different count rates in the central and ring fibres. During the Nov 25th count rate

3. OPTICAL POLARIMETRY OF THE CRAB PULSAR

in channel 0 was on the level of 1.9×10^5 Hz, and in the ring fibres $\lesssim 2.0 \times 10^4$ Hz, while during Nov 27th we had 1.5×10^5 Hz and $\lesssim 5.0 \times 10^4$ Hz for channel 0 and ring fibres, respectively. Summarising, it is important to notice that for all observations the central channel was saturated, i.e. the count rates were well above the saturation threshold, i.e. 37 kHz. For the second set of data (Nov 27th) it might have happened that some of the ring fibres were also saturated. The most saturated channels were 1 and 6. The values of the polarisation degree and the position angle for all channels and for all sets of observations are gathered in the *right* side of the Tab. 3.5. It is important to notice that, even if the central fibre was suffering pile-up, the calculated position angle for each single observation of BD+64 104 is pretty constant. This is caused by the fact that the position angle, being nothing else than the phase of the maximum of the modulated incoming light, is not (under the condition that any modulation is observed) so strongly dependent on the pile-up effect. Saturation is important in the case of calculating the polarisation degree, which is the amplitude of the measured light modulation. If the channel is saturated then the values of the polarisation degree are not reliable. We can observe this by comparing results in Tab. 3.5. For the central fibre there is significant difference in the polarisation degree for the first and second sets of data. When seeing was higher the light from the observed very bright star was more smoothly distributed among all channels, therefore an increase of p in the central fibre is observed. Seeing conditions, being an equivalent to the count rates, did not affect significantly the measured values of p in the ring fibres. Only in the case of channel 1 the polarisation degree is much smaller during the Nov 27 observations than Nov 25. This is strongly connected with the fact that, during the second observation, this channel, among all of the ring channels, was the most saturated one.

Taking into account the resulting θ and p (Tab. 3.7) of the HST polarisation standard BD+64 104 (being a very bright star for the OPTIMA instrument) we can conclude that for the purpose of calibrating the north direction of our instrument it is safe and valid to use values of the polarisation angle from the central fibre (Tab. 3.5, marked with the grey background). The averaged value of $\theta_{\text{BD+64104}}$ amounts to 96.74 ± 0.37 (see Tab. 3.7). From these calibration observations we learned that we had to shift the RPF angles by 92° . The angles θ given here and hereafter in text and in tables are the E -vector position angles relative to celestial north (N to E). The amplitude of sinusoidally modulated intensity of the incoming light is not correct in the case of saturation. Thus, probably the best estimate of the polarisation degree of BD+64 104 comes from the sum of the light detected in the ring fibres. The obtained

value, $4.72 \pm 0.30\%$, is somehow smaller than the value measured by the HST table ($5.65 \pm 0.053\%$), but one has to remember that our value is obtained from the ring fibres measuring "background" around the star. Because the star is very bright, and seeing was more than $1''0$, the light of the star was scattered into the ring fibres. In this case bad seeing (high value) is an advantage, because it naturally defocuses our target.

We also performed observations of the unpolarised HST standard, i.e. G191B2B (Tab. 3.4). Data for this target were taken on Nov 26 21:30 for about 10 minutes with seeing being on the level of $1''0$. We found a very small polarisation degree for this star, as expected, and thus the position angle has little meaning. During observations the count rate was on the level of 1.5×10^5 Hz and $< 4 \times 10^4$ Hz in the central and ring fibres, respectively. Even though the channel 0 was saturated our result, $0.05 \pm 0.02\%$ (Tab. 3.7), is in a good agreement with the value $0.09 \pm 0.048\%$ obtained by [Turnshek et al. \(1990\)](#). The averaged value from the background fibres is higher. It amounts to $0.33 \pm 0.02\%$, and is probably partly caused by the polarised sky background.

For the purpose of the instrument calibration we also chose from the [Turnshek et al. \(1990\)](#) atlas of *Hubble Space Telescope* photometric, spectroscopic, and polarimetric calibration objects a star with brightness that should assure count rates lower than the pile-up threshold. GD50 (Tab. 3.4) is a photometric standard, thus we expect its light not to be polarised. Observations of this target were performed on November the 27th at 21:52 with recorded count rate in the central channel of $(1.0 - 1.5) \times 10^4$ Hz and in the ring channels < 1000 Hz. Results of p_{GD50} are shown in the Tab. 3.6, file A. The source had polarisation degree below 1% (measured in the central fibre), whereas the measured p within the ring fibres was much greater. These values correspond to the sky background polarisation. However, the sky background could have been more highly polarised. The contribution of the night sky to the observed count rates was on the level of one quarter in each fibre only, i.e. the background ring fibres were contaminated by the source. Thus, the signal measured in the ring fibres was most probably depolarised and could have higher polarisation degree in reality.

Table 3.5: Measurements of the HST polarisation standard BD+64 104 (the files from 1 to 5). Table consists of two parts: the *left* side part gives information about the arbitrary file number, date and time of observation and length of exposure, whereas the *right* side part gives p (above) and θ (below) as a function of single observation and channel. Additionally, last row (assigned as “1 \div 6”) shows p and θ values obtained as a function of different data sets after averaging the Stokes parameters from all ring channels. Columns titled “1 \div 2” “3 \div 5” and “1 \div 5” give the p and θ values for single channel, as well as for sum of the ring fibres (last row), obtained after summing all existing data of the target from Nov 25th, Nov 27th and both days together, respectively.

File	Date and Time of Observations	Exposure [s]	File	Channel	1	2	3	4	5	1 \div 2	3 \div 5	1 \div 5
1	25 Nov 2003 22:07:01	140	0	p	1.30	1.35	1.98	1.86	1.67	1.33	1.83	1.59
				θ	96.6	96.8	96.2	96.9	97.2	96.7	96.8	96.7
2	25 Nov 2003 22:09:46	130	1	p	4.57	4.64	3.71	3.60	4.21	4.60	3.81	3.87
3	27 Nov 2003 21:33:35	110		θ	100.3	96.6	98.0	96.5	98.3	98.4	98.0	98.0
4	27 Nov 2003 21:36:08	120	2	p	5.16	5.17	4.59	4.84	5.57	5.16	4.99	5.04
				θ	96.0	94.7	98.0	96.8	96.8	95.3	97.2	96.6
5	27 Nov 2003 21:38:34	120	3	p	5.38	5.16	5.49	5.08	5.04	5.25	5.20	5.22
				θ	94.3	92.9	95.5	95.9	97.4	93.5	96.2	94.6
			4	p	4.67	4.34	4.14	4.98	4.27	4.49	4.46	4.48
				θ	99.1	98.6	98.5	100.5	103.5	98.8	100.7	99.5
			5	p	5.51	5.26	5.53	5.58	5.38	5.38	5.50	5.46
				θ	96.7	94.3	97.9	96.2	97.1	95.5	97.0	96.5
			6	p	4.62	5.00	5.06	4.52	4.80	4.81	4.80	4.79
				θ	98.6	98.7	93.6	93.6	91.7	98.6	93.0	93.7
1 \div 6			1 \div 6	p	5.06	4.95	4.47	4.37	4.73	5.00	4.51	4.63
				θ	96.7	95.1	96.8	95.8	96.4	95.8	96.3	96.2

Table 3.6: Measurements of the HST polarisation standard G191B2B (files from 1 to 4) and the HST photometric standard GD50 (file A). Table consists of two parts: the *left* side part gives information about the arbitrary file number, date and time of observation and length of exposure, whereas the *right* side part gives p as a function of single observation and channel. Moreover, last row (assigned as “1 \div 6”) shows p value obtained as a function of different data sets after averaging the Stokes parameters from all ring channels. Column titled “1 \div 4” gives the p value for single channel, as well as for sum of the ring fibres (last row), obtained after summing all existing data of G191B2B from Nov 26th. For GD50 we had only one 10 minutes observation.

File	Date and Time of Observation	Exposure [s]	File.	1	2	3	4	1 \div 4	A
1	26 Nov 2003 21:33:08	160	0	p 0.04	0.07	0.03	0.06	0.03	0.08
2	26 Nov 2003 21:36:22	150	1	p 0.37	0.48	0.47	0.21	0.31	0.30
3	26 Nov 2003 21:41:01	130	2	p 0.75	0.41	0.65	0.85	0.62	0.44
4	26 Nov 2003 21:43:53	130	3	p 0.84	0.46	0.80	0.72	0.63	0.61
A	27 Nov 2003 21:52:17	590	4	p 0.30	0.66	0.69	0.47	0.43	0.62
			5	p 0.16	0.56	0.36	0.16	0.20	0.23
			6	p 0.14	0.21	0.04	0.42	0.18	0.53
			1 \div 6	p 0.35	0.34	0.30	0.32	0.27	0.22

3. OPTICAL POLARIMETRY OF THE CRAB PULSAR

Table 3.7: Results of the OPTIMA at NOT measurements of the HST polarisation standards (for details see Tab. 3.4). Presented values are the average and standard deviation calculated on the basis of the single measurements shown in the Tab. 3.5 and 3.6, considering all single channels, as well as the sum of six ring fibres.

HST Pol. Stand.	BD+64 104	G191B2B
Channel	p [%]	θ [°]
0	1.63 ± 0.30	96.74 ± 0.37
1	4.15 ± 0.48	98.14 ± 1.62
2	5.07 ± 0.37	96.46 ± 1.22
3	5.23 ± 0.20	95.20 ± 1.70
4	4.48 ± 0.34	100.04 ± 2.09
5	5.45 ± 0.13	96.44 ± 1.35
6	4.80 ± 0.23	95.24 ± 3.21
1÷6	4.72 ± 0.30	96.16 ± 0.71

3.4 Results

3.4.1 Nebular contribution

The Crab Nebula is one of the most intensively studied objects in the sky. The cause and the heart of the nebula is the Crab pulsar, the first pulsar with optically detected pulses (Cocke, Disney, & Taylor 1969) and an extensively studied source throughout the whole electromagnetic spectrum from radio to γ -rays. Closer to the outer boundary of the nebula are the filaments - the chemically enriched material ejected during the supernova explosion observed by Chinese astronomers in 1054. The Crab synchrotron nebula is a relativistic magnetised plasma that is powered by the spin-down energy of the pulsar. It was the first recognised astronomical source of synchrotron radiation. The synchrotron nature of the radiation was confirmed by the optical polarisation observations (Woltjer 1957). The conversion efficiency of the nebula is quite high, with 10–20% of the spin-down energy released by the pulsar appearing as synchrotron radiation. The inner synchrotron nebula is a region consisting of jets, a torus of X-ray emission, small-scale variations in polarisation and spectral index, and complexes of sharp wisps. Most theoretical models generally associate the sharp wisps seen at the visible and radio wavelengths with the location of the shock wave between the pulsar and the synchrotron nebula.

For a long time the imaging investigations of the Crab Nebula were limited in a fundamental way by the spatial resolution of the data, not being able to reveal a wealth of subarcseconds structures. A breakthrough in the optical studies of the structure of the Crab Nebula was undertaken by using the Wide Field and Planetary

Camera 2 (WFPC2) on board of the *Hubble Space Telescope*. [Hester et al. \(1995\)](#) performed this observation with a $0''.1$ resolution. Below we shortly describe the most important HST results that are important in the context of this thesis.

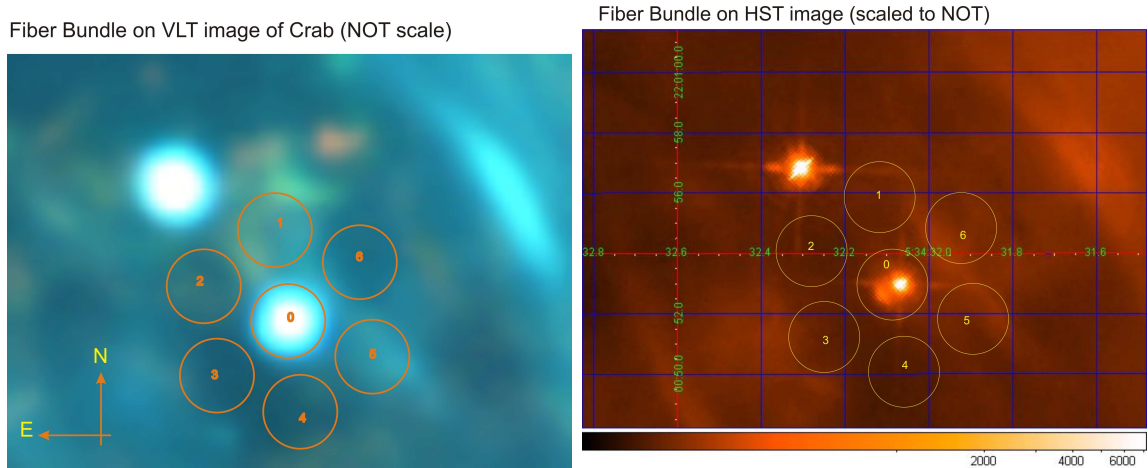


Figure 3.16: An enlargement of the VLT and HST image of the Crab Nebula, *left* and *right* panel, respectively. The pulsar is identified with the lower/right of the two stars near the geometric centre of the nebula, immediately left of the small arc-like feature. The VLT photo is based on a composite of three images taken through three different optical filters: B (429 nm; here rendered as blue), R (657 nm; green) and S II (673 nm; red) during periods of 0.65 arcsec (R, S II) and 0.80 (B) seeing, respectively. The second image is an enlargement of the co-added HST WFPC2 images of 12 observations of the Crab Nebula between 2000 and 2001 with the F547M filter. Only in the HST image the inner knot is resolved, it is located $0''.65$ to the SE of the pulsar. North is up; East is left. In both cases the OPTIMA fibre bundle (Fig. 3.2), centred on the pulsar and scaled with the NOT focal plane scale, is over plotted.

[Hester et al. \(1995\)](#) discovered a bright knot of visible emission located $0''.65$ to the southeast of the pulsar, along the axis of the system. This inner knot, along with a second similarly sharp but fainter knot (hereafter outer knot) located at a distance of $3''.8$ from the pulsar, lies at an approximate position angle of $\sim 115^\circ$ east to north. Both knots are aligned with the X-ray and optical jet to the southeast of the pulsar and are elongated in the dimension roughly perpendicular to the jet direction, with lengths of $\sim 0''.5$. Both, the inner and outer knot appear to be present but not well resolved in the images of the Crab Nebula previously taken by ground based telescopes. Comparison of these two classes of images can be seen in the Fig. 3.16. We show an enlargement of a smaller area in the centre of the VLT and HST images. The pulsar is identified with the lower/right of the two stars near the geometric centre of the nebula, immediately left of the small arc-like feature. Additionally the

3. OPTICAL POLARIMETRY OF THE CRAB PULSAR

OPTIMA fibre bundle centred on the pulsar and scaled with the NOT focal plane scale (Tab. 3.1) is over plotted. The VLT image is a three colour (filters: 429, 657, 673 nm here rendered as blue, green, red, respectively; seeing was $0''.80$ for the first filter, and $0''.65$ for the other two) composite of the Crab Nebula as observed with the FORS2 instrument in imaging mode in the morning of November 10, 1999. On the other hand the HST image is an enlargement of the co-added HST WFPC2 images of 12 observations of the Crab Nebula in between 2000 and 2001 with the F547M filter (see Fig. 1 in [Ng & Romani \(2006\)](#), observations group index 6). This figure was kindly supplied by Roger Romani (private communication). For our data analysis the most important conclusion coming from overlaying the OPTIMA fibre bundle on both VLT and HST images is the fact that within the central fibre we are not able to resolve the Crab pulsar from the inner knot. Moreover, it is clear that with the seeing being bigger than $1''.0$ the target light is somewhat spread into the ring channels. Evidence of this effect can be seen in the Fig. 3.17 where the intensities measured by respective ring fibres are folded with the pulsar phase. Obviously the pulse emission is detected. The integrated contribution of the pulsar light incoming to the ring fibres is 19.5, 30.9, 33.8, 16.7, 14.1, 13.0 percent for the channels from 1 to 6, respectively. We corrected this effect by adding the pulsed counts to the counts recorded by the central fibre. Additionally, there may be contributions of photons coming from the outer knot (not very clearly seen on the images, but an indication of it can be seen on the southeast side in between the fibres 3 and 4). It is also noteworthy to mention that the ring fibres see different nebulosity patches.

To obtain the polarisation characteristics of the pulsar neighbourhood we assumed that within the DC phase range the contribution of the pulsar emission to the ring fibres was minimal. Therefore, during our calculations for the channels from 1 to 6 we consider only the light coming within the ‘off-pulse’ phase range, i.e. 7% phase range of the whole rotational cycle of the Crab pulsar. It is indicated with a dashed region in Fig. 3.17. The calculated polarisation degree and position for each of the single OPTIMA detectors are presented in the Tab. 3.8. By averaging the Stokes parameters over all background channels we obtained $p = 9.6\%$ and $\theta = 140^\circ$ for the region surrounding the pulsar. For the single seven apertures we compared our results with previous ones by over plotting them on the polarisation sky map of the very close neighbourhood presented by [Smith et al. \(1988\)](#). Close to the pulsar the nebular polarisation is quite uniform (at $\sim 9 - 11\%$) but the position angles change steadily with radial distance. 2-3 arc seconds from the pulsar the mean value is

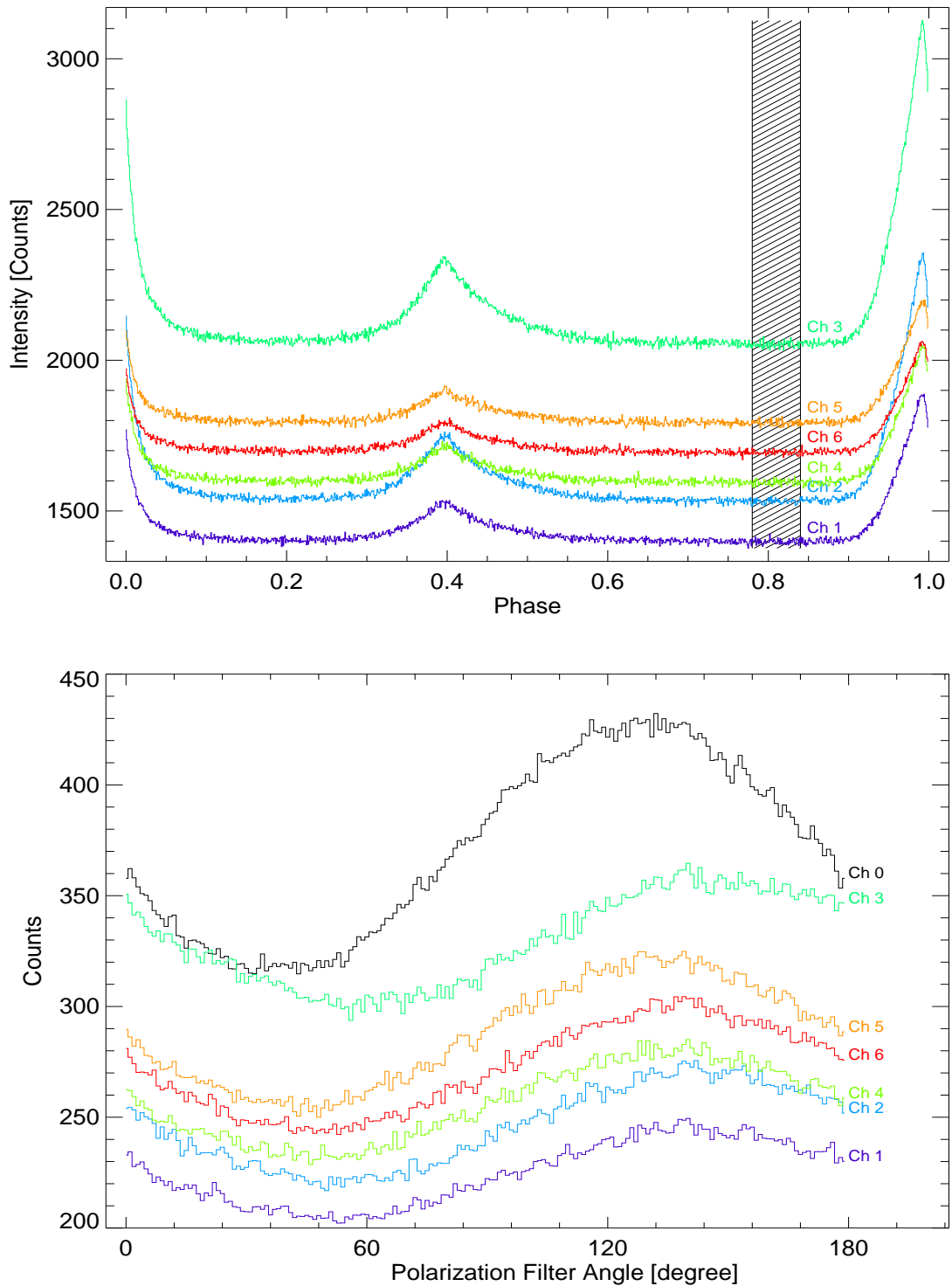
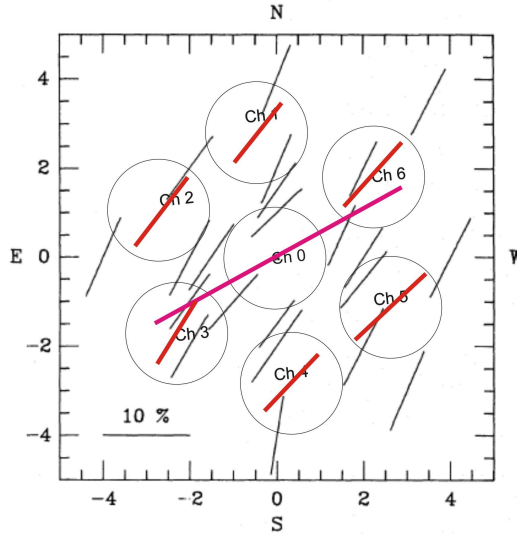


Figure 3.17: *Upper*: Light curves obtained from photons recorded by the ring fibres APDs. All events were folded with the rotational parameters of the Crab pulsar. Dashed region between 0.78–0.84 phases indicates phase range of data that were later taken to calculate θ and p for the ring fibres. *Bottom*: The sinusoidal modulation of the incoming polarised light, summed over the pulsar phase. Its amplitude varies for different channels, because each channel is observing a bit different sky region.

3. OPTICAL POLARIMETRY OF THE CRAB PULSAR

Table 3.8: *Left:* p and θ results of the OPTIMA at NOT measurements of the Crab Nebula measured at the DC phase range of the Crab pulsar light curve (0.78–0.84, for details see upper panels of Fig. 3.17 and 3.18). *Right:* polarisation of the Crab Nebula as measured at minimum phase of the pulsar light curve. The axes are calibrated in arcseconds centred on the pulsar, source [Smith et al. \(1988\)](#). Scaled OPTIMA fibre bundle is over plotted. The aperture of a single fibre is $2''.35$. Pink line for central fibre and red lines for ring fibres represent our measurements.

Channel	p [%]	θ [°]
0	33.20	118.9
1	8.95	141.6
2	10.22	142.6
3	8.69	148.3
4	9.21	136.5
5	11.42	133.1
6	10.18	138.0
1÷6	9.62	139.8



around 140° but beyond 5 arc seconds the position angle exceed 155° and it is very direction-dependent ([McLean et al. 1983](#)).

3.4.2 Time alignment between optical and radio wavelengths

Precise timing of pulsar light curves throughout the electromagnetic spectrum can be used to constrain theories of the spatial distribution of various emission regions and their specific propagation delays. In the radio regime this concept has been applied in the so called *frequency mapping* analysis. By dint of recent observations at different energies, it became clear that the Crab pulsar emission maxima of IP and MP are not aligned in phase at different wavelengths of the electromagnetic spectrum, from radio to γ energy range. Comparing the visible and UV light curves obtained from HST, [Percival et al. \(1993\)](#) were among the first to show that the phase separation between the two peaks, ipso facto the phases of the pulse maxima, change with energy. Since then many authors have measured this effect in an attempt to understand its relation to and impact on the emission mechanism. However, the techniques used by different authors to measure the phase separation (i.e. the phases of the peak maxima) have varied. Therefore, this might cause method-dependent biases. [Eikenberry & Fazio](#)

(1997) showed that the peak-to-peak separation appears to be a more or less smooth function of energy from infrared to γ -ray energies. The separation decreases with energy over the range from 0.5 to 10^6 eV from 0.4087 ± 0.0003 to 0.398 ± 0.003 , respectively. There is some evidence of a turnover or a break in this trend at energies of 0.7 eV (H band pass filter). No default method exists for determining the position of the peak of the profile. For our purpose and using our high statistics light curve it was enough to determine the peak phases just by looking for the maximum intensity. This gave us the phase values for the MP: 0.993 ± 0.001 and the IP: 0.398 ± 0.001 (Tab. 3.9). Our peak-to-peak separation is on the level of 0.4050 ± 0.0014 . It is in very good agreement with the values obtained by Eikenberry & Fazio (1997) for the visual pass band, i.e. 0.4057 ± 0.0003 , and from a previous OPTIMA observation Straubmeier (2001) of 0.4060 ± 0.0003 .

Optical, X-ray and γ -ray maxima of the MP are leading the radio pulse. At the X- and γ -rays energies the picture is very much consistent, whereas at the optical wavelength results obtained by different authors varies significantly. The reported values of the time lags between TOA of optical and radio maxima are as follow: $344 \pm 40 \mu\text{s}$ (Rots et al. 2004, RXTE data), $280 \pm 40 \mu\text{s}$ (Kuiper et al. 2003, INTEGRAL data), and $241 \pm 29 \mu\text{s}$ (Kuiper et al. 2003, EGRET data). The uncertainty of the latter value does not include the EGRET absolute timing uncertainty of better than $100 \mu\text{s}$. At optical wavelengths the situation is quite different and does not provide such a coherent picture. Several authors reported the optical peak leading the radio peak by a time shift of $140 \pm 78 \mu\text{s}$ (Sanwal 1999), $100 \pm 20 \mu\text{s}$ (Shearer et al. 2003), and $273 \pm 100 \mu\text{s}$ lately found by Oosterbroek et al. (2006). On the other hand Golden et al. (2000b) reported that the optical pulse trails the radio pulse by about $80 \pm 60 \mu\text{s}$. Additionally, Romani et al. (2001) concluded that both, radio and optical, peaks are coincident to better than $30 \mu\text{s}$, but they did not take into account the uncertainty of the radio ephemeris being on the level of $150 \mu\text{s}$ in their error calculations. From our measurements we conclude that the optical is leading the radio by a time shift of $231 \pm 68 \mu\text{s}$. The uncertainty in this value is $33 \mu\text{s}$ in the determination of the optical peak of the MP and $60 \mu\text{s}$ in the radio ephemeris.

Our value of the optical phase difference between the MP and the IP of 0.4050 ± 0.0014 is consistent with the latest optical measurements carried out by Oosterbroek et al. (2006), who obtained 0.4054 ± 0.0004 . Both values, as it has already been shown by Eikenberry & Fazio (1997), are not consistent with the X-ray results, e.g. obtained from RXTE data by Rots et al. (2004) of 0.4001 ± 0.0002 . This implies that the details of the pulse profile in X-rays and in optical domain are different. In a simple

3. OPTICAL POLARIMETRY OF THE CRAB PULSAR

geometrical model (ignoring relativistic effects) a time shift of $\sim 231 \mu\text{s}$ indicates that possibly the optical radiation is formed $\sim 70 \text{ km}$ higher in the magnetosphere than the radio emission. The difference in phase of 0.007 could also be interpreted as an angle between the radio and optical beam of $\sim 2.5^\circ$.

3.4.3 Polarisation characteristics of the Crab pulsar

The Crab pulsar is detected at all phases of rotation (Fig. 3.18), i.e. also in the so-called ‘off-pulse’ phase with an intensity of about 2% compared to the intensity of the MP maximum. In the literature one can find that the measured level of the DC differs from author to author. For example very early measurements performed by Peterson et al. (1978) gave the ‘unpulsed background’ from the Crab pulsar on the level of 3.6% of the main peak intensity. Much lower values were obtained by Jones et al. (1981) and later by Smith et al. (1988): 0.6% and 1.2%, respectively. In addition Percival et al. (1993) claims that the ‘off-pulsed’ flux has an intensity less than 0.9% of the peak flux (visible and UV data from *HST*, 2σ upper limit), whereas a fractional flux derived by Golden et al. (2000a) from photometric analysis gives $\sim 1\%$.

For the background (nebula and sky) subtraction we took the averaged Stokes parameters recorded in the ring fibres over the ‘off-pulse’ phase. After subtracting this steady component from the raw central channel a measurement of the three Stokes parameters as a function of the rotational pulsar phase was derived (see Fig. 3.15). The first Stokes parameter is of course intensity I . Pulse phase colour coded I , measured in counts, is shown in the *upper* panel of Fig. 3.18. The same, but normalised, is shown on the logarithmic scale in the *bottom* panel. The colour coded Stokes parameters Q , U as a vector diagram are shown in Fig. 3.19. Colours refer to the pulse phases as indicated in Fig. 3.18 and the scale is such that $I = 100$ at the maximum light, i.e. maximum of the MP. The MP and IP maxima are indicated with diamonds. Points belonging to the MP phases follow an outer ellipse (*upper* panel), whereas these belonging to the IP an inner one (*bottom* panel). In both cases the direction is counter-clockwise. Noteworthy is that already from the Stokes parameters it is easy to see that there is sudden change in the pattern near the radio phase, i.e. where the red triangles change to the black ones. As the next step of the data analysis the polarisation characteristics - the position angle and the degree of polarisation of the E-vector - were calculated from the Stokes parameters. The results, plotted with a resolution of 1000 phase bins, are presented in Fig. 3.20 and 3.21, respectively.

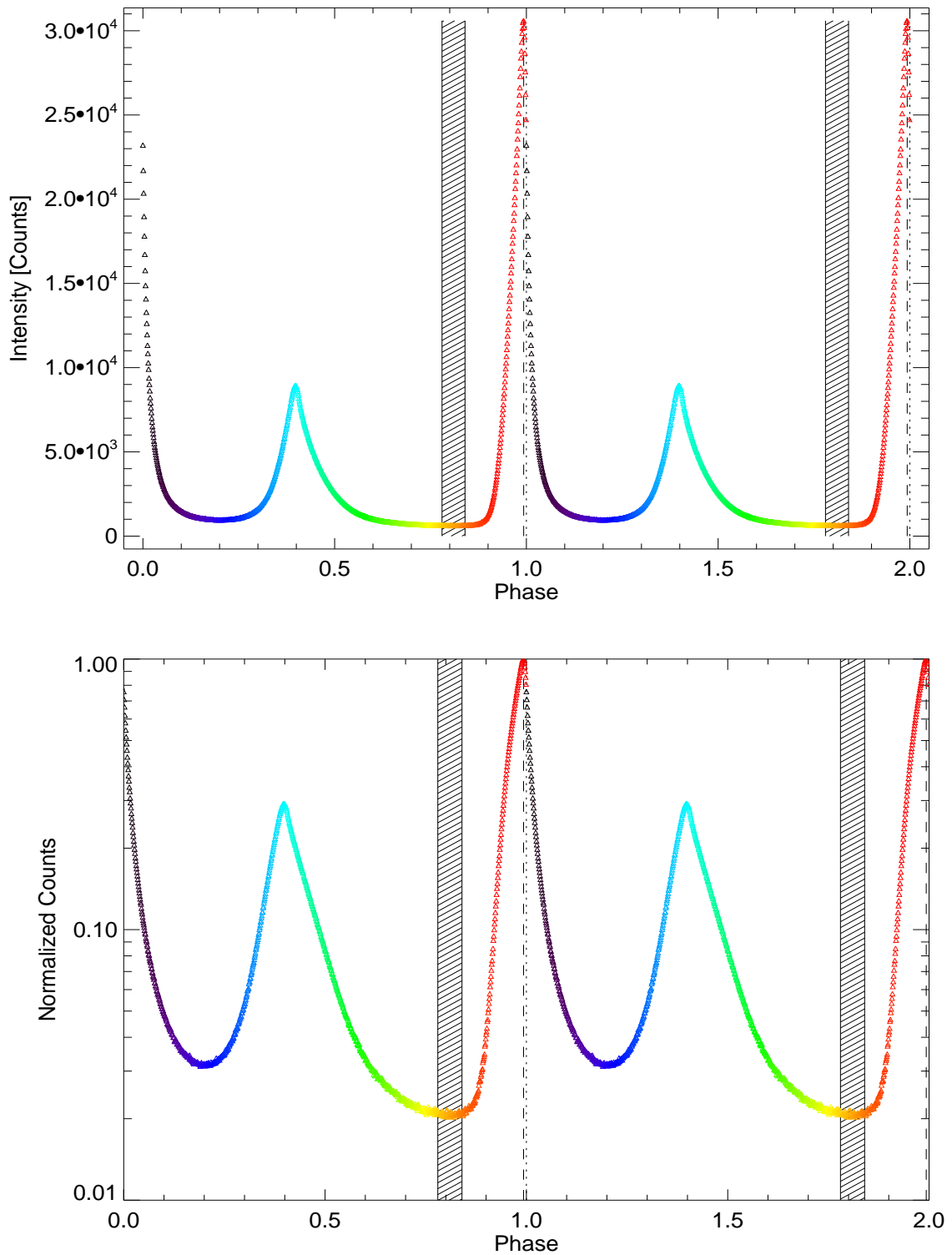


Figure 3.18: The Crab pulsar light curve after sky background and nebula subtraction obtained by OPTIMA at NOT. Time resolution is $33 \mu\text{s}$, i.e. 1000 bins per cycle. *Upper*: measured intensity in counts, *bottom*: normalised counts plotted with a logarithmic scale. Two periods are shown for clarity.

3. OPTICAL POLARIMETRY OF THE CRAB PULSAR

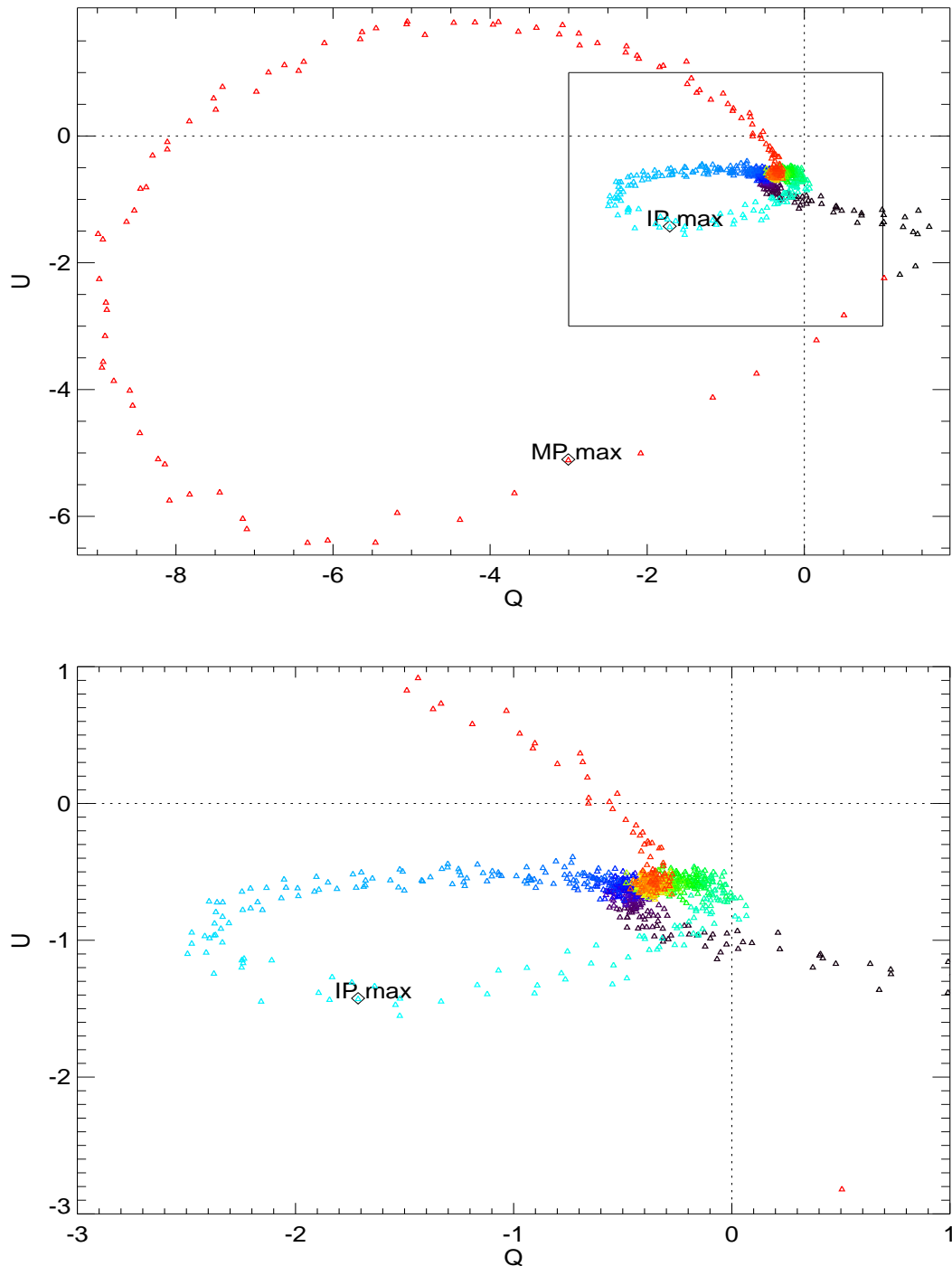


Figure 3.19: Stokes parameters Q , U as a vector diagram. Colours refer to the pulse phases as indicated in Fig. 3.18. The scale is such that $I = 100$ at the maximum light. Phases of the MP and IP maxima are indicated with diamonds. Triangles belonging to the MP and IP follow in a counter-clockwise direction an outer and inner ellipse, respectively. *Bottom* panel shows a zoomed region around the IP phases as it is indicated with a black frame in the *upper* panel. Dashed lines are the horizontal and vertical line at the zero level.

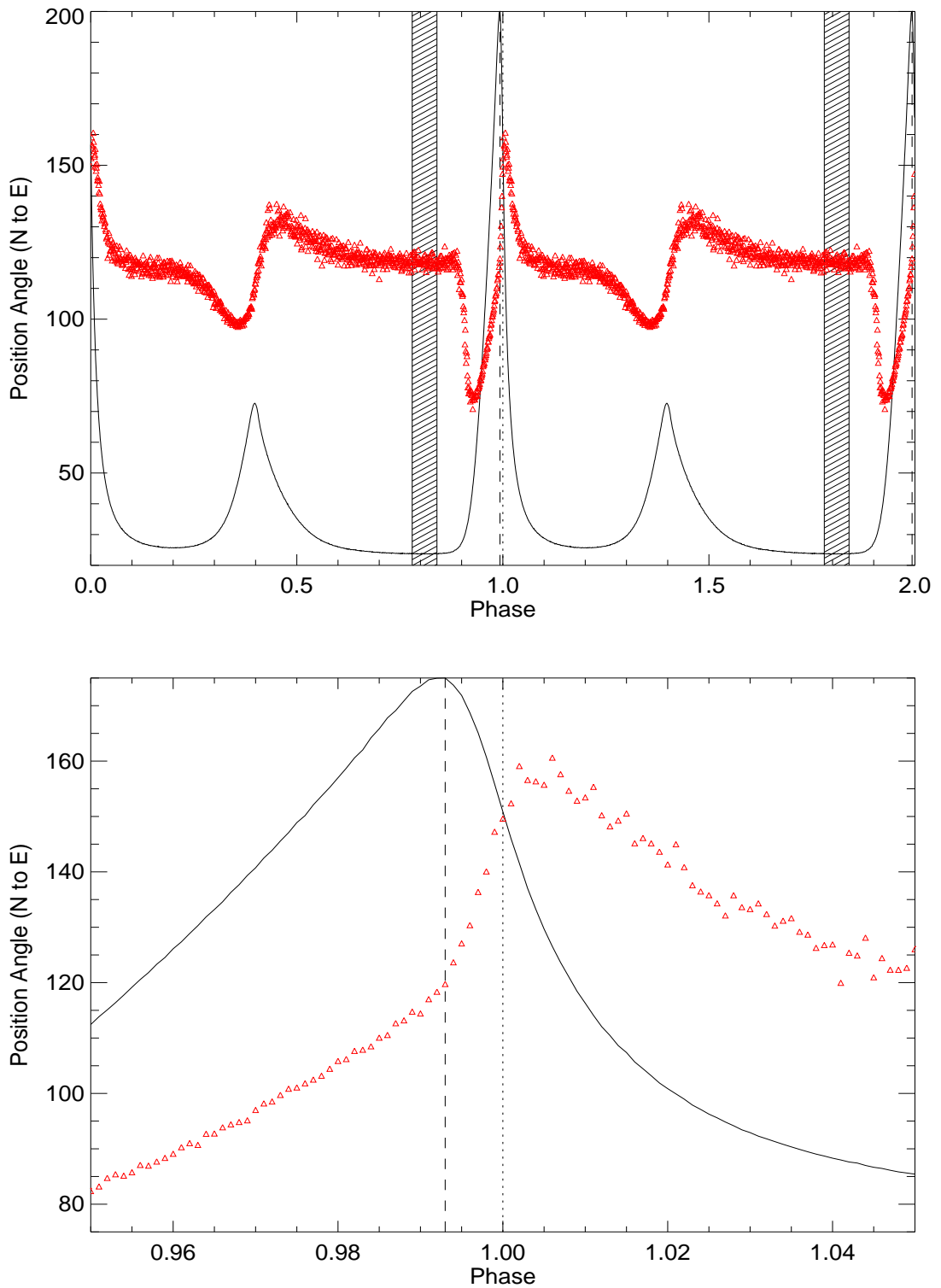


Figure 3.20: *Upper*: the Crab pulsar position angle θ as a function of rotational phase. The pulse profile (solid line) and DC phase range (dashed region) are indicated also. Two periods are shown for clarity. *Bottom*: the same, but zoomed around phase zero. Changes of θ are aligned with the MP maximum of the optical light (dashed line), but also with the zero phase, i.e. with the radio phase of the MP (dotted line).

3. OPTICAL POLARIMETRY OF THE CRAB PULSAR

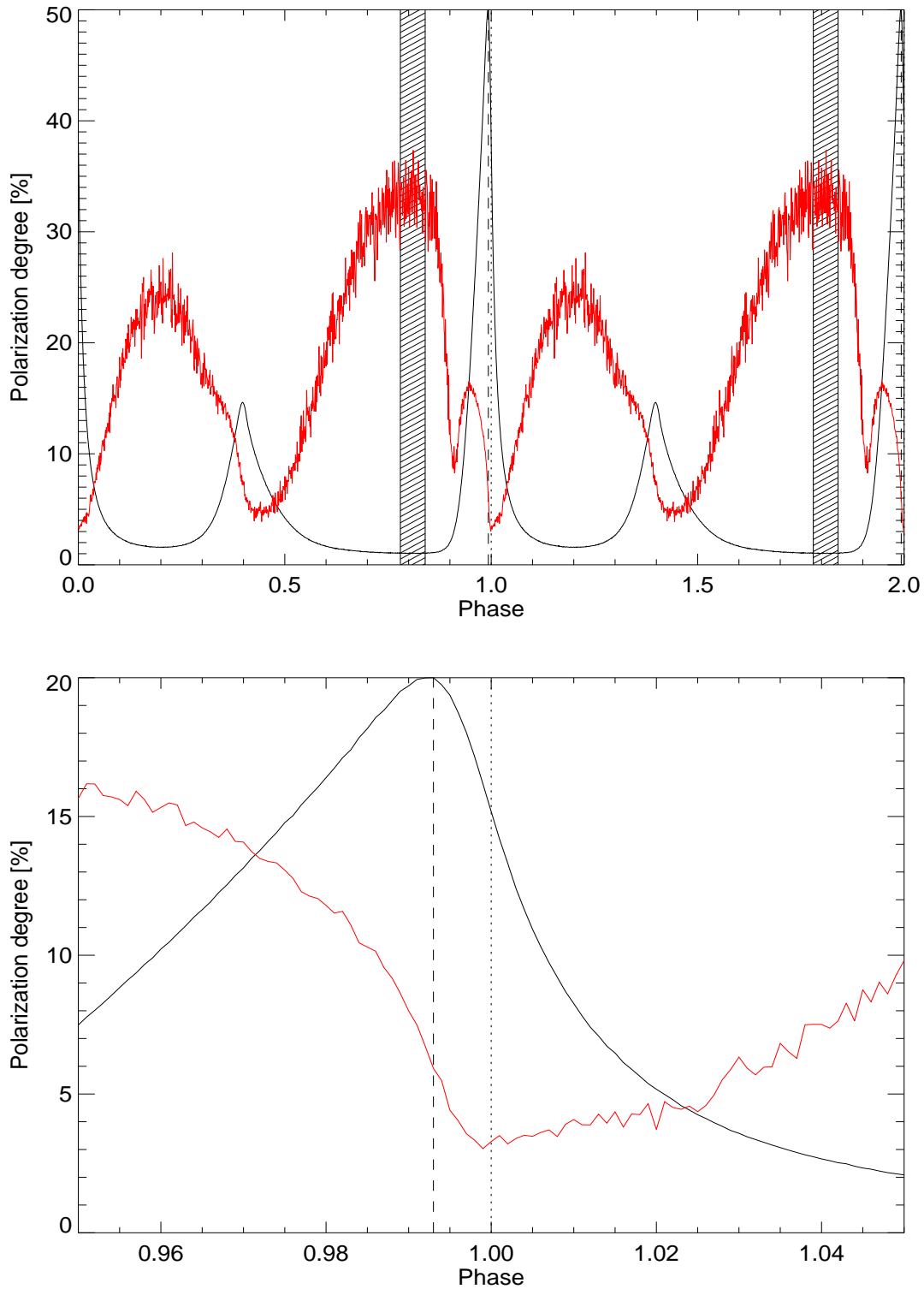


Figure 3.21: *Upper*: the Crab pulsar polarisation degree p as a function of rotational phase. The pulse profile (solid line) and DC phase range (dashed region) are indicated also. Two periods are shown for clarity. *Bottom*: the same, but zoomed around the phase zero. Minimum of p is for the radio phase (dotted line), and not for the maximum phase of the optical MP (dashed line).

3.4.4 Polarisation characteristics of the Crab pulsar after DC subtraction

The apparent constancy of the position angle within the phase range 0.78–0.84 (Fig. 3.20, *upper panel*) may suggest that the optical emission from the Crab pulsar consists of two components - pulsed and unpulsed. The pulsed component is characterised by a highly variable position angle and polarisation degree. The unpulsed (i.e. DC) component is characterised by constant intensity on the level of 2% of the main pulse intensity, fixed $\theta \sim 119^\circ$, and a degree of polarisation on the level of 33%. The source of emission of the DC is unknown. There are various ideas from where in the magnetosphere or the nebula this component might arise. It is also possible that the inner knot (located only $0''.65$ apart from the pulsar and being a persistent feature throughout the sequences of *HST* images, Hester et al. (2002)) is responsible for the ‘off-pulse’ emission. Assuming that the unpulsed component is present at all phase angles and has constant polarisation we obtained the polarisation characteristics of the ‘pulsed component’ separately by subtracting the respective Stokes parameters I , Q , U from the linear polarisation data. The results are presented in Fig. 3.22, 3.23, and 3.24. After subtracting the ‘unpulsed component’ the position angle and polarisation degree in the phases where the intensity is very low are not well defined. Because the Stokes parameters go basically to zero for these rotational phases, the values of θ and p become very noisy.

The polarisation degree of the ‘off-pulse’ component obtained in this work differs from the values presented by other authors (e.g. Jones et al. (1981): $\sim 70\%$; Smith et al. (1988): $\sim 47\% \pm 10\%$). This might be caused by two reasons. Firstly, different groups treat background subtraction in different ways. Additionally, all mentioned observations were taken during different epochs and with different instrumentation. Secondly, the observed variation might be caused by the intrinsic mechanism of the pulsar and/or nebula radiation. We note also that one would expect a change in flux of ~ 0.066 over the 22 years between Jones et al. (1981) and our observations, following the phenomenologically derived $\dot{L}_V \sim 0.003 \text{ mag yr}^{-1}$ (Pacini 1971), empirically confirmed most recently by Nasuti et al. (1997).

3.5 Summary and discussion

The Crab pulsar emits highly anisotropic radiation which spans a wide range of wavelengths, from radio to extreme γ -rays. Knowledge of polarisation characteristics of this radiation is of fundamental importance in our attempts to find the mechanisms

3. OPTICAL POLARIMETRY OF THE CRAB PULSAR

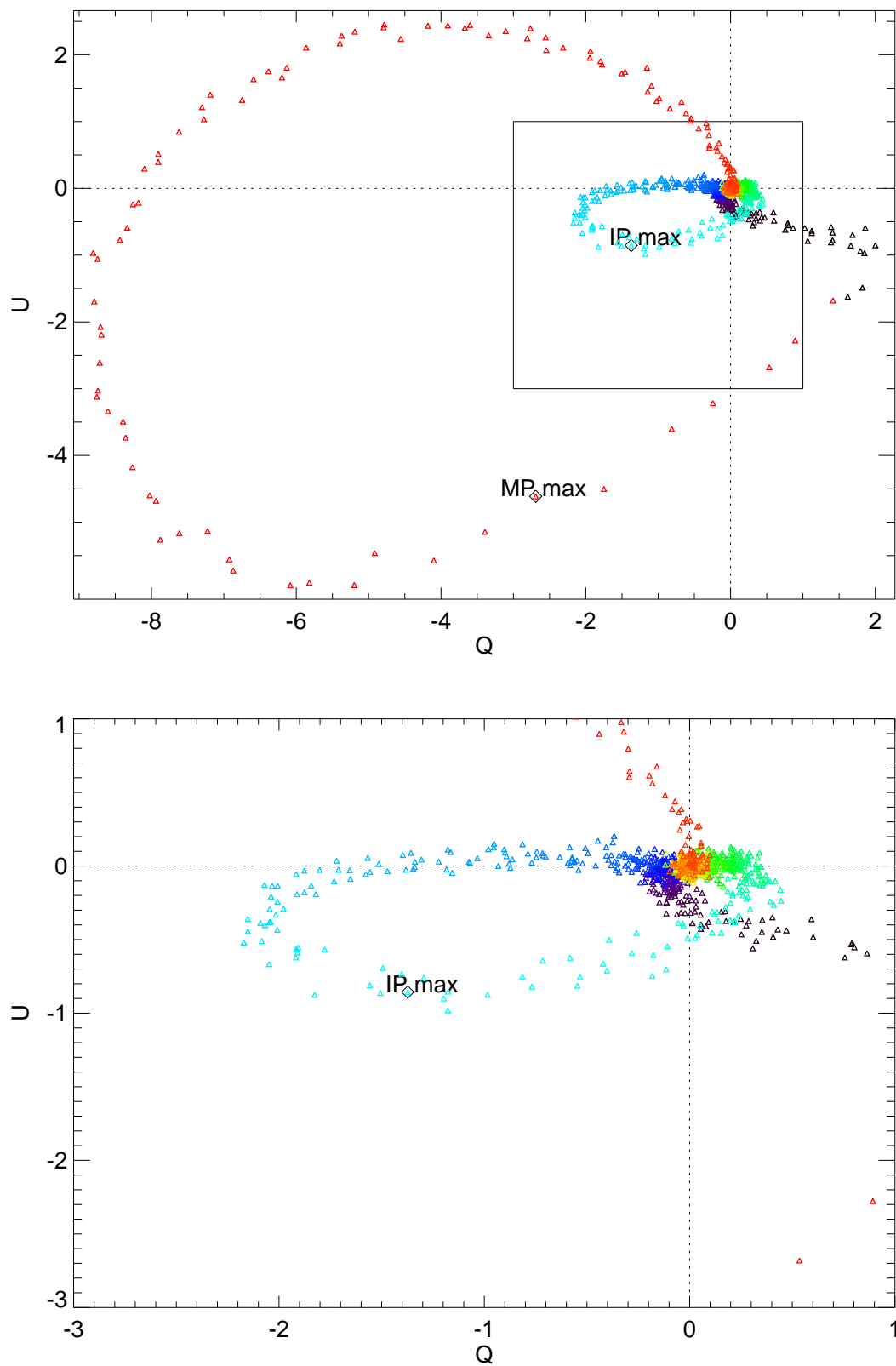


Figure 3.22: The same as in Fig. 3.19 but after DC subtraction.

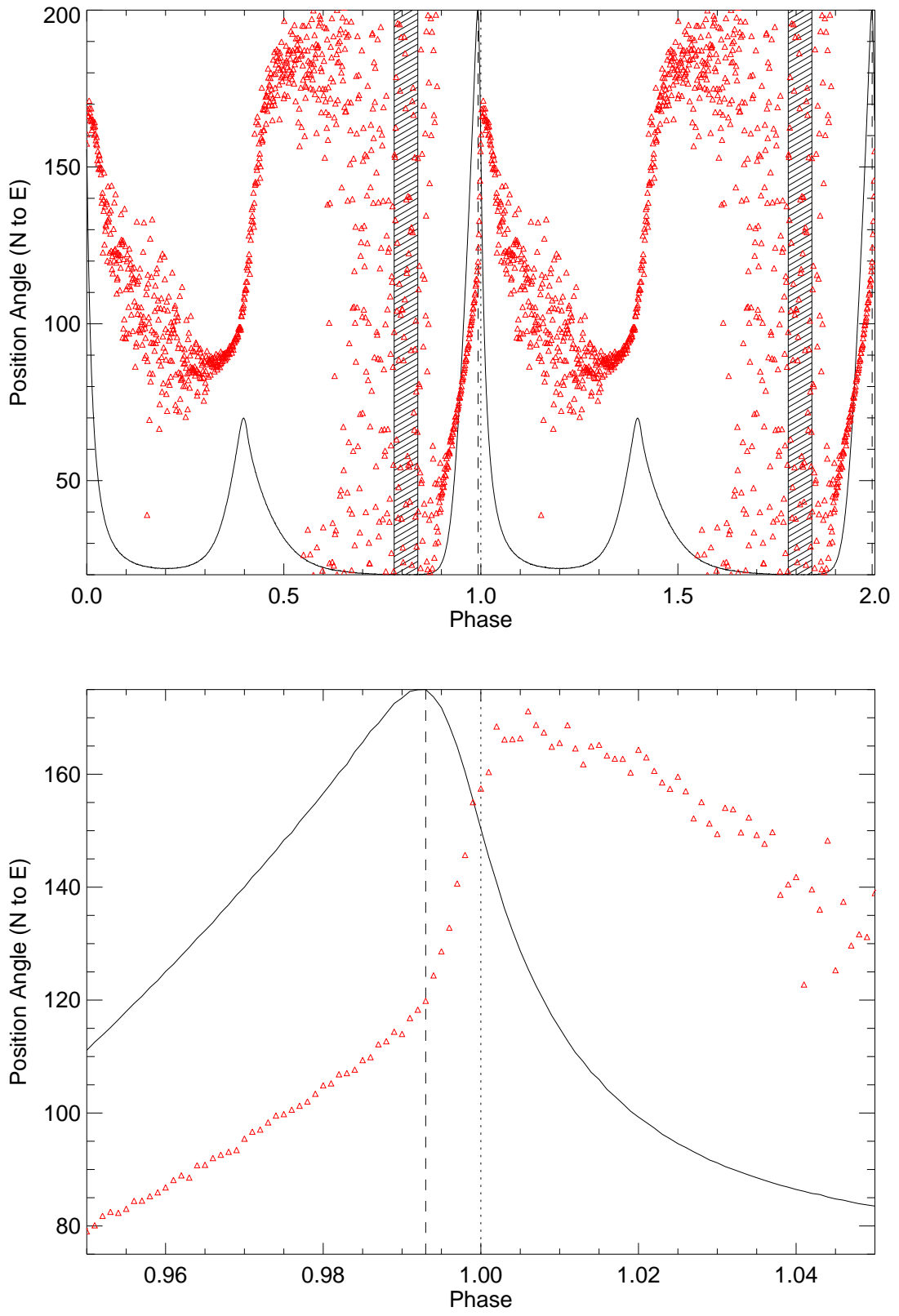


Figure 3.23: The same as in Fig. 3.20 but after DC subtraction.

3. OPTICAL POLARIMETRY OF THE CRAB PULSAR

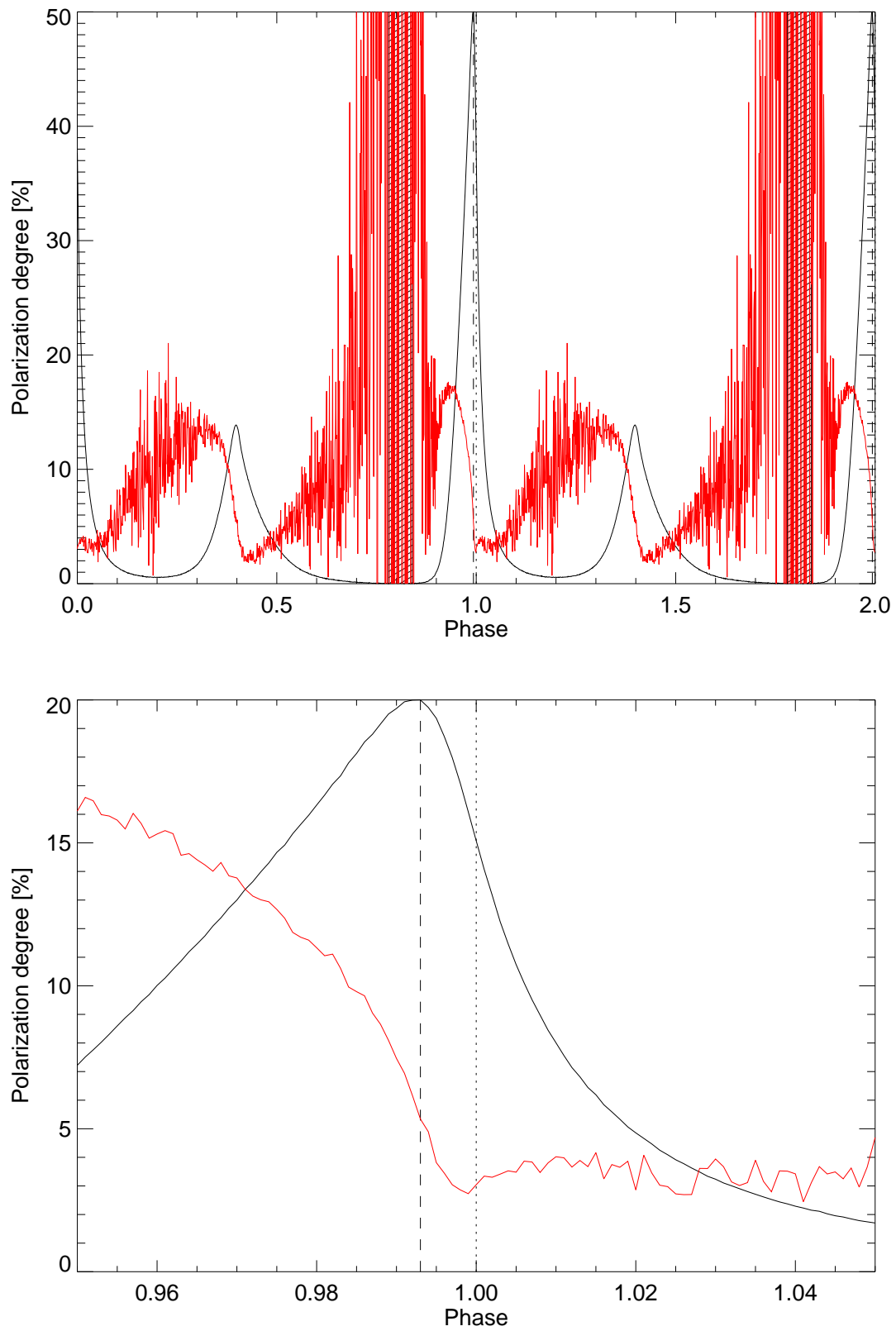


Figure 3.24: The same as in Fig. 3.21 but after DC subtraction.

Table 3.9: p and θ for three selected Crab pulsar phases, i.e. the radio phase, and the phases of both optical maxima, MP and IP. Values before and after DC component subtraction are shown.

Phase	After DC Subtraction				
	p [%]	θ [°]	p [%]	θ [°]	
Radio	0.000	3.29	149.60	3.04	157.46
max of MP	0.993	5.92	119.75	5.34	119.87
max of IP	0.398	7.61	109.87	5.83	105.98

responsible for Crab’s magnetospheric activity. Good quality X-ray and gamma-ray polarimetry with satellite observatories is expected to be available for pulsar studies (among other types of objects) in the near future. Present-day state of instrumentation is sufficient to carry out optical polarimetry of this object with unprecedented quality. Our project to study the Crab Pulsar with OPTIMA and NOT is, to the best of our knowledge, the most recent and most complete one. The observations with $33 \mu\text{s}$ time resolution are a factor of 4 better than the previous best observations. We have completely resolved the polarisation characteristics of both peaks of the Crab pulsar, MP and IP, in the optical pass bands (see Fig. 3.25). Moreover, we were able to better characterise the polarised emission between the peaks, i.e. in the so called ‘bridge’ as well as the DC (often referred as the ‘off-pulse’ component) regions. We find that the MP of the Crab pulsar arrives $231 \pm 68 \mu\text{s}$ before the peak of the radio pulse.

The phase averaged polarisation degree of the Crab pulsar amounts to 9.82% with a position angle of 109.5° . After the DC subtraction it is 5.48% and 96.3° , respectively. Minimum polarisation degree occurs at the phase of 0.999 (see Tab. 3.9), very close to the radio pulsar phase, with $p = 3.3\%$, $\theta = 149.6^\circ$ before the DC subtraction, and with $p = 3.0\%$, $\theta = 157.5^\circ$ after DC subtraction. During the IP the minimum value of p is on the level of 5%, before DC subtraction. Similar to the MP case, it is also shifted (with respect to the phase of the optical maximum) to the leading wing of the pulse. The value of p changes after DC subtraction to $\sim 2\%$. This means that the situation is inverted: before the DC subtraction the minimum of p is reached during the main pulse, whereas after this subtraction the minimum polarisation degree is observed during the inter pulse.

Our results agree generally well with previous measurements (e.g. Kanbach et al. 2005; Smith et al. 1988), but they show details with much better definition and statistics (see Fig. 3.26 for comparison). The behaviour of θ as a function of phase observed for the Crab pulsar at optical wavelengths (Fig. 3.20) differ from those

3. OPTICAL POLARIMETRY OF THE CRAB PULSAR

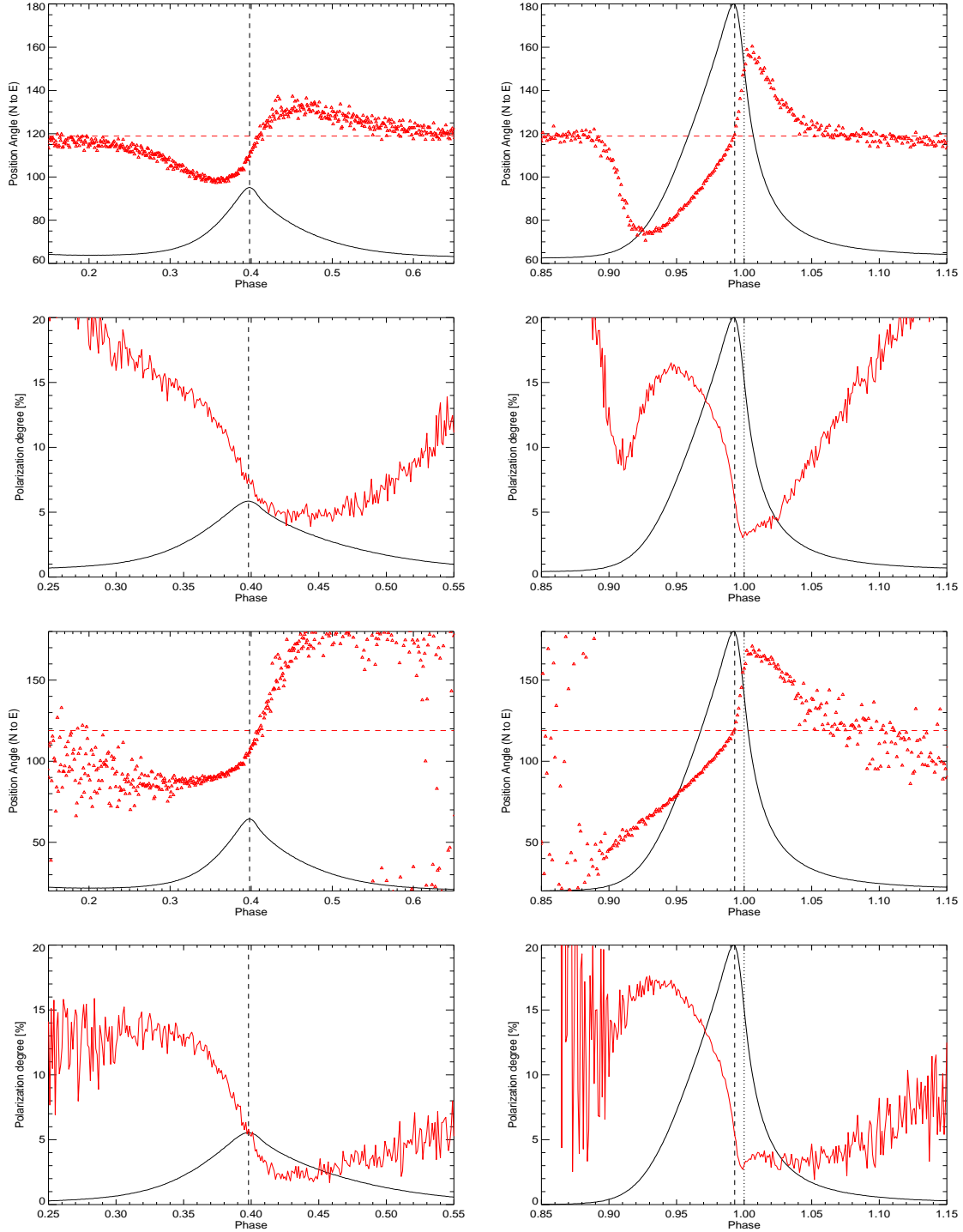


Figure 3.25: Polarisation characteristics, θ and p for both optical peaks: *left* and *right* column is for the IP and MP, respectively. First two rows show the polarisation characteristics of the Crab peaks before DC (phase range: 0.78–0.84, $\theta = 118.9^\circ$, $p = 33\%$) subtraction, whereas the succeeding two rows after this subtraction. Black dashed lines indicates the optical maximum phases of the peaks, black dotted line indicates the radio phase. Red dashed horizontal line shows the $\theta_{DC} = 118.9^\circ$. For clarity the light curve of the Crab pulsar is over plotted (black solid-line).

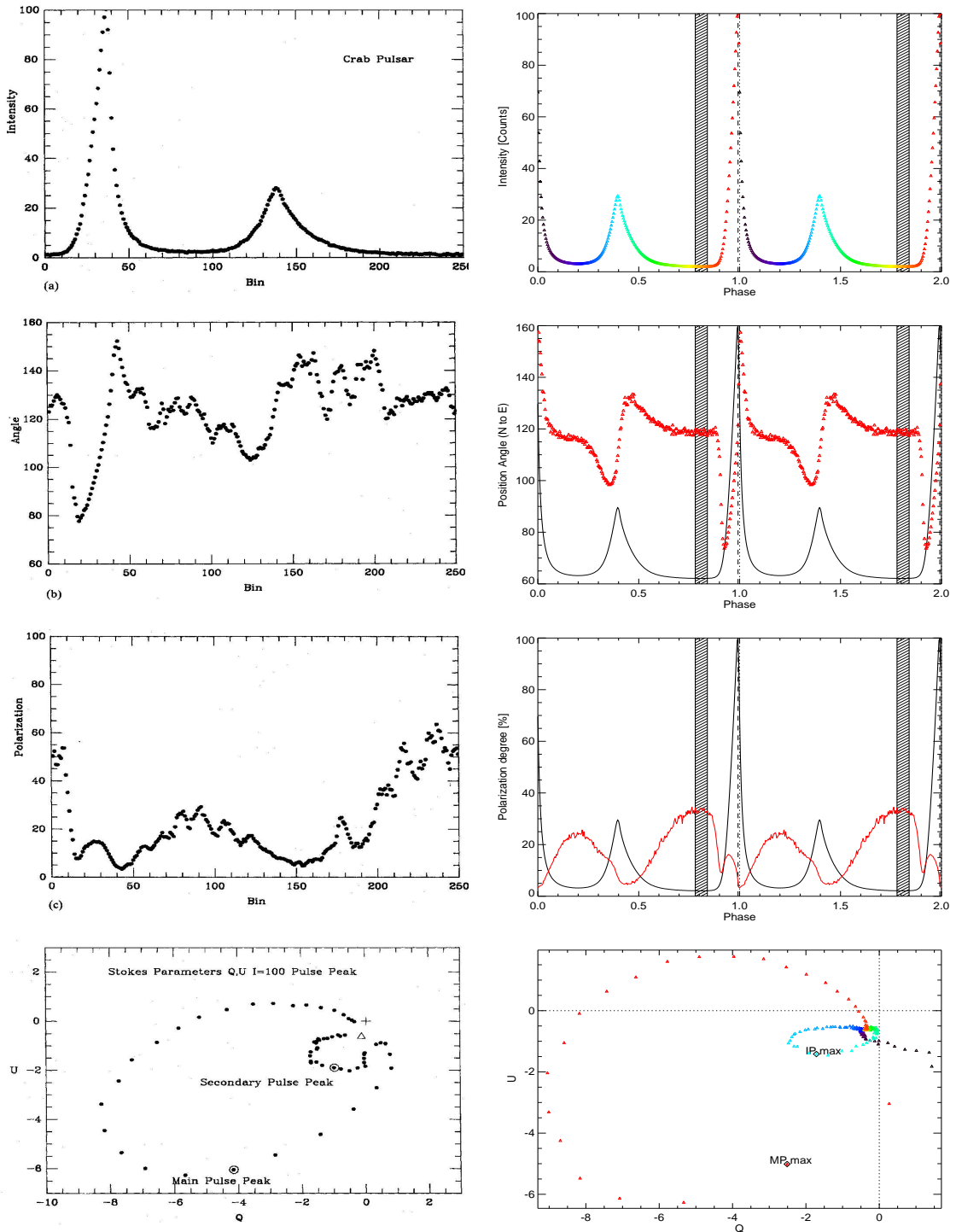


Figure 3.26: Comparison of the results obtained by [Smith et al. \(1988\)](#) and this work *right* and *left* column, respectively. From *top* to *bottom*: the intensity, position angle, polarisation degree, and the Stokes parameters Q , U plotted as a vector diagram as a function of the pulsar phase. There are 250 bins per cycle in both cases, the only difference is that for clarity we show two periods. As a DC component [Smith et al.](#) took 50 out of 250 bins, whereas we took only 7% of the rotational period.

3. OPTICAL POLARIMETRY OF THE CRAB PULSAR

observed at radio wavelengths (e.g. Karastergiou et al. 2004; Moffett & Hankins 1999; Słowikowska et al. 2005a). Two factors may be responsible for this difference: different propagation effects, and different intrinsic emission mechanisms. In particular, the former factor plays an essential role in such high-energy emission models like the outer gap model or the two-pole caustic model: in both models high-energy emission comes from a very wide range of altitudes, contrary to radio emission which originates within a narrow range of altitudes. For comparison the light curves and polarisation characteristics obtained within the framework of three high energy magnetospheric emission models of pulsars, i.e. the polar cap model, the two-pole caustic model, and the outer gap model are shown in Fig. 3.27.

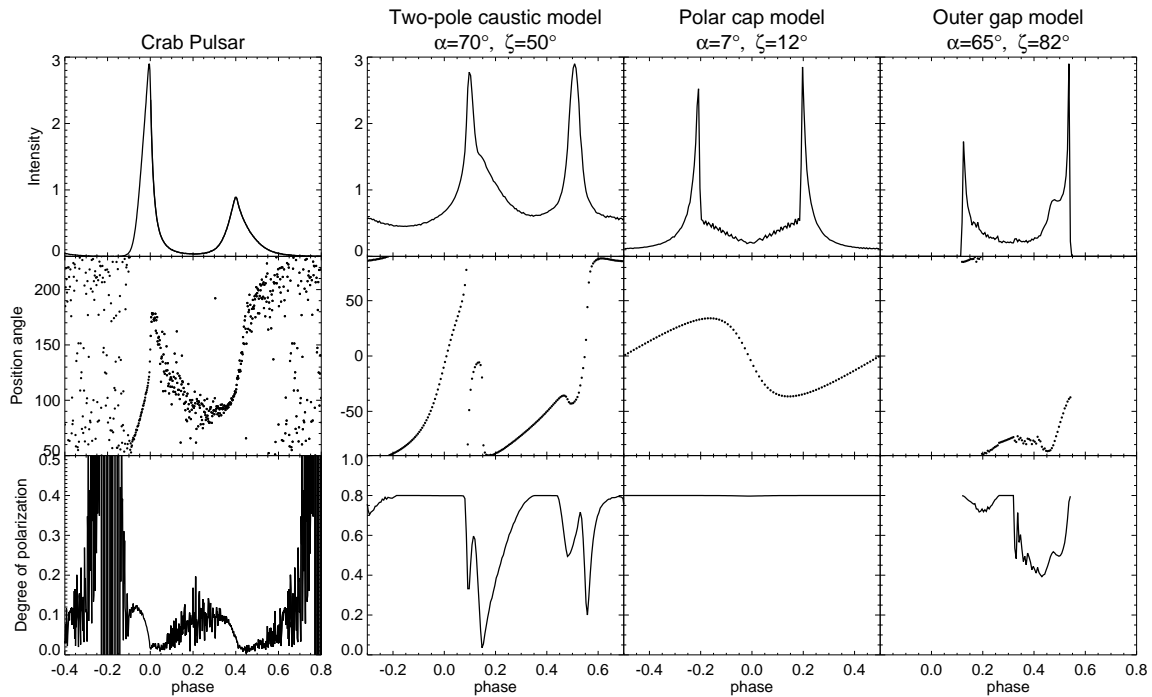


Figure 3.27: The optical light curve, the position angle θ and the degree of polarisation p calculated with the following models of high energy radiation from pulsars, from *left* to *right*: the polar cap model, the two-pole caustic model, and the outer gap model (Dyks et al. 2004b). In the first column, the data from Calar Alto observations (Kanbach et al. 2005) are shown for comparison. Courtesy J. Dyks.

The two-pole caustic model (Dyks & Rudak 2003) predicts fast swings of the position angle and minima in the polarisation degree, similar to what is observed. Polar cap model and outer gap model are not able to reproduce the observational polarisation characteristics of the Crab pulsar. Another model, placing the origin of the pulsed optical emission from the Crab in a striped pulsar wind zone has recently been

proposed by [Pétri & Kirk \(2005\)](#). This model features also polarisation characteristics that bear a certain resemblance to the observations.

3.6 Conclusions

The optical emission from the Crab pulsar is highly polarised, especially in the bridge and ‘off-pulse’ phases. The position angle θ and polarisation degree p of linear polarisation as a function of rotation phase show well determined properties:

- a) the polarisation characteristics of the two pulse components, MP and IP, are very similar;
- b) the polarisation degree is minimal at the phases of the maximum radio intensity, therefore, it is NOT aligned with the optical peaks;
- c) there is a well defined bump in polarisation degree on the rising flank of MP,
- d) there is an indication of such a bump also for IP, especially after the DC subtraction;
- e) the polarisation angle swings through a large angle in both peaks: after subtraction of an assumed constant polarisation component (intensity on the level of 2% of the MP) the angle swing is 130° and 100° for the MP and IP, respectively.

Theoretical models, like the two-pole caustic model ([Dyks, Harding, & Rudak 2004a](#)) or the striped pulsar wind model ([Pétri & Kirk 2005](#)) are able to reproduce (at least qualitatively) some of these properties, e.g. (a) and (e). However, full explanation of the properties (a) to (e) will require more detailed models to be developed.

Chapter 4

PSR B0540-69 - the Crab twin in the Large Magellanic Cloud

4.1 Introduction

PSR B0540-69, a 50 ms pulsar located in the Large Magellanic Cloud (LMC), is one of the most distant pulsars known ($d = 49.4 \pm 3.36$ kpc, [Taylor & Cordes 1993](#)). [Seward et al. \(1984\)](#) discovered the pulsar at the position of supernova remnant SNR 0540-693 by using the *Einstein* X-Ray Observatory. Shortly after its discovery a bright synchrotron wind nebula was confirmed in the optical waveband ([Chanan et al. 1984](#)). The optical pulsations were soon detected by [Middleditch & Pennypacker \(1985\)](#) with a mean pulsed magnitude of 22.5. In the radio band the pulsar is quite a faint source ([Manchester et al. 1993](#)), though [Johnston & Romani](#) recently reported the discovery of the first giant pulses from this pulsar ([Johnston & Romani 2003](#)). Since 1984 PSR B0540-69 has been observed by: HST ([Boyd et al. 1995](#); [Serafimovich et al. 2004](#)), VLT ([Serafimovich et al. 2004](#)), BeppoSAX ([Mineo et al. 1999](#)), GINGA ([Deeter et al. 1999](#)), Chandra X-ray Observatory ([Gotthelf & Wang 2000](#); [Kaaret et al. 2001](#)), ASCA ([Hirayama et al. 2002](#)) and RXTE ([de Plaa et al. 2003](#)).

PSR B0540-69 is often referred to as an extragalactic ‘twin’ of the Crab pulsar (Tab. 4.1). Both pulsars have similar rotational parameters, characteristic age, spin-down luminosity and both are embedded in synchrotron plerionic nebulae (Figs. 4.1 and 1.7). Here the similarity ends. Pulse profiles and spectra of PSR B0540-69 and PSR B0531+21 differ significantly. The Crab pulse profile shows a sharp double-peak structure, whereas the profile of LMC pulsar consists of a single broad peak. However, this broad pulse peak might be formed as a superposition of two Gaussian components separated of about 0.2 in phase ([de Plaa et al. 2003](#)). The X-ray spectrum of PSR

Table 4.1: Properties of PSR B0540-69 and the Crab pulsar.

Parameter	PSR B0540-69	PSR B0531+21
P (s)	0.05035	0.03308
\dot{P} (s s $^{-1}$)	4.79×10^{-13}	4.23×10^{-13}
n	2.08	2.51
d (kpc)	49.40	2.0
τ_c (kyr)	1.67	1.24
B_s (G)	4.97×10^{12}	3.78×10^{12}
L_{sd} (erg s $^{-1}$)	1.5×10^{38}	4.6×10^{38}
Nebula size (pc)	0.6×0.9	1.5×1.5

B0540-60 (de Plaa et al. 2003) differs from the Crab spectrum. Additionally, unlike the Crab pulsar, PSR B0540-69 is not a γ -ray pulsar.

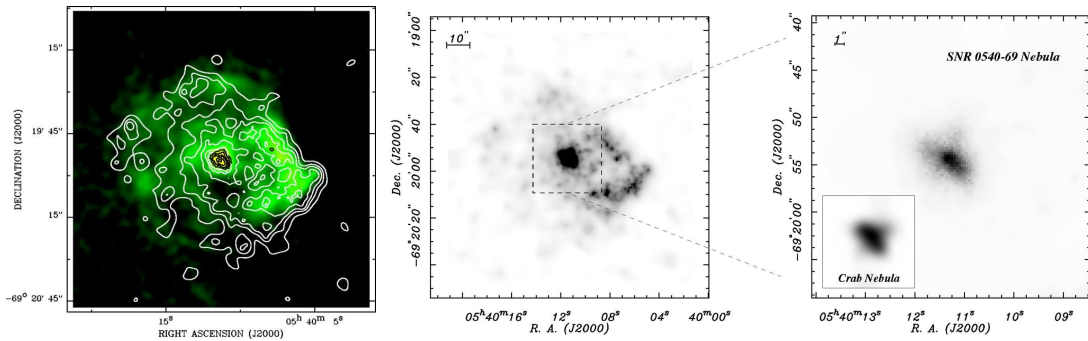


Figure 4.1: *Left*: The X-ray and radio maps of the region of SNR 0540-693. PSR B0540-69 is located in the centre. Contours reflect the Chandra HRC X-ray intensity distribution, whereas the green-scale map denotes the radio emission at 6 cm (Manchester et al. 1993). *Middle*: The X-ray Chandra HRC image centred on the pulsar. Region indicated by the central box is enlarged and displayed in the next panel. *Right*: Close-up image around the pulsar. There is a marginal evidence for a jet-like feature emanating from the pulsar. *Inset*: The Crab Nebula image, placed at the distance of the LMC. The image was blurred to the Chandra HRC resolution. Both nebulae are similar in size. Moreover, they have broadly similar shape and overall brightness morphology [Gotthelf & Wang (2000)].

4.2 The *INTEGRAL* satellite

The International Gamma-Ray Astrophysics Laboratory (*INTEGRAL*) is a 15 keV – 10 MeV gamma-ray observatory mission, consisting of the spectrometer SPI and the imager IBIS (Sec. 4.4), with concurrent source monitoring in X-rays - the Joint

4. PSR B0540-69 - THE CRAB TWIN IN THE LARGE MAGELLANIC CLOUD

European Monitor for X-rays (JEM-X, 3–35 keV, Sec. 4.5) and in the optical range - the Optical Monitoring Camera (OMC, V, 500–600 nm).

High resolution spectroscopy over the entire energy range permits spectral features to be uniquely identified and line profiles to be determined for physical studies of the source and its surrounding. The fine imaging capability of *INTEGRAL* within a large field of view allows an accurate source localisation. The identification of the gamma-ray emitting objects with their counterparts at other wavelengths enables to distinguish extended regions from point sources. Characteristic parameters of two main *INTEGRAL* instruments; spectrometer SPI and imager IBIS are presented in Tab. 4.2

Table 4.2: Characteristics of the two main *INTEGRAL* instruments, the spectrometer SPI and the imager IBIS

	SPI	IBIS
Energy range	20 keV – 8 MeV	15 keV – 10 MeV
Detectors	19 Ge cooled to 85 K	16384 CdTe (ISGRI) 4096 CsI (PICsIT)
Detector area (cm ²)	500	2600 (CdTe), 3100 (CsI)
Spectral resolution (FWHM)	2.3 keV @ 1.3 MeV	9 keV @ 100 keV
Field of view (fully coded)	16°(corner to corner)	9° × 9°
Angular resolution (FWHM)	2.5°(point source)	12'
Source location (radius)	< 1.3° (depending on the source strength)	< 1' (for 10 σ source)
Absolute timing accuracy (3 σ)	129 μ s	61 μ s

4.3 Observations

We gathered more than one million seconds of PSR B0540-69 observations with *INTEGRAL*. One *INTEGRAL* orbit that lasts three sidereal days makes one revolution. The satellite was pointed to the LMC during nine revolutions (Tab. 4.3); six of them took place in January 2003 and three of them a year later, in January 2004. Because of the dithering of the *INTEGRAL* satellite, single observation consists of many *pointings* that last about 30 minutes and are separated by *slews*. Each pointing and slew, or only a part of them if they are too long, is called a *Science Window* (ScW). Single observation usually consists of several ScWs. Detailed information about the strategy of scientific observations, as well as about the hierarchical data storage and data repositories can be found in the "Introduction to the *INTEGRAL* data analysis"¹.

¹<http://isdc.unige.ch/index.cgi?Soft+download>

Table 4.3: Time span of the *INTEGRAL* LMC observations. A total of 813 ScWs within nine revolutions were selected. First column gives the *INTEGRAL* orbit (revolution) number. Second column shows the arbitrary numbers of ScWs given in brackets, as well as a total number of ScWs in revolution. Next columns show revolution start and end time given in MJD TT and UTC, respectively.

Rev	Number of ScWs	TSTART	TSTOP	TSTART	TSTOP
0027	(1-92) 92	52641.33	52643.98	2003Jan02 at 07:57:54	2003Jan04 at 23:38:55
0028	(93-177) 85	52644.33	52646.97	2003Jan05 at 08:01:21	2003Jan07 at 23:29:57
0029	(178-271) 94	52647.33	52649.97	2003Jan08 at 07:55:09	2003Jan10 at 23:20:02
0033	(272-367) 96	52659.29	52661.94	2003Jan20 at 06:58:11	2003Jan22 at 22:34:56
0034	(368-459) 92	52662.29	52664.93	2003Jan23 at 07:09:39	2003Jan25 at 22:19:59
0035	(460-552) 93	52665.27	52667.94	2003Jan26 at 06:29:29	2003Jan28 at 22:34:58
0150	(553-631) 79	53009.26	53011.93	2004Jan05 at 06:14:46	2004Jan07 at 22:29:59
0151	(632-726) 95	53012.23	53014.92	2004Jan08 at 05:37:33	2004Jan10 at 22:14:57
0152	(727-813) 87	53015.22	53017.93	2004Jan11 at 05:25:23	2004Jan13 at 22:21:52

Additional information is provided in the manuals published by *INTEGRAL* Science Data Centre (ISDC) team. For the purpose of our project we used public *INTEGRAL* software - Off-line Science Analysis (OSA, v5.1). It is supported by ISDC. For the timing analysis we used our own IDL procedures.

Detailed description of the data selection

We used all available *INTEGRAL* data of PSR B0540-69. Until now the LMC was observed during the following nine revolutions: 0027, 0028, 0029, 0033, 0034, 0035, 0150, 0151 and 0152 (Tab. 4.3). It resulted in 813 ScWs operated in the pointing mode. The exposure time in seconds, as well as the position angle in degrees as a function of selected ScWs is shown in the Fig. 4.2. Arbitrary ScW numbers corresponding to different revolutions are given in Tab. 4.3. Afterwards, we made the following selection. Using `idx_find`¹ we requested for: ScW being of pointing type, pulsar located in the fully illuminated field of view (that is 9° and 4°8 for IBIS and JEM-X, respectively), and both instrument modes being equal to 41, i.e. `IBISMODE=41` and `JMX2MODE=41`. We obtained two lists of ScWs fulfilling the terms of our criteria. The IBIS list consists of 617 ScWs, and the JEM-X one of 409 ScWs. None the less, in both cases the final number of used ScWs decreased during the analysis. It was caused by different reasons that are discussed in the according paragraphs.

Both, IBIS and JEM-X are coded mask instruments, therefore it is not possible to deal with one source at a time. Each source contributes to the background of the other sources detected in the field of view (FoV) of the instrument. Thus, all

¹This procedure allows to select ScWs fulfilling terms of user criteria.

4. PSR B0540-69 - THE CRAB TWIN IN THE LARGE MAGELLANIC CLOUD

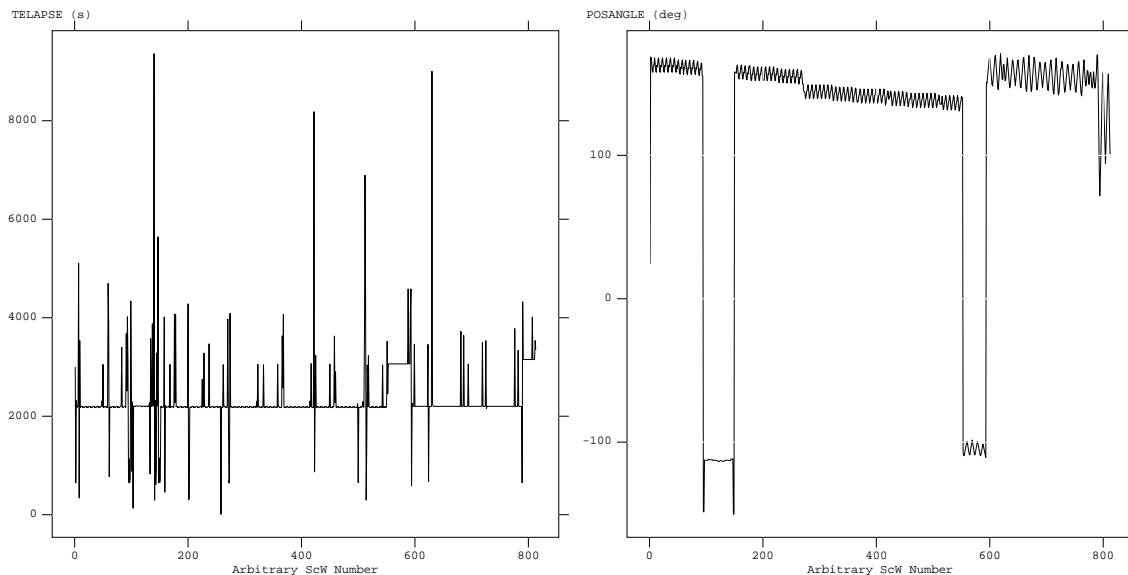


Figure 4.2: Total exposure time ($TELAPSE \equiv TSTOP - TSTART$, see Tab. 4.3) in seconds (*left*) and position angle in degrees (*right*) as a function of 813 ScWs obtained during the *INTEGRAL* observations of LMC.

sources brighter or comparable with the target have to be included in the user (input) catalogue. For the purpose of the analysis we created our own catalogue. It is based on the general *INTEGRAL* catalogue (v.24) and consists of seven sources visible in the IBIS FoV. Detailed information of the selected sources is shown in Tab. 4.4. The IBIS FoV is larger than the JEM-X FoV, therefore EX0 0748-676 was not visible by the X-ray instrument. Consequently only the first six sources listed in Tab. 4.4 were taken into account during the JEM-X analysis.

4.4 IBIS/ISGRI data analysis and results

IBIS is a gamma-ray telescope on-board of the *INTEGRAL* satellite with powerful diagnostic capabilities of fine imaging, source identification and spectral sensitivity in both continuum and lines. It is able to localise weak sources at low energy to better than a few arcminutes accuracy (Tab. 4.2). Its energy resolution is 7% at 100 keV and 9% at 1 MeV. IBIS is a γ -ray imager consisting of two simultaneously operating detectors, ISGRI and PICsIT, covering the energy range from 20 keV to 10 MeV. First layer (ISGRI) is made of Cadmium-Telluride (CdTe) solid-state detector and the second (PICsIT) of Cesium-Iodide (CsI) scintillator crystals. This configuration ensures a good broad line and continuum sensitivity over the wide spectral range covered by IBIS. Our analysis is based on the ISGRI single events. Incoming photon

4.4 IBIS/ISGRI data analysis and results

Table 4.4: Catalogue of selected sources used for the IBIS/ISGRI and JEM-X analysis. Coordinates are given in the increasing order of RA. Additionally the ISGRI (I_FLAG) and JEM-X (J_FLAG) detection flags are given; 0 - undetected, 1 - detected. However, the flag values are obtained for the standard settings of the data analysis performed by ISDC team. Especially the minimum detection sigma parameter could play a role here. The source coordinates were taken from the *INTEGRAL* General Reference Catalogue (v.24) containing all sources detected by *INTEGRAL* and being brighter than 1 mCrab above 1 keV. Only the pulsar position was changed. We used the coordinates given by [Kaaret et al. \(2001\)](#) on the basis of the Chandra observation.

NAME	SOURCE_ID	α [°]	δ [°]	I_FLAG	J_FLAG
LMC X-2	J052029.2-715736	80.12167	-71.96000	0	1
LMC X-4	J053249.2-662214	83.205	-66.37056	1	1
SN 1987A	J053530.0-691600	83.875	-69.26667	0	0
LMC X-3	J053856.4-640501	84.735	-64.08361	0	1
LMC X-1	J053938.7-694436	84.91125	-69.74333	1	1
PSR B0540-69	J054007.7-692005	85.04675	-69.33194	1	0
EXO 0748-676	J074833.8-674509	117.1408	-67.7525	1	0

is stopped in a single pixel of the ISGRI layer, generating an electric pulse. The pulse amplitude yields the energy of the incident photon. However, above 50 keV the energy is a function of not just the pulse height but also the pulse rise time. In that case both measured values are used to determine the energy of the photon.

We constructed pulsar ephemeris from the Rossi X-ray Timing Explorer Mission Proportional Counter Array (RXTE PCA) observations. The RXTE data were taken between December, 7 2002 and January, 30 2003, as well as between January, 3 and February, 27 2004. The ephemeris obtained for both epochs are presented in Tab. 4.5, respectively. Note that second frequency derivative for the time span 53007–53062 MJD (Rev. 150–152) is not significant. The RXTE PCA 2–10 keV pulse profile constructed by using the data collected over December 2002 and January 2003 and folded accordingly to the pulsar ephemeris is shown in Fig. 4.3, *left panel*. The pulse profiles obtained from the data collected between January and February 2004 in three energy bands: 2–10, 10–20, and 20–30 keV are shown in Fig. 4.3, *right panel*. It is clear that the pulse duty cycle increases, while the pulsed fraction likely decreases with energy. The exact number of the pulsed fraction defined as $f = \frac{N_P}{N_P + N_{DC}}$ can not be derived because of the unknown background level. The ephemeris for 2003 and 2004 observations are not absolute, and the alignment of the corresponding RXTE pulse profiles is not absolute either. Absolute timing would require defining the anchor point in the profile and referencing to this phase.

4. PSR B0540-69 - THE CRAB TWIN IN THE LARGE MAGELLANIC CLOUD

Table 4.5: PSR B0540-69 ephemeris.

Parameter & Value	Value
α_{2000}	05 ^h 40 ^m 11 ^s .221
δ_{2000}	-69°19'54''98
Rev. 27, 28, 29, 33, 34 and 35	
Val. range (MJD)	52620–52670
t_0 (TDB MJD)	52625.000000000
ν_0 (Hz)	19.779298587915
$\dot{\nu}_0$ (10^{-10} Hz s ⁻¹)	-1.87410
$\ddot{\nu}_0$ (10^{-20} Hz s ⁻²)	2.51
Rev. 150, 151, 152	
Val. range (MJD)	53007–53062
t_0 (TDB MJD)	53007.000000000
ν_0 (Hz)	19.773116586988(11189)
$\dot{\nu}_0$ (10^{-10} Hz s ⁻¹)	-1.87256(11)
$\ddot{\nu}_0$ (10^{-21} Hz s ⁻²)	3.413(4.92)

Since October 18, 2004 all public *INTEGRAL* data are available in two formats: revision 1 (Rev.1) and revision 2 (Rev.2). In Rev.2, the correction of all JD time stamps for the offsets between the On Board Time (OBT) of each instrument is done. In Rev.2 the data correction (COR) step, as well as the instrumental Good Time Interval (GTI) and deadline handling (DEAD) steps are performed by ISDC team by using OSA (v.4.2) at the science window level. During the COR step the data are corrected for instrumental effects, such as energy and position corrections, while the GTI step generates, selects and merges Good Time Intervals to produce a unique GTI that is later used for selecting events. The net observing time is also computed in this step. Dead and live times are computed during DEAD step of the analysis. The dead time is the time during which the instrument was not capable to register, for different reasons, the incoming photons within GTI. However, the data correction implemented in OSA 5.1 is much better. Therefore, it is highly recommended by the ISDC team to rerun these three steps (COR, GTI, DEAD) over the used data. We performed these correction steps over all selected ScWs, although it is very time and disc-space consuming.

It is known from the ISGRI limitations that a problem on-board IBIS causes, under some circumstances, event times to be shifted by 2 seconds. The OSA software corrects for it, but still the possible jumps might occur. Such behaviour can be verify by checking the value under the FITS flag keyword TIMECORR. For accurate timing

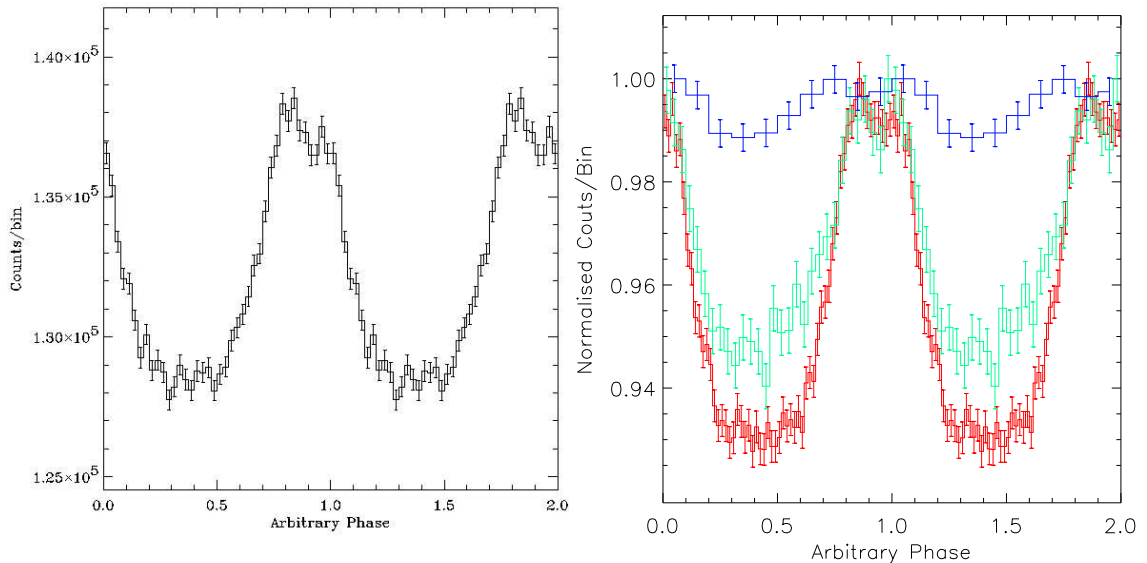


Figure 4.3: *Left*: RXTE PCA 2–10 keV pulse profile of PSR B0540-69 obtained from the data collected between December, 7 2002 and January, 30 2003. *Right*: RXTE PCA normalised pulse profiles of PSR B0540-69 obtained from the data collected between January, 3 and February, 27 2004. The red, green, and blue light curves corresponds to 2–10, 10–20, and 20–30 keV energy bands, respectively. The pulse duty cycle changes significantly with energy. The background level is unknown, therefore the pulsed fraction can not be measured.

it is recommended to use only the data with no possible jump, i.e. TIMECORR=0. Therefore, we used only ScWs with TIMECORR equal 0. The most update version of the known limitations, including list of ScWs for which the two-second jumps have been detected, can be found on the ISDC web pages ¹.

A standard and stand-alone tool `ii_pif_built` is used to calculate the ISGRI Photo Illumination Fraction (PIF) for a given source. Once the PIF map is made, it is straightforward to filter event lists based on the PIF threshold. By applying the PIF filter, one can reduce the background and optimise the signal to noise ratio. From experience, we choose $\text{PIF} > 0.5$ as the event selection criterion. We run `ii_pif_built` procedure with pulsar position ($\alpha_{2000} = 85^{\circ}046754167$, $\delta_{2000} = -69^{\circ}331938889$, [Kaaret et al. \(2001\)](#)) as an input parameter to compute the PIF for each event. By using the `evts_extract` script only single events (`evttype=0`, $7 < \text{RISE_TIME} < 90$) were selected. Additionally, the noisy pixels (`SELECT_FLAG=0`) were filtered out. The procedure `evts_extract` allows to barycentre the events, however at this point we did not use it. Firstly, the instrument time corrections were applied, i.e. $111 \pm 10 \mu\text{s}$ and $185 \pm 10 \mu\text{s}$ for IBIS and JEM-X, respectively ([Walter et al. 2003](#)) and then derived

¹ http://isdc.unige.ch/Soft/download/osa/osa_sw/osa_sw-5.1/osa_issues.txt

4. PSR B0540-69 - THE CRAB TWIN IN THE LARGE MAGELLANIC CLOUD

times of arrivals (TOAs) were barycentred. Afterwards, only events with the energy ≤ 300 keV were selected. For these events we stored their TOAs, PIF and energy values. TOAs belonging to the first and second set of observations were then folded according to the corresponding RXTE ephemeris (Tab. 4.5). Hence, we obtained two sets of the pulsar light curves in five energy bands: 17–25, 25–40, 40–100, 100–200, and 200–300 keV. The ephemeris are not absolute, therefore to sum up the light curves from both observations we used the cross-correlation method. As the template we used light curve with the highest significance, i.e. the light curve obtained for JEM-X data in the 6–10 keV energy band (see Sec. 4.5). In the light curves only the events with $\text{PIF} > 0.5$ are included, i.e. with probability of illuminating the pixel by the source being higher than 50%. The results are presented in Fig. 4.4.

By standard data processing (`ibis_science_analysis`) we produced the sky images for each individual ScW. The source is very faint, therefore it was not detected on high significance level in single ScWs. The OSA software allows to gather the single ScWs belonging to different observations. Thus, we used all selected ScWs to produce the mosaic maps. They correspond to the same five energy bands used for the light curve extraction. In the mosaic maps the PSR B0540-69 was detected in four lower energy bands with following significances: 13.8, 11.2, 7.6 and 6.2, respectively (Figs. 4.6, 4.7). There was no significant detection above 200 keV.

For the faint sources the recommended spectral extraction method is based on the mosaic sky images. To derive the spectrum we used the count rate values obtained from these images. We derive the spectrum of the total source exclusively from the ISGRI data, treating the calibration of JEM-X as not applicable to such a weak source. The photon spectrum can be fitted with a power law of index -2.22, which is compatible with the result found by [Götz et al. \(2006\)](#). The spectrum and the power law fit are shown in Fig. 4.5.

4.4 IBIS/ISGRI data analysis and results

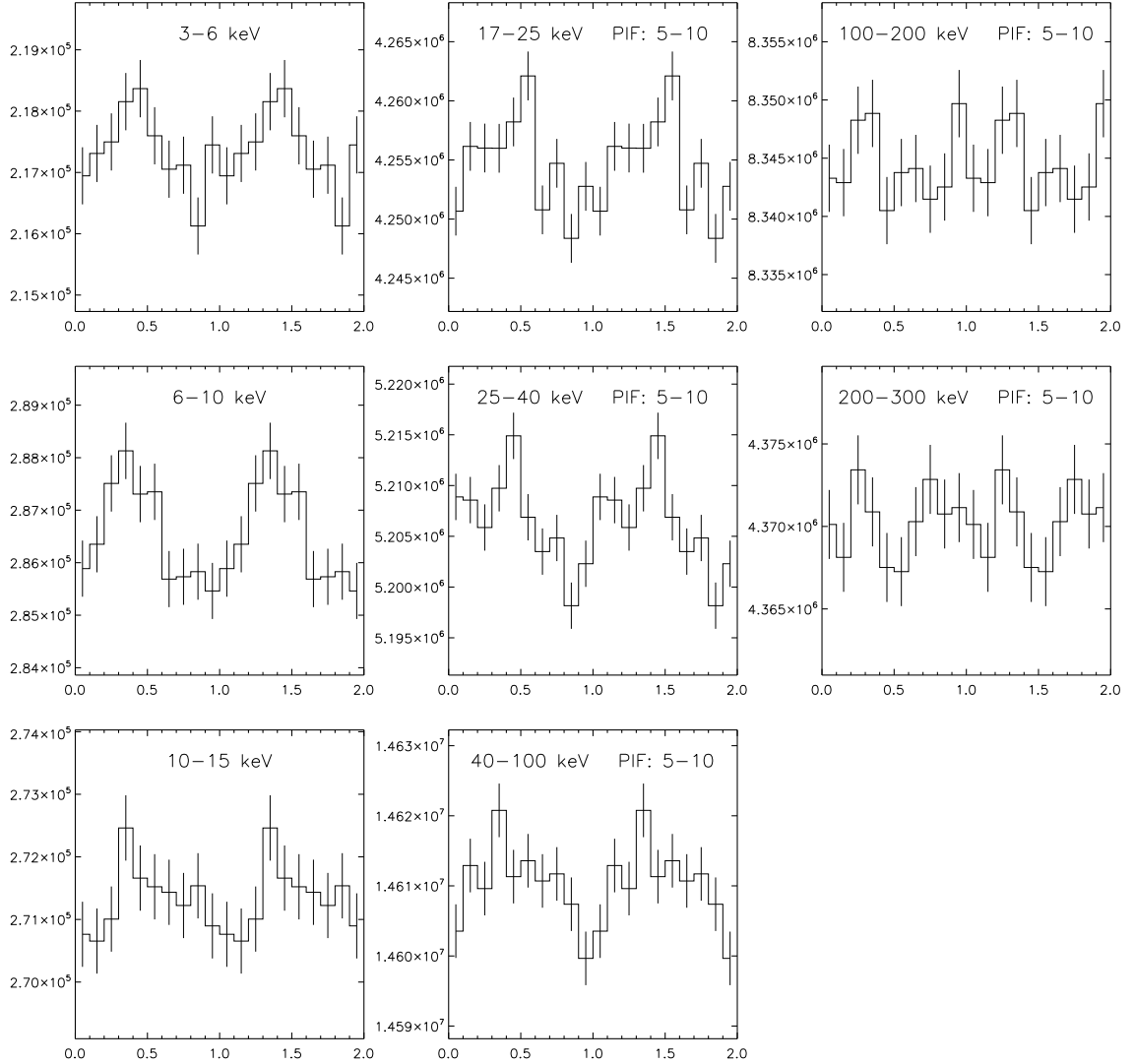


Figure 4.4: PSR B0540-69 light curves obtained from JEM-X (*left column*) and IBIS (*middle and right columns*) instruments. The energy bands are indicated in each panel, two cycles are shown for clarity. The PIF values in the description of PIF ranges were multiply by 10.

4. PSR B0540-69 - THE CRAB TWIN IN THE LARGE MAGELLANIC CLOUD

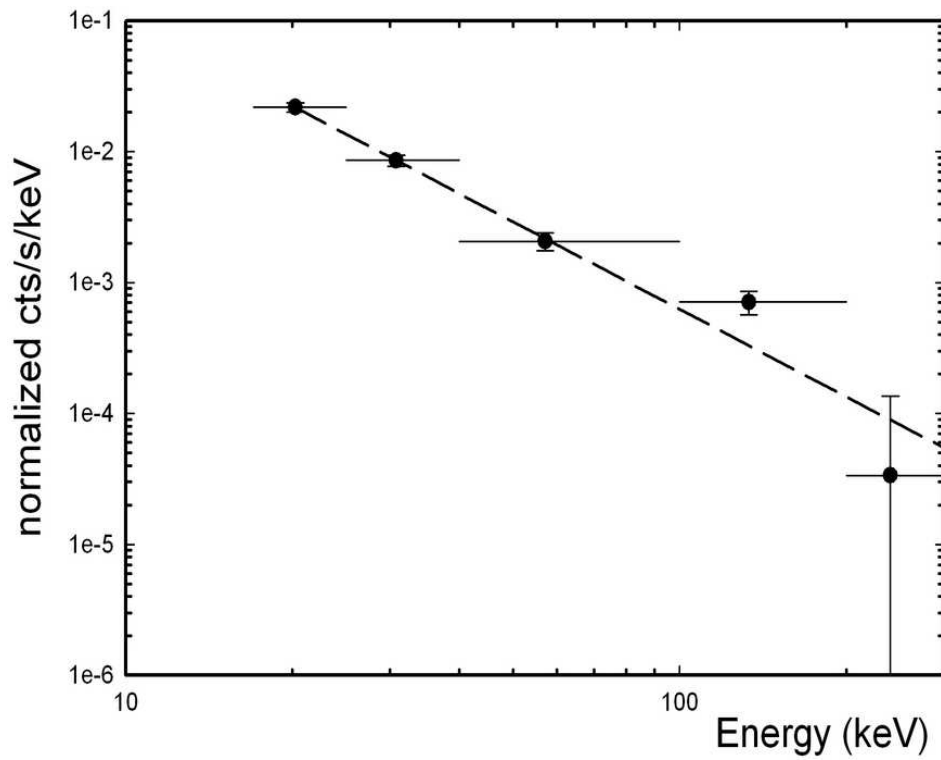


Figure 4.5: PSR B0540-69 spectrum in 17–300 keV energy range. Above 200 keV only upper limit was derived. The dashed line indicates the power law fit.

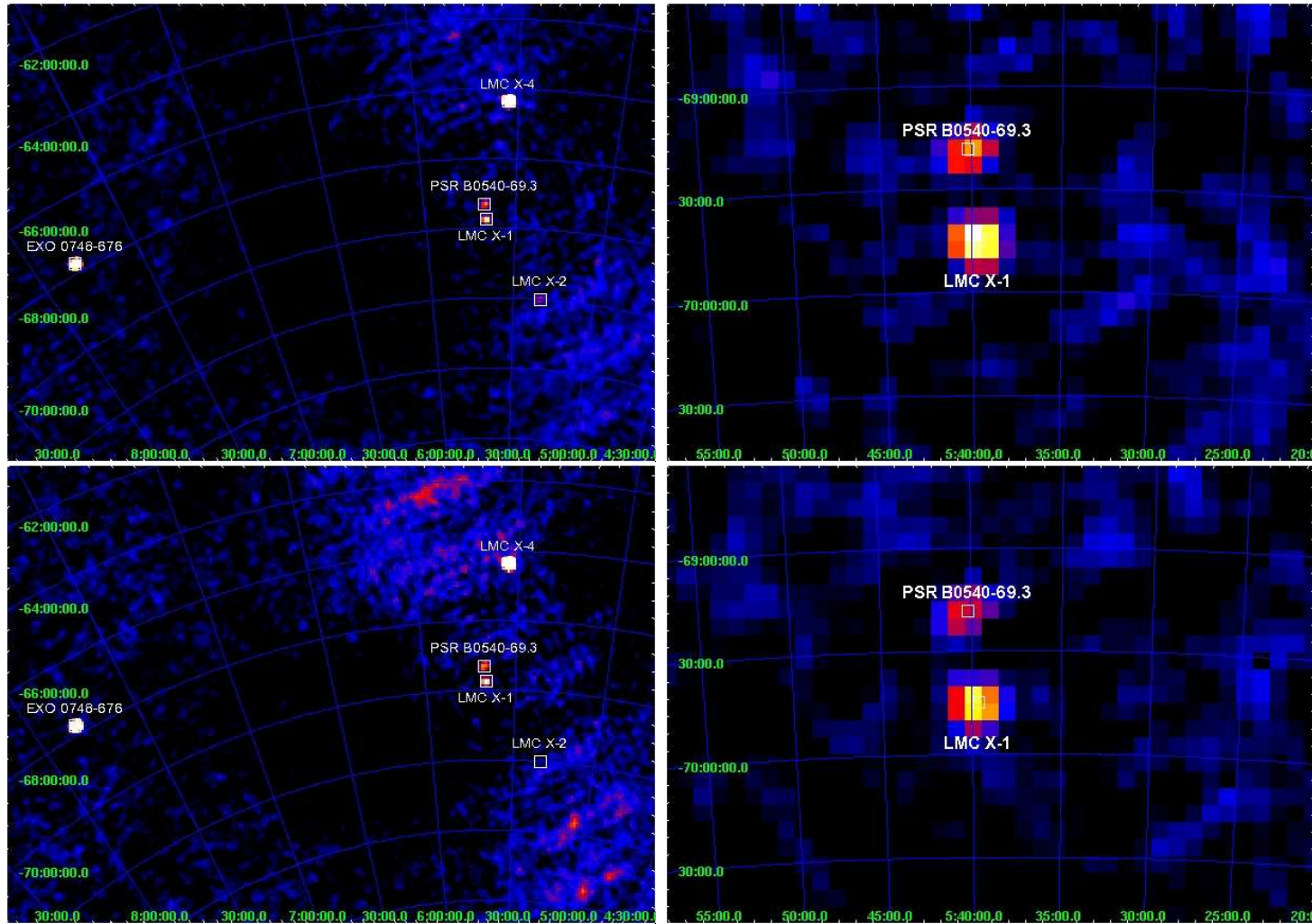


Figure 4.6: The IBIS/ISGRI significance mosaic images of the LMC region (*left*) and the close-up of the pulsar neighbourhood (*right*). Maps are for the 17–25 keV (top) and 25–40 keV (bottom) energy ranges. PSR B0540-69 was detected with following significance 13.8σ and 11.2σ , respectively.

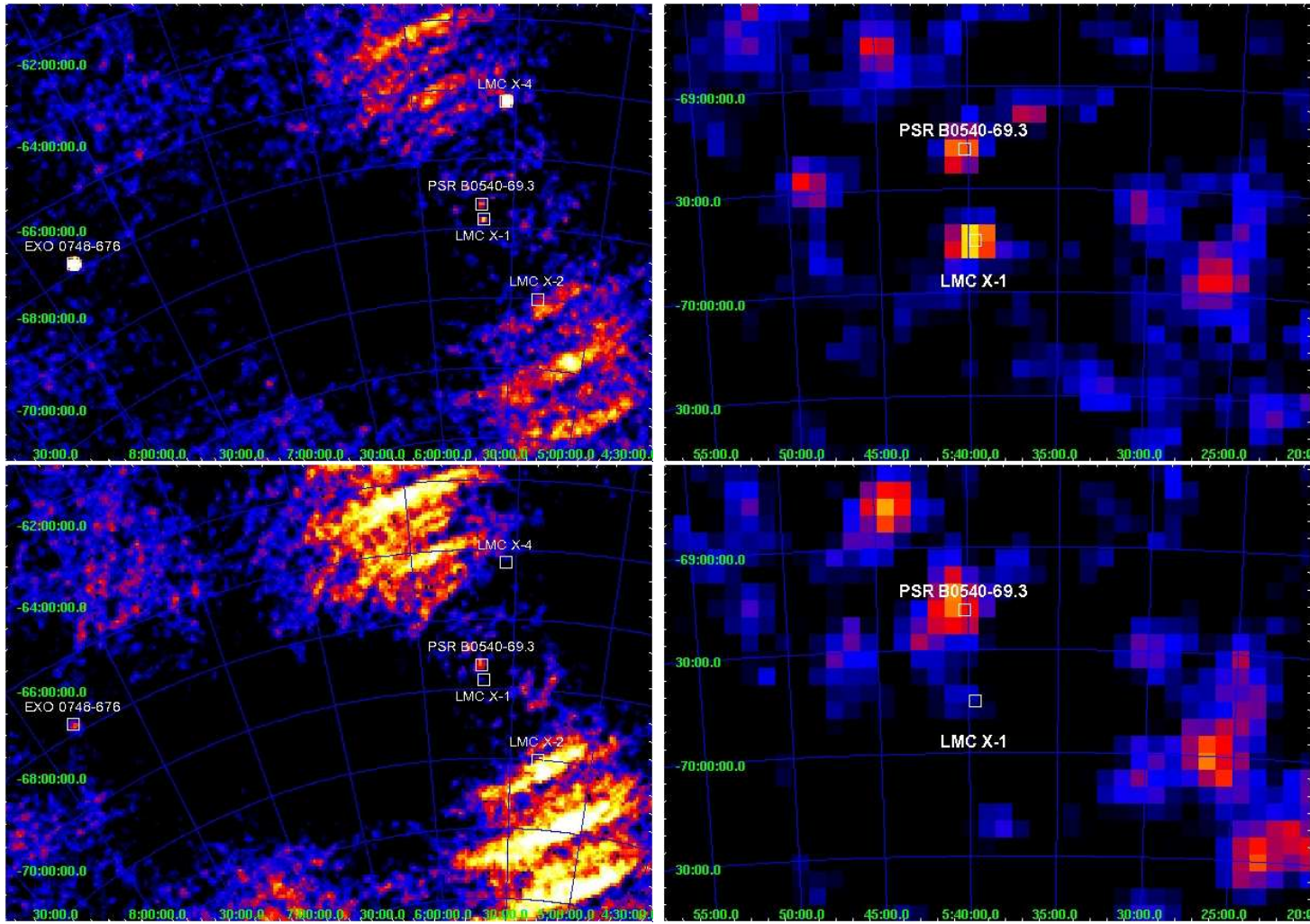


Figure 4.7: The IBIS/ISGRI significance mosaic images of the LMC region (*left*) and the close-up of the pulsar neighbourhood (*right*). Maps are for the 40–100 (top) and 100–200 keV (bottom) energy ranges. PSR B0540-69 was detected with following significance 7.6σ and 6.2σ , respectively.

4.5 JEM-X data analysis and results

Joint European Monitor for X-rays (JEM-X) operates simultaneously with the main γ -ray *INTEGRAL* instruments. It is based on the same principles as IBIS and SPI instruments: sky imaging accomplished by a coded aperture mask based on a Hexagonal Uniformly Redundant Array (HURA). Its energy range is 3–35 keV, angular resolution at FWHM is $3'$, fully illuminated field of view is 4.8° , while time resolution is on the level of $122 \mu\text{s}$ and 1 ms for relative and absolute timing, respectively. We used the data of the full imaging telemetry format only, i.e. the image resolution of the detector was 256×256 pixels, timing resolution $1/8192 \text{ s} = 122 \mu\text{s}$, and spectral resolution 256 Pulse Height Amplitude (PHA) channels. The position determination accuracy depends on the number of source and background counts and on the position in the FoV. The off-axis collimator blocks some of the source photons and beyond the fully coded FoV the coding is incomplete. There has been a shift in the position correction procedure after the beginning of the reprocessing *INTEGRAL* revision 1 data to the revision 2 at ISDC. Therefore, when using `jemx_science_analysis` we always started the analysis from the correction (COR) level, even for Rev.2 data.

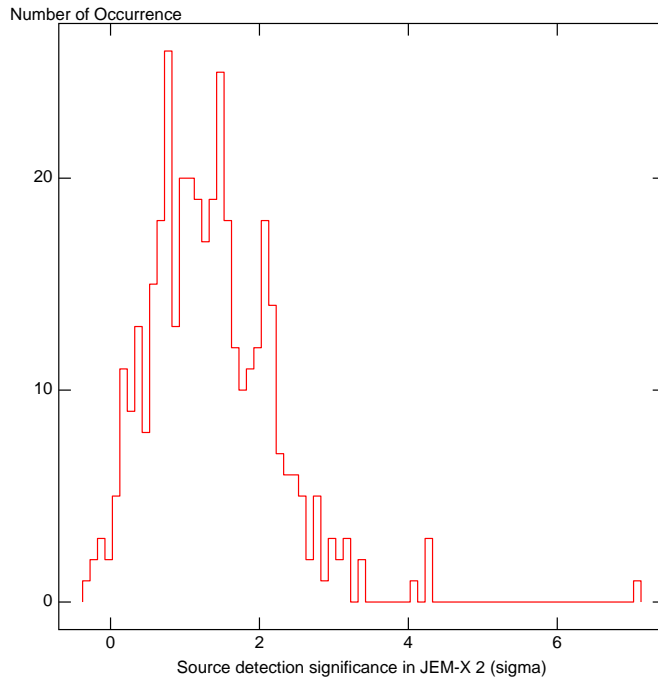


Figure 4.8: Distribution of the detection significance of PSR B0540-69.3 in 388 single JEM-X ScWs (75 bins, bin size: 0.1, minimum -0.37 , maximum 7.04 , mean 1.35 , standard deviation 0.84).

4. PSR B0540-69 - THE CRAB TWIN IN THE LARGE MAGELLANIC CLOUD

At the beginning 409 ScWs fulfilled our selection criteria for JEM-X. After first run of `jemx_science_analysis` 388 ScWs remained. Some of them showed a ‘negative selection’ error, whereas some did not have the fully coded imaging events. Similarly to the IBIS/ISGRI analysis we used the user catalogue to obtain the images and light curves of PSR B0540-69. The list of sources included during the analysis is the same as in the case of ISGRI, except EXO 0748-676. This source was not in the FoV of JEM-X during the LMC observations.

The source was not detected above the 3σ level in almost all single ScWs (Fig. 4.8). All the individual images from the different science windows gathered in the observation group can be combined in the second step of image reconstruction, and produce JEM-X mosaic images. The combined images have longer exposure time. As a consequence, weaker sources which are not visible in single ScW can appear in the mosaic images. This is the case of the PSR B0540-69, Figs. 4.9 and 4.10. The JEM-X light curves were obtained in similar way as the IBIS/ISGRI light curves. The pulsar profile in the following energy bands: 3–6, 6–10, 10–15 keV are shown in Fig. 4.4 (*left column*).

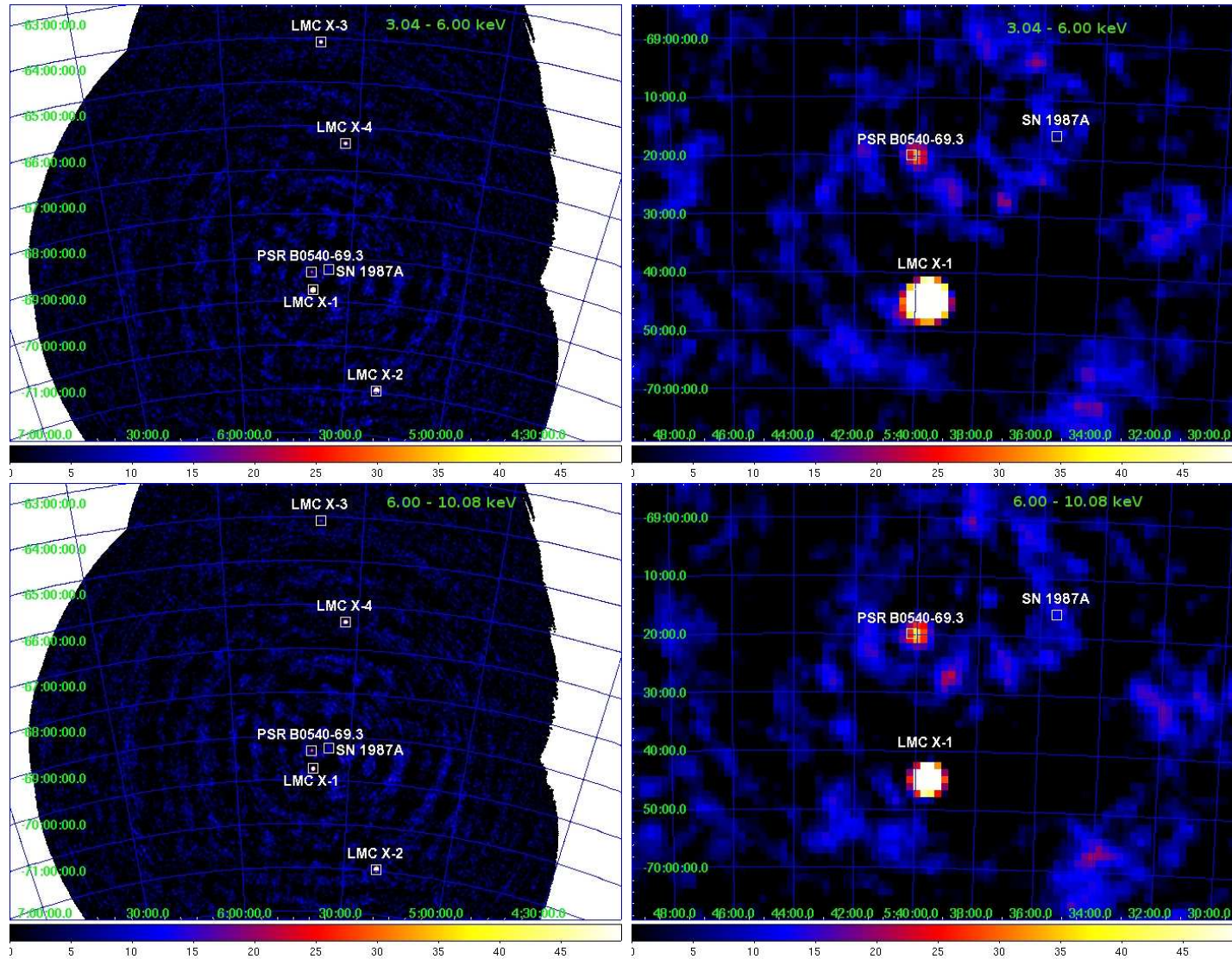


Figure 4.9: The JEM-X significance mosaic images of the LMC region (*left*) and the close-up of the pulsar neighbourhood (*right*). Maps are for the 3–6 (top) and 6–10 keV (bottom) energy range. PSR B0540-69 has been detected with following significance 32.6σ and 37.1σ , respectively.

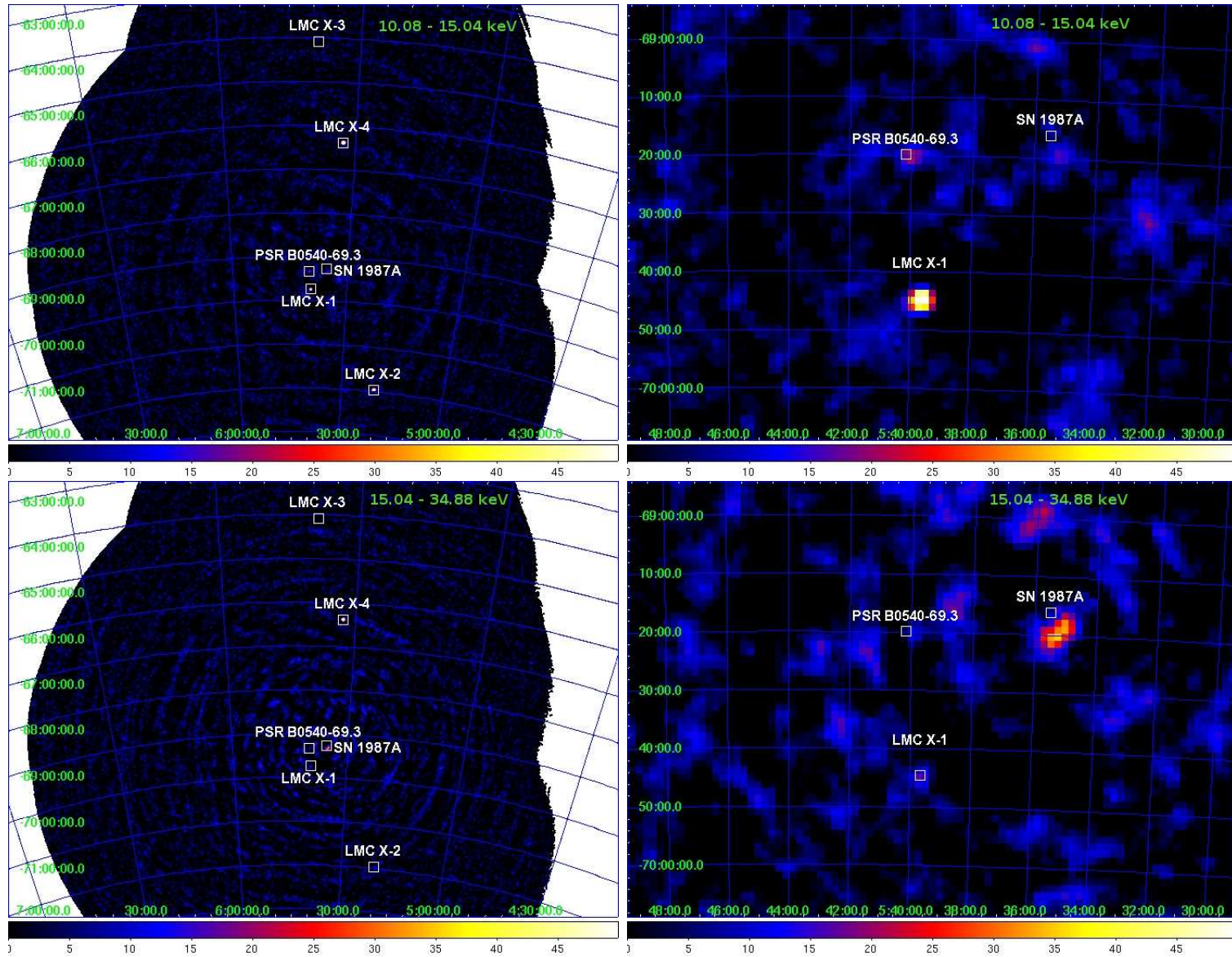


Figure 4.10: The JEM-X significance mosaic images of the LMC region (*left*) and the close-up of the pulsar neighbourhood (*right*). Maps are for the 10-15 keV (top) and 15-35 keV (bottom) energy range. PSR B0540-69 has been detected with following significance 21.9σ and 11.6σ , respectively.

4.6 Summary

The INTEGRAL analysis presented here is based on the *INTEGRAL* observations of the LMC obtained in January 2003 and 2004 with a total exposure of ~ 1.5 Ms. In the mosaic maps from the total exposure (JEM-X and IBIS/ISGRI) a source at the location of PSR B0540-69 is clearly visible up to energies of 200 keV. After barycentric correction and determination of the pulsar phases, based on the ephemeris available from contemporaneous RXTE data, the light curves show the characteristic shape of a broad pulse up into the 40-100 keV band. At higher energies no significant pulsation is detectable.

For the first time PSR B0540-69 has been detected up to ~ 200 keV with pulsations visible up to 100 keV. The total source photon spectrum can be fitted with a power law with photon index -2.2 and the flux in the range 17 – 300 keV is about 6×10^{-11} ergs $^{-1}$ cm $^{-2}$. The pulsed fraction of the total emission decreases with energy and only upper limits could be derived above 100 keV assuming a light curve profile from lower energies. [Cheng & Wei \(1995\)](#) predict in an outer gap emission model for the parameters of PSR B0540-69 a significant downturn of the synchrotron spectrum around 50 keV, which seems to be confirmed by our result.

Chapter 5

PSR B1929+10 revisited in X-rays

5.1 Introduction

Studying the thermal evolution of neutron stars by confronting observation and theory can give us an insight into the composition of matter in the stellar interior. However, our knowledge of NS interiors, the composition and equation of state of supernuclear dense matter of NS cores is uncertain and strongly model dependent. Therefore, a whole range of possible equations of state with different composition of the NS inner cores results in different cooling histories of neutron star interiors (e.g. [Lattimer & Prakash 2004](#)). NS cooling models predict that at an age of more than one million years cooling NSs become too cold to emit X-rays from their surface (e.g. [Yakovlev & Pethick 2004](#)). Hence, X-ray radiation of old (conventionally pulsars with the spin-down age greater than or equal to 1 Myr) isolated radio pulsars is expected to consist of a magnetospheric component and, possibly, a thermal component emitted from small areas at the NS surface heated by relativistic particles accelerated in the pulsar's polar cap (PC) zones. The X-ray emission of old pulsars allows to examine the properties and evolution of magnetospheric radiation, probe the particle acceleration mechanisms operating in the magnetospheres, and constrain the PC heating and emission models.

Although most of the ~ 1700 currently known radio pulsars have the calculated characteristic age greater than 1 Myr only three old, nonrecycled pulsars have been detected in the X-ray energy band up to now. First detections of PSR B1929+10 ([Helfand 1983](#)), PSR B0950+08 ([Seward & Wang 1988](#)) and PSR B0823+26 ([Sun et al. 1993](#)) were close to the sensitivity limits of the observing instruments. All mentioned objects have the spin-down age $\tau_c \geq 10^6$ yrs, magnetic fields of about $10^{11} - 10^{12}$ G, and are located in the relatively close neighbourhood, i.e. distances

of about 120–380 pc. Here we concentrate in PSR B1929+10 and the ephemeris and general characteristics for this pulsar are presented in Tab. 5.1.

Table 5.1: Pulsar characteristics of PSR B1929+10 (PSR J1932+1059).

Parameter ^a	Value
Right Ascension (J2000)	19 ^h 32 ^m 13 ^s .855
Declination (J2000)	10°59′32″.41
Validity range (MJD)	48336 – 48661
Epoch (MJD)	48498.000000419
Frequency	4.4146634668424 Hz
Frequency derivative	$-2.26475 \times 10^{-14} \text{ s}^{-2}$
Age (τ_c)	3.1 Myr
Magnetic field (B_s)	$0.5 \times 10^{12} \text{ G}$
Distance ^b	$331 \pm 10 \text{ pc}$
Spin-down luminosity (L_{sd})	$3.9 \times 10^{33} \text{ erg s}^{-1}$

^a ephemeris from [D’Amico & Nicastro \(1992\)](#), see <http://pulsar.princeton.edu/ftp/gro>

^b From parallax measurements by [Briskin et al. \(2002\)](#)

5.2 Previous results

PSR B1929+10 is one of the closest and oldest known ordinary pulsar that has been detected in X-rays. Consecutive investigations of this object in X-rays were based on ROSAT PSPC-B, ASCA SIS, combined ROSAT and ASCA, and recently *XMM – Newton* observations performed by [Yancopoulos et al. \(1994\)](#) [hereafter Y94], [Wang & Halpern \(1997\)](#) [WH97], [Słowikowska et al. \(2005b\)](#) [S05] and [Becker et al. \(2006\)](#) [B06], respectively.

Y94 used the ROSAT PSPC-B observations with exposure time of 45 ks. After background subtraction they obtained a total of 420 ± 25 photons in the 0.1–2.0 keV band. The inferred luminosity was $1.2 \times 10^{30} \text{ ergs s}^{-1}$ (i.e. 3×10^{-4} of the pulsar’s spin-down luminosity) for a source distance of 250 pc¹ with assumed opening solid angle for the radiation of 4π steradians. Furthermore, folding the barycentred arrival times of the selected events, Y94 fitted the pulse shape using a sinusoid and this yielded a pulsed fraction of 0.28 ± 0.10 (0.1–2.0 keV). The spectrum was fitted with

¹At that time the distance to the pulsars was assumed to be 250 pc

5. PSR B1929+10 REVISITED IN X-RAYS

a black-body temperature $T \approx 3.2 \times 10^6$ K assuming an absorbing hydrogen column density of $1.5 \times 10^{20} \text{ cm}^{-2}$. Hence, from simple estimation $r = (L_X/4\pi\sigma T^4)^{1/2}$, the calculated intrinsic emitting area has a radius of less than 40 m and corresponds to only $\sim 10^{-5}$ of the stellar surface area. Moreover, this radius is significantly smaller than the canonical radius of polar cap that for the pulsar parameters is ~ 300 m, with assumption that the NS radius is 10 km.

WH97 used ASCA data from October 1994 (exposure time 54 ks) and fitted the spectrum of PSR B1929+10 over the 0.5–5.0 keV range also with a single black-body. The neutral hydrogen column density was not included as a free parameter in that fit. It was fixed at $1 \times 10^{20} \text{ cm}^{-2}$. They derived a temperature of $T = (5.14 \pm 0.53) \times 10^6$ K and a bolometric flux of $1.71 \times 10^{-13} \text{ erg cm}^{-2} \text{ s}^{-1}$. The luminosity was calculated for the same distance of 250 pc used by Y94 and it amounted to $1.28 \times 10^{30} \text{ erg s}^{-1}$ in the 0.5–5.0 keV energy range. An intrinsic emitting area obtained by WH97 amounted to $3.2 \times 10^7 \text{ cm}^2$. A power law model with energy index $\alpha = 0.79 \pm 0.23$ fitted almost as well as the single component thermal model. Even though a thermal model provided better overall fits, the inferred emitting areas were surprisingly small. In the timing analysis WH97 extracted events within a 2.5 radius around the X-ray counterpart of PSR B1929+10 from both GIS 2 and 3 instruments with energies between 0.5 and 5.0 keV, and obtained 747 counts, 413 of which were estimated to belong to the background. The light curve was characterised by a single broad maximum, similar to the ROSAT soft X-ray profile, with a modulation significance of about 3.1σ , while the pulse fraction was estimated to be 0.35 ± 0.15 (0.5–5 keV).

Even though ASCA has a broader bandwidth and greater spectral resolution than ROSAT in the band near 1 keV, Wang & Halpern (1997) did not confirmed unambiguously Y94’s interpretation, because they could not conclusively distinguish between a thermal and non-thermal origin of the radiation.

5.3 Observations

In Słowikowska et al. (2005b) study we revisited the ROSAT PSPC-B and ASCA data. Moreover, we also included ROSAT HRI data from a combination of 3 observations lasting 346 ks in total, together with data from a 30 ks RXTE exposure (Tab. 5.2). The main goal was to characterise the timing and spectral properties of PSR B1929+10 in more detail using all available archive X-ray data (Tab. 5.2).

ROSAT, the Röntgen Satellite, observed PSR B1929+10 as prime target several times during its mission lifetime with either the PSPC (Position Sensitive Propor-

Table 5.2: Archival X-ray observations of PSR B1929+10.

Instrument	ROSAT			
Detector	PSPC-B	HRI		
Obs. start	30/03/91	09/10/95	02/10/96	13/04/97
Obs. end	25/04/91	07/11/95	21/10/96	28/04/97
On - Time (ks)	43.57	104.125	136.598	106.019
Instrument	ASCA		RXTE	
Detector	GIS	SIS	PCA	
Obs. start	17/10/94	17/10/94	21/11/97	
Obs. end	19/10/94	19/10/94	21/11/97	
On - Time (ks)	56.448	53.323	29.65	

tional Counter) or with the HRI (High-Resolution Imager) in the focal plane. In this study we used all available ROSAT data i.e. observations with the PSPC-B (30 March 1991 – 25 April 1991; 43.6 ks exposure) and with the HRI, which pointed three times at PSR B1929+10 for a total combined exposure of 346.7 ks, see Tab. 5.2. These HRI acquisitions were taken between 9th October and 7th November 1995 for 104.1 ks, between 2nd and 21st October 1996 for 136.6 ks, and between 13th and 28th April 1997 for 106.0 ks. The standard correlation between the ROSAT spacecraft clock and UTC does not permit absolute timing of the events down to millisecond accuracy (see Appendix B).

Two more datasets for PSR B1929+10 were available from the Advanced Satellite for Cosmology and Astrophysics (ASCA) and the Rossi X-ray Timing Explorer (RXTE), see Tab. 5.2. Our target was observed by ASCA between 17th and 19th October 1994 with exposure times 56.5 and 53.3 ks for the GIS (Gas Imaging Spectrometer) and the SIS (Solid-state Imaging Spectrometer), respectively. To support timing analyses at millisecond scales only data from the high and medium rate telemetry modes of GIS can be used. From RXTE we used PCA (Proportional Counter Array) data taken on 21st November 1997. The instrument operated in Good Xenon mode for 29.65 ks. PCA comprises five identical co-aligned gas-filled proportional counter modules. Each module is referred to as a PCU (Proportional Counter Unit), numbered from 0 to 4. The absolute systematic uncertainty of the RXTE/PCA event times in TDB is estimated to be $\pm 5 \mu\text{s}$ after MJD 50567 (1997 April 29 UT) and

5. PSR B1929+10 REVISITED IN X-RAYS

$\pm 8 \mu\text{s}$ prior to MJD 50567 ¹.

5.4 Timing analysis

5.4.1 ROSAT PSPC-B

Point-like X-ray emission was clearly detected from the vicinity of the radio position of the pulsar ($\alpha_{2000} = 19^{\text{h}}32^{\text{m}}13^{\text{s}}.922$, $\delta_{2000} = 10^{\circ}59'32''.07$; Pavlov et al. 1996) on the ROSAT PSPC-B Maximum Likelihood Ratio map (MLR map, see e.g. Kuiper et al. 1998). The numbers of source and background counts are derived simultaneously by this method. In the timing analysis we extracted events within an optimum radius (the radius where the signal-to-noise ratio S/N maximises) of $50''$ from the X-ray centroid. The time tags of the 604 events (energy range 0.1–2.5 keV) falling within this radius have subsequently been barycentred and folded using appropriate pulsar parameters (Tab. 5.1) to obtain the pulse-phase distribution shown in the left panel of Fig. 5.1. The profile is characterised by one broad maximum and deviates from a statistically flat distribution at a 4.2σ level applying a Z_1^1 method (Buccheri et al. 1983). The sinusoidal shape of X-ray pulse profile is in sharp contrast to the strongly peaked radio profile.

In order to quantify the pulsed fraction we have applied two methods, one based on bootstrapping (Swanepoel et al. 1996) and another based on sinusoid fitting. For broad sinusoidal profiles it is expected that the bootstrap method will systematically underestimate the genuine pulsed fraction because parts of the leading and trailing wings of the broad profile are considered to be part of the interval used to construct the unpulsed level. Applying the bootstrap method we obtain a pulsed fraction defined as $f_{\text{pulsed}} = \frac{N_{\text{P}}}{N_{\text{P}} + N_{\text{DC}}}$ of 0.24 ± 0.07 . The number of pulsed counts N_{P} follows directly from the bootstrap method, while the number of DC source counts (N_{DC}) requires an estimate of the number of background counts within the extraction radius of $50''$. From the MLR map we could estimate that 140.5 ± 2.2 background counts are expected within the extraction radius (see corresponding background level in Fig. 5.1, *left panel*).

Because the pulse profile shows one broad maximum, sinusoid fitting using one harmonic provides an adequate description of the measured distribution. Applying sinusoid fitting to the 0.1–2.5 keV PSPC-B pulse profile (see Fig. 5.3, *left panel*) we find a pulse fraction of 0.36 ± 0.08 which is indeed slightly higher than the bootstrap

¹<http://heasarc.gsfc.nasa.gov/docs/xte/abc/time.html>

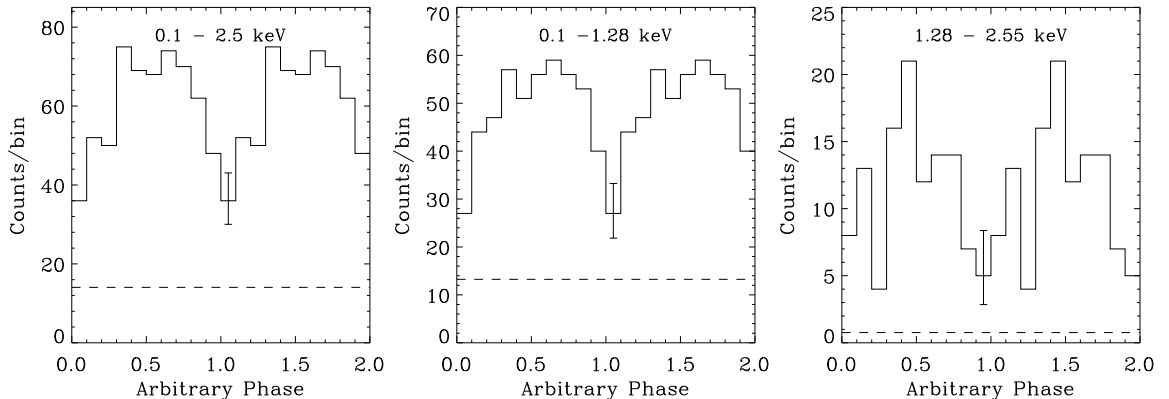


Figure 5.1: PSR B1929+10 phase histograms from ROSAT PSPC-B data in three energy ranges, *left panel*: 0.1–2.5 keV, *middle panel*: 0.1–1.28 keV, *right panel*: 1.28–2.5 keV. Two cycles are shown for clarity. A typical error bar is shown on each panel. The significances for deviations from statistically flat distributions are 4.15σ (604 events), 3.0σ (490 events), 3.0σ (114 events), respectively. The background levels, as determined from spatial analyses, are presented as dashed lines.

result, but at the same time still consistent with the value found earlier by Y94 (0.28 ± 0.10).

By selecting the events further on energy we applied the same sinusoid fitting method to the 0.1–1.28 keV and 1.28–2.5 keV pulse profiles. These two profiles are shown in Fig. 5.1, *middle panel* is for 0.1–1.28 keV energy interval and *right panel* for higher energy range, 1.28–2.5 keV. For both light curves the modulation significance amounts to 3.0σ , while the pulsed fractions are 0.33 ± 0.09 and 0.42 ± 0.13 , respectively. These values are the same within their statistical uncertainties. We compared the shapes of the 0.1–1.28 keV and 1.28–2.5 keV light curves by applying a χ^2 -test (Zavlin & Pavlov 1998):

$$\chi^2 = \sum_{i=1}^N \frac{(mn_i - nm_i)^2}{m^2n_i + n^2m_i}, \quad (5.1)$$

where N is the number of the phase bins, n_i and m_i are the numbers of counts in the i -th bin for the two light curves, and n and m are the sum of n_i and m_i , respectively. This equation implies that the relative errors (e.g., $\sigma_i^{(n)}/n_i$) remain constant when the original light curves are scaled for comparing their shapes. The analysis showed that for those two light curves $\chi^2 = 17.66$ for 9 degrees of freedom. Hence, the reduced χ^2 of 1.96 implies the possibility that the pulse shape changes with energy ($\lesssim 3\%$ probability for being the same). Moreover, recent findings of Becker et al. (2006) confirm the pulse profile dependence on energy. The fraction of

5. PSR B1929+10 REVISITED IN X-RAYS

pulsed photons derived from the *XMM Newton* observations in the 0.2–10 keV band is $32 \pm 4\%$. Within narrower energy ranges 0.2–1.0, 1.0–2.1 and 2.1–10 keV the pulsed fraction was found at the level of $24 \pm 5\%$, $44 \pm 6\%$ and $17 \pm 17\%$, respectively.

At the same time, similar behaviour has been observed by [Zavlin & Pavlov \(2004, hereafter ZP04\)](#) using the latest *XMM-Newton* data for another old pulsar emitting pulsed X-rays, PSR B0950+08. They showed that for this pulsar both the pulse shape and the pulsed fraction change with energy. In their work the light curve of PSR B0950+08 is presented in four energy bands: 0.2–0.5, 0.5–1.0, 1.0–5.0 and 0.2–5.0 keV. The pulsed fractions for these energy ranges are $33 \pm 18\%$, $60 \pm 13\%$, $57 \pm 13\%$ and $41 \pm 10\%$, respectively. For energies above 0.5 keV the pulse profile consists of two relatively narrow peaks with a high pulsed fraction ($\approx 60\%$), which points to a non-thermal magnetospherical origin of the X-ray emission. The lower energy light curve shows a broad single pulse with a lower pulsed fraction of about 33%. ZP04 claim that this energy dependence can be explained by the presence of another, most likely thermal, component.

5.4.2 ROSAT HRI

For the three long ROSAT HRI observations the timing analysis consisted in extracting the events from an $11''$ aperture around the centroid of the PSR B1929+10 counterpart and subsequently folding the barycentred event times using an appropriate pulsar ephemeris. The obtained, separately for each observation, pulse profiles (Fig. 5.2 shows *left, middle and right panels* for the following time spans of the data acquisitions 9 Oct–7 Nov 1995, 2–21 Oct 1996 and 13–28 Apr 1997, respectively) have all a low modulation significance, between 2 and 3σ , although the broad bump can easily be discerned in all three light curves.

On account of the absolute timing limitations (see Appendix B) we cross-correlated each of the three HRI profiles with the 0.1–2.5 keV PSPC-B profile. In the cross-correlation procedure we used the light curves binned into 360 bins. This means that the width of a single bin corresponds to $629 \mu\text{s}$. The obtained shift values were as follow 0.615, 0.395 and 0.525 for the first, second, and third HRI acquisitions, respectively. After applying the phase shifts the combination of the three separate profiles yielded a phase distribution which deviates from a flat distribution at the 3.7σ level (Fig. 5.3, *middle panel*)¹. In this case the sinusoid fitting method yielded a pulsed fraction of 0.21 ± 0.05 , lower, but still consistent with the PSPC-B value. The

¹see Appendix B for the results from a different approach involving event TDB timestamp folding using just one single ephemeris for the combination of the three HRI observations

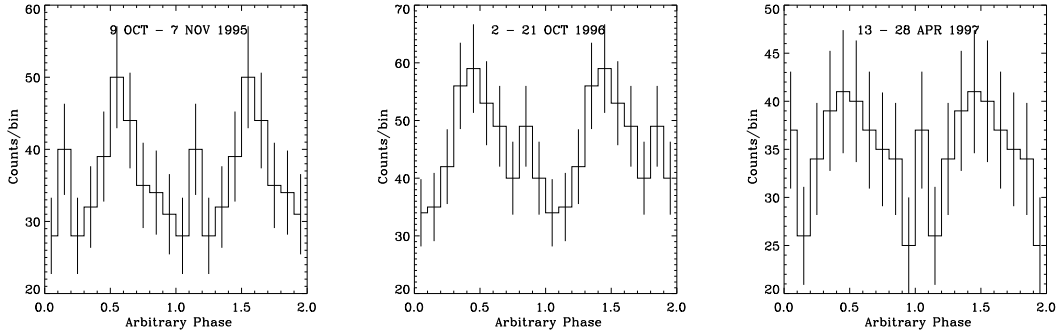


Figure 5.2: PSR B1929+10 phase histograms from ROSAT HRI data for three different acquisitions of which the observing time span is given at the top of each panel. Two cycles are shown for clarity. Error bars are shown in each panel. The significance for a deviation from a statistically flat distribution is about 2σ for each of these three datasets.

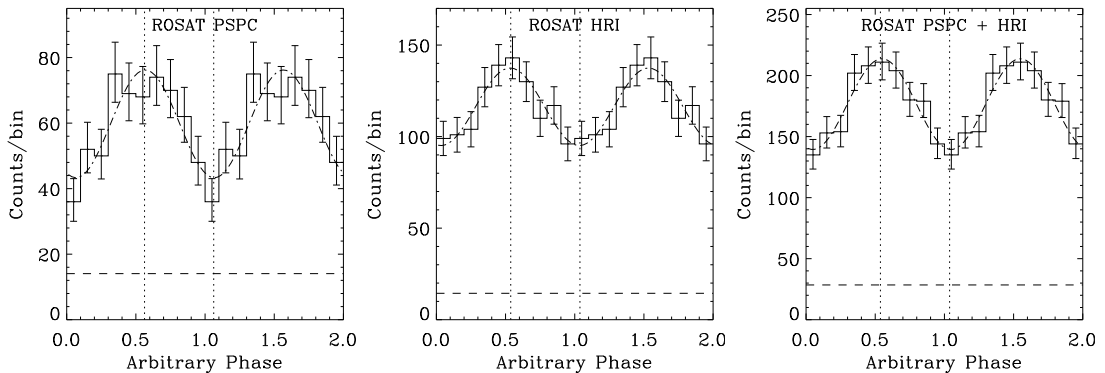


Figure 5.3: Light curves for the ROSAT PSPC-B and HRI observations of PSR B1929+10. *Left panel:* only PSPC-B (0.1–2.5 keV), *centre panel:* only HRI (0.1–2.4 keV), *right panel:* combined PSPC-B and HRI. Two cycles are shown for clarity. Error bars are shown in each panel. The significances for deviations from statistically flat distributions are 4.15σ , 3.7σ and 5.6σ , respectively. The dashed horizontal lines indicate the background levels determined from spatial analyses. The vertical dotted lines correspond to minimum and maximum phases of the sinusoid fits (the dot - dashed curves).

combined ROSAT PSPC-B and HRI profile is shown in the right panel of Fig. 5.3, and it deviates from being flat at a 5.6σ level. The pulsed fraction of this profile amounts to 0.25 ± 0.04 .

5.4.3 ASCA GIS

Of the two detector systems aboard ASCA only the GIS detectors have sufficient timing resolution to support timing analyses at millisecond scales. Data from the

5. PSR B1929+10 REVISITED IN X-RAYS

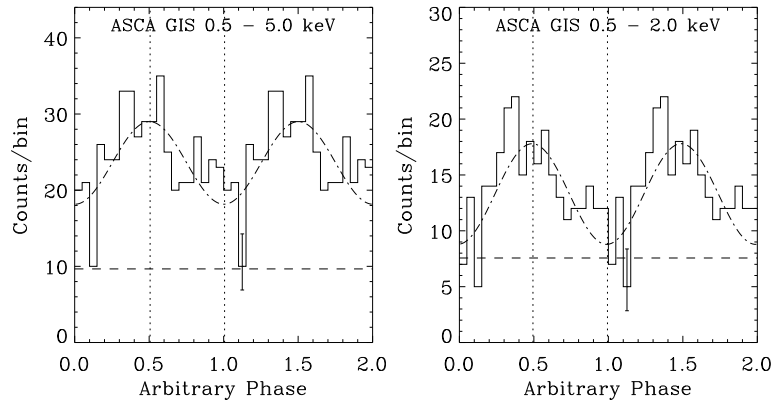


Figure 5.4: The ASCA profiles of PSR B1929+10 in two energy intervals: *left panel* 0.5–5.0 keV (significance 2.7σ , 493 events) and *right panel* 0.5–2.0 keV (significance 3.1σ , 282 events). The dot - dashed curves indicate the sinusoid fitted to the data, while the vertical dotted lines correspond to the minimum and maximum phases of the fits. In both panels the horizontal dashed lines indicate the background levels determined from spatial analyses. A typical error bar is shown in each panel. Two cycles are shown for clarity.

high and medium rate telemetry modes were used. The 3.9 ms timing resolution valid for these rates was sufficiently accurate to sample the pulse period of 227 ms (see Tab. 5.1). In the spatial analysis a Maximum Likelihood method, similar to that used for the ROSAT PSPC-B and HRI data, provided the optimum position for the X-ray counterpart of PSR B1929+10. An extraction radius of $130''$ from this position was found to optimise the S/N ratio. In the 0.5–5 keV energy interval, the same as used by WH97, 493 event time tags were barycentred and subsequently folded through appropriate timing parameters to yield the corresponding pulse profile. This profile is shown in Fig. 5.4 *left panel* and deviates from uniformity at a 2.7σ level. The same broad enhancement is visible as in the ROSAT profiles at softer X-ray energies. Constraining the energy to the 0.5–2.0 keV interval (282 events), fully overlapping the ROSAT energy window, yielded a significance of 3.1σ (see Fig. 5.4 *right panel*). Note, that in the 2.0–5.0 keV energy range (211 events) the profile is consistent with being flat, which means that the main contribution to the pulsed fraction comes from photons with energies lower than 2 keV. The pulsed fractions derived from sinusoid fitting for the integral (0.5–5 keV) and the ROSAT overlapping (0.5–2.0 keV) energy ranges are 0.36 ± 0.11 and 0.69 ± 0.18 , respectively. The latter value is high, but because of its large error it is still consistent with the ROSAT numbers, especially in comparison with the high pulsed fraction of 1.28–2.55 keV PSPC-B light curve (0.42 ± 0.13).

Moreover, we can compare our results with those for PSR B0950+08 presented by ZP04. In the energy band 0.2–5.0 keV, fully overlapping the ASCA band, they got a pulsed fraction of $41 \pm 10\%$, while for 0.5–1.0 keV band it increased to 60%. Hence, we argue that the overall situation with respect to the energy dependency of the pulsed fraction is very similar for both pulsars.

5.4.4 RXTE PCA

Finally, we have analysed RXTE PCA (2–60 keV) data from a 30 ks observation of PSR B1929+10 (Obs. id. 20156; 21–Nov–1997) obtained in Good Xenon mode, time tagging each event with a $0.9 \mu\text{s}$ time resolution. For the timing analysis we used `fasebin` program belonging to the `FTOOLS`¹ package to select events from the top layer of each involved PCU, consequently to barycentre the times of the selected events, and finally to fold the barycentred event times with an appropriate ephemeris.

Table 5.3: Observed parameters for the radio pulsar B1929+10 based on radio observations made at the Toruń Radio Astronomy Observatory. The numbers in parentheses represent uncertainties in the least significant digits.

Parameter & Value	Value
Right Ascension	$19^{\text{h}}32^{\text{m}}13^{\text{s}}.924(1)$
Declination	$10^{\circ}59'32''.44(2)$
Validity range (MJD)	50608–50959
Epoch (MJD TDB)	50700.0
Frequency	4.4146591771439(133) Hz
First frequency derivative	$-2.26596(64) \times 10^{-14} \text{ Hz s}^{-1}$
Second frequency derivative	$3.91(84) \times 10^{-24} \text{ Hz s}^{-2}$

The ephemeris used in the folding procedure within `fasebin` was derived from the regular pulsar radio timing measurements with 32m Toruń Centre for Astronomy radio telescope. During Toruń pulsar timing observations a dual-channel, circular polarisation L-band receiving system at frequencies around 1.73 GHz and a $2 \times 64 \times 3$ MHz pulsar back-end, the Penn State Pulsar Machine 2 (PSPM-2 [Konacki et al. 1999](#)), are used. Data analysis was performed with the standard `TEMPO`² software package. To check occurrence of any timing irregularities broad range of data was used. Time span covers almost five years, i.e. from Jun, 8th 1997 up to Jun, 1st 2002 and that

¹<http://heasarc.gsfc.nasa.gov/lheasoft/ftools/>

²<http://pulsar.princeton.edu/tempo>

5. PSR B1929+10 REVISITED IN X-RAYS

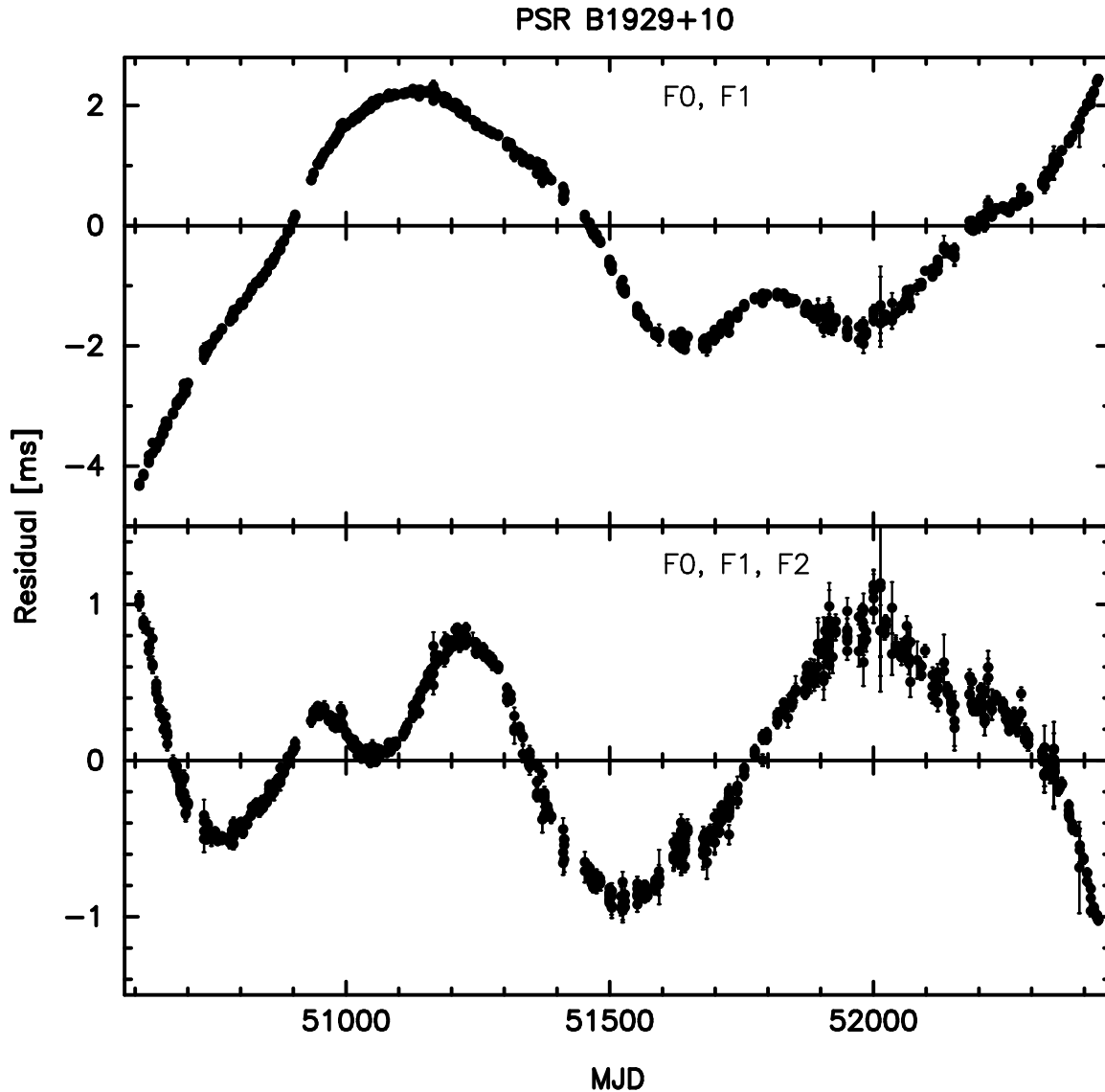


Figure 5.5: Residuals of PSR B1929+10 radio timing data. In the applied model pulsar positional and rotational parameters were fitted. *Upper* panel shows residuals after including rotational frequency and its first derivative in the model, whereas *bottom* panel shows residuals obtained by including the second-order frequency derivative in the timing model fitting process. Timing noise is clearly visible.

corresponds to 50607–52426 MJD (Fig. 5.5). In the applied model the pulsar position and its rotational parameters, as well as the reference phase of the first observed pulse TOA (time of arrival) were fitted. Results are shown in Fig. 5.5. In the first case only the frequency, and its first derivative were fitted (*upper* panel), whereas later the second frequency derivative was set as an additional free parameter (*bottom* panel). In both cases pulsar timing noise is clearly visible.

Therefore, to derived reliable ephemeris to fold the RXTE counts we restricted

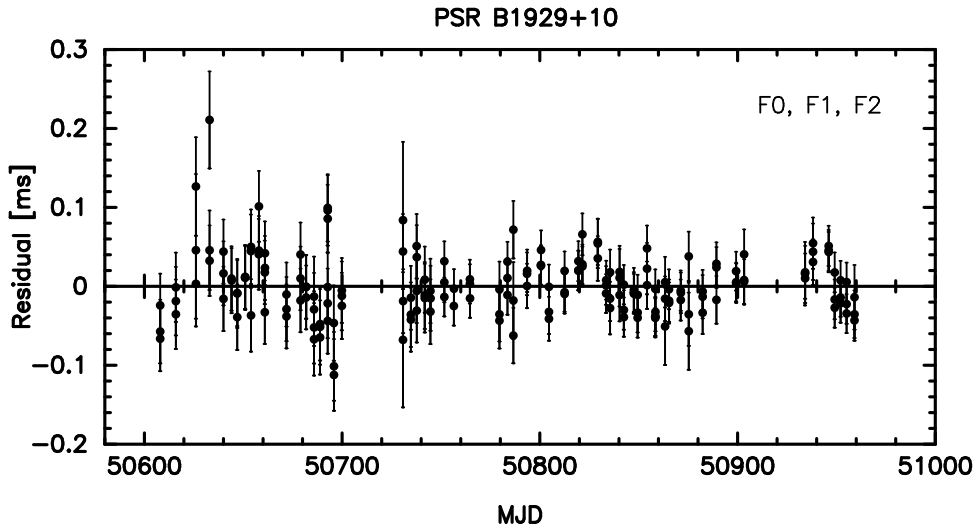


Figure 5.6: The same as in *bottom* panel of Fig. 5.5. The fit was performed for the restricted time span of the data ranging to one year. We got $\chi^2 = 194.48$ for 181 degrees of freedom, and RMS at the level of $32.15\mu s$.

the time span to one year chosen in a way that the Nov, 21st 1997 (50773 MJD) fell approximately in the middle of this range. By using TEMPO procedure to fit the model parameters to selected TOAs the ephemeris in the CGRO format were derived. Residuals are shown in Fig. 5.6, whereas astrometric and rotational parameters of PSR B1929+10 obtained from Torun radio timing are presented in Tab. 5.3.

The folding procedure embedded in *fasebin* resulted in pulse phase histograms for each of the 256 PHA channels. Unfortunately, in none of the PHA channels or channel intervals (2–4, 4–8, 8–16, 16–32 keV) significant pulsed emission has been detected. The lack of detection might be caused by rather short exposure time.

5.5 Comparison of the X-ray and radio profile

Five intensity profiles as a function of radio frequency are shown in Fig. 5.7 (Kramer et al. (1997) and von Hoensbroech & Xilouris (1997)). They were obtained from the public data base maintained by the European Pulsar Network¹. The radio pulse profile of PSR B1929+10 consists of two pulses separated by 0.5 in phase: a multi-component main pulse (for its detailed studies see Weisberg et al. (1999)) and a much weaker inter pulse (Fig. 5.7). According to the the standard pulsar model (Ruderman & Sutherland 1975) the integrated pulse width is expected to decrease monotonically with frequency. This suggests that higher radio frequencies are emitted in the lower

¹<http://www.mpifr-bonn.mpg.de/pulsar/data/>

5. PSR B1929+10 REVISITED IN X-RAYS

regions of the pulsar magnetosphere, i.e. closer to the surface of the neutron star. This phenomenon, called the radius to frequency mapping (RFM), is well established. The multifrequency observations of pulsars have confirmed the narrowing of pulse profiles with frequency. [Weisberg et al. \(1999\)](#) discuss extensively radio multifrequency observations.

During our (S05) data analysis we did not perform a comparison between radio and X-ray pulsar light curves, because in the first case (i.e. for the ROSAT and ASCA data) we did not have radio observations that would have allowed us to obtain the corresponding radio profiles. Moreover, ROSAT observations do not permit absolute timing ([Appendix B](#)). In the second case, i.e. the RXTE observations, we were unlucky again. This time we possessed the required radio information, but we did not find any significant pulsed signal from the high energy data. So far the only absolutely phase aligned radio and X-ray pulsar profiles are presented in [Fig. 7](#) in recent publication of [Becker et al. \(2006\)](#). We reproduce this as [Fig. 5.8](#).

The sinusoidal shape of X-ray pulse profile is in sharp contrast to the strongly peaked radio profile. In B06 the 0.2–10 keV *XMM – Newton* pulse profile of PSR B1929+10 is shown together with a radio profile observed at 1.4 GHz. The high energy profile reveals a significant deviation from a sinusoidal pulse shape. The X-ray pulse profile consists of at least two pulse peaks: a broader component and a narrow one. The broader component appears to have substructures that look like two narrower pulse peaks, not fully resolved even in the *XMM – Newton* data. The second main component, i.e. the narrow peak, appears at energies ≥ 1 keV. Some indication of such behaviour has been already shown by us in the ROSAT PSPC-B data ([Fig. 5.1](#), *left* panel), but with low statistics. Moreover, this narrow X-ray component appears to be slightly phase shifted from the location of the main radio peak, although both components overlap reasonably well in phase.

5.6 Spectral analysis

By studying the X-ray spectrum and temporal modulation of this and other similar objects, we hope to learn about the origin of the X-ray emission. If the spectrum is thermal and the projected area is small relative to that of the star, we conclude that there is a “hot-spot” on the neutron star surface. If the spectrum is non-thermal, it might be an indication of magnetospheric emission.

In the spectral analysis we first derived the total (= pulsed plus DC) number of counts assigned to the X-ray counterpart of PSR B1929+10 in several narrow

Table 5.4: Fits to the combined ROSAT and ASCA spectrum in the energy range 0.1–10 keV.

Parameter	Power Law Fit
C^a	$6.41_{-0.4}^{+0.4} \times 10^{-5}$
α	$2.54_{-0.13}^{+0.12}$
N_H	$9.8_{-1.0}^{+1.4} \times 10^{20} \text{ cm}^{-2}$
χ^2_ν	1.146/27
Parameter	Double Black-Body Fit
C_1^b	$0.0117_{-0.0018}^{+0.0017}$
kT_1	$0.176_{-0.004}^{+0.004} \text{ keV}$
C_2^b	$7.879_{-1.26}^{+1.32} \times 10^{-5}$
kT_2	$0.595_{-0.03}^{+0.02} \text{ keV}$
N_H	$4.43_{-1.12}^{+2.08} \times 10^{20} \text{ cm}^{-2}$
χ^2_ν	1.132/25

^a Normalisation at 1 keV ($\text{ph cm}^{-2} \text{ s}^{-1} \text{ keV}^{-1}$)

^b BB normalisation ($\text{ph cm}^{-2} \text{ s}^{-1} \text{ keV}^{-3}$)

energy slices using a spatial (MLR) analysis which takes into account the presence of nearby sources. We applied this approach to the ROSAT PSPC-B (20 energy bins in the interval 0.1–2.5 keV) and ASCA GIS 2+3 (10 energy bins in the interval 0.5–10 keV) data. In contrary to WH97 we chose for ASCA the GIS data, because the GIS sensitivity is higher than the SIS sensitivity for energies beyond ~ 5 keV and because of uncertainties in the SIS efficiency for energies below 1 keV. In the combined ROSAT PSPC-B and ASCA GIS 2+3 spectral fits we used the latest upgrades for the response matrices and we took into account the vignetting corrections for the 3/7 off-axis ASCA observation.

The spectral models fitted to the combined data set consist of an absorbed single power law (PL), an absorbed single black-body, an absorbed black-body plus power law and an absorbed double black-body (BB). The best fits were obtained for an absorbed single power law (Fig. 5.9, *upper panel*) and an absorbed double black-body model (Fig. 5.9, *lower panel*). The fit results for these two cases, each with a free hydrogen column density, are shown in Table 5.4.

We found that the PL model fits the data almost as well as the double BB model, yielding the photon index $\alpha = 2.54_{-0.13}^{+0.12}$ and the absorbing hydrogen column density

5. PSR B1929+10 REVISITED IN X-RAYS

$N_{\text{H}} = 9.8_{-1.0}^{+1.4} \times 10^{20} \text{ cm}^{-2}$. Then the derived flux f in the range 0.1–10 keV amounts to $(6.05 \pm 0.49) \times 10^{-13} \text{ erg cm}^{-2} \text{ s}^{-1}$. Together with a distance d of $331 \pm 10 \text{ pc}$ adopted from (Briskin et al. 2002) it implies an isotropic X-ray luminosity, $L_{\text{X}}(0.1 - 10 \text{ keV}) = 4\pi d^2 f$, of $(7.9 \pm 0.8) \times 10^{30} \text{ erg s}^{-1}$. From recent VLBA parallax measurements, Chatterjee et al. (2004) obtained an even larger distance of $361_{-8}^{+10} \text{ pc}$, which would change our 0.1–10 keV isotropic luminosity to $(9.4 \pm 0.9) \times 10^{30} \text{ erg s}^{-1}$. The 0.1–10 keV isotropic X-ray luminosity represents 2×10^{-3} of the spin-down power \dot{E} (see Table 1) of PSR B1929+10 for the 331 pc distance estimate. For the 0.1–2.4 keV band we obtain an isotropic X-ray luminosity of $(7.1 \pm 0.7) \times 10^{30} \text{ erg s}^{-1}$ which translates to $L_{\text{X}}(0.1 - 2.4 \text{ keV})/\dot{E}$ ratio of 1.8×10^{-3} . This value is compatible with e.g. the $(L_{\text{X}}(0.1 - 2.4 \text{ keV}), \dot{E})$ empirical relation found by Seward & Wang (1988): $\log L_{\text{X}} = 1.39 \log \dot{E} - 16.6$ and later confirmed by Verbunt et al. (1996): $L_{\text{X}} \approx 10^{-3} \dot{E}$.

In the case of the double black-body model we are dealing with two different thermal X-ray components with temperatures $2.0_{-0.05}^{+0.05} \times 10^6 \text{ K}$ and $6.9_{-0.35}^{+0.23} \times 10^6 \text{ K}$ for T_1 and T_2 , respectively. For the characteristic age of PSR B1929+10 ($\tau \simeq 3.1 \text{ Myr}$) cooling models predict a surface temperature of the neutron star to be $\leq 10^5 \text{ K}$, much too low to be responsible for the observed X-ray spectrum of PSR B1929+10. However, a plausible explanation could be that the observed X-ray radiation originates from a heated polar cap characterized by two different thermal components (see e.g. Cheng & Zhang 1999). The simultaneous double BB fit to the ROSAT and ASCA data implies emission luminosities of $L_1 = (1.56 \pm 0.25) \times 10^{30} \text{ erg s}^{-1}$ and $L_2 = (1.47 \pm 0.25) \times 10^{29} \text{ erg s}^{-1}$ for T_1 and T_2 components, respectively. The derived luminosities allow us to calculate the areas A of the emitting regions responsible for the detected X-rays. Following the simple estimations for the area $A = L_{\text{X}}/\sigma T^4$ we obtain the following numbers: $A_1 = 1.72 \times 10^9 \text{ cm}^2$, $A_2 = 1.13 \times 10^6 \text{ cm}^2$ for the 2 MK and 7 MK black-body components, respectively. The A_1 and A_2 values as measured at the NS surface have to be corrected for the gravitational redshift (g_r) relating the areas derived from observations and the intrinsic emitting areas on the star. The gravitational redshift is described by the relation

$$g_r = (1 + z)^{-1} = \left[1 - \frac{2GM}{c^2 R_{\text{NS}}} \right]^{1/2}, \quad (5.2)$$

and for the canonical values $M = 1.4M_{\odot}$ and $R_{\text{NS}} = 10 \text{ km}$ it amounts to 0.766. Because $A_{\text{int}} = A g_r^2$ we obtained $A_{\text{int},1} = 1.01 \times 10^9 \text{ cm}^2$ and $A_{\text{int},2} = 6.69 \times 10^5 \text{ cm}^2$.

The derived areas correspond to only $\sim 0.8 \times 10^{-4}$ and $\sim 5.3 \times 10^{-8}$ of the stellar surface, assuming $R_{\text{NS}} = 10 \text{ km}$. On the other hand, we also compare the emitting

areas to the canonical polar cap size. It is defined by the locus of the last closed dipole field line (e.g. Michel 1991). For the parameters of PSR B1929+10 the intrinsic polar cap area is

$$A_{PC} = \frac{2\pi^2 R_{NS}^3}{cP} = 2.9 \times 10^9 \text{ cm}^2, \quad (5.3)$$

where P is the pulsar period, and R_{NS} was assumed to be 10 km. The derived $A_{int,1}$, and $A_{int,2}$ values are smaller by only a factor of 3 and significantly smaller ($\sim 2 \times 10^{-4}$) than A_{PC} area in the low- and high-temperature component case, respectively. This shows that for thermal emission model, the X-ray emission area of PSR B1929+10 is roughly consistent with the conventional size of a heated polar cap. The discrepancy between $A_{int,1}$ and A_{PC} of the factor of 3 can be realistic if we consider the complicated distribution of the magnetic field on the surface of a neutron star, distortion of the surface black-body spectrum due to propagation of the radiation through a pulsar magnetosphere and the beam solid angle.

In conclusion, for thermal interpretation the result means that the observed X-ray emission does not have its origin in the cooling emission from the entire surface of the neutron star, because the implied temperature is unexpectedly high for such an old pulsar. Furthermore, the derived emitting area is extremely small in comparison to the NS surface area.

5.6.1 High value of the neutral hydrogen column density

The N_H value obtained from the double BB fit is about four and that obtained from the PL-fit about eight times larger than the N_H value used by Y94 and WH97. In both cases the newly derived column densities are consistent with the updated (radio) distance determined by Brisken et al. (2002) from VLBA data, and the hydrogen distribution measured in the direction of the pulsar (Frisch & York 1983). Additionally, as Pavlov et al. (1996) have already mentioned, values of N_H obtained from the direct measurements of stars in the neighbourhood of the pulsar are rather controversial. They differ from $\lesssim 10^{19}$ up to 10^{21} cm^{-2} . This behaviour is illustrated in Fig. 5.10. The presented data, gathered in Tab. 5.5, were obtained using the ISM hydrogen Column Density Search Tool ¹ available on the Extreme Ultraviolet Explorer (EUVE) web page. For further discussion we will concentrate on only five out of the ten selected sources from the EUVE database nearest to PSR B1929+10. These are: σ Aql, ϵ Del, o Her, WD1910+047 and ES Vul. The first two sources are approximately halfway

¹<http://stdata.stsci.edu/euve/ism/ismform.html>

5. PSR B1929+10 REVISITED IN X-RAYS

Table 5.5: The parameters of ten EUVE sources placed in the pulsar direction as derived by the ISM hydrogen Column Density Search Tool.

HD Name	Name	l	b	d^a	N_{H}^b
HD180968	ES Vul	56.4	4.9	408.0	20.99♠
—	WD1910+047	39.7	-2.5	210.0	19.00†
HD170740	—	21.1	-0.5	279.0	21.04♠
HD163472	V2052 Oph	27.2	12.6	349.0	21.12♠
HD166014	σ Her	55.2	21.6	200.0	19.65‡
HD161056	—	18.7	11.6	263.0	21.20♠
HD164284	66 Oph	31.0	13.4	184.0	20.90★
HD162094	—	59.5	27.3	320.0	20.50♣
HD195810	ϵ Del	55.4	-16.6	150.0	19.52‡
HD185507	σ Aql	43.3	-8.1	140.0	21.01♣

^a Distance (in parsecs) between the star and the Earth.

^b Reference ♠ [Diplas & Savage \(1994\)](#), † [Paerels & Heise \(1989\)](#), ‡ [Welsh et al. \(1991\)](#), ★ [Bohlin et al. \(1983\)](#), ♣ [Brown et al. \(1991\)](#).

between the Earth and the pulsar, whereas the third and fourth source are at a two-third way and the last source is about 80 pc farther from the observer than the pulsar is. The dependence of the logarithm of the interstellar hydrogen column densities on the distances for all ten sources, as well as for PSR B1929+10, is shown in the upper panel of Fig. 5.10. It is quite clear that, in some cases, even if the source is not very far away the logarithm of N_{H} can be as large as 21, as it happens for example for σ Aql. On the contrary, ϵ Del being roughly at the same distance as σ Aql, or σ Her and WD1910+047 distant only about 50 pc from σ Aql all do have rather small values of the logarithm of N_{H} . This suggests that the interstellar medium is very patchy in that direction. The spatial distribution of all sources in the Galactic coordinates (l , b) is shown in the bottom panel of Fig. 5.10. For the pulsar and the five chosen stars their names and the values of their distances and N_{H} (in brackets) are presented. We can distinguish two regions. The first region encircles the surface with borders determined by the positions of the following sources WD1910+047, ϵ Del and σ Her. For this region, which is placed around 150–200 pc away, the average value of neutral hydrogen column density is at the level of $2.4 \times 10^{19} \text{ cm}^{-2}$. The second region, overlapping the first one, seems to be much smaller and elongates along the line connecting σ Aql, PSR B1929+10 and ES Vul. The average N_{H} is at the level of $9.92 \times 10^{20} \text{ cm}^{-2}$ here and it is about 40 times larger than that of region one.

From the spatial distribution of the interstellar extinction (Neckel et al. 1980) we were able to reconstruct similar values of N_{H} for the described stars. For this purpose we first used the general maps to identify our field of interest designated after Neckel, Klare, & Sarcander by the running numbers 50/-5.0 for PSR B1929+10, 52/0.0 for ES Vul and 42/-4.0 for WD1910+047 and σ Aql. (Because the maps were available only for the galactic belt, ϵ Del was out of range). Subsequently, from the $A_V(r)$ diagrams of the mentioned regions and by using the following relations $R = \frac{A_V}{E_{(B-V)}}$ and $\frac{N_{\text{H}}}{E_{(B-V)}} = 4.8 \times 10^{21} \text{ atoms cm}^{-2} \text{ mag}^{-1}$ (Bohlin et al. 1978) we obtained the following values of N_{H} , 1.03×10^{21} , 1.26×10^{21} , 3.25×10^{20} and $2.17 \times 10^{21} \text{ atoms cm}^{-2}$ for PSR B1929+10, ES Vul, WD1910+047, σ Aql, respectively. One can notice that a significant disagreement occurs only in the case of WD1910+047. The reason of this is that WD1910+047 is near the border of the region 42/-4.0 and moreover the relation $A_V(r)$ is not very well depicted for this region.

Finally, our results are supported by outcomes from a numerical algorithm developed by Hakkila et al. (1997) calculating three-dimensionally the visual interstellar extinction and its error from the galactic longitude, galactic latitude and distance. After using their extinction code for the pulsar parameters (l , b , d) we obtained a visual interstellar extinction A_V of 0.55 and error σ_{A_V} of 0.27 which results in $E_{B-V} = 0.177 \pm 0.087$ and finally $N_{\text{H}} = (8.5 \pm 4.2) \times 10^{20} \text{ cm}^{-2}$, which is fully consistent with our values of N_{H} based on PL and double BB fits.

At last we would like to mention that all the data collected on the EUVE server come from the database published in *The Distribution of Neutral hydrogen in the Interstellar Medium* by Fruscione et al. (1994), plus some additional new measurements from Diplas & Savage (1994).

5.7 The X-ray emitting trail

PSR B1929+10 is a very unique pulsar among old canonical pulsars. It is accompanied by a linearly extended diffuse emission that was discovered by Wang et al. (1993) in their archival study of the Galactic soft X-ray background using deep ROSAT PSPC images. The nebula appears as an elongated diffuse X-ray feature in the direction opposite to the pulsar's proper motion suggesting an interpretation in terms of an X-ray-emitting trail behind the pulsar. The pulsar wind is confined by the ram-pressure arising from the high pulsar's velocity through the interstellar medium. Analysing the *XMM – Newton* observations, Becker et al. (2006) confirm the existence of this emission with a trail morphology lying in a direction opposite to the transverse motion

5. PSR B1929+10 REVISITED IN X-RAYS

of the pulsar ($\mu_\alpha = 94.09 \pm 0.11$ and $\mu_\delta = 42.99 \pm 0.16$ mas yr⁻¹, $V_\perp = 177_{-5}^{+4}$ km s⁻¹; Chatterjee et al. (2004)). The *XMM – Newton* maps, see Fig. 5.11, show clearly diffuse extended emission at the position of the putative X-ray trail seen already in the ROSAT PSPC data (Wang et al. 1993). Contour lines, obtained from a reanalysis of the ROSAT PSPC and HRI observations (A. Słowińska), are overlaid on the *XMM – Newton* maps (W. Becker). Because of the instrument characteristics and the dependence on the source spectrum, it is much harder to detect the trail structure in the HRI data. It was possible only after applying an adaptive kernel smoothing procedure. Then the resulting structure becomes visible and matches with the shape of the trail seen in ROSAT PSPC and *MXM – Newton* images. The trail spectrum is non-thermal and characterised by a power law photon index of ~ 2 (B06). It is interpreted as synchrotron emission in the shock between the pulsar wind and the surrounding medium.

Radio data from the Effelsberg 11 cm radio continuum survey show an elongated feature that roughly coincides with the X-ray trail (Fig. 5.12, left). Three not fully resolved radio sources seen in the NRAO VLA Sky Survey (NVSS) survey data at 1.4 GHz match with part of the elongated radio feature seen at 11 cm (Fig. 5.12, right). The result obtained from the X-ray trail along with the possible discovery of its radio counterpart are exciting (B06). Follow-up radio observations of the trail region at different wavelengths are currently scheduled for fall 2006 in order to further constrain its existence and, if detected, provide polarisation information and the spectral index in the radio regime.

5.8 Summary and conclusions

Our revisited analysis of X-ray data of PSR B1929+10 from ROSAT, ASCA and RXTE observations yielded an improved timing signal at soft X-rays of 5.6σ for the combined ROSAT PSPC-B/HRI pulse profile, and a non-detection for energies beyond ~ 2 keV (RXTE PCA). Analysing the pulse profiles at soft X-rays (ROSAT PSPC-B) in two different energy bands yielded the pulsed fractions 0.33 ± 0.09 in the 0.1–1.28 keV band, 0.42 ± 0.13 in the 1.28–2.5 keV band, and 0.69 ± 0.18 for the 0.5–2 keV ASCA GIS band.

A spectral analysis of the combined ROSAT/ASCA data in the 0.1–10 keV energy range indicated that both an absorbed power law (non-thermal) model and an absorbed double black-body model provide an adequate description of the observed X-ray spectrum. For the double BB model a plausible explanation could be that

the observed X-ray radiation originates from a heated polar cap characterised by two different thermal components (Cheng & Zhang 1999). The derived hydrogen column densities (N_{H}) are in both cases much larger than the value used in previous X-ray studies. However, the newly determined N_{H} values are more consistent with the updated (increased) distance to PSR B1929+10 in combination with the measured hydrogen distribution in the direction of the pulsar.

A recent observation performed with the *XMM-Newton* satellite (B06) allows to validate results obtained by Słowiowska et al. (2005b). Improved statistic shows that the pulsar's X-ray spectrum is best described by a single power law model with photon index of $2.72_{-0.09}^{+0.12}$ (being in good agreement with our result, see Tab. 5.4), whereas the pure thermal emission spectrum consisting of two black-body components is regarded as rather unlikely. Furthermore, Becker et al. (2006) show that a combination of thermal and non-thermal spectral model (BB+PL) is possible, but the inferred contribution to the flux from the thermal emission of heated polar caps is not more than 7%. Noteworthy is the fact, that all spectral models considered by Becker et al. (2006) give, in comparison with values used by Y94 and WH97, a higher value of N_{H} , e.g. $(0.35 \pm 0.11) \times 10^{21} \text{ cm}^{-2}$ for double BB fit, and even $(1.6 \pm 0.2) \times 10^{21} \text{ cm}^{-2}$ for a single PL case. Thus, the high value of N_{H} obtained by Słowiowska et al. (2005b) have been confirmed. Besides giving the constrains for the high energy pulsar emission, the large collecting area of the *XMM – Newton* satellite has allowed, for the first time, spectral analysis of the emission from the pulsar's X-ray trail (B06).

Słowiowska et al. (2005b) performed timing and spectral analyses for PSR B1929+10, one of the oldest ($\sim 10^7$ years) of the ordinary pulsars detected in X-rays, using archival ROSAT, ASCA and RXTE data. Pulsed emission was detected at more than five sigma level for the combined ROSAT PSPC-B and previously unpublished HRI data. Our pulse profile is in agreement with that obtained by Yancopoulos et al. (1994) (ROSAT PSPC-B) but now with better statistics. The pulsed fraction in the ROSAT X-ray band is 0.25 ± 0.04 . The pulsed signal has also been detected in the ASCA GIS data (0.5–5 keV) with a similar pulsed fraction that amounts to 0.36 ± 0.11 . No significant timing signal is found in the RXTE PCA data (> 2 keV). The most important result from this work is derived from the spectral analysis. We found that the combined ROSAT PSPC-B and ASCA GIS spectrum can satisfactorily be described by a power law as well as by a double black-body model but not by a single black-body model or black-body plus power law model, as was presented earlier by Yancopoulos et al. (1994) and Wang & Halpern (1997) for ROSAT and ASCA data, respectively. In both cases the derived N_{H} value is higher than that adopted in earlier works, but

5. PSR B1929+10 REVISITED IN X-RAYS

our result is fully consistent with the larger pulsar distance estimates ([Brisken et al. 2002](#); [Chatterjee et al. 2004](#)) in combination with the hydrogen distribution measured in the direction of the pulsar ([Frisch & York 1983](#)). Our results have been recently verified by [Becker et al. \(2006\)](#) who used the *XMM – Newton* observations.

5.8 Summary and conclusions

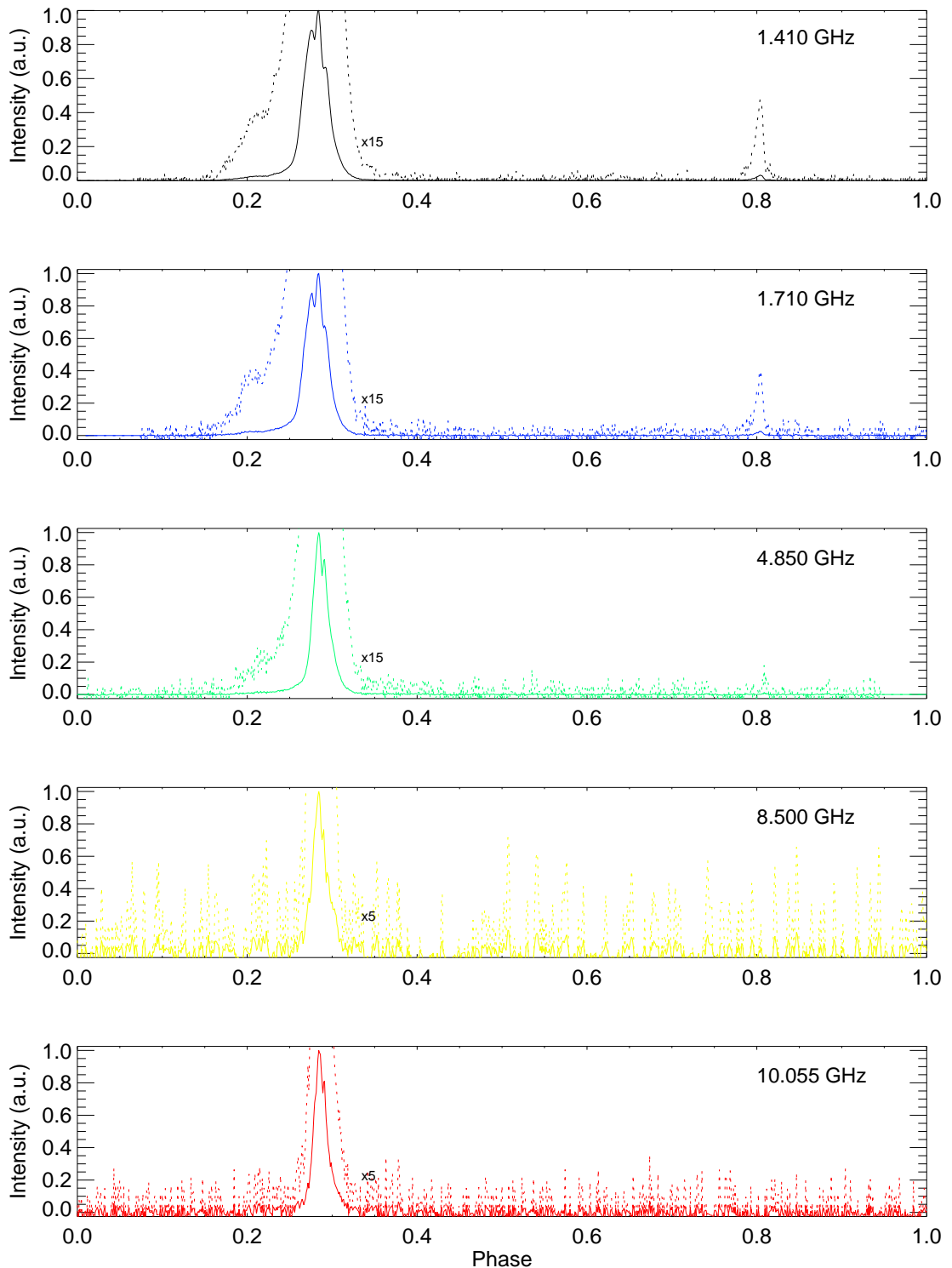


Figure 5.7: Normalised total intensity of PSR B1929+10 as a function of radio frequency (Kramer et al. (1997) and von Hoensbroech & Xilouris (1997)). Data were taken from the public data base maintained by the European Pulsar Network. The dotted lines show the same profile magnified by a few times to better visualise the weak inter pulse component around 0.8 phase. Profiles were aligned with the maximum at 1.41 GHz.

5. PSR B1929+10 REVISITED IN X-RAYS

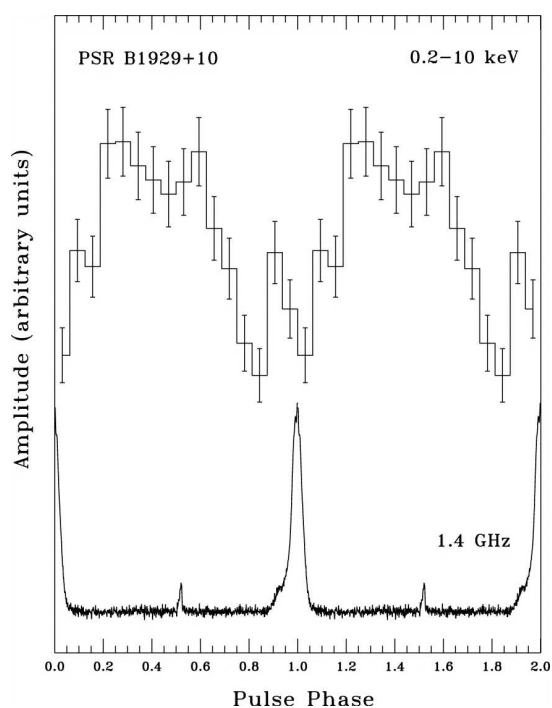


Figure 5.8: *Upper*: integrated pulse profile of PSR B1929+10 as observed in the 0.2–10 keV band with the *XMM – Newton* satellite. *Bottom*: the radio profile at 1.4 GHz obtained with the Jodrell Bank radio observatory and plotted on a logarithmic scale to better characterise the weak inter pulse component. Both profiles are phase aligned. Two phase cycles are shown for clarity. [Becker et al. (2006)]

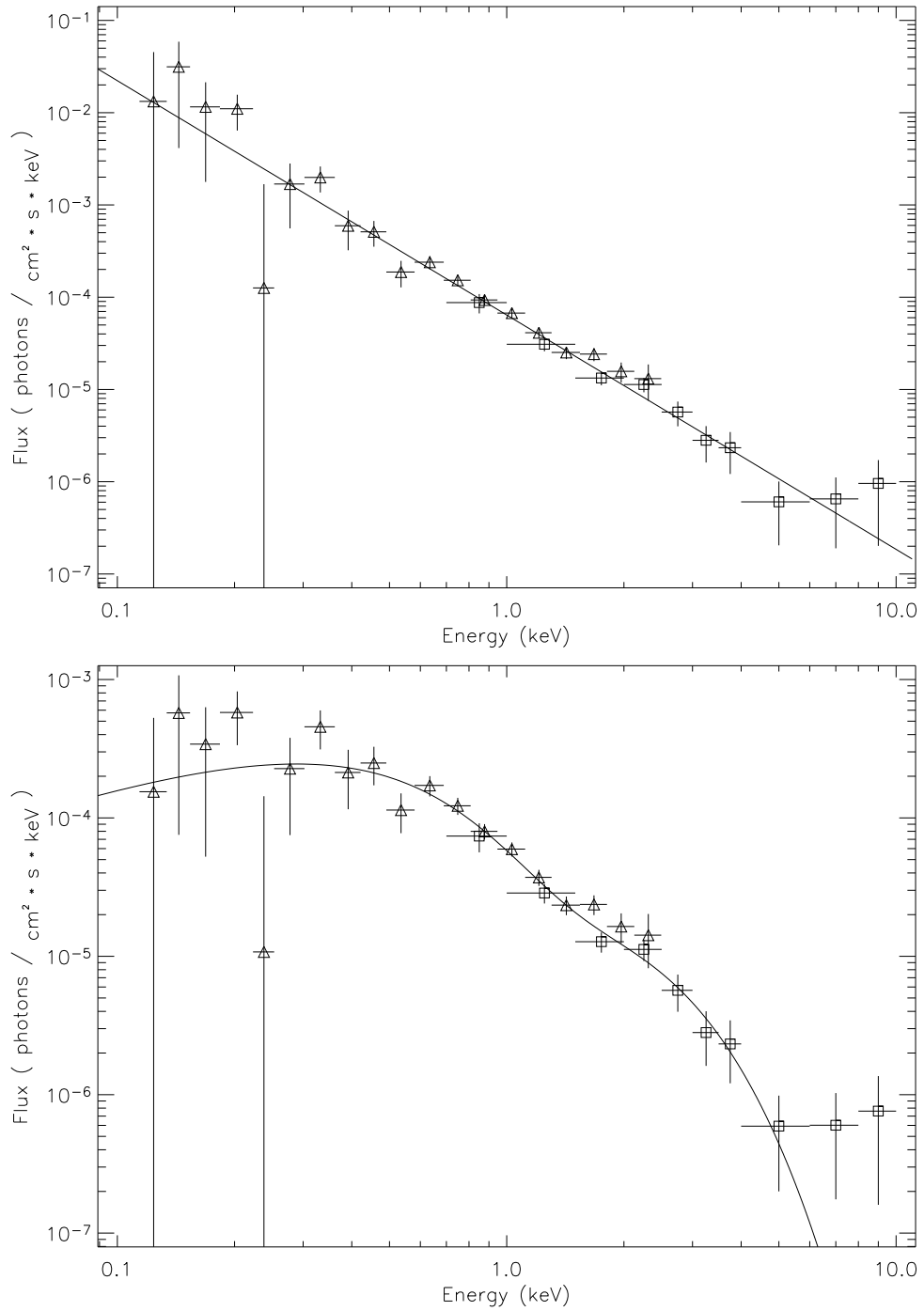


Figure 5.9: 0.1–10 keV spectrum of PSR B1929+10 from combined ROSAT PSPC-B (open triangles) and ASCA GIS 2+3 (open squares) data: *upper panel* an absorbed single power law model, *lower panel* an absorbed double black-body model.

5. PSR B1929+10 REVISITED IN X-RAYS

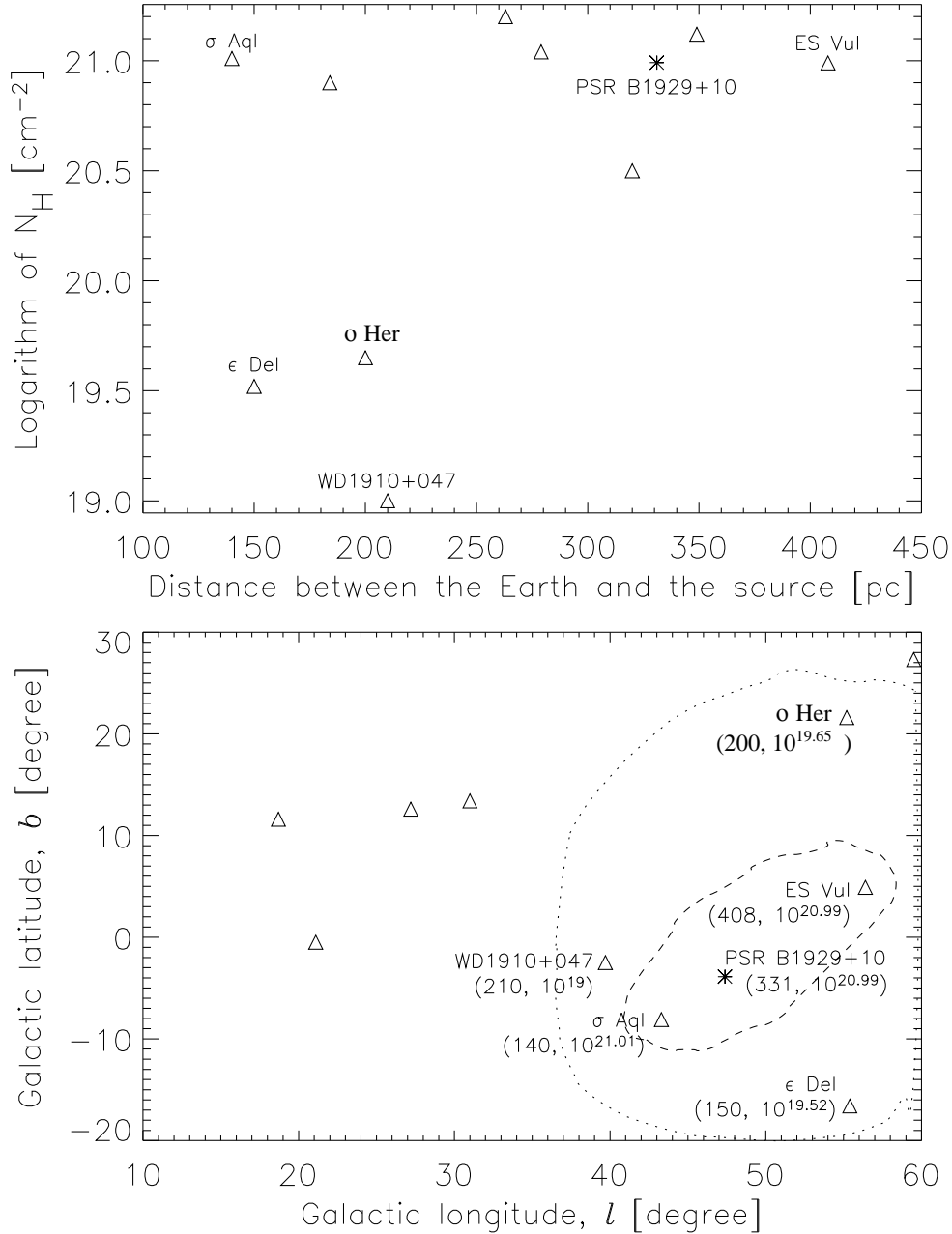


Figure 5.10: *Upper panel:* the dependence of the logarithm of the interstellar hydrogen column densities on the distances for ten stars from the EUVE database and the pulsar. For the discussion only five stars were selected and they are labelled in the figure. In the *bottom panel* the spatial distribution of the mentioned sources in the Galactic coordinates l , b is shown. The stars of interest and the pulsar are labelled. Additionally, the distance in parsecs and the N_{H} value in cm^{-2} for each object is given in brackets. Dotted and dashed lines encircle two regions with different mean N_{H} values, $2.4 \times 10^{19} \text{ cm}^{-2}$ for the more extended region and $9.92 \times 10^{20} \text{ cm}^{-2}$ for the smaller one.

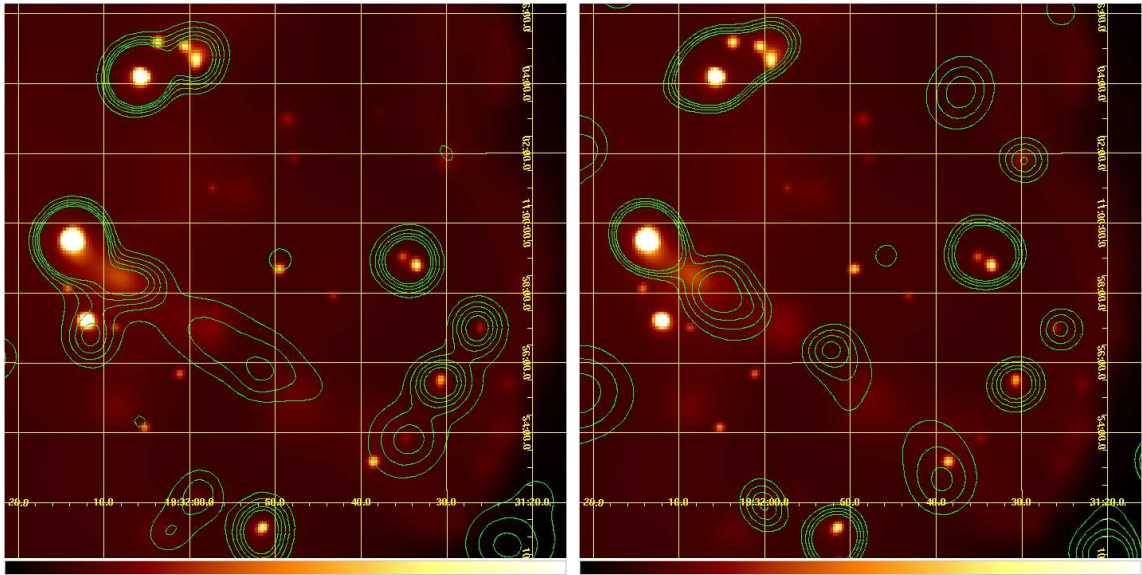


Figure 5.11: PSR B1929+10 and its environment as seen in the 0.2–10.0 keV energy band by *MXX-Newton's* detectors. Contour lines from the ROSAT PSPC and HRI image are overlaid in the *left* and *right* panel, respectively. The angular resolution of the ROSAT detectors are 25'' in the PSPC and 5'' in the HRI, respectively, while that of *XMM – Newton* is 15''. [Maps W. Becker; contours A. Słowikowska]

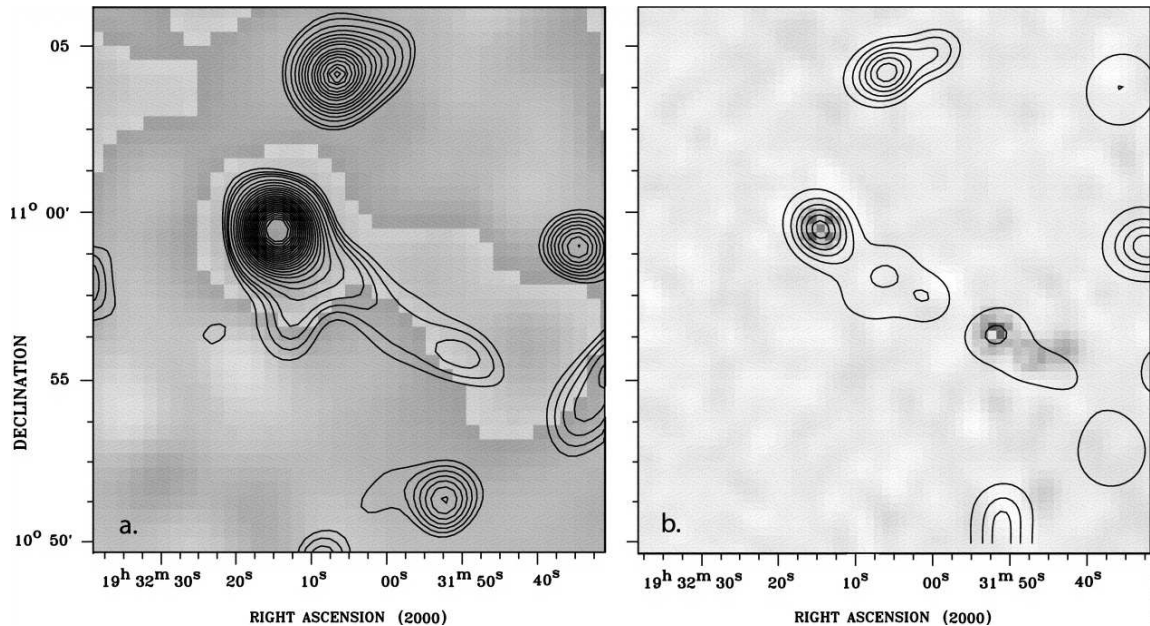


Figure 5.12: *Left*: contour lines from the ROSAT PSPC overlaid on part of the Effelsberg 11 cm radio map. *Right*: contour lines from the ROSAT HRI overlaid on part of the 1.4 GHz NRAO VLA Sky Survey (NVSS) image. [Becker et al. (2006)]

Chapter 6

Closing remarks

Pulsar astronomy is truly a multiwavelength field. Neutron stars as rotation-powered pulsars are now observed across the entire electromagnetic spectrum from radio waves to gamma rays. In this thesis the results of radio, optical, and X-ray studies of three classical pulsars are presented. By arranging the observations, followed by data reduction and analysis we attempted to broaden our knowledge of these objects. Conclusions and possible implications from this work were discussed in the corresponding chapters, and they will not be fully repeated here. Below a brief summary of the results is given, as well as future projects are discussed.

First two chapters are dedicated to the Crab pulsar. One might expect that after 38 years of extensive studies we should know almost everything about this source. However, it turned out not to be the case and it is still worth to point the telescopes at this source. In Chapter 1 we presented our discovery of giant radio pulses (GRPs) occurring at the phases of high frequency component (HFCs, [Jessner et al. \(2005\)](#); [Słowikowska et al. \(2005a\)](#)). Our finding challenges the idea that GRPs are aligned exclusively with the main pulse (MP) and the inter pulse (IP). It weakens the hypothesis that GRP phenomenon is somehow connected with the non-coherent high energy emission. In order to study the evolution of giant pulses with frequency, as well as to investigate their fluxes, time structures, and polarisation we have applied recently for the observing time at the Effelsberg telescope. We propose observations of the Crab pulsar at 14.6 and 23 GHz to study spectral and polarimetric properties of GRPs at the IP and HFCs phases, and to search for possible new components in its average radio profile. Simultaneous observations at the lower frequencies of 0.6, 2.2 and 4.8 GHz will be performed at the 64-m radio telescope in Kalyazin (Russia). Such observations will allow to investigate the physical relation between HFCs and regular MP and IP at lower frequencies and compare their properties in a broad frequency range. It might also provide new constraints to the location and configuration of

emission regions in the Crab pulsar. This project is going to be performed by the end of 2006.

Polarisation measurements of pulsars and of their synchrotron nebulae provide deep insights into the highly magnetised relativistic environment of young rotating neutron stars and allow to test current magnetospheric and wind models. Apart from the radio band, polarisation is best measured in the optical. Chapter 2, the most extensive one, describes the results of our polarimetric campaign of the Crab pulsar at Nordic Optical Telescope with OPTIMA. Our results reveal complex behaviour of polarisation degree and position angle of rotational phase. These high-quality results with time resolution of about $30 \mu\text{s}$ will certainly stimulate a significant revision of major pulsar models. Pulsar polarisation characteristics obtained with such high time resolution establish the OPTIMA instrument with the rotating polarisation filter as a very power full polarisation system.

We decided to extend our polarimetric studies to other pulsars. PSR B0540-69 is one of the brightest optical pulsars and similar to the Crab pulsar. It is embedded in a synchrotron nebula visible at optical wavelengths. We successfully applied for the HST time to observe PSR B0540-69 and its compact nebula with the Advanced Camera for Surveys (ACS) and the Wide Field Channel (WFC) detector using UV and visual polarisation filters. Thanks to the superb angular resolution of ACS, these observations will allow us to resolve the pulsar from its nebular background, providing the first firm measure of the pulsar phase-averaged polarisation. Thus the number of pulsars with measured optical polarisation will hopefully increase. The observations will also provide the first detailed polarisation map of the nebula, including the jet and the torus seen in previous WFPC2 images. Our proposal has been already approved and we expect that the observations will be performed in Winter 2006.

To obtain the high time resolution photometry of the second and third brightest optical pulsars - PSR B0540-69 and PSR B0833-45 (Vela) - we are preparing an observational campaign at Southern African Large Telescope. These pulsars are of average magnitude of $V \sim 22.7$ and 23.6 , respectively, thus the large collecting power of SALT is essential to conduct the measurements. For our purpose we propose to use OPTIMA as a guest instrument. The immediate results of such measurements would be: optical light curves of PSR B0540-69 and Vela with very high statistical accuracy and the first determination of the phase dependent linear polarisation of these pulsars.

Chapters 3 and 4 present the X-ray data analysis and results of PSR B0540-69 and PSR B1929+10, respectively. In the first case, despite of long exposure time

6. CLOSING REMARKS

the results are not of high significance. Yet, the interesting piece of information we managed to obtain is the total spectrum of this object extending, for the first time, up to 200 keV. Chapter 4 deals with the archive X-ray data of one of the oldest observed X-ray pulsar, PSR B1929+10. Neutron stars are born with temperatures of more than 10^{12} K during the collapse of massive stars. They start to cool down directly after they are born. The cooling process strongly depends on the physical properties of superdense matter inside them. X-ray observations of neutron stars have already shown that their radiation may have three different origins: (1) whole surface is so hot that it emits thermal X-rays; (2) charged particles moving in strong magnetic field produce non-thermal X-rays; (3) thermal X-rays come from the reheated polar caps. Our reanalysis of the archival data of PSR B1929+10 attempted to identify possible origin of its X-rays. Unfortunately, we were not able to distinguish explicitly between the thermal and non-thermal source of emission (Słowikowska et al. 2005b). However, our non-thermal model seems to be confirmed by recent *XMM-Newton* observations (Becker et al. 2006). These results suggest that the observed X-ray emission of this pulsar is due to the magnetospheric emission and not due to hot polar caps. The heating of the polar surface regions by particle bombardment is not efficient enough to produce significant thermal X-ray component.

Pulsar phenomenon, nearly forty years after the discovery by Jocelyn Bell, is still not well understood, and therefore more observations with sensitive instruments in all energy domain are needed.

Appendix A

OPTIMA data files

For the main data analysis 83 out of 160 files were selected as acceptable for analysis (about the selection criteria see Sec. 3.2.3). First part of the file name contains object name plus additionally abbreviated name of used filters, in this case it were infrared and rotating polarisation filters, second part of the file name contains the date and the UTC time when the data acquisition started. Number of files given in the table are hereafter used as an arbitrary file number, see e.g. Fig. 3.9 or 3.10.

A. OPTIMA DATA FILES

Table A.1: Log of good data file names

No.	File Name	No.	File Name
0	Crab-IR+Pol 25Nov2003 (25-11-2003 23-02-42)	42	Crab-IR+Pol 26Nov2003 (26-11-2003 23-21-48)
1	Crab-IR+Pol 25Nov2003 (25-11-2003 23-12-45)	43	Crab-IR+Pol 26Nov2003 (26-11-2003 23-31-51)
2	Crab-IR+Pol 25Nov2003 (25-11-2003 23-22-48)	44	Crab-IR+Pol 26Nov2003 (26-11-2003 23-41-54)
3	Crab-IR+Pol 25Nov2003 (25-11-2003 23-32-51)	45	Crab-IR+Pol 26Nov2003 (26-11-2003 23-51-57)
4	Crab-IR+Pol 25Nov2003 (25-11-2003 23-42-54)	46	Crab-IR+Pol 26Nov2003 (27-11-2003 00-02-01)
5	Crab-IR+Pol 25Nov2003 (25-11-2003 23-52-57)	47	Crab-IR+Pol 26Nov2003 (27-11-2003 00-12-04)
6	Crab-IR+Pol 25Nov2003 (26-11-2003 00-03-01)	48	Crab-IR+Pol 26Nov2003 (27-11-2003 00-22-07)
7	Crab-IR+Pol 25Nov2003 (26-11-2003 00-13-04)	49	Crab-IR+Pol 26Nov2003 (27-11-2003 00-32-10)
8	Crab-IR+Pol 25Nov2003 (26-11-2003 00-23-07)	50	Crab-IR+Pol 26Nov2003 (27-11-2003 00-42-13)
9	Crab-IR+Pol 25Nov2003 (26-11-2003 00-33-10)	51	Crab-IR+Pol 26Nov2003 (27-11-2003 00-52-16)
10	Crab-IR+Pol 25Nov2003 (26-11-2003 00-43-58)	52	Crab-IR+Pol 26Nov2003 (27-11-2003 01-03-27)
11	Crab-IR+Pol 25Nov2003 (26-11-2003 00-54-01)	53	Crab-IR+Pol 26Nov2003 (27-11-2003 01-13-30)
12	Crab-IR+Pol 25Nov2003 (26-11-2003 01-04-04)	54	Crab-IR+Pol 26Nov2003 (27-11-2003 01-23-33)
13	Crab-IR+Pol 25Nov2003 (26-11-2003 01-14-07)	55	Crab-IR+Pol 26Nov2003 (27-11-2003 01-33-36)
14	Crab-IR+Pol 25Nov2003 (26-11-2003 01-24-10)	56	Crab-IR+Pol 26Nov2003 (27-11-2003 01-43-39)
15	Crab-IR+Pol 25Nov2003 (26-11-2003 01-34-13)	57	Crab-IR+Pol 26Nov2003 (27-11-2003 01-53-42)
16	Crab-IR+Pol 25Nov2003 (26-11-2003 01-44-16)	58	Crab-IR+Pol 26Nov2003 (27-11-2003 02-03-45)
17	Crab-IR+Pol 25Nov2003 (26-11-2003 01-54-19)	59	Crab-IR+Pol 26Nov2003 (27-11-2003 02-13-48)
18	Crab-IR+Pol 25Nov2003 (26-11-2003 02-04-22)	60	Crab-IR+Pol 26Nov2003 (27-11-2003 02-41-53)
19	Crab-IR+Pol 25Nov2003 (26-11-2003 02-14-25)	61	Crab-IR+Pol 26Nov2003 (27-11-2003 02-52-44)
20	Crab-IR+Pol 25Nov2003 (26-11-2003 02-24-28)	62	Crab-IR+Pol 26Nov2003 (27-11-2003 03-02-47)
21	Crab-IR+Pol 25Nov2003 (26-11-2003 03-05-20)	63	Crab-IR+Pol 26Nov2003 (27-11-2003 03-08-17)
22	Crab-IR+Pol 25Nov2003 (26-11-2003 03-15-59)	64	Crab-IR+Pol 26Nov2003 (27-11-2003 03-18-49)
23	Crab-IR+Pol 25Nov2003 (26-11-2003 03-52-43)	65	Crab-IR+Pol 26Nov2003 (27-11-2003 03-28-52)
24	Crab-IR+Pol 25Nov2003 (26-11-2003 04-02-46)	66	Crab-IR+Pol 26Nov2003 (27-11-2003 03-38-55)
25	Crab-IR+Pol 25Nov2003 (26-11-2003 04-13-21)	67	Crab-IR+Pol 26Nov2003 (27-11-2003 03-48-58)
26	Crab-IR+Pol 25Nov2003 (26-11-2003 04-23-24)	68	Crab-IR+Pol 26Nov2003 (27-11-2003 03-59-01)
27	Crab-IR+Pol 25Nov2003 (26-11-2003 04-33-27)	69	Crab-IR+Pol 26Nov2003 (27-11-2003 04-09-04)
28	Crab-IR+Pol 25Nov2003 (26-11-2003 04-43-30)	70	Crab-IR+Pol 26Nov2003 (27-11-2003 04-19-07)
29	Crab-IR+Pol 25Nov2003 (26-11-2003 04-53-33)	71	Crab-IR+Pol 26Nov2003 (27-11-2003 04-29-10)
30	Crab-IR+Pol 25Nov2003 (26-11-2003 05-03-36)	72	Crab-IR+Pol 26Nov2003 (27-11-2003 04-39-13)
31	Crab-IR+Pol 25Nov2003 (26-11-2003 05-13-39)	73	Crab-IR+Pol 26Nov2003 (27-11-2003 04-49-16)
32	Crab-IR+Pol 25Nov2003 (26-11-2003 05-23-42)	74	Crab-IR+Pol 26Nov2003 (27-11-2003 04-59-19)
33	Crab-IR+Pol 25Nov2003 (26-11-2003 05-33-45)	75	Crab-IR+Pol 26Nov2003 (27-11-2003 05-09-22)
34	Crab-IR+Pol 25Nov2003 (26-11-2003 05-43-48)	76	Crab-IR+Pol 26Nov2003 (27-11-2003 05-19-25)
35	Crab-IR+Pol 25Nov2003 (26-11-2003 05-53-51)	77	Crab-IR+Pol 26Nov2003 (27-11-2003 05-29-28)
36	Crab-IR+Pol 25Nov2003 (26-11-2003 06-03-54)	78	Crab-IR+Pol 26Nov2003 (27-11-2003 05-37-31)
37	Crab-IR+Pol 25Nov2003 (26-11-2003 06-13-57)	79	Crab-IR+Pol 26Nov2003 (27-11-2003 05-47-56)
38	Crab-IR+Pol 25Nov2003 (26-11-2003 06-24-01)	80	Crab-IR+Pol 26Nov2003 (27-11-2003 05-57-59)
39	Crab-IR+Pol 26Nov2003 (26-11-2003 22-51-02)	81	Crab-IR+Pol 26Nov2003 (27-11-2003 06-08-02)
40	Crab-IR+Pol 26Nov2003 (26-11-2003 23-01-42)	82	Crab-IR+Pol 26Nov2003 (27-11-2003 06-18-05)
41	Crab-IR+Pol 26Nov2003 (26-11-2003 23-11-45)		

Appendix B

ROSAT timing

Timing analysis with the ROSAT PSPC and HRI instruments at millisecond accuracies is certainly no trivial task. Several authors analysing different fast spin-down powered pulsars encountered severe problems in attempts to phase align the ROSAT profiles with profiles obtained at different wavelengths or to phase align ROSAT profiles from different ROSAT observations mutually.

For instance, in [Greiveldinger et al. \(1995\)](#) the pulse maximum in the 0.1-2.4 keV range for the 150 ms pulsar PSR B1509-58 was found at 0.13 ± 0.05 with respect to the radio pulse, while it is nowadays known that the pulse maximum occurs between 0.27-0.30 (pulse shape is weakly energy dependent) for energies in excess of ~ 0.5 keV (see e.g. [Kuiper et al. 1999](#), and references therein for the ASCA 0.7-2.2 keV profile overlapping the ROSAT energy band). Furthermore, [Seward et al. \(2000\)](#) reported on radio/soft X-ray alignment problems for the Vela pulsar (89 ms) analysing ROSAT HRI data, which manifest themselves as absolute phase errors of about 0.2. In this case the problems are probably related to (an) ignored leap second jump(s) in the spacecraft clock-to-UTC (SCC-TO-UTC) conversion relation (see later this section). Moreover, studying the Geminga pulsar (237 ms) at soft X-rays [Halpern & Wang \(1997\)](#) reported discrepancies in the phase alignment of different ROSAT Geminga observations, which could be traced back to leap second ignorance in the PROS software. Finally, in [Kuiper et al. \(2001\)](#) a ROSAT HRI 0.1-2.4 keV pulse profile for the Crab pulsar (33 ms) was shown based on a 7.98 ks observation (RH400639N00) performed over the time period from 4 - 15 March 1995. In this observation four consecutive (ROSAT) orbital intervals could be identified yielding a stable pulse profile. The most dominant chunk showed the Crab first pulse at phase

B. ROSAT TIMING

0.82 (the other chunks at 0.88, 0.86 and 0.85, indicating the drift within an observation), while 0.9915 (INTEGRAL/RXTE/Chandra/XMM) is expected. Contrary to the scatter in the phase arrival of the first Crab pulse, which is within the range of scatter of the SCC-TO-UTC correlation, the overall shift of ~ -0.18 ($\simeq -6$ ms) is hard to explain.

Giving these problems we initiated ROSAT timing studies ourselves using fast spin-down powered pulsars with a) a *known* phase relation to radio frequencies, b) which are sufficiently strong to show a significant timing signal in relatively short observations and c) which have a *stable* soft X-ray profile over the entire soft X-ray band (i.e. no strong energy dependent behaviour like observed e.g. for the Vela and Geminga pulsars, which are moreover also weak X-ray pulsars). The only two sources meeting these criteria are the Crab pulsar (PSR B0531+21) and PSR B1509-58. Our (CGRO based) timing software used for this purpose has successfully been applied to timing data from a wide variety of high-energy instruments (CGRO EGRET/COMPTEL/BATSE, RXTE PCA/HEXTE, Chandra etc.) and takes leap seconds jumps correctly into account (verified for e.g. CGRO Crab, Vela etc data). The ROSAT ¹ timing data can be easily processed by this software because the ROSAT SCC timestamps could be converted to UTC timestamps (=default from the CGRO instruments) applying the SCC-TO-UTC time correlation model specified in the ssc-to-utc.tfits file (retrievable from <http://wave.xray.mpe.mpg.de/rosat/calibration/timing>).

For PSR B1509-58 we found 4 different ROSAT observations (RP500041A00/A01; PSPC - Feb. 1991, 1992 resp. and RH400409N00/A01; HRI - Feb./Sept. 1994) useful for absolute timing studies. Phase folding the solar system barycentered TDB (converted from UTC) timestamps of events extracted from circular regions centered on the pulsar position (extraction radii PSPC/HRI are 50'' and 12'', respectively) with well established/verified pulsar ephemerides from the Princeton and ATNF pulsar databases yielded for *all* four observations the pulse maximum of the asymmetric pulse in the range 0.60-0.68.

For the Crab pulsar we selected 6 different PSPC/HRI observations performed between 2-3-1991 and 22-3-1997 encompassing 5 different periods in which leap second adjustments have been applied. These Crab observations were: RF500065N00, PSPC 1.9 ks 2-3-1991; RH141890N00/RH141892N00, HRI 1.4/1.8 ks 16/17-9-1992; RH400639N00 HRI 7.9 ks 4/15-3-1995; RH500464N00 HRI 32.6 ks 9/29-3-1996; and

¹It is interesting to note that the ROSAT mission with a life time of about 8.5 year (1-6-1990 – 12-2-1999) overlapped 8 time intervals in which new leap seconds were introduced.

RH400867N00 HRI 33.5 ks 20/22-3-1997. Applying again established/verified Crab pulsar ephemerides (Princeton and Jodrell Bank databases) in the folding process we found the first Crab pulse at arrival phases between 0.83-0.91 for the 4 observations selected before 31-12-1995, and in the range 0.03-0.10 for the 2 observations selected after 31-12-1995, while an arrival phase of 0.9915 is expected (note that all PSR B1509-58 observations had been performed before 31-12-1995). The Crab first pulse arrival phases of the 2 sets can be made compatible (i.e. within the rms of the SCC-UTC time correlation) by assuming that the leap second insertion at 31-12-1995 was not accounted for in the two observations after this date. Adding, for these two observations, 1 second to the UTC timestamps derived from the regular SCC-UTC time correlation model put the first Crab pulse in the range 0.94-1.01.

Comparing now the Crab/PSR B1509-58 alignment results for the observations performed before 31-12-1995 it is worth-mentioning that the apparent offset of 0.37(4), found for PSR B1509-58, from the established value of 0.27 can be understood if for whatever reason all four PSR B1509-58 suffered from the ignorance of a 1 second addition i.e. adding 1 second to the UTC times derived from the regular SCC-UTC correlation put the maximum of the PSR B1509-58 pulse at ~ 0.25 . Postulating a minor overall timing correction of about 3-6 ms in addition to this 1 second put both the Crab and PSR B1509-58 pulses at their expected phase locations (within the rms of the SCC-UTC time correlation).

From this study it should be clear that the direct combination of different ROSAT observations, performed at different widely separated dates crossing leap second insertion dates, can be very tricky in the case of weak pulsars in order to increase the signal-to-noise ratio. Therefore, in the HRI timing study of PSR B1929+10 we decide to combine the separately correlated (with the PSPC profile, see §3.2.) HRI pulse profiles to obtain the total detection significance of the pulsed signal. Later on we verified this approach by using one single, specially prepared from Jodrell Bank TOAs, PSR B1929+10 ephemeris (validity time interval 49927-50595 MJD; reference epoch 50261 MJD TDB) overlapping all three HRI observations in the folding process taking into account that two PSR B1929+10 HRI observations had been performed after 31-12-1995 and one before (and thus 1 second should be added to the latter to align with the former; see notes on the Crab timing).

Bibliography

- Argyle, E. & Gower, J. F. R. 1972, *ApJ*, 175, L89 [2.4.1](#)
- Baade, W. & Zwicky, F. 1934a, *Proceedings of the National Academy of Science*, 20, 259 [1.1](#)
- Baade, W. & Zwicky, F. 1934b, *Phys. Rev.*, 46, 76 [1.1](#)
- Backer, D. C., Foster, R. S., & Sallmen, S. 1993, *Nature*, 365, 817 [1.1](#)
- Backer, D. C., Kulkarni, S. R., Heiles, C., Davis, M. M., & Goss, W. M. 1982, *Nature*, 300, 615 [1.1](#)
- Becker, W., Kramer, M., Jessner, A., et al. 2006, *ApJ*, 645, 1421 [5.2](#), [5.4.1](#), [5.5](#), [5.7](#), [5.8](#), [5.8](#), [5.12](#), [6](#)
- Bohlin, R. C., Jenkins, E. B., Spitzer, Jr., L., et al. 1983, *ApJS*, 51, 277 [5.5](#)
- Bohlin, R. C., Savage, B. D., & Drake, J. F. 1978, *ApJ*, 224, 132 [5.6.1](#)
- Boldt, E. A., Desai, U. D., & Holt, S. S. 1969, *ApJ*, 156, 427 [2.1](#)
- Boyd, P. T., van Citters, G. W., Dolan, J. F., et al. 1995, *ApJ*, 448, 365 [4.1](#)
- Briskin, W. F., Benson, J. M., Goss, W. M., & Thorsett, S. E. 2002, *ApJ*, 571, 906 [5.1](#), [5.6](#), [5.6.1](#), [5.8](#)
- Brown, A., Drake, S. A., van Steenberg, M. E., & Linsky, J. L. 1991, *ApJ*, 373, 614 [5.5](#)
- Buccheri, R., Bennett, K., Bignami, G. F., et al. 1983, *A&A*, 128, 245 [5.4.1](#)
- Burgay, M., D'Amico, N., Possenti, A., et al. 2003, *Nature*, 426, 531 [1.1](#)
- Chanan, G. A., Helfand, D. J., & Reynolds, S. P. 1984, *ApJ*, 287, L23 [4.1](#)

BIBLIOGRAPHY

- Chatterjee, S., Cordes, J. M., Vlemmings, W. H. T., et al. 2004, *ApJ*, 604, 339 [5.6](#), [5.7](#), [5.8](#)
- Cheng, K. S., Ho, C., & Ruderman, M. 1986, *ApJ*, 300, 500 [1.4](#)
- Cheng, K. S., Ruderman, M., & Zhang, L. 2000, *ApJ*, 537, 964 [2.6](#)
- Cheng, K. S. & Wei, D. M. 1995, *ApJ*, 448, 281 [4.6](#)
- Cheng, K. S. & Zhang, L. 1999, *ApJ*, 515, 337 [5.6](#), [5.8](#)
- Cocke, W. J., Disney, M. J., Muncaster, G. W., & Gehrels, T. 1970, *Nature*, 227, 1327 [3.1](#)
- Cocke, W. J., Disney, M. J., & Taylor, D. J. 1969, *Nature*, 221, 525 [2.1](#), [3.4.1](#)
- Cocke, W. J., Ferguson, D. C., & Muncaster, G. W. 1973, *ApJ*, 183, 987 [3.1](#)
- Comella, J. M., Craft, H. D., Lovelace, R. V. E., Sutton, J. M., & Tyler, G. L. 1969, *Nature*, 221, 453 [2.1](#)
- Cordes, J. M., Bhat, N. D. R., Hankins, T. H., McLaughlin, M. A., & Kern, J. 2004, *ApJ*, 612, 375 [2.2](#), [2.4.1](#)
- Cordes, J. M., Freire, P. C. C., Lorimer, D. R., et al. 2006, *ApJ*, 637, 446 [1.1](#)
- Cordes, J. M., Kramer, M., Lazio, T. J. W., et al. 2004, *New Astronomy Reviews*, 48, 1413 [1.3](#)
- D'Amico, N. & Nicastro, L. 1992, Princeton University [5.1](#)
- de Plaa, J., Kuiper, L., & Hermsen, W. 2003, *A&A*, 400, 1013 [4.1](#), [4.1](#)
- Deeter, J. E., Nagase, F., & Boynton, P. E. 1999, *ApJ*, 512, 300 [4.1](#)
- Diplas, A. & Savage, B. D. 1994, *ApJS*, 93, 211 [5.5](#), [5.6.1](#)
- Donovan, J., Lommen, A., Arzoumanian, Z., et al. 2004, in *IAU Symp. 218: Young Neutron Stars and Their Environments*, ed. F. Camilo & B. M. Gaensler, 335 [2.6](#)
- Drake, F. D. & Craft, H. D. 1968, *Nature*, 220, 231 [1.1](#)
- Dyks, J., Harding, A. K., & Rudak, B. 2004a, *ApJ*, 606, 1125 [1.4](#), [3.6](#)

BIBLIOGRAPHY

- Dyks, J., Harding, A. K., & Rudak, B. 2004b, in IAU Symp. 218: Young Neutron Stars and Their Environments, ed. F. Camilo & B. M. Gaensler, 373–374 [3.27](#)
- Dyks, J. & Rudak, B. 2003, ApJ, 598, 1201 [1.4](#), [3.5](#)
- Edwards, R. T. & Stappers, B. W. 2004, A&A, 421, 681 [2.4.2](#)
- Eikenberry, S. S. & Fazio, G. G. 1997, ApJ, 476, 281 [3.4.2](#)
- Ferguson, D. C. 1973, ApJ, 183, 977 [3.1](#)
- Ferguson, D. C., Cocke, W. J., & Gehrels, T. 1974, ApJ, 190, 375 [3.1](#)
- Fishman, G. J., Harnden, F. R., & Haymes, R. C. 1969, ApJ, 156, L107 [2.1](#)
- Frisch, P. C. & York, D. G. 1983, ApJ, 271, L59 [5.6.1](#), [5.8](#)
- Fritz, G., Henry, R. C., Meekins, J. F., Chubb, T. A., & Friedman, H. 1969, Science, 164, 709 [2.1](#)
- Fruscione, A., Hawkins, I., Jelinsky, P., & Wiercigroch, A. 1994, ApJS, 94, 127 [5.6.1](#)
- Gold, T. 1968, Nature, 218, 731 [1.1](#)
- Gold, T. 1969, Nature, 221, 25 [1.1](#)
- Golden, A., Shearer, A., & Beskin, G. M. 2000a, ApJ, 535, 373 [1.5](#), [3.3.4](#), [3.4.3](#)
- Golden, A., Shearer, A., Redfern, R. M., et al. 2000b, A&A, 363, 617 [3.4.2](#)
- Gotthelf, E. V. & Wang, Q. D. 2000, ApJ, 532, L117 [4.1](#), [4.1](#)
- Götz, D., Mereghetti, S., Merlini, D., Sidoli, L., & Belloni, T. 2006, A&A, 448, 873 [4.4](#)
- Gower, J. F. R. & Argyle, E. 1972, ApJ, 171, L23 [2.2](#), [2.5](#)
- Greiveldinger, C., Caucino, S., Massaglia, S., Oegelman, H., & Trussoni, E. 1995, ApJ, 454, 855 [B](#)
- Hakkila, J., Myers, J. M., Stidham, B. J., & Hartmann, D. H. 1997, AJ, 114, 2043 [5.6.1](#)
- Halpern, J. P. & Wang, F. Y.-H. 1997, ApJ, 477, 905 [B](#)

- Hankins, T. H., Kern, J. S., Weatherall, J. C., & Eilek, J. A. 2003, *Nature*, 422, 141
[2.2](#), [2.3.2](#), [2.5](#)
- Helfand, D. J. 1983, in *IAU Symp. 101: Supernova Remnants and their X-ray Emission*, ed. J. Danziger & P. Gorenstein, 471–484 [5.1](#)
- Hessels, J. W. T., Ransom, S. M., Stairs, I. H., et al. 2006, *Science*, 311, 1901 [1.1](#)
- Hester, J. J., Mori, K., Burrows, D., et al. 2002, *ApJ*, 577, L49 [3.4.4](#)
- Hester, J. J., Scowen, P. A., Sankrit, R., et al. 1995, *ApJ*, 448, 240 [3.4.1](#), [3.4.1](#)
- Hewish, A., Bell, S. J., Pilkington, J. D., Scott, P. F., & Collins, R. A. 1968, *Nature*, 217, 709 [1.1](#), [1.1](#)
- Hirayama, M., Nagase, F., Endo, T., Kawai, N., & Itoh, M. 2002, *MNRAS*, 333, 603
[4.1](#)
- Hulse, R. A. & Taylor, J. H. 1974, *ApJ*, 191, L59 [1.1](#)
- Jessner, A., Słowikowska, A., Klein, B., et al. 2005, *Advances in Space Research*, 35, 1166 [2.2](#), [6](#)
- Johnston, S. & Romani, R. W. 2003, *ApJ*, 590, L95 [4.1](#)
- Jones, D. H. P., Smith, F. G., & Wallace, P. T. 1981, *MNRAS*, 196, 943 [1.4](#), [3.1](#),
[3.4.3](#), [3.4.4](#)
- Kaaret, P., Marshall, H. L., Aldcroft, T. L., et al. 2001, *ApJ*, 546, 1159 [4.1](#), [4.4](#), [4.4](#)
- Kanbach, G. 2002, in *Neutron Stars, Pulsars, and Supernova Remnants*, ed. W. Becker, H. Lesch, & J. Trümper, 91 [1.4](#)
- Kanbach, G., Kellner, S., Schrey, F. Z., et al. 2003, in *SPIE Proc. Instrument Design and Performance for Optical/Infrared Ground-based Telescopes*, ed. M. Iye & A. F. M. Moorwood, Vol. 4841, 82–93 [3.2.2](#), [3.1](#), [3.2](#)
- Kanbach, G., Słowikowska, A., Kellner, S., & Steinle, H. 2005, in *AIP Conf. Proc. 801: Astrophysical Sources of High Energy Particles and Radiation*, ed. T. Bulik, B. Rudak, & G. Madejski, 306–311 [3.5](#), [3.27](#)

BIBLIOGRAPHY

- Karastergiou, A., Jessner, A., & Wielebinski, R. 2004, in IAU Symp. 218: Young Neutron Stars and Their Environments, ed. F. Camilo & B. M. Gaensler, 329–330 [2.4.2](#), [3.5](#)
- Kaspi, V. M. & Helfand, D. J. 2002, in ASP Conf. Ser. 271: Neutron Stars in Supernova Remnants, ed. P. O. Slane & B. M. Gaensler, 3 [1.2](#)
- Kellner, S. 2002, Master’s thesis, TU-München [3.2.2](#)
- Kern, B., Martin, C., Mazin, B., & Halpern, J. P. 2003, ApJ, 597, 1049 [3.1](#)
- Knight, H. S., Bailes, M., Manchester, R. N., & Ord, S. M. 2006, astro-ph/0608155 [2.6](#)
- Konacki, M., Lewandowski, W., Wolszczan, A., Doroshenko, O., & Kramer, M. 1999, ApJ, 519, L81 [5.4.4](#)
- Kramer, M., Karastergiou, A., Gupta, Y., et al. 2003, A&A, 407, 655 [2.6](#)
- Kramer, M., Stairs, I. H., Manchester, R. N., et al. 2006, Science, 1132305 [1.1](#), [1.2](#)
- Kramer, M., Xilouris, K. M., Jessner, A., et al. 1997, A&A, 322, 846 [5.5](#), [5.7](#)
- Kristian, J., Visvanathan, N., Westphal, J. A., & Snellen, G. H. 1970, ApJ, 162, 475 [3.1](#)
- Kuiper, L., Hermsen, W., Bennett, K., et al. 1998, A&A, 337, 421 [5.4.1](#)
- Kuiper, L., Hermsen, W., Cusumano, G., et al. 2001, A&A, 378, 918 [B](#)
- Kuiper, L., Hermsen, W., Krijger, J. M., et al. 1999, A&A, 351, 119 [B](#)
- Kuiper, L., Hermsen, W., Walter, R., & Foschini, L. 2003, A&A, 411, L31 [3.4.2](#)
- Large, M. I., Vaughan, A. E., & Mills, B. Y. 1968, Nature, 220, 340 [1.1](#)
- Lattimer, J. M. & Prakash, M. 2001, ApJ, 550, 426 [1.1](#)
- Lattimer, J. M. & Prakash, M. 2004, Science, 304, 536 [1.1](#), [5.1](#)
- Lorimer, D. R. 2005, Living Reviews in Relativity, 8, 7 [1.3](#)
- Lorimer, D. R. & Kramer, M. 2005, Book Review: Handbook of Pulsar Astronomy, Cambridge Observing Handbooks for Research Astronomers (Cambridge University Press) [2.1](#)

BIBLIOGRAPHY

- Lundgren, S. C., Cordes, J. M., Ulmer, M., et al. 1995, *ApJ*, 453, 433 [2.2](#), [2.4.1](#)
- Lyne, A. G., Brinklow, A., Middleditch, J., Kulkarni, S. R., & Backer, D. C. 1987, *Nature*, 328, 399 [1.1](#)
- Lyne, A. G., Burgay, M., Kramer, M., et al. 2004, *Science*, 303, 1153 [1.1](#)
- Manchester, R. N., Fan, G., Lyne, A. G., & Kaspi, V. M. 2006, *ApJ*, 649, 235 [1.3](#)
- Manchester, R. N., Hobbs, G. B., Teoh, A., & Hobbs, M. 2005, *AJ*, 129, 1993 [1](#)
- Manchester, R. N., Lyne, A. G., Camilo, F., et al. 2001, *MNRAS*, 328, 17 [1.1](#)
- Manchester, R. N., Mar, D. P., Lyne, A. G., Kaspi, V. M., & Johnston, S. 1993, *ApJ*, 403, L29 [4.1](#), [4.1](#)
- Mazzuca, L., Sparks, W. B., & Axon, D. 1998, Instrument Science Report NICMOS 98-017, (Baltimore: STScI) [3.3.4](#)
- McLean, I. S., Aspin, C., & Reitsema, H. 1983, *Nature*, 304, 243 [3.4.1](#)
- Melrose, D. 2004, in *IAU Symp. 218: Young Neutron Stars and Their Environments*, ed. F. Camilo & B. M. Gaensler, 349 [1.4](#)
- Michel, F. C. 1991, *Theory of neutron star magnetospheres* (Chicago, IL, University of Chicago Press, 1991, 533 p.) [5.6](#)
- Middleditch, J. & Pennypacker, C. 1985, *Nature*, 313, 659 [4.1](#)
- Middleditch, J., Pennypacker, C. R., & Burns, M. S. 1987, *ApJ*, 315, 142 [3.1](#)
- Mignani, R. P., de Luca, A., & Caraveo, P. A. 2004, in *IAU Symp. 218: Young Neutron Stars and Their Environments*, ed. F. Camilo & B. M. Gaensler, 391 [1.4](#), [3.1](#)
- Mignani, R. P., De Luca, A., Caraveo, P. A., & Becker, W. 2002, *ApJ*, 580, L147 [1.4](#)
- Mineo, T., Cusumano, G., Massaro, E., et al. 1999, *A&A*, 348, 519 [4.1](#)
- Moffett, D. A. & Hankins, T. H. 1996, *ApJ*, 468, 779 [1.6](#), [2.1](#), [2.3](#)
- Moffett, D. A. & Hankins, T. H. 1999, *ApJ*, 522, 1046 [2.4.2](#), [3.5](#)
- Mühlegger, M. 2006, Master's thesis, TU-München [3.3.5](#)

BIBLIOGRAPHY

- Muslimov, A. G. & Harding, A. K. 2003, ApJ, 588, 430 [1.4](#)
- Muslimov, A. G. & Harding, A. K. 2004, ApJ, 606, 1143 [1.4](#)
- Nasuti, F. P., Mignani, R., Caraveo, P. A., & Bignami, G. F. 1997, A&A, 323, 839 [3.4.4](#)
- Nather, R. E., Warner, B., & Macfarlane, M. 1969, Nature, 221, 527 [2.1](#)
- Neckel, T., Klare, G., & Sarcander, M. 1980, A&AS, 42, 251 [5.6.1](#)
- Neugebauer, G., Becklin, E. E., Kristian, J., et al. 1969, ApJ, 156, L115 [2.1](#)
- Ng, C.-Y. & Romani, R. W. 2006, ApJ, 644, 445 [3.4.1](#)
- Oosterbroek, T., de Bruijne, J. H. J., Martin, D., et al. 2006, astro-ph/0606146 [3.4.2](#)
- Oppenheimer, J. R. & Volkoff, G. M. 1939, Phys. Rev., 55, 374 [1.1](#)
- Ostriker, J. P. & Gunn, J. E. 1969, ApJ, 157, 1395 [1.2](#)
- Pacini, F. 1967, Nature, 216, 567 [1.1](#)
- Pacini, F. 1971, ApJ, 163, L17 [3.4.4](#)
- Paerels, F. B. S. & Heise, J. 1989, ApJ, 339, 1000 [5.5](#)
- Pavlov, G. G., Stringfellow, G. S., & Cordova, F. A. 1996, ApJ, 467, 370 [5.4.1](#), [5.6.1](#)
- Percival, J. W., Biggs, J. D., Dolan, J. F., et al. 1993, ApJ, 407, 276 [3.4.2](#), [3.4.3](#)
- Peterson, B. A., Murdin, P., Wallace, P., et al. 1978, Nature, 276, 475 [3.1](#), [3.4.3](#)
- Pétri, J. & Kirk, J. G. 2005, ApJ, 627, L37 [1.4](#), [3.5](#), [3.6](#)
- Radhakrishnan, V. & Cooke, D. J. 1969, Astrophys. Lett., 3, 225 [3.1](#)
- Rankin, J. M., Campbell, D. B., Isaacman, R. B., & Payne, R. R. 1988, A&A, 202, 166 [2.4.2](#)
- Rankin, J. M., Comella, J. M., Craft, H. D., et al. 1970, ApJ, 162, 707 [2.2](#), [2.4](#)
- Richards, D. W. & Comella, J. M. 1969, Nature, 222, 551 [1.1](#), [2.1](#)
- Romani, R. W. 1996, ApJ, 470, 469 [1.4](#)

BIBLIOGRAPHY

- Romani, R. W., Miller, A. J., Cabrera, B., Nam, S. W., & Martinis, J. M. 2001, *ApJ*, 563, 221 [2.6](#), [3.4.2](#)
- Rots, A. H., Jahoda, K., & Lyne, A. G. 2004, *ApJ*, 605, L129 [3.4.2](#)
- Ruderman, M. A. & Sutherland, P. G. 1975, *ApJ*, 196, 51 [1.4](#), [5.5](#)
- Sallmen, S., Backer, D. C., Hankins, T. H., Moffett, D., & Lundgren, S. 1999, *ApJ*, 517, 460 [2.2](#)
- Sanwal, D. 1999, PhD thesis, The University of Texas at Austin [3.4.2](#)
- Serafimovich, N. I., Shibanov, Y. A., Lundqvist, P., & Sollerman, J. 2004, *A&A*, 425, 1041 [4.1](#)
- Seward, F. D., Alpar, M. A., Flanagan, C., et al. 2000, *ApJ*, 536, 948 [B](#)
- Seward, F. D., Harnden, F. R., & Helfand, D. J. 1984, *ApJ*, 287, L19 [1.1](#), [4.1](#)
- Seward, F. D. & Wang, Z.-R. 1988, *ApJ*, 332, 199 [5.1](#), [5.6](#)
- Shearer, A. & Golden, A. 2002, in *Neutron Stars, Pulsars, and Supernova Remnants*, ed. W. Becker, H. Lesch, & J. Trümper, 44 [1.4](#)
- Shearer, A., Stappers, B., O'Connor, P., et al. 2003, *Science*, 301, 493 [2.6](#), [3.4.2](#)
- Słowikowska, A., Jessner, A., Klein, B., & Kanbach, G. 2005a, in *AIP Conf. Proc. 801: Astrophysical Sources of High Energy Particles and Radiation*, ed. T. Bulik, B. Rudak, & G. Madejski, 324–329 [2.4.2](#), [3.5](#), [6](#)
- Słowikowska, A., Kuiper, L., & Hermsen, W. 2005b, *A&A*, 434, 1097 [5.2](#), [5.3](#), [5.8](#), [6](#)
- Smith, F. G., Jones, D. H. P., Dick, J. S. B., & Pike, C. D. 1988, *MNRAS*, 233, 305 [1.4](#), [3.1](#), [3.4.1](#), [3.8](#), [3.4.3](#), [3.4.4](#), [3.5](#), [3.26](#)
- Sparks, W. B. & Axon, D. J. 1999, *PASP*, 111, 1298 [3.3.4](#), [3.3.4](#), [3.3.4](#)
- Staelin, D. H. & Reifenstein, E. C. 1968, *Science*, 162, 1481 [1.1](#), [1.1](#), [2.1](#), [2.1](#)
- Stairs, I. H. 2004, *Science*, 304, 547 [1.1](#)
- Standish, Jr., E. M. 1982, *A&A*, 114, 297 [3.3.2](#)
- Straubmeier, C. 2001, PhD thesis, TU-München [3.2.2](#), [3.3.2](#), [3.4.2](#)

BIBLIOGRAPHY

- Sun, X., Trumper, J., Dennerl, K., & Becker, W. 1993, *IAU Circ.*, 5895, 2 [5.1](#)
- Swanepoel, J. W. H., de Beer, C. F., & Loots, H. 1996, *ApJ*, 467, 261 [5.4.1](#)
- Taylor, J. H. & Cordes, J. M. 1993, *ApJ*, 411, 674 [4.1](#)
- Taylor, J. H. & Weisberg, J. M. 1989, *ApJ*, 345, 434 [1.2](#)
- Tennant, A. F., Becker, W., Juda, M., et al. 2001, *ApJ*, 554, L173 [1.5](#)
- Thompson, D. J. 2004a, in *IAU Symp. 218: Young Neutron Stars and Their Environments*, ed. F. Camilo & B. M. Gaensler, 399 [1.4](#), [1.5](#)
- Thompson, D. J. 2004b, in *ASSL Vol. 304: Cosmic Gamma-Ray Sources*, ed. K. S. Cheng & G. E. Romero, 149 [1.4](#), [1.5](#)
- Thorsett, S. E., Arzoumanian, Z., McKinnon, M. M., & Taylor, J. H. 1993, *ApJ*, 405, L29 [1.1](#)
- Turnshek, D. A., Bohlin, R. C., Williamson, II, R. L., et al. 1990, *AJ*, 99, 1243 [3.3.5](#), [3.4](#), [3.3.5](#)
- van Leeuwen, J., Cordes, J. M., Lorimer, D. R., et al. 2006, *astro-ph/0604392* [1.1](#)
- Verbunt, F., Kuiper, L., Belloni, T., et al. 1996, *A&A*, 311, L9 [5.6](#)
- von Hoensbroech, A. & Xilouris, K. M. 1997, *A&A*, 324, 981 [5.5](#), [5.7](#)
- Walter, R., Rodriguez, J., Foschini, L., et al. 2003, *A&A*, 411, L427 [4.4](#)
- Wampler, E. J., Scargle, J. D., & Miller, J. S. 1969, *ApJ*, 157, L1 [3.1](#)
- Wang, F. Y.-H. & Halpern, J. P. 1997, *ApJ*, 482, L159 [5.2](#), [5.8](#)
- Wang, Q. D., Li, Z.-Y., & Begelman, M. C. 1993, *Nature*, 364, 127 [5.7](#)
- Weisberg, J. M., Cordes, J. M., Kuan, B., et al. 2004, *ApJS*, 150, 317 [2.4.2](#)
- Weisberg, J. M., Cordes, J. M., Lundgren, S. C., et al. 1999, *ApJS*, 121, 171 [5.5](#)
- Welsh, B. Y., Vedder, P. W., Vallergera, J. V., & Craig, N. 1991, *ApJ*, 381, 462 [5.5](#)
- Wolszczan, A. & Frail, D. A. 1992, *Nature*, 355, 145 [1.1](#)
- Woltjer, L. 1957, *Bull. Astron. Inst. Netherlands*, 13, 301 [3.4.1](#)

BIBLIOGRAPHY

- Woods, P. M. & Thompson, C. 2004, Soft Gamma Repeaters and Anomalous X-ray Pulsars: Magnetar Candidates [1.2](#)
- Yakovlev, D. G. & Pethick, C. J. 2004, ARA&A, 42, 169 [5.1](#)
- Yancopoulos, S., Hamilton, T. T., & Helfand, D. J. 1994, ApJ, 429, 832 [5.2](#), [5.8](#)
- Young, M. D., Manchester, R. N., & Johnston, S. 1999, Nature, 400, 848 [1.1](#), [1.2](#)
- Zavlin, V. E. & Pavlov, G. G. 1998, A&A, 329, 583 [5.4.1](#)
- Zavlin, V. E. & Pavlov, G. G. 2004, ApJ, 616, 452 [5.4.1](#)